Inaugural dissertation

for

obtaining the doctoral degree

of the

Combined Faculty of Mathematics, Engineering and Natural Sciences

of the

Ruprecht - Karls - University

Heidelberg

Presented by

M.Sc. Ann-Kathrin Mehnert

Born in: Bruchsal, Germany

Oral examination: 25.07.2025

Dissecting Antiviral Immune Evasion by the Hepatitis E Virus ORF2 Protein in Persistent Hepatocyte Infection

Referees: Prof. Dr. Ralf Bartenschlager

Dr. Viet Loan Dao Thi

Acknowledgments

First and foremost, I would like to express my deepest gratitude to my supervisor, Dr. Viet Loan Dao Thi, for granting me the opportunity to pursue my PhD within her research group. Dear Loan, your support, encouragement, and mentorship have guided me safely through the past five years. I am sincerely thankful for your continuous availability for scientific discussions, as well as for your readiness to listen to any concerns or challenges I faced along the way. I truly appreciate the many opportunities for both professional and personal growth that you have offered me.

My sincerest gratitude goes to Prof. Dr. Ralf Bartenschlager for kindly agreeing to serve as the first referee for my dissertation as well as for his valuable scientific advice during my TAC meetings and the weekly seminars of the Department for Molecular Virology. I am likewise grateful to Prof. Dr. Alexander Dalpke and Prof. Dr. Martin Müller for generously agreeing to be part of my PhD defense committee.

Further, I would like to acknowledge Prof. Dr. Volker Lohmann and Prof. Dr. Maike Hofmann for their support as members of my TAC committee, as well as Dr. Marco Binder and Prof. Dr. Steeve Boulant for their invaluable scientific input throughout my PhD.

This PhD project would not have been possible without the contributions from numerous collaboration partners. I am particularly grateful to Sebastian Stegmaier and Dr. Vladimir Gonçalves Magalhães from the group of Dr. Marco Binder for conducting the overexpression experiments in A549 cells and sharing their valuable expertise on cell-intrinsic antiviral signaling. I would also like to acknowledge Dr. Carlos Ramírez Álvarez from the group of Prof. Dr. Carl Herrmann for performing the scRNA-seq analysis, as well as Dr. Thibault Tubiana for the AlphaFold modeling. My sincere thanks further go to Daniel Kirrmaier from the research group of Prof. Dr. Michael Knop and to Céline Schneider from the research group of Prof. Dr. Henrik Kaessmann for kindly sharing reagents and equipment during the library preparation for the scRNA-seq experiment. Finally, I am grateful for the expert support provided by Dr. Vibor Laketa, Dr. Sylvia Olberg, and Dr. Severina Klaus from the IDIP Imaging Facility.

I am deeply grateful to all current and former PhD students of the Dao Thi lab with whom I had the pleasure of working: Charlotte Decker, Rebecca Fu, Huanting Chi, Jungen Hu, Sarah Prallet, Patrick Bröscky, Elif Toprak, and Paula Jordan. Your companionship both in and outside of the lab, your support, and our shared scientific curiosity created an inspiring environment that made this journey truly enjoyable. A big thank you goes to Andrew Freistaedter, whose tireless efforts keep the lab running smoothly.

I would like to extend my sincere gratitude to the remaining groups at the CIID, in particular the Departments for Virology and Molecular Virology, for generously sharing reagents and their expertise. I am also thankful to the Collaborative Research Center TRR179 for funding my PhD and fostering a collaborative environment that enabled scientific exchange and allowed me to connect with many inspiring fellow researchers. In addition, I would like to acknowledge the graduate schools HBIGS and IRTG for providing an academic framework throughout my PhD.

During the course of this PhD, I had the pleasure of supervising eight talented Bachelor's and Master's students, whose dedication and hard work significantly contributed to advancing this project: Gülcan Gerstner, Carl Niklas Schneider, Miriam Martens, Valentina Neukel, Noa Gamet, Lena Sarah Müller, Yllka Kabashi, and Carla Siebenkotten. A special thank you goes to Carla, whose tremendous support during the final months of experiments was invaluable.

This dissertation has been proofread and reviewed by Vladimir Gonçalves Magalhães, Valentina Neukel, and Patrick Bröscky, to whom I am deeply grateful for their valuable feedback and constructive input.

Finally, I would like to express my heartfelt gratitude to my family and all my friends for their unfailing support and constant encouragement throughout this journey. Especially to my parents Petra and Michael and my brother Pascal – thank you for your love and your belief in me, for making everything possible, and for always supporting the paths I chose. To Katharina and Annika – thank you for staying in (or returning to) Heidelberg after our Master's and for facing the challenges of a PhD together. To Tina – how lucky I am to have gained a great friend by supervising your Master's thesis. And to my partner Fabian – you entered my life during the most demanding time of this PhD, and I am beyond grateful that you chose to walk through it with me.

To all those who have accompanied, supported, and inspired me along the way, thank you!

Summary

Hepatitis E virus (HEV) is a major cause of acute viral hepatitis worldwide. While genotype 1 (HEV-1) and HEV-2 exclusively result in acute infections, HEV-3 and HEV-4 infections are at a high risk of becoming chronic in immunocompromised individuals. HEV is a single-stranded RNA virus encoding three viral proteins: the viral replicase, ORF1, the capsid protein, ORF2, and ORF3, a protein essential for virion release. In hepatocytes, HEV induces a cell-intrinsic antiviral response through the expression of type III interferons (IFNs) and IFN-stimulated genes (ISGs). HEV replication can persist despite this sustained antiviral signaling, suggesting the presence of immune evasion strategies. Even though all viral proteins have been proposed to antagonize antiviral and inflammatory signaling pathways, their contributions to persistent HEV replication remain unclear. To identify the determinants of HEV persistence, I aimed to perform a comprehensive characterization of the HEV-induced cell-intrinsic antiviral response across different hepatocellular systems, in bulk and at the single-cell level.

First, I evaluated the integrity of the relevant antiviral and inflammatory signaling pathways in the hepatoma cell line HepG2/C3A and pluripotent stem cell-derived hepatocyte-like cells (HLCs). I further sought to identify the pattern recognition receptors (PRRs) specifically contributing to HEV sensing. Then, I aimed to assess the viral antagonisms mediated by the HEV proteins ORF2 and ORF3. In a comprehensive side-by-side comparison, I found that ORF2 from HEV-3 and HEV-1, rather than ORF3, interferes with antiviral and inflammatory signaling downstream of PRRs. By co-immunoprecipitation, I demonstrated that ORF2 directly interacts with TANK binding kinase 1 (TBK1), a central hub of antiviral signaling, through an unidentified interaction motif. To clarify the impact of the ORF2-mediated antagonism in the context of full-length HEV infection, I exploited HEV-3 mutants lacking expression of ORF2 (ΔORF2) or ORF3 (ΔORF3). Electroporation with ΔORF2 RNA and infection with trans-complemented ΔORF2 virus particles in HepG2/C3A cells and HLCs resulted in significantly impaired viral replication. This was a direct consequence of the increased expression of antiviral response genes due to the absent TBK1 inhibition, which is mediated by intracellular ORF2. Using spatial RNA fluorescence *in situ* hybridization and single-cell RNA-sequencing, I demonstrated that both actively infected cells and uninfected bystanders are the sources of the ISG response in HEV infection. In both cell types, a similar ISG subset was induced, which was globally enhanced in the absence of the ORF2 protein. These findings emphasized the persistence of HEV replication in a directly antiviral environment. Moreover, I observed that ΔORF2 replication is more vulnerable to the effectors of the antiviral response, revealing an additional and hitherto unrecognized, protective function of ORF2. Using a synchronized infection approach, I found that ORF2 drives the establishment of a balance between HEV

replication and the antiviral response, following a replication-limiting bottleneck early in infection. I concluded that the various identified strategies of antiviral immune evasion mediated by ORF2 are essential for enabling persistent HEV replication in the presence of a sustained yet dampened IFN and ISG response.

The results obtained during the course of my PhD, which are presented in this dissertation, contribute to elucidating the multifaceted functions of the capsid protein ORF2 within the HEV life cycle. They further identify the antiviral immune evasion strategies mediated by ORF2 as central determinants for persistent HEV replication in hepatocytes. My findings thus provide a foundation for exploring the crosstalk between HEV-infected hepatocytes and professional immune cells in the future, and for the investigation of intergenotypic differences in the antiviral response. Ultimately, these studies will provide novel insights into decisive factors for the pathogenesis of acute and chronic manifestations of HEV infection.

Zusammenfassung

Das Hepatitis-E-Virus (HEV) ist weltweit eine der Hauptursachen für akute virale Hepatitis. Während Genotyp 1 (HEV-1) und HEV-2 ausschließlich akute Infektionen hervorrufen, können Infektionen mit HEV-3 und HEV-4 insbesondere bei immungeschwächten Individuen mit einem hohen Risiko zu chronischen Verläufen führen. HEV ist ein einzelsträngiges RNA-Virus, das für drei virale Proteine kodiert: die viral Replikase ORF1, das Kapsidprotein ORF2, und ORF3, welches für die Freisetzung neuer Virionen essenziell ist. In Hepatozyten verursacht HEV eine zellintrinsische antivirale Antwort, die sich durch die Expression von Typ-III-Interferon und Interferon-stimulierten Genen auszeichnet. Die HEV-Replikation persistiert trotz dieser bestehenden antiviralen Antwort, was auf das Vorhandensein von Mechanismen zur Immunevasion hindeutet. Laut bisheriger Studien haben alle HEV-Proteine das Potenzial, die antivirale Immunantwort zu inhibieren. Die genaue Relevanz dieser Mechanismen für die HEV-Replikation ist jedoch noch nicht geklärt. Mit dem Ziel, zentrale Faktoren der HEV-Persistenz zu identifizieren, habe ich die durch HEV induzierte antivirale Immunantwort in verschiedenen hepatozellulären Modellsystemen umfassend charakterisiert – sowohl auf der Ebene der Gesamtzellpopulation als auch auf der Einzelzellebene.

Zunächst evaluierte ich die Vollständigkeit und Funktionalität der relevanten antiviralen und inflammatorischen Signalwege in der Hepatomzelllinie HepG2/C3A und in hepatozytenähnlichen Zellen (*hepatocyte-like cells*, HLCs), die ich aus pluripotenten Stammzellen differenziert hatte. Darüber hinaus versuchte ich, die Mustererkennungs-rezeptoren (*pattern recognition receptors*, PRRs) zu identifizieren, die zur HEV-Erkennung durch die antivirale Antwort beitragen. Anschließend war es mein Ziel, die Inhibitionsstrategien der viralen Proteine ORF2 und ORF3 zu charakterisieren. In einem umfassenden, direkten Vergleich kam ich zu dem Ergebnis, dass das ORF2-Protein von HEV-1 und HEV-3 – nicht jedoch das ORF3-Protein – mit antiviralen und inflammatorischen Signalwegen, ausgehend von den PRRs, interferiert. Mittels Co-Immunpräzipitation konnte ich zeigen, dass ORF2 direkt mit der TANK-bindenden Kinase 1 (TBK1), einer zentralen Komponente der antiviralen Antwort, interagiert. Die Bindestelle des ORF2-Proteins konnte jedoch nicht identifiziert werden. Um den Einfluss der TBK1-Inhibition durch ORF2 auf die HEV-Infektion zu analysieren, nutzte ich HEV-3-Mutanten, die entweder das ORF2-Protein (ΔORF2) oder das ORF3-Protein (ΔORF3) nicht exprimierten. Mittels Elektroporation der ΔORF2-Mutante oder durch Infektion mit transkomplementierten ΔORF2-Virionen in HepG2/C3A-Zellen oder HLCs stellte ich eine verringerte virale Replikation fest. Ursache dieses Phänotyps war eine verstärkte Expression von Genen der antiviralen Antwort aufgrund der fehlenden TBK1-Inhibition durch das intrazelluläre ORF2-Protein. Mithilfe von RNA-Fluoreszenz-in-situ-Hybridisierung und Einzelzell-RNA-Sequenzierung stellte ich fest, dass die antivirale Antwort

sowohl von aktiv infizierten Zellen als auch von umgebenden, uninfizierten Zellen, den sogenannten Bystander-Zellen, ausgelöst wird. In beiden Zelltypen wurde die Expression ähnlicher antiviraler Gene induziert, jedoch deutlich stärker in Abwesenheit des ORF2-Proteins. Diese Erkenntnisse wiesen verstärkt darauf hin, dass die HEV-Replikation inmitten einer antiviralen Umgebung persistiert. Darüber hinaus konnte ich zeigen, dass die Replikation der ΔORF2-Mutante empfindlicher gegenüber den Effektormolekülen der antiviralen Antwort ist, was auf eine zusätzliche, bislang unbekannte protektive Funktion des ORF2-Proteins hinweist. Mithilfe eines synchronisierten Infektionsexperiments konnte ich zeigen, dass das ORF2-Protein eine zentrale Rolle bei der Etablierung eines Gleichgewichts zwischen viraler Replikation und antiviraler Antwort spielt, das infolge eines replikationslimitierenden Engpasses früh in der Infektion entsteht. Ich schlussfolgerte, dass die von mir identifizierten Strategien der Immunevasion durch das ORF2-Protein entscheidend für eine persistierende HEV-Replikation sind, die trotz einer kontinuierlichen, jedoch abgeschwächten antiviralen Antwort aufrechterhalten wird.

Die Erkenntnisse meiner Doktorarbeit haben wesentlich dazu beigetragen, die vielfältigen Funktionen des HEV-Kapsidproteins ORF2 im HEV-Lebenszyklus weiter aufzuklären. Darüber hinaus konnte ich die durch das ORF2-Protein vermittelten Strategien der Immunevasion als zentrale Faktoren für die HEV-Persistenz identifizieren. Diese Ergebnisse bilden eine Grundlage für zukünftige Studien, die sowohl die Interaktion zwischen HEV-infizierten Hepatozyten und professionellen Immunzellen als auch Unterschiede in der durch verschiedene HEV-Genotypen ausgelösten antiviralen Antwort analysieren werden. Letztlich werden solche Untersuchungen neue Einblicke in entscheidende Faktoren der Pathogenese akuter und chronischer HEV-Infektionen ermöglichen.

Table of Contents

List of Figures

List of Tables

List of Abbreviations

βTRCP	Beta-transducin repeat containing protein
AAV	Adeno-associated virus
AFP	Alphafetoprotein
ALB	Albumin
ALR	Absent in melanoma-2 (AIM2)-like receptors
APC	Antigen-presenting cell
ARM	Arginine-rich motif
BMP4	Bone morphogenetic protein 4
bp	Base pair(s)
CARD	Caspase activation and recruitment domain
CCL	CC-chemokine ligand
cDNA	Complementary DNA
cGAMP	Cyclic guanosine monophosphate-adenosine monophosphate
cGAS	cGAMP synthase
CLR	C-type lectin receptor
Co-IP	Co-immunoprecipitation
CpG	Cytosine-phosphate-guanine
CRE	*Cis*-reactive element
CRISPR	Clustered regularly interspaced short palindromic repeats
crRNA	CRISPR RNA
Cryo-EM	Cryo-electron microscopy
CTD	C-terminal domain
DAMP	Damage-associated molecular pattern
DC	Dendritic cell
DC-SIGN	Dendritic cell-specific intercellular adhesion molecule 3-grabbing non-integrin
DE	Definitive endoderm
Dectin	Dendritic cell-associated C-type lectin
DKO	Double knockout
DSB	Double strand break
dsDNA	Double-stranded DNA
dsRNA	Double-stranded RNA
eHEV	Quasi-enveloped hepatitis E virus
EPO	Electroporation
ER	Endoplasmic reticulum
ERGIC	ER-Golgi intermediate compartment
ESCRT	Endosomal sorting complexes required for transport
GE	Genome equivalents
GEM	Gel bead in emulsion
GFP	Green fluorescent protein
gRNA	Genomic RNA
HAV	Hepatitis A virus
HBV	Hepatitis B virus
HCV	Hepatitis C virus
Hel	Helicase
HepProg	Hepatocyte progenitor
hESC	Human embryonic stem cell
HGF	Hepatocyte growth factor
HIV	Human immunodeficiency virus
HLC	Hepatocyte-like cell
HNF4α	Hepatocyte nuclear factor 4 alpha
HR	Homologous recombination
HRP	Horseradish peroxidase
HVR	Hypervariable region
IκBα	Inhibitor of kappa B alpha
IAV	Influenza A virus
IF	Immunofluorescence
IFIT1	Interferon-induced protein with tetratricopeptide repeats 1
IFITM	Interferon-induced transmembrane protein
IFN	Interferon
IFNAR	Interferon alpha/beta receptor
IFNLR1	Interferon lambda receptor 1
IgG	Immunoglobulin G
IKK	Inhibitor of kappa B (IκB) kinase
IL	Interleukin
IL10RB	Interleukin 10 receptor subunit beta
imHep	Immature hepatocyte
Indel	Insertion-deletion
INV	Inversion
IRAK	Interleukin-1 receptor-associated kinase
IRF	Interferon regulatory factor
iPSC	Induced pluripotent stem cell
ISG	Interferon-stimulated gene
ISG15	Interferon-stimulated gene 15
ISGF3	Interferon-stimulated gene factor 3
ISRE	Interferon-stimulated regulatory element
IVT	*In vitro* transcribed
JAK	Janus kinase
JR	Junction region
kb	Kilobases
KO	Knockout
LGP2	Laboratory of genetics and physiology 2
LPS	Lipopolysaccharide
LSEC	Liver sinusoidal endothelial cell
MAPK	Mitogen-activated protein kinase
MAVS	Mitochondrial antiviral signaling protein
MDA5	Melanoma differentiation-associated protein 5
MEF	Mouse embryonic fibroblast
MeT	Methyltransferase
MOI	Multiplicity of infection

mRNA	Messenger RNA
MVB	Multivesicular body
Mx1	Myxovirus resistance protein 1
MyD88	Myeloid differentiation primary response protein 88
NF-κB	Nuclear factor kappa B
NHEJ	Non-homologous end joining
nHEV	Naked hepatitis E virus
NK cell	Natural killer cell
NLR	Nucleotide oligomerization domain (NOD)-like receptor
OAS2	Oligoadenylate synthetase 2
Oct-4A	Octamer-binding transcription factor 4A
ORF	Open reading frame
ORF2c	Cleaved ORF2
ORF2g	Glycosylated ORF2
ORF2i	Intracellular ORF2
OSM	Oncostatin M
PAMP	Pathogen-associated molecular pattern
PBMC	Peripheral blood mononuclear cell
PCP	Papain-like cysteine protease
PCR	Polymerase chain reaction
pDC	Plasmacytoid dendritic cell
PHH	Primary human hepatocytes
PRR	Pattern recognition receptor
RBV	Ribavirin
RdRp	RNA-dependent RNA polymerase
RIG-I	Retinoic acid-inducible gene I
RIP1	Receptor interacting protein 1
RLR	RIG-I-like receptor
RNA-FISH	RNA fluorescence *in situ* hybridization
RNP	Ribonucleoprotein
RT	Reverse transcription
RT-qPCR	Quantitative reverse transcription polymerase chain reaction
SARS-CoV-2	Severe acute respiratory syndrome coronavirus 2
SDS-PAGE	Sodium dodecyl sulfate polyacrylamide gel electrophoresis
scRNA-seq	Single-cell RNA-sequencing
SeV	Sendai virus
SFTSV	Severe fever with thrombocytopenia syndrome virus
sgRNA	Subgenomic RNA
shRNA	Short hairpin RNA
SN	Supernatant
ssRNA	Single-stranded RNA
STAT	Signal transducer and activator of transcription
STING	Stimulator of interferon genes
TAK1	Transforming growth factor β-activated kinase-1
TANK	TRAF family member associated NF-κB activator
TBK1	TANK binding kinase 1
TIR	Toll/Interleukin-1 receptor
TLR	Toll-like receptor
TNF	Tumor necrosis factor
TNFAIP3	Tumor necrosis factor-induced protein 3
tracrRNA	*Trans*-acting RNA
TRAF	Tumor necrosis factor receptor-associated factor
TRIM5α	Tripartite motif-containing protein 5 alpha
TRIF	TIR domain-containing adaptor protein inducing IFNβ
TXN	Transfection
TYK2	Tyrosine kinase 2
UMAP	Uniform manifold approximation and projection
UTR	Untranslated region
VLP	Virus-like particle
WT	Wild type

1 Introduction

1.1 Hepatitis E Virus

Hepatitis E virus (HEV) was recognized for the first time in 1978 during a major hepatitis outbreak in Kashmir Valley in India[1]. In 1983, the etiological agent of this enterically transmitted acute non-A, non-B hepatitis was isolated and later termed HEV[2]. What was initially believed to be a solely waterborne disease in lower-income countries with poor sanitary conditions was later also found to impact industrialized countries. In the 1990s, a novel HEV genotype was isolated from domestic pigs in the United States[3], and since then, seroprevalence among humans has been detected in the United States, Europe, and many higher-income countries[4,5]. Due to the mild or entirely absent symptoms in most cases and the resulting lack of control, hepatitis E has been referred to as a "silent epidemic" of Europe[6]. Despite significant advancements in research over the past decades, HEV remains an understudied pathogen among the hepatitis viruses.

1.1.1 Epidemiology and Pathogenesis of Hepatitis E

HEV is one of the leading causes of acute hepatitis worldwide. According to the World Health Organization, 20 million HEV infections occur annually, of which 3.3 million cases are symptomatic. These numbers have been mathematically modeled based on HEV genotype 1 (HEV-1) and HEV-2 incidences in Africa and Asia in 2005[7]. In 2015, 44,000 deaths have been attributed to hepatitis E[8]. Based on immunoglobulin G (IgG) seropositivity, a recent meta-analysis estimated that approximately 12.5% of the global population and 9.3% of the European population have experienced HEV infections[9]. The highest seroprevalence of 21.8% is found in Africa[10,11].

HEV is classified within the *Hepeviridae* family, which is divided into the subfamilies of *Orthohepevirinae*, associated with mammals and birds, and *Parahepevirinae*, which exclusively contains the fish-infecting genus *Piscihepevirus*[12]. In contrast to the *Parahepevirinae*, the host ranges of the four genera classified within the *Orthohepevirinae* are more diverse. Members of the *Paslahepevirus* genus are found in different mammals, while the *Avihepevirus* genus is restricted to birds, mainly chickens. Viruses from the *Rocahepevirus* genus infect rodents, and the *Chirohepevirus* genus is found in bats. Eight genotypes have been assigned to the *Paslahepevirus balayani* species, of which five have been associated with human infections. HEV-1 and HEV-2 are restricted to humans, whereas HEV-3 and HEV-4 can infect a wider range of host species, including humans, domestic pigs, and wild boars. HEV-3 additionally infects deer, rabbits, and dolphins. The natural hosts, transmission routes, clinical manifestations, and geographic distribution of HEV-1 to HEV-4 are summarized in

Table 1. HEV-5, HEV-6, and HEV-8 of the *Paslahepevirus balayani* species have only been detected in non-human mammals, however, a single spillover event from camel to human has been reported for HEV-7[13]. Only recently, zoonotic transmission of rat HEV to humans, classified within the *Rocahepevirus ratti* species, has been discovered in China[14] and subsequently, also in Canada[15] and Europe[16].

Table 1: Characteristics of the HEV genotypes that infect humans.

HEV genotype	Natural hosts	Transmission routes	Clinical manifestations	Geographic distribution
HEV-1	Humans	Fecal-oral through drinking water contamination	Self-limiting, acute hepatitis Fulminant hepatitis in pregnant women	China, Indian subcontinent, Northern Africa
HEV-2	Humans	Fecal-oral through drinking water contamination	Self-limiting, acute hepatitis	Central Africa, Mexico
HEV-3	Humans, pigs, wild boars, deer, rabbits, dolphins	Zoonotic through animal products Blood transfusions	Self-limiting, acute hepatitis Chronic in immunocompromised individuals	Argentina, Australia, Europe, Japan, New Zealand, USA
HEV-4	Humans, pigs, wild boars	Zoonotic through animal products Blood transfusions	Self-limiting, acute hepatitis Chronic in immunocompromised individuals	Eastern China, Japan, Vietnam

While HEV-1 is endemic to China and lower-income countries of the Indian subcontinent and Northern Africa, HEV-2 has mostly been detected in Mexico and Central Africa (reviewed in [17]). Sporadic and locally confined waterborne transmissions are usually the result of drinking water contaminations with human feces in areas with poor sanitation conditions (reviewed in [17]). They have been attributed to broken water pipelines, consumption of water from rivers or shallow wells, or insufficient chlorination of water supplies[17,18].

HEV-3 has been found on every continent and is distributed across higher-income regions, including Europe, the United States, some Latin American countries, Japan, Australia, and New Zealand, whereas detection of HEV-4 is limited to eastern China, Japan, and Vietnam (reviewed in [19]). Transmission of HEV-3 and HEV-4 to humans occurs zoonotically and, in most cases, through the consumption of animal products, such as undercooked meat (reviewed in [19]). Domestic pigs are the main source of HEV-3 and HEV-4 infections, followed by wild boars. In 2021, one study estimated a global HEV seroprevalence of 60% among domestic pigs and an active infection rate of 13%[20]. A German study found that 10% of pork liver and liver sausages tested positive for HEV RNA between 2019 and 2020[21]. Although the presence of HEV RNA is not a direct evidence for infectivity, it reinforces the risk for zoonotic transmission of HEV through meat products. Furthermore, several studies have found that the

HEV seroprevalence among pig farmers, slaughterhouse workers, and forestry workers is higher than that of the general population (reviewed in [22]), suggesting that close contact with infected animals increases the risk for transmission. Furthermore, animal feces can contaminate agricultural watering systems and thereby result in an accumulation of HEV on fruits and vegetables (reviewed in [19,23]). Lastly, blood transfusions remain an underestimated route of HEV transmission (reviewed in [24]). Although the estimated prevalence of infectious blood donations is significantly below 1%, specifically 0.19% in Germany[25], transfusion-transmitted HEV poses a major risk for immunocompromised patients.

Hepatitis E usually manifests as acute, self-limiting hepatitis, resolving in less than one month[8]. Infections with HEV can remain asymptomatic or result in typical symptoms of acute hepatitis, such as nausea, malaise, abdominal pain, and jaundice[8]. It is generally associated with 1–2% fatality rate in immunocompetent patients due to acute liver failure. Fulminant cases of hepatitis can develop in pregnant women following HEV-1 infection during the third trimester, linked to a 25% maternal mortality or fetal stillbirth rate (reviewed in [26,27]). The reasons for these fatal outcomes remain unclear, but contributing factors might be the altered immune status of the pregnant mother to protect the fetus, or nutritional deficiencies (reviewed in [27]). Infections with HEV-3 and HEV-4 can progress to chronicity in immunocompromised individuals, potentially leading to liver fibrosis and cirrhosis (reviewed in [19,26]). Vulnerable patient groups include solid organ transplant recipients and individuals living with human immunodeficiency virus (HIV)/acquired immunodeficiency syndrome (AIDS).

Until today, there is no HEV-specific direct antiviral treatment available. Acute hepatitis E does usually not require antiviral therapy due to its self-limiting progression. Among solid organ transplant recipients with chronic hepatitis E, viral clearance is achieved in one third of cases by lowering the immunosuppressive therapy (reviewed in [28]). Treatment with PEGylated interferon alpha (IFNα) can be used in liver transplant patients but is contraindicated for many other solid organ transplantations (reviewed in [28]). Off-label use of the nucleoside analogue ribavirin (RBV) has been more extensively applied (reviewed in [28]), but several viral mutants with enhanced replication or reduced sensitivity to RBV treatment have emerged[29-31]. Hecolin, an effective capsid-derived HEV vaccine, has only been licensed in China (reviewed in [32]).

HEV infections have been associated with numerous extrahepatic manifestations, most commonly neurological symptoms such as Guillain-Barré syndrome, along with renal, pancreatic, and hematological manifestations (reviewed in [33]). Even though HEV can replicate in neurons and cell lines derived from other human tissue[34-36], a causal relationship between HEV infection and these extrahepatic manifestations has not been confirmed. Immune complex deposits have been suggested as a potential mechanism of renal manifestations[37].

1.1.2 Molecular Virology of HEV

The genome of HEV is a positive-sense, single-stranded RNA (ssRNA) molecule of approximately 7.2 kilobases (kb) in length (Figure 1). As the 5'-untranslated region (UTR) is capped with a 7-methylguanosine cap, and the 3'-UTR is polyadenylated, the HEV genome resembles a typical eukaryotic messenger RNA (mRNA). The genomes of HEV-2 to HEV-4 encode three open reading frames (ORFs), designated as *ORF1*, *ORF2*, and *ORF3* (reviewed in [26,38]). HEV-1 additionally encodes a small *ORF4,* located within the *ORF1* sequence and only expressed under endoplasmic reticulum (ER) stress to enhance viral replication[39]. The nucleotide sequences of *ORF2* and *ORF3* partially overlap, with the first nucleotide of the *ORF3* start codon located 11 nucleotides upstream of *ORF2*. Different *cis*-reactive elements (CREs), characterized by stem loop structures, have been identified within the HEV genome and are important for viral replication[40-42]. The 23-nucleotide junction region (JR) between the coding sequences of *ORF1* and *ORF2/3* also forms a stem loop structure[43]. This intragenomic promoter regulates the synthesis of the bicistronic subgenomic RNA (sgRNA)[44], which is also capped and polyadenylated (Figure 1). While the ORF1 protein is directly translated from the genomic RNA (gRNA) using the host's translation machinery, the ORF2 and ORF3 proteins are synthesized from the sgRNA template[45]. The immediate translation ORF1 initiates viral replication as this protein harbors the domains of the viral replicase. Newly produced full-length gRNA and the smaller, approximately 2.2 kb-long sgRNA are synthesized from an antisense replication intermediate (Figure 1; reviewed in [26,38]).

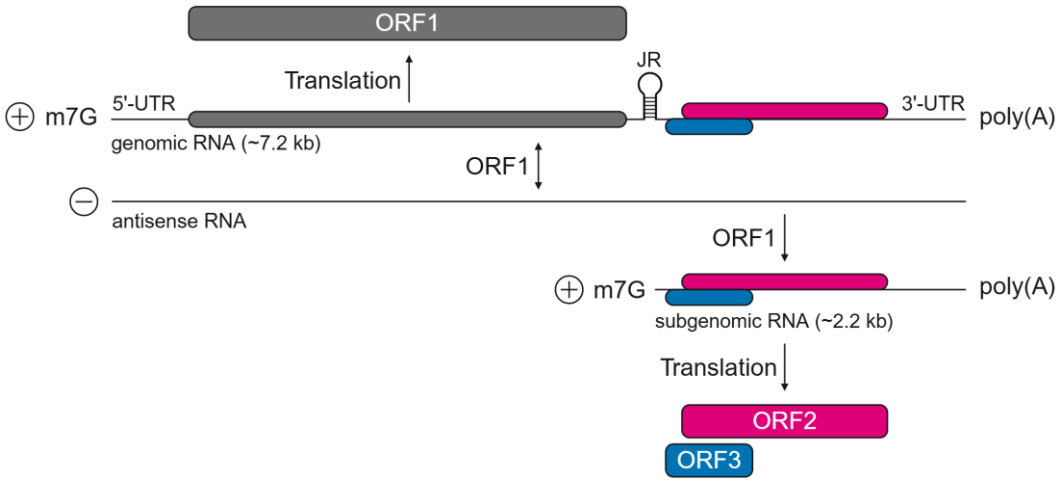

Figure 1: The HEV genome, viral RNA species, and translation of viral proteins.
The HEV genome is a positive-sense, ssRNA with a length of ~7.2 kilobases (kb), containing a 7-methylguanosine (m7G) cap at the start of the 5'-untranslated region (UTR) and a poly(A) tail at the end of the 3'-UTR. The junction region (JR) between the coding sequences of *ORF1* and *ORF2/3* contains a stem loop structure that serves as the promoter for the ~2.2 kb subgenomic RNA. The ORF1 protein is directly translated from the genomic RNA and mediates replication via an antisense RNA intermediate. The ORF2 and ORF3 proteins are translated from the subgenomic RNA, which is also capped and polyadenylated. (Created with BioRender.com)

The viral replicase ORF1

Originally, the seven putative functional domains of the large non-structural HEV ORF1 polyprotein (Figure 2) have been inferred by computational sequence comparison with other positive-strand RNA viruses[46]. The methyltransferase (MeT) domain has been suggested to possess guanine-7-methyltransferase and guanylyl transferase activities, indicating its probable role in HEV genome capping[47]. The functions of the Y domain remain elusive, but it has recently been proposed to serve as an extension of the MeT domain, based on sequence comparisons with members of the alphavirus-like virus superfamily[48]. One of the most controversial ORF1 domains is the papain-like cysteine protease (PCP), predicted due to its sequence similarity with the protease domain of rubella virus[46]. For many positive-strand RNA viruses, such as flaviviruses or alphaviruses, polyprotein processing into functional subunits by a virus-encoded protease is an integral part of their life cycle (reviewed in [49]). However, the protease activity of the PCP and processing of the ORF1 polyprotein remain a matter of debate, as many studies have presented conflicting results. Instead, ORF1 might act as a non-processed polyprotein with flexible subdomains guiding its activity (reviewed in [49,50]). The hypervariable region (HVR) of the ORF1 polyprotein differs in sequence and in length between HEV genotypes. Many insertions and mutations have been discovered in the HVRs of virus isolates from chronic patients, which are likely important for host adaptation (reviewed in [50]). Furthermore, the presence of a conserved region in the HVR of zoonotically transmitted HEV genotypes suggests a role in transmission and species tropism[51]. The functions of the X domain, also called the macrodomain, have not been studied in detail. In contrast, the predicted helicase (Hel) domain of ORF1 is likely involved in unwinding RNA duplex structures during viral replication. And lastly, the RNA-dependent RNA polymerase (RdRp) is responsible for the synthesis of new viral RNA molecules, binding to the 3'-end and the poly(A) tail of the HEV genome[52]. It further contains a conserved GDD amino acid motif, essential for the catalytic activity of the RdRp by binding of divalent magnesium ions, as shown for rubella virus[53].

Importantly, recent studies employing AlphaFold for three-dimensional protein structure predictions identified only five functional ORF1 domains, interconnected by the disordered HVR: a combined MeT-Y domain, a domain similar to a fatty acid binding domain (FABD), followed by X, Hel, and RdRp[54,55] (Figure 2). Notably, a PCP or protease-like domain was absent in these predictions. Together with the growing evidence for the lack of ORF1 processing, our understanding of this viral protein is currently changing.

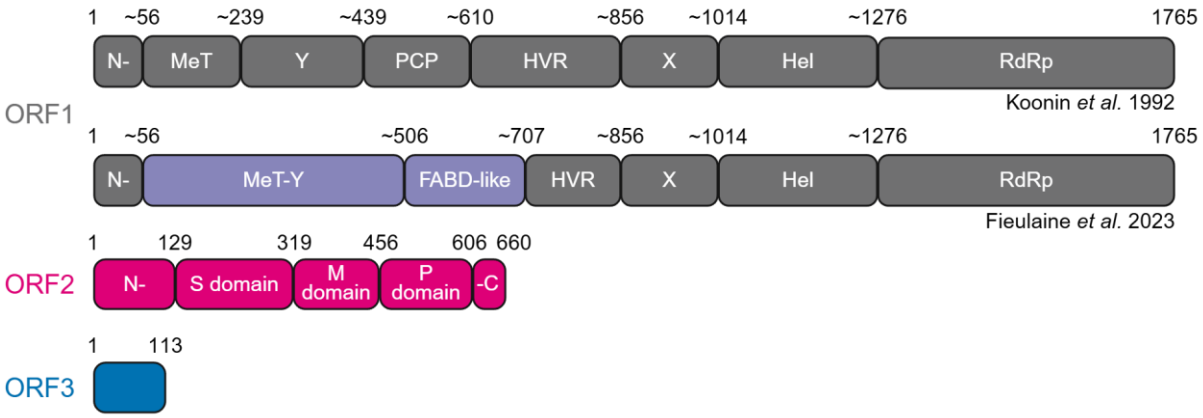

Figure 2: Sizes and functional domains of the HEV proteins ORF1, ORF2, and ORF3.
According to Koonin *et al.*[46], the ORF1 protein domains downstream of the N-terminal region include a methyltransferase (MeT), the Y domain, a papain-like cysteine protease (PCP) domain, the hypervariable region (HVR), the X domain, a helicase (Hel) and the RNA-dependent RNA polymerase (RdRp). In contrast, Fieulaine *et al.*[54], together with another study[55], proposed only five domains: a combined MeT-Y domain and a domain reminiscent of a fatty acid binding domain (FABD), both highlighted in purple, alongside the previously suggested X, Hel, and RdRp domains, connected by the unstructured HVR. The ORF2 protein has been divided into the following domains: the N-terminal region, the shell (S) domain, the middle (M) domain, the protruding (P) domain, and a C-terminal region. The ORF3 protein consists of 113 amino acids. The numbers in this figure indicate amino acid positions of the respective protein in the HEV-3 Kernow-C1/p6 strain, which harbors an insertion in the HVR[56,57], although the original analysis by Koonin *et al.*[46] was based on an HEV-1 strain. (Created with BioRender.com)

The multifunctional capsid protein ORF2

The HEV ORF2 protein has first been recognized as the structural component of the viral capsid. While the native, icosahedral HEV capsid, which has a diameter of 27–30 nm, displays a triangulation number of T = 3, most structural studies have been based on virus-like particles (VLPs) with a T = 1 symmetry (reviewed in [58]). Upon expression in insect cells, the first 111 and the last 52 amino acids are proteolytically cleaved, and the resulting truncated ORF2 protein assembles into VLPs[59]. Analysis of the crystal structure revealed three domains: the shell (S) domain, forming the surface of the VLP, the middle (M) domain, building protrusions, and the protruding (P) domain, which constitutes the spikes that likely interact with the host cell receptor[60] (Figure 2 and Figure 3). A study suggested that ORF2 interacts with the 5'-end of the viral genome[61], and cryo-electron microscopy (cryo-EM) revealed that the N-terminal portion of ORF2 likely interacts with the viral RNA[62]. Moreover, the capsid-associated ORF2 found in feces of patients is truncated by 58 amino acids at the C-terminus (Figure 3), suggesting proteolytic cleavage of the capsid subunits in the intestine[63].

Many studies in recent years have proposed that the ORF2 protein is more versatile than solely constituting the viral capsid. To date, at least three different ORF2 isoforms have been identified (Figure 3). Their functions, however, require further clarification. Two glycosylated isoforms, ORF2g and the cleaved ORF2c, starting at amino acids S34 and S102[64], respectively, are found in cell culture supernatants and patient sera[65-67]. They likely serve as

immunological decoys as they are recognized by patient antibodies[64,66]. Both isoforms are glycosylated at positions N137 and N562[64] (Figure 3), but they also carry O-glycosylations and sialylations, which remain poorly characterized[64,66,67]. A 23-amino acid signal peptide, located at the N-terminus of ORF2 (Figure 3), guides the protein to the ER for secretion along the secretory pathway[66]. Unlike ORF2g and ORF2c, the intracellular ORF2 isoform (ORF2i) is not glycosylated[66,67]. While it also gives rise to the structural component of the viral capsid, ORF2i has been suggested to fulfill multiple functions, and it likely interacts with various cellular proteins[68-70]. Apart from its main localization in the cytosol, nuclear translocation of ORF2i has also been reported[64,69].

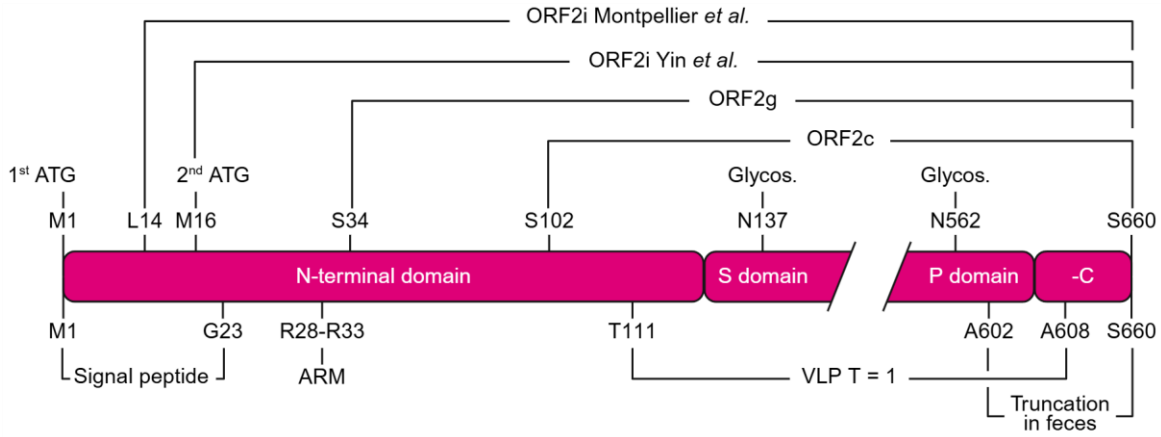

Figure 3: Domains, isoforms, and post-translational modifications of the HEV ORF2 protein.
Downstream of the first start codon (ATG), the HEV ORF2 protein encodes an N-terminal signal peptide, followed by an arginine-rich motif (ARM). The intracellular ORF2 isoform (ORF2i) was reported to start at L14[67] or M16[66], the latter constituting the second putative start codon of ORF2. The glycosylated ORF2 (ORF2g) and cleaved ORF2 (ORF2c) isoforms, starting at amino acids S34 and S102, are derived from the first start codon by proteolytic cleavage. They are N-glycosylated (Glycos.) at positions N137 and N562. The self-assembling virus-like particle (VLP) with a triangulation number of T = 1 is obtained from amino acids T111 to A608. Capsid-derived ORF2 found in feces of patients has a C-terminal truncation starting from A602. (Created with BioRender.com)

There is conflicting evidence on how the three ORF2 isoforms are generated. Yin and colleagues have identified two start codons, M1 and M16, located at the N-terminus of the ORF2 sequence[66] (Figure 3). By individual mutations, they proposed that ORF2g is derived from the first start codon, whereas ORF2i is expressed from the second one. Accordingly, they identified M16 as the first amino acid of ORF2i using mass spectrometry. In contrast, a different study reported ORF2i to start at position L14[67] (Figure 3). It was suggested that an N-terminal arginine-rich motif (ARM) with the sequence RRRGRR, located at positions 28 to 33 (Figure 3), might serve as the master regulator of ORF2 maturation, expressed from the first start codon[69]. Mutation of the ARM resulted in enhanced secretion of ORF2g and a decrease in intracellular ORF2i. In addition, the nuclear translocation of ORF2i was abrogated, suggesting that this motif also functions as a nuclear localization signal. Three putative nuclear export signals have been identified in the ORF2 sequence[69]. The authors proposed a model where the N-terminus of the ORF2 polypeptide is co-translationally inserted into the ER membrane,

guided by its signal peptide[69]. This is followed by cleavage of the signal peptide, translocation of the ORF2 polypeptide into the ER, post-translational modification such as glycosylation, and proteolytic cleavage to give rise to ORF2g and ORF2c, which are then released along the secretory pathway[69]. Alternatively, the positive charge of the ARM can favor cytosolic retention of ORF2, resulting in proteolytic cleavage at L14 to give rise to ORF2i. The detailed mechanism of this proposed regulation by the ARM has not been elucidated yet. Until today, it remains unclear whether the three ORF2 isoforms are produced from the two putative start codons, or whether they are processed from a single ORF2 polyprotein, regulated by the ARM.

The accessory protein ORF3

The small HEV protein ORF3 has a length of only 113 amino acids (Figure 2). It is phosphorylated at residue S70[71], and a hydrophobic, cysteine-rich region at its N-terminus is palmitoylated, likely mediating its membrane association[72]. Several studies have established that the ORF3 protein is essential for the release of newly assembled virions *in vitro* and *in vivo* along the exosomal pathway[73,74], but it is dispensable for virus attachment, entry, replication, and virion assembly[75]. Virion budding is specifically mediated by the interaction of a PSAP motif in ORF3 with the endosomal sorting complexes required for transport (ESCRT) machinery protein Tsg101[76,77]. Furthermore, the ORF3 protein was suggested to possess ion channel activity, likely also essential for virion release[78].

1.1.3 The HEV Life Cycle

The liver is the body's largest solid internal organ and fulfills a myriad of functions in synthesis, storage, and redistribution of macromolecules as well as in detoxification of harmful substances (reviewed in [79]). Due to the constant exposure to microbial products, pathogens, and harmless food antigens from the gut, the liver is also a central immune tissue that maintains a balance between tolerance and activation (reviewed in [80,81]). Within the roughly hexagonal liver lobules, the blood from the portal vein is combined with blood from the hepatic artery in the sinusoids (Figure 4). The liver sinusoidal endothelial cells (LSECs) are fenestrated with pores, making them highly permeable to allow access of the blood to the underlying thin, brick-like layers of hepatocytes. These are, with approximately 60% of the total cell population, the most abundant cell type of the liver. Along with their many other functions, hepatocytes produce bile, which is secreted apically into the bile canaliculi (Figure 4). These drain into the bile ducts, which are lined with cholangiocytes and establish a connection back to the gastrointestinal tract (Figure 4). Together, hepatocytes and cholangiocytes constitute the parenchymal cell types of the liver. Apart from the LSECs, the non-parenchymal cell types include Kupffer cells and hepatic stellate cells. Kupffer cells are liver-resident macrophages, which are statically positioned at the endothelial lining, monitoring the blood circulation for

pathogens and microbial molecules (reviewed in [80]). The hepatic stellate cells are positioned in the subendothelial space, they interact with immune cells, and are key players in chronic liver inflammation and fibrogenesis (reviewed in [82]).

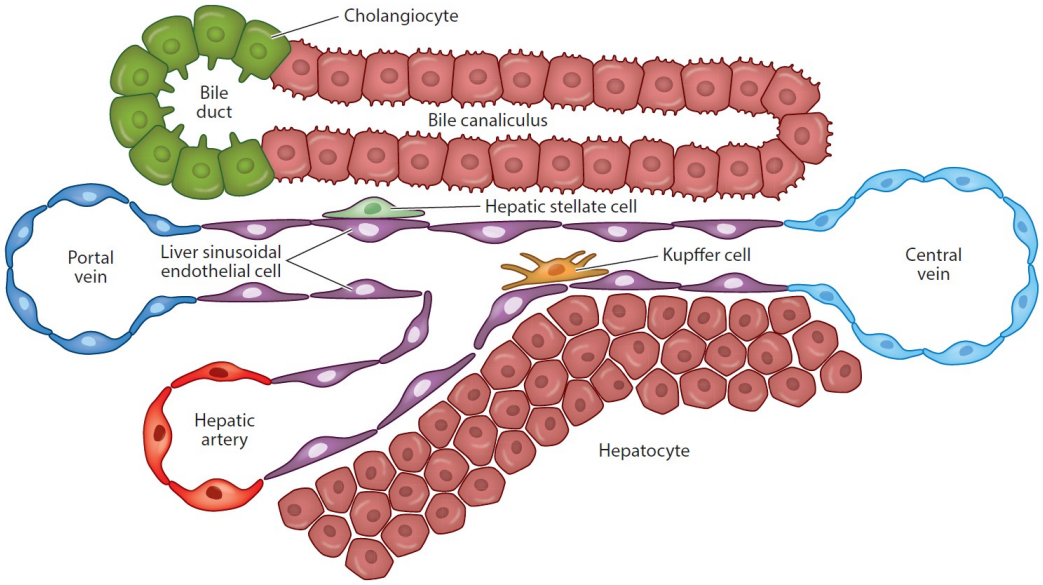

Figure 4: The microanatomy of the human liver.
Blood from the portal vein and the hepatic artery are combined in the liver sinusoids, which drain into the central vein. The fenestrated liver sinusoidal endothelial cells allow access of the blood to the basolateral side of the hepatocytes. The apical sides of the hepatocytes are exposed to bile canaliculi. Bile secreted from the hepatocytes is transported to the bile duct, which is lined with cholangiocytes. Liver-resident macrophages, the Kupffer cells, are positioned on the luminal side of the endothelial lining, while the hepatic stellate cells are located in the subendothelial space, called the Space of Disse. Adapted from Bram et *al.*[83]

HEV is transmitted enterically along the gut-liver axis (Figure 5) and enters the body in most cases through the digestive tract. Similar to hepatitis A virus (HAV), HEV is as a non-enveloped virus that acquires a host membrane-derived quasi-envelope, devoid of viral glycoproteins, upon budding from infected cells (reviewed in [84]). The highly infectious naked HEV (nHEV) is ingested orally and excreted in the stool of patients, whereas quasi-enveloped HEV (eHEV) is found in the bloodstream[85,86]. The first barrier that HEV encounters is the intestinal epithelium. ORF2 protein found in intestinal biopsies from a chronically infected patient, together with the capacity of HEV to replicate in intestinal cell culture systems, indicate that HEV causes active infection of the intestinal epithelium[76,87]. However, virions are mainly released apically from polarized intestinal epithelial cells[76,87]. As the bloodstream is located at the basolateral side, it remains unclear how HEV virions cross the intestinal epithelial barrier. HEV reaches the liver through the portal vein and is thought to infect hepatocytes from their basolateral side. Following replication in hepatocytes, eHEV is shed apically into the bile canaliculi, leading to the bile duct, where the quasi-envelope is removed by the action of bile acids[86,87], and consequently, nHEV is shed with the feces[88,89]. A small portion of eHEV is released basolaterally into the bloodstream[86,87], likely enabling spread within the host.

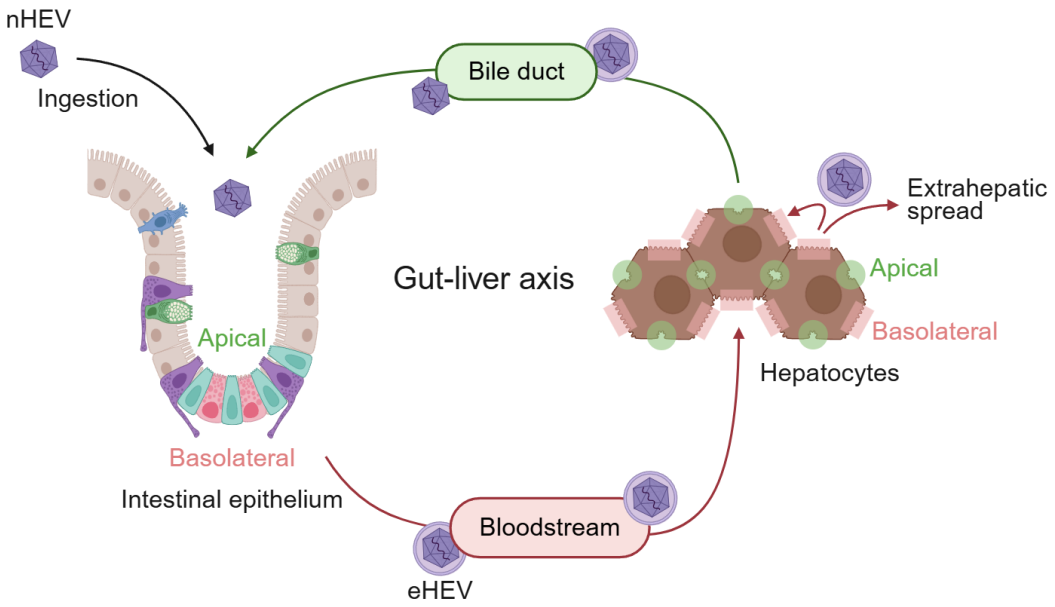

Figure 5: Transmission of HEV along the gut-liver axis.
Naked HEV (nHEV) is ingested orally and crosses the intestinal epithelial barrier along an unknown route to reach the bloodstream. Quasi-enveloped HEV (eHEV) circulates in the bloodstream, infects hepatocytes from their basolateral side, and is secreted apically from hepatocytes into the bile duct, where the quasi-envelope is removed by bile acids. Basolaterally secreted eHEV potentially reinfects hepatocytes and spreads within the host. (Created with BioRender.com)

HEV entry

Due to the different accessibilities of ORF2, nHEV and eHEV likely infect their target cells through different pathways (reviewed in [90]). The *bona fide* entry receptor for HEV has not yet been identified, but several attachment factors have been suggested. Heparan sulfate proteoglycans[91], glucose-related protein 78[92], epidermal growth factor receptor[93], and several integrins, including integrin α3[94], integrin α2 (personal note from Rebecca Fu, Research group of Dr. Viet Loan Dao Thi), and integrin β1[95] have been associated with attachment of nHEV to hepatocytes. In contrast, eHEV entry appears to be, at least partially, mediated by the phosphatidylserine receptor TIM-1, as the quasi-envelope is enriched in phosphatidylserines[96]. The mechanisms of nHEV internalization through endocytosis remain controversial. One study suggested that nHEV does not traffic through the early and late endosomes, which are characterized by the presence of the small guanosine triphosphate hydrolases (GTPases) Rab5 and Rab7, respectively[86], but penetrates close to the plasma membrane. The work of my colleague Rebecca Fu, together with another study, however, indicated that nHEV enters through the Rab11-positive recycling endosome, converges with the Rab7-positive late endosome, and later requires the lysosome for release of the genome into the target cell[95,97]. In contrast, eHEV is internalized through clathrin-mediated endocytosis and traffics through the early and late endosomes to the lysosome, where the genome is released[86,95].

HEV replication

Upon release of the HEV gRNA into the cell, the viral replicase ORF1 is translated by the host's translation machinery. As described in chapter 1.1.2, HEV replication produces an antisense RNA intermediate, from which the full-length viral genome and the sgRNA are transcribed. Many positive-strand RNA viruses replicate in the cytoplasm and remodel host membranes to create so-called replication organelles, concentrating the components of the replication machinery and shielding the viral RNA from recognition by the host cell (reviewed in [98]). However, such virus-induced membrane alterations have not been observed in HEV-infected cells, and the replication site has not been conclusively determined. Some studies suggested associations with the endosomal network and the endocytic recycling compartment, as demonstrated by the co-localization of HEV RNA, ORF1, ORF2, and ORF3 proteins with specific markers, such as Rab5, CD63, or Rab11[99-102]. On the other hand, connections with the ER-Golgi-intermediate compartment (ERGIC) and multivesicular bodies (MVBs) have been made[99,100,103]. The true HEV replication site therefore remains to be identified.

HEV assembly and release

Similarly, the assembly site of HEV virions has not been determined, but it is likely closely linked to the replication compartment[100,101,103]. Nonetheless, it has been established that the ORF3 protein is indispensable for the successful secretion of newly assembled virions from cells (reviewed in [104]). Through its conserved PSAP motif, ORF3 interacts with Tsg101, resulting in ESCRT-mediated budding of HEV virions into MVBs[76,77]. Upon fusion with the plasma membrane, quasi-enveloped virions are released from infected cells, resembling exosome-like particles[105]. The contribution of the proposed ion channel function of ORF3 to viral egress remains uncertain[78].

1.2 The Cell-Intrinsic Innate Immunity

Humans are constantly exposed to a variety of different pathogens. To prevent infections, the human immune system has evolved as a tightly regulated network of different cell types and a multitude of protective mechanisms. At the same time, damage to the host must be limited by preventing self-recognition. The innate immune system provides a rapid but non-specific response to pathogens within hours. In contrast, the adaptive immune system responds with a delay, but it specifically adapts to the immunogenic antigens of the individual pathogens. Elimination of an infection can thus only be achieved through the intricate interplay between innate and adaptive immune responses (reviewed in [106-108]).

The innate immune system comprises physical barriers, such as the different mucosal linings of the human body, innate immune cell types, and effector molecules. Dendritic cells (DCs)

possess typical protrusions to monitor their environment and engulf pathogens and pathogen-derived molecules through endocytosis, phagocytosis, and micropinocytosis (reviewed in [109]). Immunogenic antigens are processed and presented to naïve T cells, which constitutes an essential link between innate and adaptive immunity. Similarly, macrophages phagocytose pathogens and also serve as antigen-presenting cells (APCs). Natural killer (NK) cells recognize activating stimuli on infected or aberrant host cells and mediate targeted cell death by release of perforin and granzymes, or they induce apoptosis without affecting healthy tissue (reviewed in [110]). A complex network of secreted effector molecules and the components of the complement system circulating in the blood complete the repertoire of the innate immune system (reviewed in [106-108]). Secreted effector molecules include cytokines, which are essential for activation and recruitment of immune cells as well as intercellular communication (reviewed in [106-108]). They are classified into different categories, including interleukins (ILs), IFNs, tumor necrosis factors (TNFs), and chemokines (reviewed in [111]). Cytokine secretion is induced upon recognition of pathogen-associated molecular patterns (PAMPs) by specialized receptors in innate immune cells, but also in the target cells of a pathogen, which is further described below.

The effectors of the adaptive immune response comprise T lymphocytes, B lymphocytes, and antibodies produced by activated B lymphocytes (reviewed in [106-108]). Characteristic features of these cells are the antigen-specific T cell and B cell receptors, which are generated by arbitrary gene segment rearrangements, a process called V(D)J recombination (reviewed in [112]). Different lymphocyte subsets, including CD4+ and CD8+ T cells, serve dedicated functions in the adaptive immune response. Upon encountering their specific antigen, naïve CD4+ T cells differentiate into various subtypes that fulfill immunomodulatory functions. CD8+ T cells become cytotoxic T lymphocytes (reviewed in [106-108]), which directly kill infected cells in an antigen-dependent manner through induction of apoptosis or release of perforin and granzymes. Activated B cells differentiate to plasma cells and produce antigen-specific antibodies. Both T lymphocytes and B lymphocytes give rise to memory cells that ensure long-lasting protection and a more rapid response of the adaptive immune system in the event of a second encounter with the same or a closely related pathogen (reviewed in [106-108]).

1.2.1 Pathogen Sensing by Pattern Recognition Receptors

Cytokine production in phagocytic innate immune cells and other cell types, such as epithelial cells, endothelial cells, and fibroblasts, is activated through the pathways of the so-called cell-intrinsic innate immunity. Proposed for the first time in 1989[113], it is well established today that conserved microbial structures and nucleic acids are recognized as PAMPs by specialized, germline-encoded pattern recognition receptors (PRRs) (reviewed in [114]). Furthermore, recent findings indicate that endogenous molecules, produced by damaged or stressed cells, can also

be sensed by PRRs as damage-associated molecular patterns (DAMPs) (reviewed in [114]). Intracellular DAMPs include adenosine triphosphate (ATP), several heat shock proteins, and mitochondrial DNA. Extracellular DAMPs mostly comprise degradation products of extracellular matrix components (reviewed in [115]). The PRRs that sense PAMPs and DAMPs are classified into five groups, based on protein homology: Toll-like receptors (TLRs), retinoic acid-inducible gene-I (RIG-I)-like receptors (RLRs), nucleotide oligomerization domain (NOD)-like receptors (NLRs), C-type lectin receptors (CLRs), and absent in melanoma-2 (AIM2)-like receptors (ALRs) (reviewed in [108,116]). These PRRs are distributed across the cell surface, on intracellular membranous compartments, or in the cytosol. They recognize a multitude of different PAMPs, including lipids, proteins, lipopolysaccharides, and nucleic acids, and the downstream effects of PRR activation are diverse (Table 2). As RLRs and TLRs are of the highest relevance for this study, they are described in more detail in separate sections below.

NLRs, CLRs, and cytosolic DNA sensors

NLRs are located in the cytosol and have a tripartite structure, consisting of leucine-rich repeats for PAMP binding, a nucleotide-binding domain facilitating oligomerization, and effector domains responsible for interaction with downstream signaling components (reviewed in [116]). NLR family members such as NOD1 and NOD2 recognize cell wall components of Gram-negative and Gram-positive bacteria, resulting in nuclear factor kappa B (NF-κB)-dependent inflammatory cytokine production (reviewed in [117]). Members of the NLRP subfamily can be activated by a variety of different PAMPs and DAMPs. Subsequent oligomerization of NLRP3 results in inflammasome formation, activation of caspase 1, and cleavage and release of IL-1β. This eventually leads to an inflammatory cell death called pyroptosis (reviewed in [118]).

CLRs are mainly found at the surface of APCs, and their specificities for fungal β-glucans, bacterial polysaccharides, or carbohydrates present on viral envelopes are determined by a carbohydrate binding region. Some prominent examples include DC-associated C-type lectins (Dectins) as well as DC-specific intercellular adhesion molecule 3-grabbing non-integrin (DC-SIGN), which mostly activate inflammatory signaling (reviewed in [114,119]).

Lastly, cytosolic PRRs that recognize double-stranded DNA (dsDNA) include ALRs and the cyclic guanosine monophosphate-adenosine monophosphate (cGAMP) synthase (cGAS). Cytosolic dsDNA can originate from genomes of bacteria or DNA viruses, or from mitochondrial DNA released upon cellular damage or stress. Activation of AIM2 results in the formation of the AIM2 inflammasome, leading to IL-1β cleavage by caspase 1 and pyroptosis through cleavage of gasdermin D (reviewed in [120]). Activated cGAS in turn produces cGAMP, a substrate that triggers the activation of the stimulator of IFN genes (STING) on the ER, resulting in IFN and inflammatory cytokine production (reviewed in [121,122]).

Table 2: The five classes of PRRs.

PRR class	Example members	Sensed PAMPs/DAMPs	Subcellular localization	Activated pathways
Toll-like receptors (TLRs)	- TLR4 - TLR3 - TLR7/8 - TLR9	- LPS - dsRNA - ssRNA - Unmethylated CpG DNA	Plasma membrane (TLR4) Endosomal membrane (TLR3/7/8/9)	IRF3/7 signaling, NF-κB signaling, MAPK signaling
RIG-I-like receptors (RLRs)	- RIG-I - MDA5	- Atypical 5'-ends of short dsRNA - Long/complex dsRNA	Cytosol	IRF3/7 signaling, NF-κB signaling
NOD-like receptors (NLRs)	- NOD1, NOD2 - NLRP3	- Bacterial peptidoglycans - Various DAMPs and PAMPs	Cytosol	- NF-κB signaling - NLRP3 inflammasome
C-type lectin receptors (CLRs)	- Dectin 1, Dectin 2, DC-SIGN	Carbohydrates (e.g., fungal, bacterial, viral)	Plasma membrane	NF-κB signaling
AIM2-like receptors (ALRs) and cytosolic PRRs sensing dsDNA	- AIM2 - cGAS	dsDNA (e.g., viral, bacterial, mitochondrial)	Cytosol	- AIM2 inflammasome - IRF3/7 signaling, NF-κB signaling

Sensing and signaling by TLRs

TLRs are the largest family of PRRs known to date and were the first to be described in the late 1990s (reviewed in [123]). They are transmembrane proteins with N-terminal leucine-rich repeats, which adopt a horseshoe-like structure and are involved in PAMP recognition. In addition, they contain a transmembrane domain and a cytoplasmic C-terminal Toll/Interleukin-1 receptor (TIR) domain, involved in signal transduction and located at the opposite side of the membrane (reviewed in [124]). The first identified TLR ligand was lipopolysaccharide (LPS), a component of the outer membrane of Gram-negative bacteria sensed by TLR4[125]. The human genome harbors ten TLR genes, of which six gene products are located on the plasma membrane at the cell surface, namely TLR1, TLR2, TLR4, TLR5, TLR6, and TLR10. While all other TLRs function as homodimers, TLR2 can heterodimerize with TLR1 or TLR6 to recognize triacylated or diacylated bacterial lipopeptides, respectively, but TLR2 also recognizes non-lipopeptidic PAMPs from different pathogens. The ligand of TLR10 remains unknown, but heterodimerization with TLR2 has been suspected due to a distinct sequence similarity with TLR1. TLR5 was shown to sense bacterial flagellin (reviewed in [123]). Although the TLRs on the plasma membrane are primarily linked to bacterial PAMPs, recognition of viral motifs has also been demonstrated (reviewed in [126]). The remaining four human TLRs, namely TLR3, TLR7, TLR8, and TLR9, are located on endosomal membranes, with the N-terminal PAMP binding domain oriented towards the endosomal lumen. These TLRs

have been associated with the recognition of microbial but also host-derived nucleic acids. TLR3 recognizes double-stranded RNA (dsRNA)[127], which is, for instance, generated as an intermediate product during RNA virus replication. In contrast, TLR7 and its homolog TLR8 sense ssRNA, whereas TLR9 binds to unmethylated cytosine-phosphate-guanine (CpG) motifs found in both bacterial and viral DNA (reviewed in [123]).

Binding to their respective PAMP induces dimerization of TLRs and activation of elaborate signaling cascades (reviewed in [123,128]). Only the most important components of these signaling complexes are highlighted here. Through homotypic interactions, the C-terminal TIR domains of a TLR dimer interact with the TIR domain of one of two major adaptor proteins, called myeloid differentiation primary response protein 88 (MyD88) and TIR domain-containing adaptor protein inducing IFNβ (TRIF). Except for TLR3, all TLRs recruit MyD88, whereas TLR4 can switch from MyD88 to TRIF upon endocytosis of the receptor. Through further homotypic interactions, MyD88 recruits IL-1 receptor-associated kinase 4 (IRAK4), which in turn activates IRAK1. Autophosphorylation of IRAK1 then results in the recruitment of TNF receptor-associated factor 6 (TRAF6), in turn activating the transforming growth factor β-activated kinase 1 (TAK1) complex. Eventually, MyD88-dependent signaling leads to the activation of transcription factors through the mitogen-activated protein kinases (MAPKs) or the inhibitor of kappa B (IκB) kinase (IKK) complex, inducing inflammatory cytokine production through NF-κB signaling (further described in chapter 1.2.2 and Figure 7). Alternatively, the IRAK protein complex can recruit TRAF3, leading to IKKα-dependent phosphorylation and activation of a transcription factor called interferon regulatory factor 7 (IRF7). This pathway is only found in plasmacytoid DCs (pDCs), which are potent producers of type I IFNs in response to viral infections (reviewed in [129]). TIR domain-dependent interaction of TLR3 and TLR4 with TRIF can recruit the TAK1 kinase complex through interaction of TRAF6 with the receptor interacting protein 1 (RIP1), resulting in subsequent activation of MAPKs and the IKK complex as described for MyD88. On the other hand, TRIF can interact with TRAF3 and activate the TRAF family member associated NF-κB activator (TANK) binding kinase 1 (TBK1) and IKKε to induce IRF3-dependent IFN production (reviewed in [123,128]), which is further described in chapter 1.2.2 and Figure 7.

Recognition of cytosolic RNA by RLRs

The family of RLRs comprises the members RIG-I, melanoma differentiation-associated gene 5 (MDA5), and laboratory of genetics and physiology 2 (LGP2) (reviewed in [130,131]). All RLRs generally localize to the cytosol, although RIG-I has also been found in the nucleus[132]. RIG-I and MDA5 harbor a central helicase domain and a C-terminal domain (CTD) (Figure 6), which cooperate for ligand binding. The N-terminal caspase activation and recruitment

domains (CARDs) mediate the downstream signal transduction through IRF3 and NF-κB by homotypic interaction with the CARD of the central adaptor protein called mitochondrial antiviral signaling protein (MAVS). In contrast, LGP2 lacks the CARDs, indicating a more regulatory role. RLRs have been associated with infections of virtually all major virus families and are thus among the most important PRRs for the cell-intrinsic innate immunity targeting viral infections, together with TLRs and cGAS/STING (reviewed in [130]).

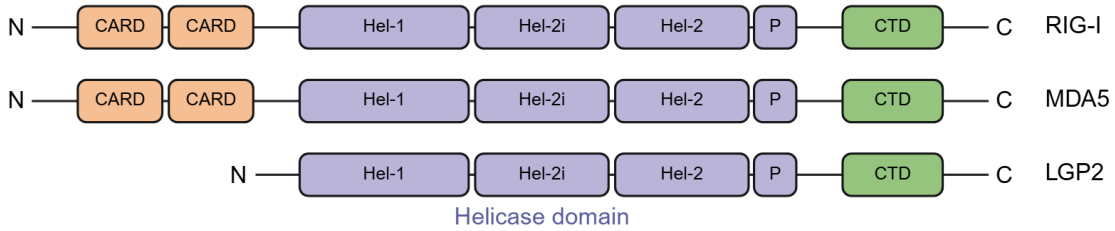

Figure 6: Domains of the RLRs RIG-I, MDA5, and LGP2.
All RLRs harbor a C-terminal domain (CTD) and a central helicase domain, divided into the two helicase subdomains Hel-1 and Hel-2, an intermediate insertion (Hel-2i), and a pincer (P) domain, which is involved in the conformational changes of the RLRs upon activation. The N-terminal caspase activation and recruitment domains (CARDs) are only found in RIG-I and MDA5 but not in LGP2. (Created with BioRender.com)

Both RIG-I and MDA5 have been described to recognize the synthetic dsRNA analogue poly(I:C), but with different length preferences. It was originally discovered that RIG-I is mainly activated by short fragments of less than 300 base pairs, while MDA5 preferentially recognizes dsRNA longer than 2 kb[133]. RIG-I further binds to unprotected tri- and diphosphorylated 5'-ends of RNA that additionally pair with a complementary RNA strand, and to 5'-terminal nucleotides which are unmethylated at their 2'-O position (reviewed in [131]). Hence, neither host mRNAs, which bear a 2'-O methylation, nor the monophosphate group at the 5'-ends of transfer RNAs (tRNAs) or ribosomal RNAs (rRNAs) are recognized by RIG-I. Negative-strand RNA viruses such as influenza A virus (IAV) are sensed by RIG-I (reviewed in [134]), but also positive-strand RNA viruses, including dengue and Zika virus[135,136]. More uncharacteristic ligands of RIG-I include, for example, a uracil-rich sequence within the hepatitis C virus (HCV) genome[137]. Moreover, the misplacement of host cellular RNAs due to viral infections can also induce RIG-I activation[138]. In absence of a ligand, RIG-I adopts a closed conformation that keeps the CARDs inaccessible and prevents them from signaling. Upon ligand binding to a pocket of the CTD, contact with the helicase domain is established, triggering a conformational change that exposes the CARDs. Successful signal transduction then requires the oligomerization of several RIG-I molecules, which is stabilized and controlled by various post-translational modifications, including, for instance, non-degradative (K63-linked) and degradative (K48-linked) ubiquitination as well as phosphorylation (reviewed in [130,131]).

In contrast to RIG-I, the ligands and activation processes of MDA5 are less well understood (reviewed in [139]). It has been demonstrated that MDA5 has a more open structure in the

absence of a ligand than RIG-I. Upon activation, MDA5 adopts a ring-like conformation around dsRNA and polymerizes in helical filaments. As contacts are established with the phosphodiester backbone of the RNA, MDA5 binding appears to be sequence-unspecific[140]. However, it was also proposed that long dsRNA might not be sufficient to activate MDA5, but rather a complex web of branched RNA is required[141]. IFN induction upon infection with picornaviruses or hepatitis D virus (HDV), for example, is fully dependent on MDA5, but appears to be partially redundant for many other viruses[139,142].

Due to the absence of the CARDs that are responsible for signal transduction, LGP2 fulfills regulatory functions affecting both RIG-I and MDA5 (reviewed in [143]). On the one hand, LGP2 cooperates synergistically with MDA5 to promote signal transduction, likely by engaging with a diverse range of RNA species and thereby promoting the nucleation of MDA5 polymers on long dsRNA. On the other hand, LGP2 was reported to function as a feedback inhibitor of both RIG-I and MDA5 signaling through RNA sequestration, direct interference with the CTD of RIG-I, and formation of a protein complex with the signaling adaptor MAVS[144-146]. As LGP2 is present at low basal levels but accumulates upon activation of the cell-intrinsic innate immune pathways, the switch between synergy and repression is assumed to be concentration-dependent. While low levels of LGP2 promote MDA5 signaling, high levels result in repression of RLR signal transduction (reviewed in [143]).

1.2.2 Interferon and Inflammatory Cytokine Induction Pathways

Signal transduction downstream of the RLRs depends on the homotypic interaction with the N-terminal CARD of the central adaptor protein MAVS, which is located as a transmembrane protein at the mitochondrial outer membrane and at peroxisomes (reviewed in [130,147]). Further signal transduction requires MAVS aggregation, resulting in the formation of fiber-like polymers[148]. Downstream of MAVS, two pathways are activated involving the four canonical and non-canonical IKK kinases, which are IKKα and IKKβ, and TBK1 and IKKε (also called IKKi), respectively. These kinases share overall 30% sequence homology across their N-terminal kinase domain, a central leucine zipper, and the helix-loop-helix motifs at the C-terminus (reviewed in [149]). TBK1 and IKKε are the central kinase hubs of the cell-intrinsic antiviral response pathway, resulting in the expression of IFNs and interferon-stimulated genes (ISGs). On the other hand, IKKα and IKKβ, together with the regulatory subunit IKKγ, also called NF-κB essential modulator (NEMO), constitute the IKK complex, mediating NF-κB activation and subsequent inflammatory cytokine induction. Although IKKγ is essential for the IKK complex, it has been demonstrated to be dispensable for TBK1/IKKε-mediated signal transduction but capable of enhancing it[147,150]. The cell-intrinsic antiviral and inflammatory cytokine response pathways are summarized in Figure 7.

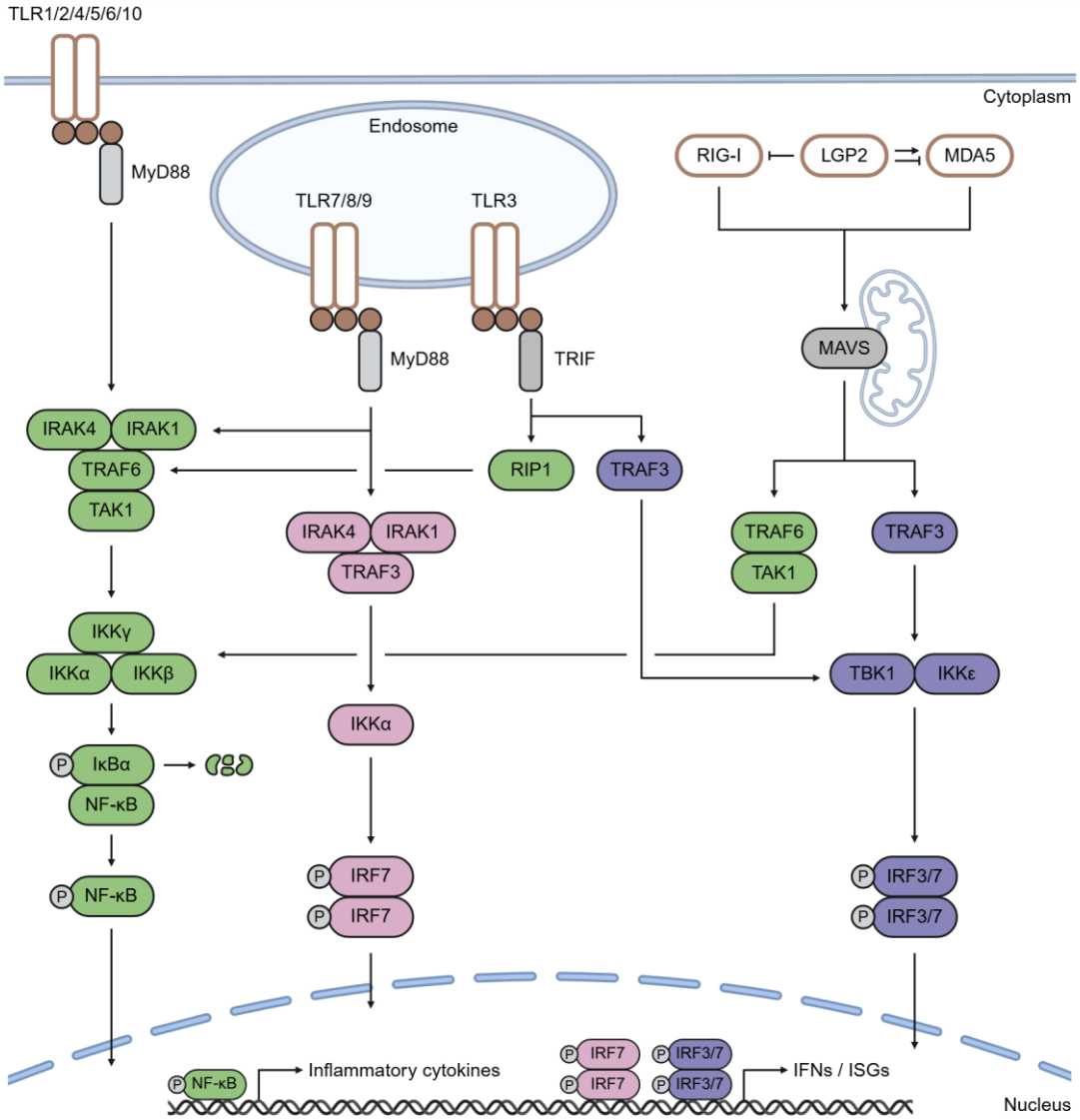

Figure 7: Cell-intrinsic antiviral and inflammatory signaling pathways downstream of RLRs and TLRs. The TLRs located at the plasma membrane induce NF-κB-dependent inflammatory cytokine expression in a MyD88-dependent manner. Recruitment of IRAK4/IRAK1/TRAF6/TAK1 activates the IKK complex, resulting in phosphorylation and degradation of IκBα and release of activated NF-κB. Endosomal TLR3 activates NF-κB through the adaptor TRIF, followed by recruitment of RIP1, TRAF6, and TAK1 to activate the IKK complex. The RLRs RIG-I and MDA5 signal through the adaptor protein MAVS, which is located at mitochondria. Recruitment of TRAF6 results in activation of the IKK complex, whereas recruitment of TRAF3 activates the TBK1/IKKε complex, which in turn phosphorylates IRF3 and IRF7. Nuclear translocation of IRF3/7 homo- and heterodimers induces IFN and ISG expression. In pDCs, endosomal TLR7/8/9 recruit either TRAF6, which activates the IKK complex, or TRAF3, resulting in phosphorylation of IRF7 by IKKα. (Created with BioRender.com)

Along the cell-intrinsic antiviral response pathway, MAVS polymers recruit TRAF3. K63-linked ubiquitination of TRAF3 in turn recruits TBK1 and IKKε, which are activated by auto- and trans-phosphorylation at S172 (reviewed in [130,149]). Various scaffolding proteins have been suggested to stabilize the complex between MAVS and TBK1/IKKε, including TANK, NAK-associated protein 1 (NAP1), and similar to NAP1 TBK1 adaptor (SINTBAD) (reviewed in [149]). Activated TBK1/IKKε then phosphorylates the transcription factors IRF3 and IRF7, followed by their homo- and heterodimerization and translocation into the nucleus. While IRF3 is found at

basal expression levels in most human cells, basal expression of IRF7 is limited to pDCs and is otherwise IFN-induced (reviewed in [151]). In the nucleus, IRF3/7 induces the transcription of IFNs and ISGs, further described in chapter 1.2.3.

Along the inflammatory cytokine response pathway, oligomerized MAVS can recruit TRAF6 and TAK1 to activate IKKα and IKKβ by phosphorylation of S176/180 and S177/181, respectively. Subsequently, the inhibitor of kappa B alpha (IκBα) is phosphorylated and marked by the beta-transducin repeat containing protein (βTRCP) for proteasomal degradation through K48-linked ubiquitination (reviewed in [152]). The transcription factor NF-κB is released, phosphorylated, and translocated into the nucleus, where it induces the transcription of mostly pro-inflammatory cytokines.

1.2.3 Interferon Signaling, Interferon-Stimulated Genes, and Their Antiviral Functions

Downstream of RLR and TLR activation, IRF3- and IRF7-mediated signaling induces the expression of IFNs and ISGs. IFNs are secreted from cells and are responsible for enhancing the ISG response in a positive feedback loop, acting on the IFN-secreting cell itself as well as surrounding cells. This so-called autocrine and paracrine signaling is particularly important in the *in vivo* tissue setting, as surrounding cells are put into an alarmed and antiviral state, obstructing or preventing infection of these cells. Moreover, secreted IFN can be sensed by incoming innate immune cells, reinforcing their recruitment and inflammatory signaling.

The three classes of IFNs

IFNs were first described in the 1950s as molecules interfering with virus infections[153]. Until today, three classes of IFNs have been identified, based on their interaction with specific receptor complexes (reviewed in [154,155]). Type I IFNs are the largest group of IFNs and comprise 17 members, of which 13 are IFNα subtypes and the remaining four are IFNβ, IFNε, IFNκ, and IFNω. Despite their ability to bind to the same receptor complex, the type I IFNs differ in their tissue distribution and receptor binding affinity, resulting in diverse biological outcomes (reviewed in [156]). Almost every cell in the human body can produce type I IFNs, but pDCs are the most prominent type I IFN inducers in an infection (reviewed in [129]). The receptor for the type I IFNs is composed of two subunits, called IFN alpha receptor 1 (IFNAR1) and IFNAR2. In their inactive state, the intracellular domains are bound to Janus kinases (JAKs), namely tyrosine kinase 2 (TYK2) and JAK1 (Figure 8). Upon binding of type I IFN, the receptor subunits and the bound JAKs are brought into close proximity, resulting in activation by trans-phosphorylation of the JAKs and conformational rearrangements. The phosphorylated tyrosines recruit signal transducer and activator of transcription (STAT) proteins via their Src homology 2 (SH2) domain. Downstream of IFNAR1/2, heterodimers consisting of tyrosine-

phosphorylated and activated STAT1 and STAT2 are formed, which additionally bind to IRF9 to form the trimeric ISG factor 3 (ISGF3) complex (Figure 8). Upon translocation into the nucleus, ISGF3 binds to IFN-stimulated regulatory element (ISRE) motifs in promoters of ISGs. Homodimers of STAT1, which bind to the γ-activated sequence (GAS) motif, are less prominently formed downstream of IFNAR1/2 activation (reviewed in [154,155]).

IFNγ is the sole member of the type II IFN group. Its expression is restricted to immune cells, such as NK cells and T lymphocytes, with important roles in bridging innate and adaptive immune responses (reviewed in [157]). However, the cognate receptor is widely distributed throughout the human body and thus, almost all cell types can respond to IFNγ. Each two IFN gamma receptor 1 (IFNGR1) and IFNGR2 subunits bind IFNγ, activating the associated JAK1 and JAK2 kinases (Figure 8). Phosphorylated STAT1 homodimers translocate into the nucleus and induce IFNγ-responsive genes through binding to GAS motifs. The ISGF3 complex is only weakly activated downstream of IFNGR1/2 (reviewed in [154,155]).

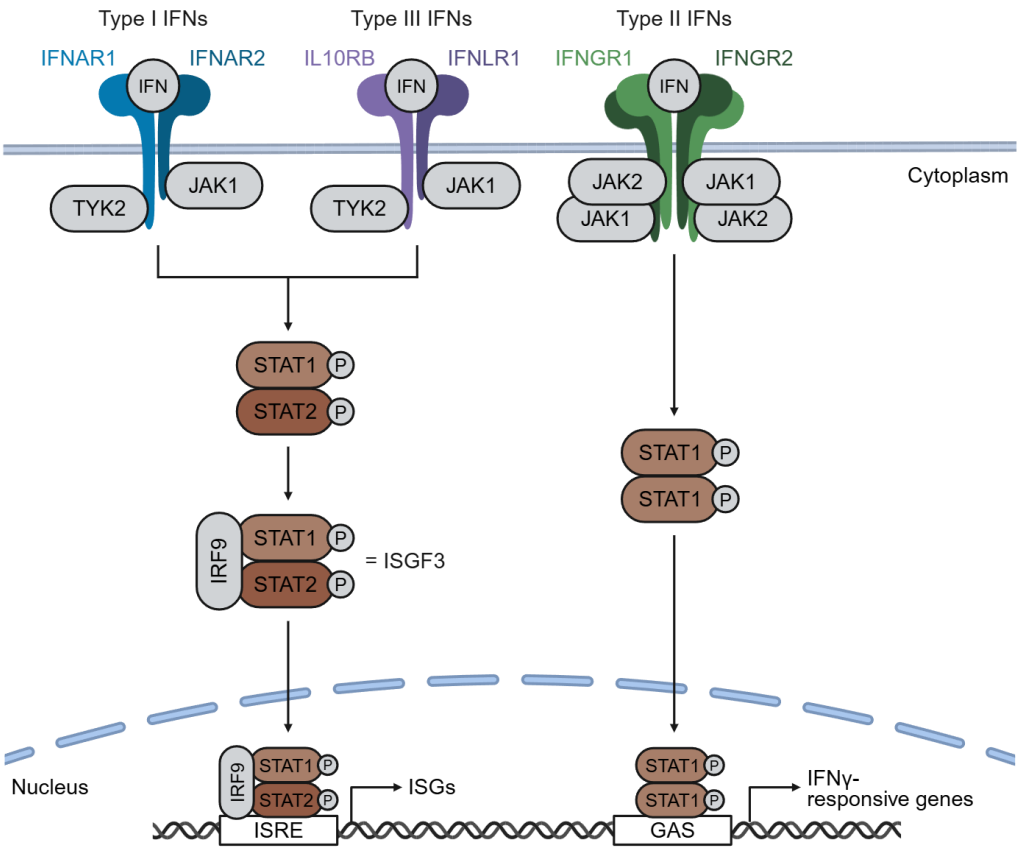

Figure 8: The JAK/STAT signaling cascade downstream of the three IFN receptors.
Type I IFNs bind to the IFNAR1/2 heterodimer, while type III IFNs bind to a heterodimeric receptor consisting of the IL10RB and the IFNLR1 subunits. Both activate the kinases TYK2 and JAK1, resulting in phosphorylation of STAT1/2 heterodimers. Recruitment of IRF9 gives rise to the ISGF3 complex, which translocates into the nucleus and binds to ISRE motifs in ISG promoters. Type II IFNs in turn activate JAK1 and JAK2 through the IFNGR1/2 receptor complex, activating STAT1 homodimers, which bind to GAS elements and induce the expression of IFNγ-responsive genes. (Created with BioRender.com)

The type III IFN group comprises three members: IFNλ1, IFNλ2, and IFNλ3. More recently, IFNλ4 was identified, but it appears to have unique functions (reviewed in [158]). The type III IFN receptor consists of IL10 receptor subunit beta (IL10RB), which is also used by cytokines such as IL10, and the high affinity subunit IFN lambda receptor 1 (IFNLR1) (reviewed in [154,155]). Downstream activation of the JAKs TYK2 and JAK1 results in the formation and nuclear translocation of the ISGF3 complex to induce ISG expression, as described previously (Figure 8). Type III IFN signaling is mostly restricted to epithelial tissues, due to the tissue-specific expression of IFNLR1 and of the type III IFNs themselves (reviewed in [159]). Therefore, type III IFNs have a particularly important role in fighting pathogen infections at mucosal and other epithelial surfaces, including the liver.

ISGs and their role as antiviral effectors

Immediately downstream of IRF3/7- and IFN- mediated signaling, ISG expression is induced, conferring an antiviral state. More than 400 ISGs have been identified by microarray, gain-of-function, and loss-of-function screens, and, more recently, by clustered regularly interspaced short palindromic repeats (CRISPR)/Cas9-based approaches (reviewed in [160]). ISGs can have diverse functions in the cellular context of the cell-intrinsic innate immunity (reviewed in [154,160]). Some PRRs, IRFs, including IRF7, and STATs are ISGs, reinforcing the pathways upstream and downstream of IFN production. Importantly, IFN expression is not replenished immediately downstream of the IFN receptors[161]. However, upregulation of PRRs through JAK/STAT signaling can enhance the expression of IFNs within infected cells due to increased viral sensing. Notably, some ISGs also function as negative feedback regulators to prevent sustained IFN signaling and chronic inflammation. Accordingly, many autoimmune diseases are associated with dysregulation of IFN production (reviewed in [162]). Examples of such negative regulators are suppressor of cytokine signaling (SOCS) proteins, which bind to phosphorylated tyrosines on the IFN receptor or the JAKs to prevent STAT binding. Similarly, ubiquitin-specific peptidase 18 (USP18) binds to IFNAR2 and prevents JAK1 recruitment (reviewed in [154]).

Many ISGs directly target and inhibit a specific step of the viral life cycles of individual viruses and virus families (reviewed in [154,160]). Some well-characterized ISGs inhibiting virus entry include myxovirus resistance protein 1 (Mx1), the IFN-induced transmembrane (IFITM) protein family, and tripartite motif-containing protein 5 alpha (TRIM5α). Mx1 can oligomerize and trap viral nucleocapsids of IAV at an early post-entry step (reviewed in [163]). IFITM proteins in turn are enriched in late endosomes and lysosomes and target viruses that utilize these compartments to enter the cytosol, for instance, by inhibiting viral fusion of IAV and severe acute respiratory syndrome coronavirus 2 (SARS-CoV-2) (reviewed in [164]). Entry of HIV-1 is

inhibited by TRIM5α, which binds to the viral nucleocapsid and induces, among others, premature capsid disassembly (reviewed in [165]). Virus translation and replication can also be affected by ISGs. Interferon-induced protein with tetratricopeptide repeats 1 (IFIT1) specifically binds to viral RNA of flaviviruses that lack 2'-O-methylation, suppressing viral translation and sequestering the RNA (reviewed in [166]). Interferon-stimulated gene 15 (ISG15), in turn, is a ubiquitin-like protein that can be covalently conjugated to both viral and cellular proteins with advantageous or detrimental effects for either of the targets (reviewed in [167]). For example, ISGylation of IRF3 hinders its polyubiquitination and proteasomal degradation, thereby enabling sustained cell-intrinsic antiviral signaling[168]. Another well-studied ISG is Viperin, which inhibits budding of many enveloped viruses at the plasma membrane, including IAV and HIV-1, preventing viral egress (reviewed in [169]).

Viral evasion strategies from cell-intrinsic innate immunity

In a continuous co-evolutionary process, the host improves its defenses against invading pathogens, while the pathogen concurrently evolves evasion strategies. Host-pathogen interactions are significantly shaped by this constant arms race, and every virus has likely developed several mechanisms to counteract the cell-intrinsic innate immunity. Such evasion strategies can occur at every level of PRR- and IFN receptor-mediated signaling. While some viruses interact with central components of these pathways and sequester or misplace them, others cleave important signal transducers. Furthermore, RNA viruses that replicate in the cytosol of their host cell exploit and remodel host structures to protect their genome and replication intermediates from cytosolic PRRs. And lastly, many viruses shut down host translation processes to avoid the production of antiviral effectors. This broad categorization of strategies contains a plethora of different host targets and viral mechanisms to evade the cell-intrinsic innate immunity (reviewed in [170,171]).

A prominent example employed by many viruses is the proteolytic cleavage of MAVS by a virus-encoded protease to disrupt downstream signaling. The protease of enterovirus 71 cleaves MAVS at multiple sites[172], and many other viral proteases were found to act similarly, including the NS3/4A protease of HCV[173,174]. Cleavage can also be directed against downstream components of the signaling cascades, including TBK1, but also the PRRs themselves (reviewed in [170,171]). Severe fever with thrombocytopenia syndrome virus (SFTSV) in turn compartmentalizes TBK1/IKKε complexes in inclusion bodies, making them inaccessible to activation by MAVS and to the downstream interaction with IRF3[175,176]. IFN-mediated signaling is also frequently impaired by viruses, promoting the degradation of IFNAR1 (IAV)[177], inducing the expression of negative feedback regulators (West Nile virus)[178], preventing STAT1/2 nuclear translocation through sequestration (Ebola virus)[179,180], or

promoting STAT2 degradation (dengue and Zika virus)[181,182]. Furthermore, viruses can impact the cell-intrinsic innate immunity more indirectly through interactions, cleavage, or induction of proteins and cellular processes that impact expression, activation, degradation, or post-translational modification of PRR- and IFN-mediated signaling pathways (reviewed in [170,171]). A detailed understanding of the intricate virus-host interactions is essential for the development of novel therapeutic intervention strategies.

1.3 The Interplay of HEV With the Cell-Intrinsic Antiviral Response

1.3.1 Cell Culture Systems to Study HEV Biology

Even though primary human hepatocytes (PHH) remain the gold standard for studying hepatotropic virus infections, high donor-to-donor variability, a limited life span, restricted accessibility, and poor genetic tractability make them challenging for many studies. Instead, the majority of commonly used cell culture systems rely on hepatoma cells, derived from hepatocellular carcinomas, due to their unlimited proliferation capacity (reviewed in [183-185]). Compared to PHH, hepatoma cells are easily accessible, genetically manipulable, and more cost-effective. However, hepatoma cells have other disadvantages, including the poor integrity of various signaling pathways. A common feature of cancerous cells is the downregulation of viral sensing, IFN induction, and the response to IFN signaling[186-188]. Furthermore, hepatoma cells lack many drug-metabolizing enzymes found in hepatocytes, rendering these cells comparatively unsuitable for antiviral drug screenings[189].

Early HEV studies were performed in the lung adenocarcinoma cell line A549 and the hepatoma cell line PLC/PRF/5[190-193]. However, continuous expression of the hepatitis B surface antigen (HBsAg) challenges any HEV-specific conclusions drawn from PLC/PRF/5 cells[194]. Other commonly used hepatoma cells for HEV research are derivatives of Huh7 cells, including Huh7.5 and S10-3 cells, as well as HepG2 cells and the HepG2/C3A subclone, which is highly susceptible to HEV infection[56,75,76,195,196]. Huh7 and Huh7.5 cells are characterized by undetectable expression of the PRRs MDA5, LGP2, and TLR3, and Huh7.5 cells additionally express a mutant, non-responsive RIG-I[197,198]. The PRR expression profile of the Huh7-derived S10-3 cell line, which was selected for its enhanced HEV infection and replication efficiency[75,199], has not been characterized in detail, but responsiveness to RIG-I stimulation appears intact[200]. HepG2/C3A cells infected with HEV were found to upregulate IFNs and ISGs, suggesting at least partially intact cell-intrinsic antiviral response pathways[199,201,202]. Given that HEV is transmitted along the gut-liver axis, and HEV-3 and HEV-4 infections can result in extrahepatic manifestations, cell lines of tissue origin other than liver are of interest for HEV research. The intestinal colon carcinoma cell line Caco-2 is permissive to HEV[56,76,195], for example, and placental and neuronal cells have also been successfully infected[34-36].

More recently, the differentiation of hepatocyte-like cells (HLCs) from induced pluripotent stem cells (iPSCs) or human embryonic stem cells (hESCs) was established as a promising compromise between hepatoma cells and PHH (reviewed in [203]). Based on readily available pluripotent stem cell lines with unlimited capacity for self-renewal, HLCs offer enhanced reproducibility and an extended life span. Furthermore, they are genetically manipulable, either at the pluripotent stem cell stage or by viral transduction of differentiated HLCs[89,204,205]. Differentiation of stem cells into various cell types besides HLCs from an isogenic background is another advantage. Despite their more mature hepatocyte profile than hepatoma cells regarding hepatic marker and metabolic enzyme expression, HLCs still retain an immature phenotype, rather resembling fetal than adult hepatocytes (reviewed in [203]). HLCs derived from iPSCs and hESCs have been reported to be susceptible to HEV infection[204,206,207]. Notably, primary isolates of all human-infecting HEV genotypes, namely HEV-1 to HEV-4, were found to replicate in stem cell-derived HLCs[204]. In contrast, clinical isolates often fail to infect or replicate in cancer-derived cell lines, highlighting another advantage of HLCs. Furthermore, HLCs differentiated on Transwells adopt a columnar polarization with apical and basolateral membranes, presenting the opportunity to study polarization-specific effects of HEV infection as well as targeted secretion of viral progeny and cellular cargo[89].

A robust cell culture system for reproducible and efficient propagation of HEV-3 has only been established in 2011 by Shukla *et al.*[56]. A fecal sample of a chronically HEV-infected HIV-1 patient was serially passaged six times over a period of seven months on the hepatoma cell line HepG2/C3A. This cell culture adaptation process resulted in the HEV-3 Kernow-C1/p6 strain, which harbors a 58-amino acid insertion of the human S17 ribosomal protein sequence in the HVR, conferring a significant growth advantage[56,57]. While this strain has been instrumental in advancing HEV research since its first introduction, the cell culture adaptation of a replicative complementary DNA (cDNA) clone for HEV-1 was only recently achieved[208]. Moreover, HEV-1- and HEV-3-derived replicons are often employed, harboring reporter genes, such as green fluorescent protein (GFP) or luciferase, as replacements of the overlapping *ORF2* and *ORF3* genes (reviewed in [184,185]).

1.3.2 The Current State of Knowledge on the HEV-Induced Cell-Intrinsic Antiviral Response

HEV induces a detectable type III IFN and ISG response in hepatocytes

Several studies have highlighted that HEV is not a stealth virus and induces IFN and ISG expression upon infection of hepatocytes and other cell types (reviewed in [209]). A comparative microarray analysis of the differential gene expression profile induced by infection of chimpanzees with HCV or the HEV-1 Sar55 strain revealed a similar, yet weaker and timely

distinct response to HEV infection[210]. Overall, a lower number of differentially expressed ISGs and a lower magnitude of expression were observed, together with lower levels of differentially expressed genes associated with the adaptive immune response. Overall, the authors suggested that HEV might be more susceptible to the effects of the cell-intrinsic innate immune response compared to HCV, albeit not excluding the possibility that differences in the viral inoculum might have resulted in the differential outcomes of infection.

In vitro, infection of HepG2/C3A cells, PHH, and stem cell-derived HLCs with HEV-1 and HEV-3 induced a type III rather than a type I IFN response, characterized by upregulation of IFNλ1 and IFNλ2/3[201,204]. Notably, a less prominent induction of IFNβ transcripts was observed in HEV-3-infected HLCs[204] and HEV-3-transfected HepaRG cells[211], a human bipotent progenitor cell line isolated from a liver tumor. However, secretion of neither IFNα nor IFNβ protein was detectable in cell culture supernatants of infected HLCs[204]. *In vivo* findings from pigs experimentally infected with an HEV-3 isolate supported the relevance of the type III IFN response, as upregulated IFNλ1 and IFNλ3, but not IFNα mRNA, were found in their liver tissue. Consequently, it has been well established that HEV infection induces primarily a type III rather than a type I IFN response in hepatocytes. Furthermore, elevated IFNλ3 serum levels were detected in acute HEV-4 infected patients from Japan, highlighting the importance of type III IFNs in containing HEV infections *in vivo*[212]. In contrast, the IFN response in HEV-infected intestinal epithelial cells remains inconclusively characterized. One study reported the induction of IFNβ but not IFNλ1 transcripts in porcine enterocytes, stimulated with a fragment of the Kernow-C1/p6 RNA genome by transfection[200]. On the other hand, Marion and colleagues observed secretion of IFNλ1 protein from primary human intestinal epithelial cells infected with HEV-1 and HEV-3 clinical isolates and the Kernow-C1/p6 strain[87].

Many studies have detected ISG upregulation upon HEV infection of hepatocytes. However, a comprehensive description of a unique transcriptional ISG profile induced upon HEV infection is lacking to date (reviewed in [209]). Interestingly, infection with HEV-1 primary isolates resulted in a stronger, steeper, and more transient ISG response in HLCs than HEV-3 primary isolates[204]. Some prominent ISGs induced in HEV-1-infected chimpanzees[210], PHH infected with a derivative of the Kernow-C1/p6 strain[202], HLCs infected with the Kernow-C1/p6 strain and HEV-1 to HEV-4 clinical isolates[204], Kernow-C1-/p6-infected HepG2/C3A cells[201], and HepG2/C3A and S10-3 cells transfected with a HEV-1 subgenomic replicon[199] included IFIT1, ISG15, Mx1, Oligoadenylate synthetase 2 (OAS2), Viperin, and interferon alpha inducible protein 27 (IFI27). However, very little is known about the specific antiviral effects that these ISGs exhibit on the HEV life cycle. Many components of the cell-intrinsic antiviral response are ISGs themselves and thus, RIG-I, MDA5, and IRF1 were shown to be functional against HEV

by enhancing viral recognition[213-215]. Moreover, ISG15 has been suggested to have immunomodulatory functions in HEV-replicating S10-3 and HepG2/C3A cells, but a direct effect on the HEV life cycle or ISGylation of HEV proteins has not been demonstrated[216,217]. Only the ISG guanylate-binding protein 1 (GBP1) was found to restrict the HEV-3 life cycle in A549 cells, likely by enhancing the targeting of viral components to the lysosome[218].

NF-κB-mediated induction of inflammatory cytokines was less extensively characterized in HEV-infected hepatocytes. While a few studies measured the expression of some inflammatory cytokines, including IL6, CC-chemokine ligand 4 (CCL4), and CCL5 in A549 cells and a subclone of the PLC/PRF/5 cell line[69,214,219], no report has exclusively focused on the potential of HEV to induce an NF-κB-mediated response.

The PRRs sensing HEV RNA remain insufficiently characterized

Comprehensive exploration and side-by-side comparisons of the PRRs potentially involved in HEV sensing have not been conducted. Most prominently, Yin and colleagues performed short hairpin (sh)RNA-based knockdown of RIG-I, MDA5, and the adaptor protein MAVS in HepG2/C3A cells, analyzing the impact on viral replication on day 5 post-infection with the Kernow-C1/p6 strain[201]. The knockdown of MAVS enhanced HEV replication most significantly, followed by MDA5 and, less prominently, RIG-I, suggesting that MDA5 might be more relevant but not exclusively responsible for sensing HEV RNA. Similarly, other studies reported that knockdown of RIG-I in A549 cells enhanced replication upon infection with the Kernow-C1/p6 strain[214], and knockdown of MDA5 in Huh7 cells supported HEV replication upon Kernow-C1/p6 electroporation (EPO)[215]. Furthermore, only knockdown of IRF3 but not IRF7 enhanced HEV replication[215]. Reconstitution of TLR3 in Huh7.5 cells impaired the replication of an HEV replicon, suggesting a potential role for TLR3 in sensing HEV RNA[199]. Otherwise, TLR3 and other TLRs have been mainly studied in peripheral blood mononuclear cells (PBMCs) of HEV-infected patients[220-222]. High expression levels of TLR3 in PBMCs have been correlated with a full recovery from HEV-1 infection, whereas patients with low TLR3 expression more frequently progress to acute liver failure[220]. While this indicates that innate immune cells, such as macrophages and DCs, are important for successful clearance of acute HEV infections, the role of TLR3 in sensing HEV in hepatocytes remains unclear.

Moreover, the specific HEV PAMP recognized by PRRs is still under investigation. One study analyzed RIG-I-dependent IFNβ and IFNλ1 induction in S10-3 cells upon transfection with less than 300-nucleotide-long fragments of the HEV genome, including the capped and uncapped 5'-UTR, the JR stem loop, and the 3'-UTR with the poly(A) tail, to stimulate RIG-I[200]. The authors identified a uracil-rich region in the 3'-UTR, upstream of the poly(A) tail, as a potent PAMP for RIG-I activation. Whether this is relevant in the context of a full-length HEV infection

remains unclear. Similarly, a different study found the cap and poly(A) tail of the HEV-3 Kernow-C1/p6 genome to be dispensable for IFN and ISG induction in the human embryonic kidney cell line HEK293T, and replication was not required to stimulate a cell-intrinsic antiviral response in HepaRG cells[211]. However, other studies demonstrated that HEV replication is necessary to elicit a detectable IFN and ISG response upon authentic HEV infection, indicated by a delayed onset of antiviral response gene expression compared to viral replication[201,204].

HEV replication persists despite a sustained cell-intrinsic antiviral response

Infection of HepG2/C3A cells and HLCs previously revealed that HEV persistently replicates despite a continuous type III IFN and ISG induction over a course of at least 12 days post-infection[201,204]. The presence of a cell-intrinsic antiviral state did neither clear nor significantly dampen viral replication, nor was the antiviral response fully suppressed by HEV. Exogenous inhibition of IFN and ISG induction via a TBK1 inhibitor resulted in the elimination of the type III IFN and ISG responses. However, this did not significantly enhance HEV replication over time[204]. The authors concluded that the evolutionary battle between HEV and its host has resulted in the development of evasion strategies protecting viral replication from the cell-intrinsic antiviral response. Accordingly, several studies have indicated that HEV replication is more resistant to exogenous treatment with type I, II, and III IFNs than, for instance, HCV[201,223,224]. This phenotype was particularly striking if IFNs were applied following the establishment of HEV replication. Yin and colleagues found that the persistent activation of JAK/STAT signaling upon HEV-3 infection in HepG2/C3A cells resulted in the retention of phosphorylated STAT1 in the cytosol instead of its nuclear translocation[201]. They suggested that a refractoriness due to the pre-existing virus-induced IFN response was responsible for the relative resistance of HEV towards exogenous IFN treatment, rather than a direct viral antagonism. Furthermore, several studies have shown that HEV-infected cells are less responsive to exogenous PRR agonists, such as poly(I:C), further substantiating the presence of viral evasion strategies from cell-intrinsic innate immune signaling[68,225,226].

Individual HEV proteins interfere with the cell-intrinsic antiviral response

All HEV proteins have been implicated in directly antagonizing the cell-intrinsic antiviral response. Most of these studies were performed by ectopic expression of individual viral proteins or subdomains of ORF1 and not analyzed in the context of authentic, full-length HEV infection. Furthermore, these studies often lack side-by-side comparisons of all HEV proteins within the same cellular system. Overall, the physiological relevance of each individually determined antagonism for the progression of authentic HEV infection remains elusive.

Several studies have analyzed the impact of ORF1 and its subdomains on the cell-intrinsic antiviral response (Figure 9). Due to the absence of a putative viral protease, HEV infection

does not lead to MAVS cleavage[201], unlike hepatitis A virus (HAV) and HCV infections[173,174,227]. Nonetheless, it was suggested that individually expressed HEV-1 X and PCP domains significantly inhibit poly(I:C)-induced expression of IFNβ in HEK293T cells[228]. Mechanistically, the X domain prevented phosphorylation of IRF3, while the PCP caused reduced ubiquitination of RIG-I and TBK1. Some less conclusive studies suggested that both MeT and PCP domains from an HEV-3 isolate interfere with RIG-I- and MDA5-mediated IFNβ induction and NF-κB signaling in HEK293T cells[225,229,230]. The negative effect of the PCP, but not of the MeT, on IFNβ promoter activity was further confirmed elsewhere[231]. However, no detailed mechanistic analysis was provided in any of these studies. Lastly, a combined MeT-Y-PCP construct from HEV-3, but not HEV-1, was proposed to prevent phosphorylation and nuclear translocation of STAT1 in HEK293T cells, thereby interfering with IFN signaling[232]. Due to the predominance of studies performed by ectopic expression of ORF1 segments, and the uncertainty about ORF1 processing and its functional domains, the physiological relevance of these suggested viral evasion mechanisms remains unclear.

Studies on the viral evasion strategies mediated by HEV ORF3 (Figure 9) have been controversial. Similar to ORF1, HEV-3 ORF3 was suggested to impair STAT1 phosphorylation in A549 cells, likely through direct interaction[226]. Furthermore, a study proposed that HEV-1 ORF3 impairs TLR3- rather than RIG-I-induced NF-κB-mediated inflammatory cytokine induction in A549 cells by impairing K63-linked ubiquitination of RIP1[233]. Another study found reduced transcription factor activation downstream of TLR7 due to HEV-1 ORF3[234]. In contrast, it was reported that ectopic expression of HEV-1 and HEV-3 ORF3 enhance IFNβ promoter activity in HEK293T and S10-3 cells by stabilizing RIG-I and extending its half-life[235], which was substantiated by a different study[231]. A similar phenotype was found upon transfection of the full-length HEV-1 Sar55 strain, but not upon transfection of a GFP-encoding replicon, lacking ORF2 and ORF3 protein expression[235]. Both ORF3 and ORF1 proteins are only present at low abundance in cell culture and in patients[64,236,237]. Therefore, the phenotypes observed upon ectopic expression of these viral proteins might not be relevant under physiological conditions.

As ORF2 is more abundantly expressed in infected cells compared to ORF1 and ORF3, it remains the most likely candidate for efficient modulation of the cell-intrinsic antiviral response (Figure 9). Upon transfection in HEK293T cells, HEV-3 ORF2 from the Kernow-C1/p6 strain, but also HEV-1 ORF2 from the Sar55 strain, resulted in reduced IRF3 phosphorylation in response to poly(I:C) stimulation and Sendai virus (SeV) infection and inhibited IFNβ promoter activity[68]. By co-immunoprecipitation (co-IP) experiments, the authors found that ORF2 directly interacts with TBK1 in transfected HEK293T and HEV-3-infected HepG2/C3A cells, thereby

preventing phosphorylation of IRF3 and its dissociation from the MAVS-TBK1 complex. This interaction was suggested to be mediated by the ORF2 ARM, as mutations of this motif restored the phosphorylation of IRF3. These findings were substantiated by a different study, additionally highlighting that TRIF- and MyD88-induced IFNβ promoter activity was also affected by the presence of ORF2[231]. Furthermore, ORF2 from an HEV-1 clinical isolate was reported to impair NF-κB-mediated signaling through direct interaction with βTRCP[238]. The presence of ORF2 resulted in decreased ubiquitination of IκBα and thus, prevented its proteasomal degradation.

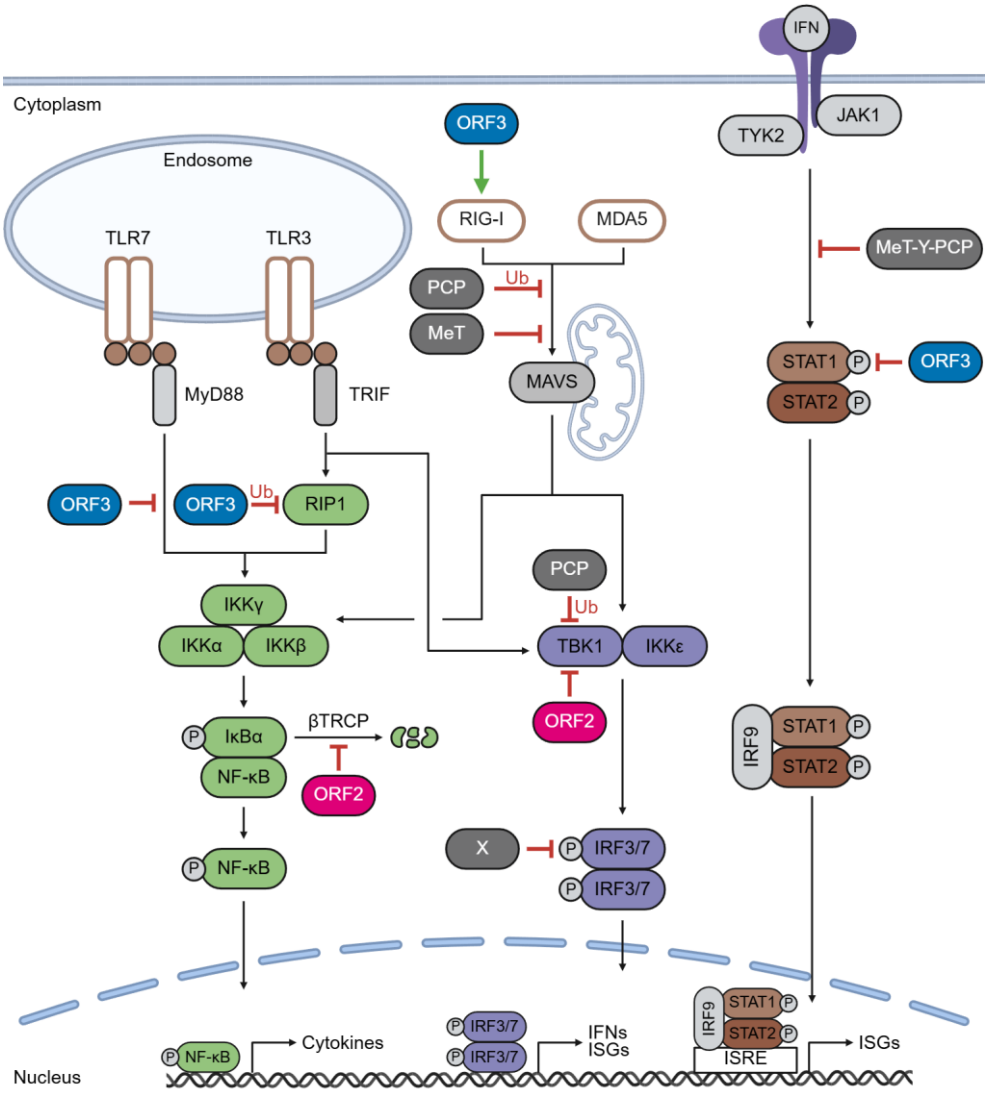

Figure 9: The cellular targets of the proposed viral antagonisms mediated by HEV ORF1, ORF2, and ORF3. The HEV ORF1 subdomains MeT and PCP have been suggested to impair RIG-I- and MDA5-mediated signal transduction, partly by preventing K63-linked ubiquitination (Ub) of RIG-I and TBK1 by the PCP. Furthermore, the X domain was proposed to impair phosphorylation of IRF3, and a combined MeT-Y-PCP product interferes with phosphorylation of STAT1. The ORF2 protein was shown to directly interact with TBK1 and βTRCP, resulting in impaired phosphorylation of IRF3 and attenuated degradation of the NF-κB inhibitor IκBα, respectively. The ORF3 protein interferes with TRIF- and MyD88-mediated inflammatory signaling, partly by impairing ubiquitination of RIP1, and ORF3 inhibits phosphorylation of STAT1. On the other hand, ORF3 can also enhance IFNβ expression by stabilizing RIG-I. (Created with BioRender.com)

2 Objectives

It was previously demonstrated that HEV replication persists in the presence of a sustained type III IFN and ISG response[201,204]. This suggested the presence of intricate viral evasion strategies to escape elimination by the antiviral response. Even though all HEV proteins have been suggested to counteract different stages of the cell-intrinsic antiviral signaling pathways[209], their relevance for the progression of authentic HEV infection in hepatocytes remains elusive. Furthermore, many questions about the HEV-specific antiviral response are unanswered, including the identification of the PRRs contributing to the sensing of HEV RNA[209]. Therefore, the overall aim of my PhD project was to perform a comprehensive characterization of the cell-intrinsic antiviral response to HEV infection, both in bulk and at the single-cell level, using different hepatocellular systems.

First, I aimed to evaluate and optimize the different hepatocellular systems selected to study the HEV-induced antiviral response. This involved a characterization of their antiviral signaling repertoire, including the PRRs, the integrity of antiviral and inflammatory signaling pathways, and the responsiveness of the relevant IFN receptors. Second, I sought to establish a strategy in hESCs to generate knockouts of central antiviral response components, integral to dissecting the HEV-induced antiviral response. And third, I attempted to identify the PRRs specifically involved in sensing HEV.

Next, I aimed to identify the viral determinants contributing to persistent HEV replication in the presence of a sustained antiviral response. To this end, I performed a comprehensive, side-by-side evaluation of the abilities of different viral proteins to interfere with PRR- and IFN-induced signaling pathways. This approach was essential for clarifying the different antagonism functions suggested for the HEV proteins ORF2 and ORF3 by previous publications. Then, I evaluated the importance of the identified antagonism for the progression of viral replication in a full-length HEV context using EPO and authentic HEV infection. These approaches aimed to dissect how the identified viral antagonism contributes to the establishment of persistent HEV replication.

Finally, I aimed to analyze the HEV-induced cell-intrinsic antiviral response at the single-cell level by spatial RNA fluorescence *in situ* hybridization and, more broadly, by single-cell RNA-sequencing. The aim of these experiments was to uncover the cellular source and potential heterogeneities of the antiviral response within a cell population composed of infected and uninfected cells. Collectively, this project aimed to provide a detailed characterization of the HEV-induced cell-intrinsic antiviral response in order to identify the determinants of HEV persistence.

3 Materials

3.1 Consumables

Table 3: List of consumables.

Name	Supplier	Catalog number
T25, T75, and T175 cell culture flasks	Sarstedt	83.3910.002 / 83.3911.002 / 83.3912.002
6-, 12-, 24-, 48-, and 96-well plates for cell culture	Greiner Bio-One	657160 / 665180 / 662160 / 677180 / 655160
6-, 12-, and 24-well plates for stem cell culture	Falcon	353046 / 353043 / 353047
100-mm cell culture dishes	Greiner Bio-One	664160
150-mm cell culture dishes	Thermo Scientific	168381
2 mL cryotubes	Greiner Bio-One	121261
0.5 mL, 1.5 mL, 2 mL, and 5 mL polypropylene tubes	Sarstedt	72.698.200 / 72.690.001 / 72.708 / 622201
0.5 mL, 1.5 mL, and 2 mL SafeLock polypropylene tubes	Eppendorf	0030121503 / 0030121872 / 0030121880
1.5 mL Protein LoBind tubes	Eppendorf	10718894
1.5 mL and 2 mL DNA LoBind tubes	Eppendorf	0030108418 / 0030108426
1.5 mL nuclease-free polypropylene tubes	Thermo Scientific	3451
15 mL and 50 mL polypropylene tubes	Falcon	352196 / 352070
38.5 mL, Open-Top Thinwall Polypropylene Tube for Ultracentrifugation, 25 x 89mm	Beckman Coulter	326823
0.2 µm and 0.45 µm filter units	Millipore	SLGV033RS / SLHA033SS
10-mm and 12-mm cover glasses	Paul Marienfeld	0111500 / 0111520
96-well qPCR plates	Kieser Biotech	GK96LOW
Blotting membranes, Amersham Hybond 0.2 PVDF	Cytiva	10600021
Blotting membranes, Amersham Hybond 0.45 PVDF	Cytiva	10600100
Gene Pulser/MicroPulser Electroporation Cuvettes, 0.2 cm gap	Bio-Rad	1652086
Gene Pulser/MicroPulser Electroporation Cuvettes, 0.4 cm gap	Bio-Rad	1652081
MACS SmartStrainers 70 µm	Miltenyi Biotec	130-098-462
Microseal 'B' PCR Plate Sealing Film	Bio-Rad	MSB1001XTU

3.2 Chemicals, Reagents, and Kits

Table 4: List of chemicals and reagents.

Name	Supplier	Catalog number
2-mercaptoethanol	Sigma-Aldrich	805740
Acetic acid	neoFroxx	LC-7167
Acrylamide/Bis Solution, 29:1	Serva	10680
Adenosine triphosphate (ATP)	Carl Roth	K054.3
Agar-Agar	Carl Roth	5210
Agarose NEEO Ultra Quality	Carl Roth	2267.5
Alt-R *S.p.* Cas9 Nuclease V3	Integrated DNA Technologies	1081058
Alt-R CRISPR-Cas9 tracrRNA, ATTO™ 550	Integrated DNA Technologies	1075927
Ammonium persulfate (APS)	Sigma-Aldrich	248614
Blasticidin	InvivoGen	ant-bl
Bovine serum albumin (BSA) (Albumin Fraktion V)	Carl Roth	8076.2
Brefeldin A (BFA)	InvivoGen	inh-bfa
Bromophenol blue	AppliChem	A2331
Calcium chloride ($CaCl_2$)	Carl Roth	A119
Chloroform	Merck	102445
cOmplete Mini Protease Inhibitor Cocktail	Roche	11836153001
Dimethyl sulfoxide (DMSO)	Carl Roth	A994.2
Desoxynucleotriphosphates (dNTPs)	Thermo Scientific	R1121
EDTA (Ethylenedinitrilotetraacetic acid), disodium salt	Merck	1.08418
EGTA (Ethylene glycol-bis(2-aminoethyl ether)-N,N,N′,N′-tetraacetic acid)	Sigma-Aldrich	E3889
Ethanol	Fisher Scientific	17740239
G418 (Geneticin)	InvivoGen	ant-gn
Gel Loading Dye, Purple (6X)	New England Biolabs	B7024S
Goat serum	MP Biomedicals	08642921
Glutathione (GT)	Sigma-Aldrich	G6013
Glycerol	Honeywell	15523
Glycine	Thermo Scientific	220910010
HEPES (4-(2-hydroxyethyl)-1-piperazineethanesulfonic acid)	Sigma-Aldrich	H7523
Hygromycin B Gold	InvivoGen	ant-hg
Isopropanol	Fisher Scientific	17140576
iTaq Universal SYBR Green Supermix	Bio-Rad	1725125
JetPRIME Reaction Buffer	Polyplus	201000003
JetPRIME Reagent	Polyplus	101000015
LB Medium Powder (Lennox)	Carl Roth	X964.4
Lipofectamine 2000	Invitrogen	11668027

Lipofectamine Stem Transfection Reagent	Invitrogen	STEM00001
Magnesium chloride ($MgCl_2$) hexahydrate	Merck	105833
Matrigel Growth Factor Reduced Basement Membrane Matrix	Corning	354230
Methanol	Sigma-Aldrich	32213
Midori Green Advance	Biozym	617004
Milk Powder Blotting Grade	Carl Roth	T145
MluI-HF	New England Biolabs	R3198
NEBuffer Set 1.1, 2.1, 3.1 and CutSmart	New England Biolabs	B7200S
Nonidet P 40 Substitute (NP-40)	Sigma-Aldrich	74385
Nuclease-free H_2O	Invitrogen	AM9938
Paraformaldehyde, 16%	Science Services	15710
Phosphate buffered saline (PBS)	Capricorn Scientific	PBS-1A-P50
Pierce Anti-HA Magnetic Beads	Thermo Scientific	88836
Pierce RIPA Lysis Buffer	Thermo Scientific	89901
Poly(C)	Sigma-Aldrich	P4903
Poly(I:C) High Molecular Weight (HMW)	InvivoGen	tlrl-pic
Polyethyleneimine (PEI)	Polysciences	23966
Poly-L-lysine	Sigma-Aldrich	P2636
Potassium chloride (KCl)	Carl Roth	6781
Potassium dihydrogen phosphate (KH_2PO_4)	Carl Roth	3904
Potassium hydroxide (KOH)	Carl Roth	P747
Precision Plus Protein Dual Color Standards	Bio-Rad	1610374
Prestained Protein Ladder Broad Range	Proteintech	PL00002
Puromycin	InvivoGen	ant-pr
Rat tail collagen I	Corning	354236
D(+)-Saccharose (Sucrose)	Carl Roth	4621
Sodium chloride (NaCl)	Carl Roth	3957
Sodium dodecyl sulfate (SDS)	Carl Roth	CN30
SPRIselect	Beckman Coulter	B23317
TEMED (N,N,N',N'-Tetramethylethylenediamine)	VWR	UPTIUP15413D
Terrific Broth (TB) Medium Powder	Carl Roth	X972.3
Tris base	Carl Roth	2449
Triton X-100	Sigma-Aldrich	X100
TRIzol Reagent	Invitrogen	15596026
Tween 20	Carl Roth	9127
Y-27632 RHO/ROCK pathway inhibitor	STEMCELL Technologies	7230

Table 5: List of kits.

Name	Supplier	Catalog number
CellTiter 96 AQueous One Solution Cell Proliferation Assay	Promega	G3582
Chromium Next GEM Single Cell 3' Kit v3.1, 16 rxns	10x Genomics	1000268
Chromium Next GEM Chip G Single Cell Kit, 48 rxns	10x Genomics	1000120
DNeasy Blood and Tissue Kit	QIAGEN	69504
Dual Index Kit TT Set A 96 rxns	10x Genomics	1000215
GoTaq G2 Hot Start Polymerase Kit	Promega	M740
High Capacity cDNA Reverse Transcription Kit	Applied Biosystems	4368814
iScript cDNA Synthesis Kit	Bio-Rad	1708891
LumiKine Xpress hIFN-β 2.0	InvivoGen	luex-hifnbv2
Mix & Go Competent Cells Kit	Zymo Research	ZYM-T3001
mMESSAGE mMACHINE T7 Transcription Kit	Invitrogen	AM1344
Monarch Total RNA Miniprep Kit	New England Biolabs	T2010S
NucleoSpin Gel and PCR Clean-Up Kit	Macherey-Nagel	740609
NucleoSpin Plasmid Kit	Macherey-Nagel	740588
NucleoBond Xtra Midi Kit	Macherey-Nagel	740410
NEBNext Library Quant Kit for Illumina	New England Biolabs	E7630
NextSeq 500/550 High Output Kit v2.5 (150 Cycles)	Illumina	20024907
Peptide-*N*-Glycosidase F (PNGase F) Kit	New England Biolabs	P0704
Phusion High-Fidelity DNA Polymerase Kit	New England Biolabs	M0530
Pierce BCA Protein Assay Kit	Thermo Scientific	23225
Pierce ECL Western Blotting Substrate	Thermo Scientific	32106
QIAquick PCR Purification Kit	QIAGEN	28104
Roboklon Universal RNA Kit	Roboklon	E3598
SuperSignal West Femto Maximum Sensitivity Substrate	Thermo Scientific	34095

3.3 Media, Buffers, and Solutions

Table 6: List of cell culture media and solutions.

Name	Supplier	Catalog number
2-mercaptoethanol (Stem cell culture)	Gibco	21985-023
Accutase	Innovative Cell Technologies	AT 104-500
B-27 Supplement (50X), custom	Gibco	0080085SA
DMEM, high glucose, GlutaMAX Supplement	Gibco	61965026
DMEM, high glucose (A549 medium)	Gibco	11965092
DMEM, high glucose, GlutaMAX Supplement, pyruvate (MEF-feeder medium)	Gibco	10569010
KnockOut DMEM/F-12	Gibco	12660012
DMEM/F-12 (hPSC-feeder medium)	Mediatech (Corning)	15-090-CV

Dimethyl sulfoxide (DMSO) (Stem cell culture)	ATCC	4-X
Dulbecco's Phosphate Buffered Saline (DPBS), no calcium, no magnesium	Gibco	14190144
Embryonic Stem Cell FBS	Gibco	16141061
Fetal Bovine Serum (FBS) Advanced, Heat Inactivated	Capricorn Scientific	FBS-HI-11A
GlutaMAX	Gibco	35050061
HCM Hepatocyte Culture Medium BulletKit	Lonza	CC-3198
KnockOut Serum Replacement (KOSR)	Gibco	10828028
Minimum Essential Medium (MEM)	Gibco	21090022
mTeSR1 Complete Kit	STEMCELL Technologies	85857
Non-Essential Amino Acids (NEAA)	Gibco	11140050
OptiMEM	Gibco	31985070
Penicillin/streptomycin (pen/strep)	Gibco	15140122
ReLeSR	STEMCELL Technologies	05872
RPMI 1640 Medium, HEPES	Gibco	22400089
STEMdiff Definitive Endoderm Differentiation kit	STEMCELL Technologies	05110
Trypsin/EDTA	Pan Biotech	P10-028100
Y-27632 RHO/ROCK pathway inhibitor	STEMCELL Technologies	72308

Table 7: List of buffers and solutions.

Buffer / Solution	Composition
Co-IP Lysis Buffer	25 mM Tris-HCl pH 7.5, 150 mM NaCl, 1 mM EDTA, 1% NP-40, 5% glycerol in H_2O
Cytomix	120 mM KCl, 0.15 mM $CaCl_2$, 10 mM KH_2PO_4, 25 mM HEPES, 2 mM EGTA, and 5 mM $MgCl_2$, adjusted to pH 7.6 with KOH, 0.2 µm sterile filtered
6X Laemmli SDS sample buffer	2.4 g SDS, 12 mg bromophenol blue, 9.4 mL glycerol, 2.4 mL of 0.5 M Tris-HCl pH 6.8, 3.8 mL H_2O, heat until in solution, add 2 mL 2-mercaptoethanol
LB medium	20 g LB Medium Powder (Lennox) in 1 L H_2O, autoclaved
LB/agar	15 g agar in 1 L autoclaved LB medium, 100 mg/L ampicillin
PBTG	10% goat serum, 1% BSA, 0.1% Triton X-100, in PBS, 0.2 µm sterile filtered
10X SDS running buffer	30 g Tris base, 144 g glycine, 10 g SDS, to 1 L with H_2O
20% Sucrose	20% w/v D(+)-Saccharose in PBS, 0.2 µm sterile filtered
50X TAE buffer	242 g Tris base, 7.43 g EDTA (disodium salt), 57.1 mL acetic acid, to 1 L with H_2O
TB medium	50 g Terrific Broth Medium Powder in 1 L H_2O, autoclaved
10X Transfer buffer	30.3 g Tris base, 144 g glycine, to 1 L with H_2O

Table 8: List of hESC and HLC media compositions.

hESC/HLC medium	Composition
Supplemented mTeSR1	32 mL mTeSR1 Basal Medium, 8 mL mTeSR1 5X Supplement
Basal RPMI	48.5 mL RPMI 1640 Medium (HEPES), 1 mL 50X B-27 Supplement (custom), 400 µL pen/strep, 250 µL GlutaMAX, 250 µL NEAA
RPMI++	20 mL Basal RPMI, 20 µL BMP4 (final conc., 20 ng/mL), 2 µL FGFb (final conc., 10 ng/mL)
RPMI + HGF	20 mL Basal RPMI, 20 µL HGF (final conc., 20 ng/mL)
Basal HCM	Based on the HCM Hepatocyte Culture Medium BulletKit, no HEGF: 48.5 mL HBM Basal Medium, 400 µL pen/strep, 1 mL BSA, 50 µL Transferrin, 50 µL Ascorbic Acid, 50 µL Insulin, 50 µL Hydrocortisone, 50 µL GA-1000
HCM + OSM	20 mL Basal HCM, 20 µL OSM (final conc., 20 ng/mL)
MEF-feeder medium	16.8 mL DMEM (high glucose, GlutaMAX, pyruvate), 3 mL Embryonic Stem Cell FBS, 200 µL pen/strep
hPSC-feeder medium	38.5 mL DMEM/F-12 (Mediatech), 10 mL KOSR, 500 µL pen/strep, 500 µL GlutaMAX, 500 µL NEAA, 50 µL 2-mercaptoethanol (for stem cell culture), 5 µL FGFb (final conc., 10 ng/mL)

conc., concentration

3.4 Cytokines, Growth Factors, and Inhibitors

Table 9: List of cytokines, growth factors, and inhibitors.

Name	Supplier	Catalog number
Bone morphogenetic protein 4 (BMP4)	Gibco	AF-120-05ET
BX795	InvivoGen	tlrl-bx7
Fibroblast growth factor basic (FGFb)	Gibco	PHG0026
Hepatocyte growth factor (HGF)	Gibco	100-39H
IFNα2A	Tebu-Bio	11100-1
IFNβ1a	Biomol	86421
IFNβ (chapter 5.2.1)	R&D Systems	8499-IF
IFNλ1	Gibco	300-02L
Oncostatin M (OSM)	R&D Systems	295-OM-010/CF
Ruxolitinib	InvivoGen	tlrl-rux-3
Tumor necrosis factor (TNF)	Abcam	ab259410

3.5 Bacteria and Viruses

Table 10: List of bacterial strains.

Name	Application	Source	Catalog number
JM109	Cloning of pBSK-HEV-Kernow-C1/p6 and derived plasmids	Promega	L2005
Stbl2	Cloning of lentiviral transfer plasmids	Invitrogen	10268019

Table 11: List of viruses.

Name	Description	Source
HEV-3 Kernow-C1/p6 WT	nHEV harvested from the lysates of S10-3 cells, electroporated with IVT RNA from pBSK-HEV-Kernow-C1/p6	This study
HEV-3 Kernow-C1/p6 ΔORF2	nHEV harvested from the lysates of S10-3/ORF2 cells, electroporated with IVT RNA from pBSK-HEV-Kernow-C1/p6-ΔORF2	This study
Mengo-Zn virus	Mengo virus with a mutation in the zinc-finger domain[239]	Research group of Dr. Marco Binder, German Cancer Research Center (DKFZ), Heidelberg
Sendai virus (SeV)	Prepared from allantoic fluid of embryonated chicken eggs	Prof. Dr. Rainer Zawatzky, DKFZ, Heidelberg

3.6 Cell Lines

Table 12: List of cell lines.

Name	Antibiotic resistance (Final concentration)	Source / Supplier	Catalog number / Reference
A549-RIG-I/MDA5^{DKO}-MDA5	Puromycin (1 µg/mL) Blasticidin (5 µg/mL)	Research group of Dr. Marco Binder, DKFZ, Heidelberg	Published in Magalhães *et al.* 2023[240]
A549-RIG-I/MDA5^{DKO}-MDA5-HEV-3-ORF2	Puromycin (1 µg/mL) Blasticidin (5 µg/mL) G418 (1 mg/mL)	Sebastian Stegmaier, Research group of Dr. Marco Binder, DKFZ, Heidelberg	This study
A549-RIG-I/MDA5^{DKO}-MDA5-HEV-1-ORF2	Puromycin (1 µg/mL) Blasticidin (5 µg/mL) G418 (1 mg/mL)	Sebastian Stegmaier	This study
A549-RIG-I/MDA5^{DKO}-MDA5-ORF3	Puromycin (1 µg/mL) Blasticidin (5 µg/mL) G418 (1 mg/mL)	Sebastian Stegmaier	This study
A549-RIG-I/MDA5^{DKO}-MDA5-GFP	Puromycin (1 µg/mL) Blasticidin (5 µg/mL) G418 (1 mg/mL)	Sebastian Stegmaier	This study
A549-RIG-I/MDA5^{DKO}-RIG-I	Puromycin (1 µg/mL) Blasticidin (5 µg/mL)	Research group of Dr. Marco Binder, DKFZ, Heidelberg	Published in Magalhães *et al.* 2023[240]
A549-RIG-I/MDA5^{DKO}-RIG-I-HEV-3-ORF2	Puromycin (1 µg/mL) Blasticidin (5 µg/mL) G418 (1 mg/mL)	Sebastian Stegmaier	This study
A549-RIG-I/MDA5^{DKO}-RIG-I-HEV-1-ORF2	Puromycin (1 µg/mL) Blasticidin (5 µg/mL) G418 (1 mg/mL)	Sebastian Stegmaier	This study
A549-RIG-I/MDA5^{DKO}-RIG-I-ORF3	Puromycin (1 µg/mL) Blasticidin (5 µg/mL) G418 (1 mg/mL)	Sebastian Stegmaier	This study
A549-RIG-I/MDA5^{DKO}-RIG-I-GFP	Puromycin (1 µg/mL) Blasticidin (5 µg/mL) G418 (1 mg/mL)	Sebastian Stegmaier	This study
A549-RIG-I/MDA5^{DKO}-TLR3	Puromycin (1 µg/mL) Blasticidin (5 µg/mL)	Sebastian Stegmaier	This study

A549-RIG-I/MDA5^{DKO}-TLR3-HEV-3-ORF2	Puromycin (1 µg/mL) Blasticidin (5 µg/mL) G418 (1 mg/mL)	Sebastian Stegmaier	This study
A549-RIG-I/MDA5^{DKO}-TLR3-HEV-1-ORF2	Puromycin (1 µg/mL) Blasticidin (5 µg/mL) G418 (1 mg/mL)	Sebastian Stegmaier	This study
A549-RIG-I/MDA5^{DKO}-TLR3-ORF3	Puromycin (1 µg/mL) Blasticidin (5 µg/mL) G418 (1 mg/mL)	Sebastian Stegmaier	This study
A549-RIG-I/MDA5^{DKO}-TLR3-GFP	Puromycin (1 µg/mL) Blasticidin (5 µg/mL) G418 (1 mg/mL)	Sebastian Stegmaier	This study
CF1 Mouse Embryonic Fibroblasts, irradiated	–	Gibco	A34181
HEK293T	–	ATCC	CRL-3216
HepG2/C3A	–	ATCC	CRL-3581
Huh7.5 (chapter 5.3.3)	–	Prof. Dr. Charles Rice, The Rockefeller University, New York City	–
Huh7.5 (chapter 5.1.3)	–	Prof. Dr. Volker Lohmann, Heidelberg University Hospital	–
Huh7.5-MDA5	Blasticidin (5 µg/mL)	Prof. Dr. Volker Lohmann	Published in Colasanti *et al.* 2023[198]
Huh7.5-RIG-I	Puromycin (2 µg/mL)	Prof. Dr. Volker Lohmann	Published in Colasanti *et al.* 2023[198]
Huh7.5-TLR3	Puromycin (2 µg/mL)	Prof. Dr. Volker Lohmann	Published in Colasanti *et al.* 2023[198]
Huh7.5-MDA5/LGP2	G418 (500 µg/mL) Blasticidin (5 µg/mL)	Carl Niklas Schneider/ Ann-Kathrin Mehnert	This study
hESC line RUES2	–	Dr. Xianfang Wu, Lerner Research Institute, Cleveland	Originally published by Lacoste *et al.* 2009[241]
RUES2 M6 WT clone	–	Ann-Kathrin Mehnert	This study
RUES2 M4 KO1 clone	–	Ann-Kathrin Mehnert	This study
RUES2 S8 KO2 clone	–	Ann-Kathrin Mehnert	This study
S10-3	–	Dr. Suzanne Emerson, Nationale Institutes of Health (NIH), Bethesda, Maryland	–
S10-3/ORF2	Puromycin (2 µg/mL)	Lars Maurer, Research group of Dr. Viet Loan Dao Thi, Heidelberg University Hospital	–

3.7 DNA and RNA Oligonucleotides

Table 13: List of primers for RT-qPCR analysis.

Number	Target	Sequence (5' → 3')	Source
552	B2m_BHK fw	AGGGAGTTTGTACCCACTGC	Charlotte Decker, Research group of Dr. Viet Loan Dao Thi, Heidelberg University Hospital
553	B2m_BHK rv	AAGCATCTCCATGACGCTTGA	Charlotte Decker
524	CCL5 fw	CCTGCTGCTTTGCCTACATTGC	This study
525	CCL5 rv	ACACACTTGGCGGTTCTTTCGG	This study
–	GAPDH fw	TCGGAGTCAACGGATTTGGT	Wüst *et al.*[242]
–	GAPDH rv	TTCCCGTTCTCAGCCTTGAC	Wüst *et al.*[242]
1	HEV ORF2 fw	GGTGGTTTCTGGGGTGAC	Wu *et al.*[204]
2	HEV ORF2 rv	AGGGGTTGGTTGGATGAA	Wu *et al.*[204]
492	HEV ORF1 fw	AGAAGCATTCTGGTGAGCCC	This study
493	HEV ORF1 rv	CAGCAACACGAAAGTCACGG	This study
156	IFIT1 fw	ACACCTGAAAGGCCAGAATG	Wu *et al.*[204]
157	IFIT1 rv	GGTTTTCAGGGTCCACTTCA	Wu *et al.*[204]
–	IFIT1 fw (chapter 5.2.1)	GAATAGCCAGATCTCAGAGGAGC	Wüst *et al.*[242]
–	IFIT1 rv (chapter 5.2.1)	CCATTTGTACTCATGGTTGCTGT	Wüst *et al.*[242]
–	IFNB1 fw	CGCCGCATTGACCATCTA	Wüst *et al.*[242]
–	IFNB1 rv	GACATTAGCCAGGAGGTTCTC	Wüst *et al.*[242]
176	IFNL1 fw	GTGACTTTGGTGCTAGGCTTG	Wu *et al.*[204]
177	IFNL1 rv	GCCTCAGGTCCCAATTCCC	Wu *et al.*[204]
174	IFNL2/3 fw	TAAGAGGGCCAAAGATGCCTT	Wu *et al.*[204]
175	IFNL2/3 rv	CTGGTCCAAGACATCCCCC	Wu *et al.*[204]
520	IL6 fw	GTCAGGGGTGGTTATTGCAT	This study
521	IL6 rv	AGTGAGGAACAAGCCAGAGC	This study
–	IRF9 fw	TCCTCCAGAGCCAGACTACT	Wüst *et al.*[242]
–	IRF9 rv	CAATCCAGGCTTTGCACCTG	Wüst *et al.*[242]
163	ISG15 fw	CTGTTCTGGCTGACCTTCG	Wu *et al.*[204]
164	ISG15 rv	GGCTTGAGGCCGTACTCC	Wu *et al.*[204]
178	OAS2 fw	ACAGCGAGGGTAAATCCTTGA	Wu *et al.*[204]
179	OAS2 rv	CAGTCCTGGTGAGTTTGCAGT	Wu *et al.*[204]
3	RPS11 fw	GCCGAGACTATCTGCACTAC	Wu *et al.*[204]
4	RPS11 rv	ATGTCCAGCCTCAGAACTTC	Wu *et al.*[204]
977	TNF fw	TAGCCCATGTTGTAGCAAACCC	This study
978	TNF rv	GGACCTGGGAGTAGATGAGGT	This study
811	TNFAIP3 fw	TCCTCAGGCTTTGTATTTGAGC	Wüst *et al.*[242]
812	TNFAIP3 rv	TGTGTATCGGTGCATGGTTTTA	Wüst *et al.*[242]

fw, forward; rv, reverse;
Numbers refer to the Primer Bank of the research group of Dr. Viet Loan Dao Thi

Table 14: List of DNA oligonucleotides for molecular cloning.

Number	Name	Purpose	Sequence (5' → 3')
370	MDA5 ampl fw AscI	Cloning of MDA5 into pWPI-Neo backbone	ATGATGGGCGCGCCATGTCG AATGGGTATTC
371	MDA5 ampl rv SpeI	Cloning of MDA5 into pWPI-Neo backbone	ATGATGACTAGTTCAATCCTC ATCACTAAATAAACAGC
433	LGP2 fw AsiSI	Cloning of LGP2 into pWPI-Bla backbone	ATGATGGCGATCGCATGGAG CTTCGGTCCTACC
432	LGP2 rv SpeI	Cloning of LGP2 into pWPI-Bla backbone	ATGATGACTAGTCTAGTCCAG GGAGAGGTCCG
546	IFNLR1 KO screening fw	*IFNLR1* KO screening	CAGCAGGTGGCCCATAAACG
547	IFNLR1 KO screening rv	*IFNLR1* KO screening	TGCCTTGTGTAGTCCATGACC
548	IFNLR1 KO inversion fw	*IFNLR1* KO screening	GTGCCTGAAGAAACAGGACC
549	IFNLR1 KO inversion rv	*IFNLR1* KO screening	GGTCCTGTTTCTTCAGGCAC
558	IFNLR1 KO clone seq fw	*IFNLR1* KO sequencing	CTGTGAGGGAGGCATTACAG
736	Neo ORF2/ORF2-HA Mut2 XhoI fw	Cloning of ORF2 and ORF2-HA into pLVX-Neo backbone	ATGATGCTCGAGACCATGTG CCCTAGGGTTGTTCT
738	Neo ORF2 NotI rv	Cloning of ORF2 into pLVX-Neo backbone	CATCATGCGGCCGCTTAAGA CTCCCGGGTTTTGCCTAC
739	Neo ORF2-HA NotI rv	Cloning of ORF2-HA into pLVX-Neo backbone	CATCATGCGGCCGCTTAAGC GTAATCTGGAACATCGTATGG GTAACTTCCACCACCGCCTG AACCTCCACCGCCAGACTCC CGGGTTTTGCCTACC
740	Neo GT1 ORF2 XhoI fw	Cloning of HEV-1 ORF2 into pLVX-Neo backbone	ATGATGCTCGAGACCATGCG CCCTCGGCCTATTTTG
741	Neo GT1 ORF2 NotI rv	Cloning of HEV-1 ORF2 into pLVX-Neo backbone	CATCATGCGGCCGCCTATAA CTCCCGAGTTTTACCCACC
742	Neo ORF3 XhoI fw	Cloning of HEV-3 ORF3 into pLVX-Neo backbone	ATGATGCTCGAGACCATGGG ATCACCATGTGC
743	Neo ORF3 NotI rv	Cloning of HEV-3 ORF3 into pLVX-Neo backbone	CATCATGCGGCCGCTCAACG GCGCAGCCCC
744	Neo GFP/GFP-HA XhoI fw	Cloning of GFP and GFP-HA into pLVX-Neo backbone	ATGATGCTCGAGACCATGGT GAGCAAGGGCGA
745	Neo GFP NotI rv	Cloning of GFP into pLVX-Neo backbone	CATCATGCGGCCGCGCGGCC GCTTACTTGTACAGC
746	Neo GFP-HA NotI rv	Cloning of GFP-HA into pLVX-Neo backbone	CATCATGCGGCCGCTTAAGC GTAATCTGGAACATCGTATGG GTAACTTCCACCACCGCCTG AACCTCCACCGCCCTTGTAC AGCTCGTCCATGCCG
866	ORF2 2RA/2A rv	RR to AA mutation in the ARM of ORF2	GTCGTCGTGGGGCGGCCAG CGGCGGTG
867	ORF2 2RA/2A fwd	RR to AA mutation in the ARM of ORF2	GCACCGCCGCTGGCCGCCC CACGACGACG
932	ORF2-WRD>AAA frag1 rv	WRD to AAA mutation in ORF2	CTGGGACTGGGCAGCCGCA GCGGAGCCAAG
933	ORF2-WRD>AAA frag2 fw	WRD to AAA mutation in ORF2	CTTGGCTCCGCTGCGGCTGC CCAGTCCCAG
872	TBK1 fw inner XhoI	Cloning of TBK1 into pLVX-Hygro backbone; first PCR; adds XhoI site	ATGATGCTCGAGATGCAGAG CACTTCTAATCATCTG

873	TBK1 rv inner	Cloning of TBK1 into pLVX-Hygro backbone; first PCR; adds GGGGSGGGGS linker sequence	ACTTCCACCACCGCCTGAAC CTCCACCGCCAAGACAGTCA ACGTTGCGAAGG
874	TBK1 rv outer NotI	Cloning of TBK1 into pLVX-Hygro backbone; second PCR	ATGATGGCGGCCGCTCACGT AGAATCGAGACCGAGGAGCG GGTTAGGGATGGGCTTCCCA CTTCCACCACCGCCTGAAC
875	TBK1 fw outer	Cloning of TBK1 into pLVX-Hygro backbone; second PCR; adds V5 tag and NotI site	ATGATGCTCGAGATGCAGAG CACTTC
880	IKKβ fw inner	Cloning of IKKβ into pLVX-Hygro backbone; first PCR; adds HiFi DNA Assembly overhang	GATCTATTTCCGGTGAATTCC TCGAGATGAGCTGGTCACCT TCCCTGAC
881	IKKβ rv inner	Cloning of IKKβ into pLVX-Hygro backbone; first PCR; adds GGGGSGGGGS linker sequence	GGTTAGGGATGGGCTTCCCA CTTCCACCACCGCCTGAACC TCCACCGCCTGAGGCCTGCT CCAGGCAGC
882	IKKβ rv outer	Cloning of IKKβ into pLVX-Hygro backbone; second PCR; adds V5 tag and HiFi DNA Assembly overhang	GAGGGAGAGGGGCGGGATC CGCGGCCGCTCACGTAGAAT CGAGACCGAGGAGCGGGTTA GGGATGGGCTTCCCACTTCC
883	IKKβ fw outer	Cloning of IKKβ into pLVX-Hygro backbone; second PCR	GATCTATTTCCGGTGAATTCC TCGAGATGAGC
444	ORF2 1° ATG to GTG rv	Mutation of first ORF2 start codon	CTAGGGCACA<u>C</u>GGTGATCCC A
445	ORF2 1° ATG to GTG fw	Mutation of first ORF2 start codon	TGGGATCACC<u>G</u>TGTGCCCTA G
550	ORF2 2° ATG-GTG rv	Mutation of second ORF2 start codon	CGGGCAGCA<u>C</u>AGGCAGAAAC
551	ORF2 2° ATG-GTG fw	Mutation of second ORF2 start codon	GTTTCTGCCT<u>G</u>TGCTGCCCG
223	GNN fw	GDD to GNN mutation of ORF1	GCCTTTAAGGGT<u>A</u>AT<u>A</u>ATTCG GTGGT
224	GNN rv	GDD to GNN mutation of ORF1	ACCACCGAAT<u>T</u>AT<u>T</u>ACCCTTA AAGGC

fw, forward; rv, reverse; Introduced mutations are <u>underlined;</u>
Numbers refer to the Primer Bank of the research group of Dr. Viet Loan Dao Thi

Table 15: List of RNA oligonucleotides for Cas9 RNP transfection.

Name	Supplier	Purpose	Sequence (5' → 3')
Guide RNA 1 175rev	Integrated DNA Technologies	*IFNLR1* KO	UUAGGUCCAUCCGUCCAGAC
Guide RNA 2 656forw	Integrated DNA Technologies	*IFNLR1* KO	GUGUGGGACCAGCAACAGCG
NTC_1 crRNA	Integrated DNA Technologies	Non-targeting crRNA	GCACUACCAGAGCUAACUCA

3.8 Plasmids

Table 16: List of plasmids.

Number	Plasmid name	Description	Source
27	pBSK-HEV-Kernow-C1/p6	Genome of the HEV-3 Kernow-C1/p6 strain under a T7 promoter	Dr. Suzanne Emerson, Nationale Institutes of Health (NIH), Bethesda, Maryland
211	pBSK-HEV-Kernow-C1/p6-ΔORF2	Genome of the HEV-3 Kernow-C1/p6 strain with both start codons of ORF2 mutated	This study
217	pBSK-HEV-Kernow-C1/p6-ΔORF2g	Genome of the HEV-3 Kernow-C1/p6 strain with a mutated first start codon of ORF2	This study
218	pBSK-HEV-Kernow-C1/p6-ΔORF2i	Genome of the HEV-3 Kernow-C1/p6 strain with a mutated second start codon of ORF2	This study
98	pBSK-HEV-Kernow-C1/p6-ΔORF3	Genome of the HEV-3 Kernow-C1/p6 strain with a mutated ORF3 start codon	Charlotte Decker, Research group of Dr. Viet Loan Dao Thi, Heidelberg University Hospital
28	pBSK-HEV-Kernow-C1/p6-GAD	Genome of the HEV-3 Kernow-C1/p6 strain with a GDD/GAD mutation in the RdRp sequence; later identified to miss a 1041-bp sequence across Hel and RdRp	Dr. Suzanne Emerson
225	pBSK-HEV-Kernow-C1/p6-GNN	Genome of the HEV-3 Kernow-C1/p6 strain with a GDD/GNN mutation in the RdRp sequence	This study
67	pCMV delta R8.2 lentiviral packaging plasmid	Encodes HIV gag/pol for lentiviral particle production	Prof. Dr. Charles Rice, The Rockefeller University, New York City
68	pCMV-VSVG	Encodes VSVG envelope protein for lentiviral particle production	Prof. Dr. Charles Rice
127	pWPI-MDA5-Neo	Lentiviral transfer plasmid encoding MDA5	This study (Carl Niklas Schneider)
–	pWPI-LGP2-Bla	Lentiviral transfer plasmid encoding LGP2; was used to establish stable cell lines, but was later accidentally discarded by Carl Niklas Schneider	This study (Carl Niklas Schneider)
289	pLVX-HEV-3-ORF2-Neo	Lentiviral transfer plasmid encoding HEV-3 ORF2	This study
290	pLVX-HEV-3-ORF2-HA-Neo	Lentiviral transfer plasmid encoding C-terminally HA-tagged HEV-3 ORF2	This study
291	pLVX-HEV-1-ORF2-Neo	Lentiviral transfer plasmid encoding ORF2 from HEV-1 (Sar55 strain)	This study
294	pLVX-ORF3-Neo	Lentiviral transfer plasmid encoding HEV-3 ORF3	This study
295	pLVX-GFP-Neo	Lentiviral transfer plasmid encoding GFP	This study
296	pLVX-GFP-HA-Neo	Lentiviral transfer plasmid encoding C-terminally HA-tagged GFP	This study

347	pLVX-ORF2-2R/2A-HA-Neo	Lentiviral transfer plasmid encoding C-terminally HA-tagged HEV-3 ORF2 with a 2R/2A mutation in the ARM	This study (Carla Siebenkotten)
359	pLVX-ORF2-WRD/AAA-HA-Neo	Lentiviral transfer plasmid encoding C-terminally HA-tagged HEV-3 ORF2 with a WRD/AAA mutation at position 87	This study
341	pLVX-TBK1-V5-Hygro	Lentiviral transfer plasmid encoding a V5-tagged TBK1	This study (Carla Siebenkotten)
344	pLVX-IKKβ-V5-Hygro	Lentiviral transfer plasmid encoding a V5-tagged IKKβ	This study (Carla Siebenkotten)

Bla, blasticidin resistance; Neo, neomycin (G418/Geneticin) resistance; Hygro, hygromycin resistance; Numbers refer to the Plasmid Bank of the research group of Dr. Viet Loan Dao Thi

3.9 Antibodies

Table 17: List of primary antibodies.

Name / Target	Species	Supplier / Source	Catalog number	Dilution
Anti-β-actin	Mouse	Sigma-Aldrich	A2228	1:4,000 for WB
Anti-Human Albumin, Ascites (Clone HSA1/25.1.3)	Mouse	Cedarlane Laboratories	CL2513A	1:1,000 for IF
Anti-α-Fetoprotein (AFP)	Mouse	Sigma-Aldrich	A8452	1:1000 for IF
FoxA2/HNF3β (D56D6) XP	Rabbit	Cell Signaling Technology	8186	1:400 for IF
HA-Tag (C29F4)	Rabbit	Cell Signaling Technology	3724	1:1000 for WB
HNF4α (C11F12)	Rabbit	Cell Signaling Technology	3113	1:500 for IF
Human IL-28 R alpha/IFN-lambda R1	Sheep	R&D Systems	AF5260	1:100 for WB
IRF-3 (D6I4C) XP	Rabbit	Cell Signaling Technology	11904	1:200 for IF
Anti-Human LGP2	Rabbit	Tecan	JP29030	1:100 for WB
MDA5 (human) polyclonal antibody (AT113)	Rabbit	Enzo Life Sciences	ALX-210-935	1:1,000 for WB
Oct-4A (C52G3)	Rabbit	Cell Signaling Technology	2890	1:400 for IF
Anti-ORF2, aa 434-457, clone 1E6	Mouse	Sigma-Aldrich	MAB8002	1:400 for IF 1:500 for WB
Anti-ORF2 polyclonal antibody	Rabbit	Dr. Patrick Behrendt, Twincore, Hannover	–	1:4,0000 for IF
Anti-ORF2 polyclonal antibody	Rabbit	Prof. Dr. Rainer Ulrich, Friedrich-Loeffler-Institut, Greifswald	–	1:6,000 for IF

Recombinant MRB198 anti-ORF3 (90 µg/mL)	Mouse	Geneva Antibody Facility, Université de Genève, Geneva, Switzerland	MRB198	1:200 for IF 1:25 for WB
Anti-RIG-I, clone Alme-1	Mouse	AdipoGen Life Sciences	AG-20B-0009	1:1,000 for WB
Anti-TLR3 antibody [40C1285]	Mouse	Abcam	ab13915	1:500 for WB
V5-Tag (D3H8Q)	Rabbit	Cell Signaling Technology	13202	1:1;1000 for WB

IF, immunofluorescence; WB, Western blot

Table 18: List of secondary antibodies.

Name / Target	Host species	Supplier / Source	Catalog number	Dilution
Anti-Mouse IgG, Alexa Fluor 488	Goat	Invitrogen	A11001	1:1,000
Anti-Mouse IgG, Alexa Fluor 568	Donkey / Goat	Invitrogen	A10037 / A11004	1:1,000
Anti-Rabbit IgG, Alexa Fluor 488	Donkey / Goat	Invitrogen	A21206 / A11008	1:1,000
Anti-Rabbit IgG, Alexa Fluor 568	Donkey / Goat	Invitrogen	A10042 / A11011	1:1,000
Peroxidase-AffiniPure (HRP) anti-Mouse IgG	Goat	Jackson ImmunoResearch	115-035-146	1:4,000
Peroxidase-AffiniPure (HRP) anti-Sheep IgG	Donkey	Jackson ImmunoResearch	713-035-147	1:4,000
Peroxidase-AffiniPure (HRP) anti-Rabbit IgG	Goat	Jackson ImmunoResearch	111-035-144	1:4,000

3.10 RNA-FISH Reagents and Probes

Table 19: List of RNA-FISH reagents and probes.

Name	Supplier	Catalog number
RNAscope H_2O_2 and Protease Reagents	Advanced Cell Diagnostics	322381
RNAscope Multiplex Fluorescent Detection Kit v2	Advanced Cell Diagnostics	323110
RNAscope Wash Buffer	Advanced Cell Diagnostics	310091
RNAscope TSA Buffer	Advanced Cell Diagnostics	322809
TSA Vivid Fluorophores 520 / 570 / 650	Advanced Cell Diagnostics	323271 / 323272 / 323273
RNAscope Probe- V-HEV-p6-ORF1	Advanced Cell Diagnostics	579831
RNAscope Probe- V-HEV-p6-ORF2	Advanced Cell Diagnostics	586651

RNAscope Probe- Hs-IFNL3-O1-C3	Advanced Cell Diagnostics	852711-C3
RNAscope Probe- Hs-IFIT1-C2	Advanced Cell Diagnostics	415551-C2
RNAscope Probe- Hs-ISG15-C3	Advanced Cell Diagnostics	467741-C3

3.11 Equipment, Devices, and Instruments

Table 20: List of equipment, devices, and instruments.

Name	Supplier	Catalog number
10x Genomics Chromium Controller	10x Genomics	120270
10x Genomics Chromium Next GEM Secondary Holder	10x Genomics	3000332
10x Genomics Magnetic Separator	10x Genomics	230003
5200 Fragment Analyzer System	Agilent	M5310AA
CFX96 Touch Real-Time PCR Detection System	Bio-Rad	–
DynaMag-2 Magnet	Invitrogen	12321D
FlexCycler2 PCR Thermal Cycler	Analytik Jena	–
GenePulser Electroporation System	Bio-Rad	–
Illumina NextSeq550 Sequencing System	Illumina	–
Intas ECL Chemostar	Intas	–
Leica TCS SP8 Confocal Microscope	Leica Microsystems	–
Mini-PROTEAN Tetra Cell System for SDS-PAGE	Bio-Rad	1658001
Mini Trans-Blot Cell System for Western blot	Bio-Rad	1703930
NanoPhotometer NP80	Implen	–
Nikon Eclipse Ts2-FL Widefield Epifluorescence Microscope	Nikon	–
RNAscope HybEZ Oven and EZ-Batch Wash Tray	Advanced Cell Diagnostics	321710/321720 and 321717
Qubit 4 Fluorometer	Thermo Scientific	–
SW 32 Ti Swinging-Bucket Rotor Set	Beckman Coulter	369650
Tecan Infinite M200 Plate Reader	Tecan	–
Ultracentrifuge, Optima L-90K	Beckman Coulter	–
ZEISS Celldiscoverer 7 Microscope	ZEISS	–

3.12 Software

Name	Application	Source / Webpage
Bio-Rad CFX Maestro 1.0	Analysis of raw RT-qPCR data	Bio-Rad Laboratories
BioRender	Preparation of schematic and descriptive figures	https://www.biorender.com/
CellProfiler 4.2.1	Segmentation and quantitative analysis of microscopy images	https://cellprofiler.org/
Fiji (ImageJ 1.54f)	Standard microscopy analysis	https://imagej.net/software/fiji/[243]

GraphPad Prism 8.0.1	Data visualization and statistical analysis	https://www.graphpad.com/
Ilastik 1.3.3post3	Segmentation of microscopy images	https://www.ilastik.org/
Inkscape 1.4	Preparation of schematic and descriptive vector graphics Assembly of final figures and adjustment of vector graphics from GraphPhad Prism for this dissertation	https://inkscape.org/
SnapGene 8.0.2	Generation of plasmid maps, design of cloning strategies, analysis of Sanger sequencing	https://inkscape.org/
ZEN 3.3 (ZEN lite)	Counting of FFU images acquired with the ZEISS Celldiscoverer 7 Microscope	https://www.zeiss.com/microscopy/de/produkte/software/zeiss-zen-lite.html

4 Methods

4.1 Molecular Cloning

4.1.1 Polymerase Chain Reaction

Polymerase chain reactions (PCRs) were performed using the Phusion High-Fidelity DNA Polymerase according to Table 21 and Table 22. Primers used for molecular cloning are listed in Table 14. 10 ng of template was used for amplification from DNA plasmids, and site-directed mutagenesis was performed by overlap extension PCR. The desired mutations were introduced by complementary reverse and forward primers of the first and the second of two overlapping PCR amplicons, respectively. These first PCR amplicons were then used in equimolar ratios, calculating with 100 ng of the larger amplicon, as input for a second PCR, producing the final, combined amplicon carrying the desired mutation. All PCR products were run on 1% agarose gels in 1X TAE buffer and visualized using Midori Green. Desired bands were excised and purified using the Macherey Nagel NucleoSpin Gel and PCR Clean-Up Kit according to the manufacturer's instructions. Products were eluted in 20 µL nuclease-free H_2O, if measured with a NanoPhotometer and used for further PCR reactions, or in 22.5 µL nuclease-free H_2O, if subjected entirely to downstream enzymatic digestion after measurement with a NanoPhotometer.

Table 21: Reaction mix for PCR using Phusion High-Fidelity DNA Polymerase.

Component	Volume
5X Phusion HF Buffer	10 µL
10 mM dNTPs	1 µL
10 µM primer forward	2.5 µL
10 µM primer reverse	2.5 µL
Template DNA	Variable
Phusion DNA Polymerase	0.5 µL
Nuclease-free H_2O	To 50 µL

Table 22: Thermal cycler program for PCR using Phusion High-Fidelity DNA Polymerase.

Step	Temperature	Time	
Initial denaturation	98 °C	30 sec	
Denaturation	98 °C	10 sec	35 cycles
Annealing	Variable	20 sec	
Elongation	72 °C	Variable	
Final extension	72 °C	5 min	
Hold	4 °C	Hold	

Annealing temperature was adjusted based on the melting temperature of the primers;
Elongation time was adjusted according to the amplicon size: 15–30 sec/kb

4.1.2 Enzymatic Restriction Digest

Restriction enzymes were purchased from New England Biolabs. PCR products were entirely subjected to enzymatic restriction digest according to Table 23 for 1 h at the respective working temperature of the enzyme, mostly 37 °C. Digested PCR products were directly cleaned using the Macherey Nagel NucleoSpin Gel and PCR Clean-Up Kit. DNA plasmid backbones were digested overnight according to Table 24 at the respective temperature. The linearized backbones were run on 1% agarose gels and excised, if a dropout of the correct size was visible, and subsequently purified using the Macherey Nagel NucleoSpin Gel and PCR Clean-Up Kit.

Table 23: Reaction mix for enzymatic restriction digest of PCR products.

Component	Volume
Purified PCR product	21.5 µL
10X CutSmart buffer (or different NEB buffer)	2.5 µL
Restriction enzyme 1	0.5 µL
Restriction enzyme 2	0.5 µL

Table 24: Reaction mix for enzymatic restriction digest of DNA plasmids.

Component	Volume
1 µg DNA plasmid	Variable
10X CutSmart buffer (or different NEB buffer)	5 µL
Restriction enzyme 1	1 µL
Restriction enzyme 2	1 µL
Nuclease-free H_2O	To 50 µL

4.1.3 DNA Ligation, Transformation of Competent Cells, and Plasmid Purification

Ligations were performed with the T4 DNA Ligase at a molar backbone:insert ratio of 1:4 (Table 25). Reactions were incubated at room temperature for 1 h or overnight at 16 °C.

Table 25: Reaction mix for ligation with T4 DNA Ligase.

Component	Volume
Digested backbone (50–100 ng)	Variable
Digested insert (ratio 1:4)	Variable
10X T4 DNA Ligase Buffer	2 µL
T4 DNA Ligase	1 µL

Competent cells were produced with the *Mix & Go* Competent Cells Kit. Stbl2 competent cells were used for amplification of standard and lentiviral plasmids. JM109 competent cells were used for amplification of pBSK-HEV-Kernow-C1/p6 and derived plasmids. 50 µL aliquots of competent cells were thawed on ice, and 5 µL of ligation reaction or 1 µL of purified plasmid was added. The tubes were flicked and incubated on ice for 5 min. The competent cells were then spread on ampicillin-containing LB-agar plates and incubated at 37 °C for 16 h. If possible, colony PCR was performed with the GoTaq G2 Hot Start Polymerase Kit to check for positive clones, according to the reaction mix in Table 26 and the thermal cycler program in Table 27. Colonies were picked, dipped into the reaction mix, and streaked onto a fresh LB-agar plate. If correct by colony PCR, 4 mL LB medium (for standard lentiviral transfer plasmids) or TB medium (for pBSK-HEV-Kernow-C1/p6 and derived plasmids) liquid cultures containing ampicillin were grown overnight. Minipreps were prepared using the Macherey-Nagel NucleoSpin Plasmid Kit and eluted in 50 µL nuclease-free H_2O. The clones were further validated by Sanger DNA sequencing at Eurofins or Microsynth. Purified plasmid preps were prepared from 150 mL LB/ampicillin overnight cultures with the Macherey Nagel NucleoBond Xtra Midi Kit and precipitated with isopropanol according to the manufacturer's instructions. DNA pellets were eventually resuspended in 300 µL nuclease-free H_2O. Midipreps were quality-checked by analytical restriction digest.

Table 26: Reaction mix for colony PCR.

Component	Volume
5X Green GoTaq Flexi Buffer	5 µL
25 mM $MgCl_2$	2 µL
10 mM dNTPs	0.5 µL
10 µM primer forward	1.25 µL
10 µM primer reverse	1.25 µL
GoTaq G2 Hot Start Polymerase	0.25 µL
Nuclease-free H_2O	14.75 µL

Table 27: Thermal cycler program for colony PCR.

Step	Temperature	Time	
Initial denaturation	95 °C	5 min	
Denaturation	95 °C	30 sec	30 cycles
Annealing	Variable	30 sec	
Elongation	72 °C	Variable	
Final extension	72 °C	5 min	
Hold	4 °C	Hold	

Annealing temperature was adjusted based on the melting temperature of the primers;
Elongation time was adjusted according to the amplicon size: 1 min/kb

4.2 Cell Culture

4.2.2 Cell Cultivation and Passaging

All cell lines used in this study were maintained at 37 °C in 95% humidity and 5% CO_2 atmosphere. Hepatoma cell lines HepG2/C3A, S10-3, and Huh7.5 and their respective derivatives were cultured in Dulbecco's Modified Eagle Medium (DMEM, high glucose, GlutaMAX), supplemented with 10% fetal bovine serum (FBS, Capricorn), and 1% penicillin/streptomycin (pen/strep), from here on referred to as cDMEM. A549 cells and their derivatives were maintained in DMEM (high glucose), 10% FBS, 1% pen/strep, and 1% non-essential amino acids (NEAA). Cell lines were routinely tested for mycoplasma by PCR. Stable cell lines with ectopic protein expression were continuously cultured under selection pressure of the respective antibiotic (Table 12). HepG2/C3A cells were grown on cell culture vessels previously coated with collagen, diluted 1:50 in phosphate buffered saline (PBS). Coated vessels were incubated at 37 °C for 30 min to 1 h and washed once with PBS. All cell lines were grown to 80–90% confluency and passaged two to three times per week at an appropriate ratio. For this, cells were washed once with PBS, incubated with trypsin until cell started detaching, resuspended in cDMEM, and distributed to fresh cell culture vessels at the respective dilution.

4.2.1 Cryopreservation and Thawing of Cells

Confluent cell lines were trypsinized as described above. Freezing medium containing 40% DMEM, 20% FBS, and 20% dimethyl sulfoxide (DMSO, Carl Roth) was added in a 1:1 ratio to the detached cells in trypsin, resuspended gently, and distributed to cryotubes (1 mL per vial). Four or eight vials were frozen from a confluent T75 flask or T175 flask, respectively, at -80 °C in a cryopreservation box and transferred to liquid nitrogen after 24 h. For thawing, cells were quickly warmed in a 37 °C water bath and added to 9 mL cDMEM. Cells were centrifuged at 1,000 rpm for 4 min to remove DMSO, the pellet was resuspended in an appropriate volume of cDMEM and transferred to a cell culture flask.

4.2.3 Generation of Stable Cell Lines by Lentiviral Transduction

For lentivirus production, 6-well plates were coated with 100 µg/mL poly-L-lysine for 15–30 min at room temperature and washed twice with PBS. 1.5 x 10^6 HEK293T cells were seeded per well to obtain ~80% confluency after 16–24 h. Transfection of HEK293T cells with the transfer plasmid encoding the gene of interest, the lentiviral packaging plasmid (pCMV delta R8.2 lentiviral packaging plasmid), and the envelope plasmid (pCMV-VSVG) was performed with JetPRIME according to Table 28. The transfection mix was incubated at room temperature for 15–30 min while the culture medium of the seeded HEK293T cells was exchanged with

pen/strep-free cDMEM. The transfection mix was added dropwise to different areas of the well, and the pen/strep-free cDMEM was exchanged after 4–6 h. One day prior to transduction, the target cells were seeded at 1.5 x 10^5 cells/well on a 6-well plate. Lentivirus-containing supernatants were collected 48 h post-transfection and sterile-filtered through a 0.45 µm filter unit. 2 mL pen/strep-free cDMEM was added to each lentivirus-containing supernatant harvested from one well of a 6-well plate. The entire virus suspension was then added to one well of the seeded target cells. The following day, the medium was exchanged with cDMEM, and antibiotic selection was started two days post-transduction. Upon reaching confluency, the transduced cells were gradually expanded. Selection was completed as soon as the non-transduced control had died. Transduced cells were continuously cultured under the respective antibiotic selection pressure.

Table 28: Reaction mix for transfection of HEK293T cells for lentivirus production.

Component	Amount per one well of a 6-well plate
JetPRIME Reaction Buffer	200 µL
Transfer plasmid	2 µg
pCMV-VSVG	0.5 µg
pCMV delta R8.2 lentiviral packaging plasmid	1.5 µg
JetPRIME Reagent	8 µL

4.2.4 Human Embryonic Stem Cell Culture

The hESC line RUES2 (R2) and the downstream differentiations were cultured on cell culture plates from Falcon, coated with ~10 µg Matrigel per cm^2. Matrigel aliquots of 0.5 mg each were thawed on ice, resuspended with a cold pipette tip in 6 mL cold KnockOut DMEM/F-12 (Gibco), and distributed to 6-well plates (1 mL/well), 12-well plates (500 µL/well), and 24-well plates (300 µL/well). Plates were incubated at 37 °C for at least 1 h before use. Before plating of cells, Matrigel-coated plates were kept at room temperature for at least 10 min. All media, except for Dulbecco's Phosphate Buffered Saline (DPBS) and ReLeSR, were pre-warmed to 37 °C before use. Stem cells were thawed quickly in a 37 °C water bath until a small ice clump remained, and 500 µL supplemented mTeSR1 medium (Table 8) was added dropwise to thaw the remaining ice. Thawed cells were centrifuged at 1,000 rpm for 4 min. The cell pellet was resuspended gently three to four times in 500 µL supplemented mTeSR1 and distributed to one or two Matrigel-coated wells of a 6-well plate, depending on the pellet size, to a total culture volume of 1.5 mL. The medium was exchanged daily, and stem cells were passaged every four days at a ratio of 1:6. For this, old medium was collected, and each well was washed with 1 mL DPBS. Then, 450 µL ReLeSR was added, and plates were swirled for 30 sec. ReLeSR

was aspirated, and plates were incubated at 37 °C for 5–8 min until the stem cell colonies started floating when gently tapping the plate. Colonies were collected in 700 µL old mTeSR1 per well with little resuspension, pooled in a 15 mL Falcon tube, and the wells were rinsed with another 700 µL old mTeSR1. After centrifugation at 1,000 rpm for 4 min, the stem cell pellets were gently resuspended six to eight times in fresh, supplemented mTeSR1, and distributed at a 1:6 ratio to Matrigel-coated 6-well plates. For cryopreservation, each well of a 6-well plate was frozen into two cryotubes (1 mL/vial). After detachment of the stem cell colonies with ReLeSR and centrifugation as described above, the stem cell pellet was resuspended gently three to four times in the appropriate volume of freezing medium, containing 50% KnockOut Serum Replacement (KOSR), 40% supplemented mTeSR1, and 10% DMSO (ATCC).

4.2.5 Differentiation of Human Embryonic Stem Cells to Hepatocyte-Like Cells

R2 cells and derivatives were differentiated to definitive endoderm (DE) using the STEMdiff Definitive Endoderm Differentiation kit. All media, except for DPBS, were pre-warmed to 37 °C before use. Old mTeSR1 medium was collected, and R2 cells were washed once with DPBS. Then, 450 µL Accutase containing 10 µM Y-27632 RHO/ROCK pathway inhibitor was added to each well of a 6-well plate and incubated at 37 °C for 8–10 min until most stem cells were detaching when gently tapping the plate. For cell collection, 1 mL old mTeSR1 was added to each well, gently resuspended several times, and pooled in a Falcon tube. Wells were rinsed once with 1 mL of old mTeSR1. The single-cell suspension was counted, and 9×10^5 cells per differentiation well were centrifuged at 1,000 rpm for 4 min. The pellet was resuspended at a concentration of 1.29×10^6 cells/mL in fresh, supplemented mTeSR1, containing 10 µM Y-27632 RHO/ROCK pathway inhibitor. After ~20 h, 95% confluent wells were washed three times with 1 mL KnockOut DMEM/F-12 and swirled for 30 sec after each wash. Then, 700 µL DE Basal Medium supplemented with 1X Supplement CJ and 1X Supplement MR was added. After ~28 h, the cells were washed three times with KnockOut DMEM/F-12, swirled, and 700 µL DE Basal Medium supplemented with 1X Supplement CJ was added to each well. Subsequently, the medium was changed daily for two consecutive days. On day 5 post-seeding, the medium was aspirated, the wells were washed with 1 mL DPBS, and 350 µL Accutase, containing 10 µM Y-27632 RHO/ROCK pathway inhibitor, was added to each well. The cells were incubated at 37 °C for 8–10 min until they were detaching when gently tapping the plate. The cells were resuspended in 500 µL non-supplemented Rosewell Park Memorial Institute (RPMI) 1640 Medium (HEPES), pooled, and wells were rinsed with 500 µL RPMI. The single-cell suspension was centrifuged at 1,000 rpm for 4 min. The cell pellet was resuspended in 400 µL RPMI++ (Table 8) per HLC differentiation well, containing 10 µM Y-27632 RHO/ROCK pathway inhibitor. Each DE well of a 12-well plate was seeded to two HLC differentiation wells on 24-well plates. RPMI++ was changed daily for four consecutive days.

On day 5 post-seeding, the medium was changed to basal RPMI + HGF (Table 8) for five consecutive days and changed daily. For the final maturation to hepatocyte-like cells (HLCs), cells were cultured in 500 µL HCM + OSM (Table 8) for five days. The medium was exchanged every two days.

4.2.6 Genetic Manipulation of Human Embryonic Stem Cells Using Cas9 Ribonucleoprotein Transfection

This procedure was derived from a protocol presented by Wu & Dao Thi[244]. All media, except for DPBS and ReLeSR, were pre-warmed to 37 °C before use. R2 cells were cultured for two passages before starting the procedure. On the day of the next passage (day 0), Cas9 ribonucleoprotein (RNP) complexes were assembled according to the manufacturer's instructions. When using separate CRISPR RNA (crRNA) and *trans*-acting RNA (tracrRNA), annealing according to the manufacturer's instructions was performed before. Reaction mixes from Table 29 and Table 30 were incubated separately for 5 min at room temperature, combined, and incubated for 15–20 min at room temperature. In the meantime, hESCs were singularized using Accutase as described previously. Cells were counted, and 4 x 10^4 cells per transfection well were centrifuged at 1,000 rpm for 4 min. The cell pellet was resuspended in transfection medium, consisting of supplemented mTeSR1 plus 10 µM Y-27632 RHO/ROCK pathway inhibitor, at a concentration of 8 x 10^4 cells/mL, and 500 µL were distributed per well to Matrigel-coated 24-well plates. For the forward transfection, 50 µL of the transfection mix containing the Cas9 RNP complexes was immediately added dropwise to the respective wells, and plates were gently rocked back and forth. The plates were incubated at 37 °C, and the medium was replaced by fresh transfection medium 4 h post-transfection. On day 1, reverse transfection was performed using the same Cas9 RNP setup as for the first transfection. One day later, 6 x 10^5 irradiated mouse embryonic fibroblasts (MEFs) were thawed according to the supplier's instructions and seeded on Matrigel-coated 6-well plates in MEF-feeder medium (Table 8), based on the cell number stated on the MEF cryotube. After 24 h, transfected hESCs were dissociated from the 24-well plates with 250 µL Accutase, containing 10 µM Y-27632 RHO/ROCK pathway inhibitor per well. Cells were counted and 5 x 10^2, 6.67 x 10^2, and 8.33 x 10^2 cells/well were seeded in duplicates onto the MEFs in hPSC-feeder medium (Table 8), containing 10 µM Y-27632 RHO/ROCK pathway inhibitor, and gently distributed. The hPSC-feeder medium was replaced daily until hESC colonies reached a size of ~1 mm. Clearly separated hESC colonies were picked with a P200 pipette tip, transferred to a 1.5 mL tube containing hPSC-feeder medium with 10 µM Y-27632 RHO/ROCK pathway inhibitor, and gently resuspended. Each hESC clone was seeded in hPSC-feeder medium with 10 µM Y-27632 RHO/ROCK pathway inhibitor to one well of a 48-well plate, containing 6 x 10^4 MEFs, which had been thawed on the previous day. The medium was exchanged daily. The hESC

clones were gradually expanded using ReLeSR as described previously. During the expansion from 12-well to 6-well plates, half of the cell suspension was subjected to genomic DNA extraction, using the DNeasy Blood and Tissue Kit, according to the manufacturer's instructions, for downstream analysis. 50 ng of genomic DNA per reaction was screened using the GoTaq G2 Hot Start Polymerase Kit according to Table 26 and Table 27.

Table 29: Reaction mix per well for Cas9 RNP complex formation.

Component	Volume / Amount
OptiMEM	21 µL
*Sp*Cas9 (3 µM dilution)	2 µL / 6 pmol
Guide RNA 1 + guide RNA 2 (3 µM dilution) or crRNA:tracrRNA duplex (3 µM dilution)	2 µL / 6 pmol

Table 30: Reaction mix per well containing Cas9 RNP transfection reagent.

Component	Volume / Amount
OptiMEM	22 µL
Lipofectamine Stem Transfection Reagent	3 µL

4.2.7 Immunostimulation With Poly(I:C), Interferon, and Tumor Necrosis Factor

For immunostimulation of HepG2/C3A cells in 24-well plates, 3 x 10^5 cells were seeded 16 h prior to stimulation. For poly(I:C) transfection, 500 ng poly(I:C) were mixed with 1 µL Lipofectamine 2000 in 50 µL OptiMEM, incubated at room temperature for 5 min, and added dropwise to the 80–90% confluent cell layer. For supernatant feeding, 50 µg poly(I:C) per well were directly added to the culture medium. IFNα2A and IFNλ1 were diluted in 500 µL cDMEM per well to final concentrations of 500 IU/mL and 5 ng/mL, respectively, and tumor necrosis factor (TNF) was diluted to a final concentration of 40 ng/mL in 500 µL cDMEM per well. Stimulations were incubated for 8 h when destined for quantitative reverse transcription polymerase chain reaction (RT-qPCR) and 24 h when destined for Western blot analysis. Immunostimulation of HLCs was performed on day 20 of the differentiation as described for parental HepG2/C3A cells, but samples for both RT-qPCR and Western blot were harvested after 24 h. HLCs derived from *IFNLR1* wild type (WT) and knockout (KO) clones were stimulated with 500 IU/mL IFNβ1a or 5 ng/mL IFNλ1 for 8 h. PRR-expressing Huh7.5 cells were transfected with 250 ng poly(I:C) and 0.5 µL Lipofectamine 2000, or supernatant-fed with 25 µg poly(I:C) per well. Huh7.5 cells were infected with Mengo-Zn virus at a multiplicity of infection (MOI) of 1, medium was changed after 1-2 h, and samples were harvested for RT-qPCR after 12 h.

4.2.9 Immunostimulation of A549-Derived Cell Lines

These methods were established and performed by Sebatian Stegmaier in the research group of Dr. Marco Binder at the German Cancer Research Center (DKFZ), Heidelberg. A549-derived cell lines were seeded at a density of 1 x 10^5 cells/well in 24-well plates. The next day, cells were infected with Mengo-Zn virus at an MOI of 1, with SeV at an MOI of 0.75, or cells were stimulated by poly(I:C) supernatant feeding at a concentration of 50 µg/mL. Supernatants for enzyme linked immunosorbent assay (ELISA) and cell lysates for RNA extraction and RT-qPCR analysis were harvested at 24 h post-stimulation, except for SeV infection, which was harvested after 4 h for RT-qPCR. Supernatants were analyzed for IFNβ secretion using the bioluminescent human IFNβ ELISA kit LumiKine Xpress hIFN-β 2.0 according to the manufacturer's instructions. For EPO of A549-derived cell lines, 2 x 10^6 cells were collected and resuspended in 200 µL Cytomix supplemented with 2 mM adenosine triphosphate (ATP) and 5 mM glutathione (GT), together with 500 ng of HMW poly(I:C) or poly(C) control. The EPO was performed in 0.2 cm gap cuvettes at 166 V and 500 µF using the Bio-Rad GenePulser Electroporation System. Electroporated cells were transferred to pre-warmed cDMEM with 1% NEAA and seeded to 24-well plates at 500 µL per well. Cell lysates were harvested for RT-qPCR analysis at different time points post-EPO.

4.3 Virology

4.3.1 *In Vitro* Transcription and Electroporation of HEV RNA

Plasmids encoding the HEV-3 Kernow-C1/p6 strain and derived sequences were *in vitro* transcribed (IVT) for EPO. The respective HEV plasmid was linearized with the enzyme MluI-HF according to Table 31. The reaction was incubated overnight at 37 °C and purified using the QIAquick PCR Purification Kit according to the manufacturer's instructions. The product was eluted in 20 µL nuclease-free H_2O. If the concentration was approximately 200 ng/µL, the *in vitro* transcription reaction was assembled using the mMESSAGE mMACHINE T7 Transcription Kit, following the manufacturer's instructions (Table 32). The reaction was incubated at 37 ° C for 2 h, and 1 µL TURBO DNase was added for 15 min at 37 °C to stop the reaction. IVT RNA was purified by lithium chloride (LiCl) precipitation: 30 µL H_2O and 30 µL LiCl were added and incubated at -20 °C for at least 1 h. The reaction was centrifuged at 13,000 rpm for 15 min at 4 °C, washed with 1 mL 70% ethanol, and centrifuged again for 5 min. The ethanol was aspirated, the pellet was dried for several minutes and resuspended in 40 µL nuclease-free H_2O. RNA aliquots of 5 µg or 10 µg were made and stored at -80 °C.

Table 31: Linearization of HEV plasmids.

Component	Volume
10 µg HEV plasmid	Variable
CutSmart buffer	10 µL
MluI-HF	3 µL
Nuclease-free H_2O	To 100 µL

Table 32: *In vitro* transcription reaction of HEV RNA.

Component	Volume
Linearized HEV plasmid	5 µL
2X NTP/CAP	10 µL
30 mM GTP	1 µL
10X Reaction Buffer	2 µL
Enzyme Mix	2 µL

For EPO of IVT HEV RNA, confluent hepatoma cells were trypsinized and collected in Falcon tubes. The cells were centrifuged at 1,000 rpm for 5–10 min, washed once with PBS, centrifuged again, and resuspended in an appropriate volume of PBS. Cells were counted, and 2 x 10^6 or 4 x 10^6 cells per small-scale or large-scale EPO, respectively, were centrifuged. The cell pellets were resuspended in Cytomix, supplemented with 2 mM ATP and 5 mM GT, both thawed on ice, at a final concentration of 10^7 cells/mL. For a small-scale EPO, 200 µL cell suspension in Cytomix was mixed with 5 µg IVT HEV RNA, transferred to a 0.2 cm gap cuvette, and electroporated at 166 V and 975 µF using the Bio-Rad GenePulser Electroporation System. For a large-scale EPO, 400 µL cell suspension in Cytomix was mixed with 10 µg IVT HEV RNA, transferred to a 0.4 cm gap cuvette, and electroporated at 270 V and 975 µF. Depending on the downstream experiment, electroporated cells were seeded in different cell culture vessels.

4.3.2 Production and Purification of HEV Wild Type and Trans-Complemented ΔORF2^{trans} Virus Particles

WT nHEV particles, from here on only called HEV, were produced in S10-3 cells, while ΔORF2^{trans} HEV particles were produced in S10-3/ORF2 cells, using HEV-3 Kernow/C1-p6 WT or ΔORF2 IVT RNA, respectively. Other than that, the procedure was the same. EPO of producer cells was performed with 0.4 cm gap cuvettes as described above, and at least 30 EPOs were performed per virus production. Each EPO was seeded to one 10 cm dish in 12 mL cDMEM. During ΔORF2^{trans} virus productions, S10-3/ORF2 cells were not kept under puromycin selection pressure. On day 3 post-EPO, each confluent dish was expanded to one 15 cm dish. Brefeldin A (BFA) was added to the producer cells at a concentration of 0.5 µg/mL

in fresh cDMEM 16 h before the HEV harvest. On day 7 post-EPO, dishes were washed once with 10 mL PBS, and cell layers were scraped in 5 mL PBS and collected in Falcon tubes. Each dish was washed with additional 3 mL of PBS. Collected cells were centrifuged at 1,000 rpm for 10 min, and the pellets were resuspended in 1 mL PBS per dish. 1.5 mL of cell suspension was distributed per 2 mL SafeLock Eppendorf tube, and four freeze-thaw cycles were performed using liquid nitrogen and a 37 °C water bath. Afterwards, tubes were centrifuged at 10,000 rpm for 2 min, and crude lysates were pooled in Falcon tubes. Of note, some experiments were performed with crude HEV lysate, which is indicated clearly in the corresponding figure legends. Otherwise, HEV particles were concentrated by ultracentrifugation through a 20% sucrose cushion. For this, 32 mL crude HEV suspension was underlaid with 5 mL 20% sucrose solution in PBS (0.2 µm-sterile filtered) in SW32 ultracentrifugation tubes, balanced, and centrifuged at 28,000 rpm for 3 h at 4 °C. The supernatant was discarded, and the HEV pellets were resuspended in 100 µL PBS per EPO. The HEV suspension was distributed to SafeLock Eppendorf tubes and centrifuged at 10,000 for 5 min to remove further impurities. The supernatant was pooled again, distributed to 50 µL aliquots, and stored at -80 °C.

4.3.3 Titration to Obtain Foci Forming Units

WT HEV stocks were titrated on 2 x 10^4 HepG2/C3A cells. The virus stock was serially diluted, and the cells were infected in triplicates with different dilutions. After five days, the plates were fixed with 4% paraformaldehyde (PFA) and stained for ORF2 protein by immunofluorescence (IF). Whole wells were imaged using the ZEISS Celldiscoverer 7 microscope, and foci were counted manually with the ZEN 3.3 (ZEN lite) software. The mean infectious titer was determined by calculating the triplicate mean of several dilutions and expressed as foci forming units (FFU)/mL.

4.3.4 Determination of HEV Genome Equivalents

For comparisons of WT and ΔORF2, HEV infections were based on the number of genome equivalents (GE) in the virus stocks. For this, RNA was extracted in duplicates from each 25 µL virus stock, filled to 100 µL with nuclease-free H_2O. 500 µL TRIzol was added per sample, together with a spike-in of 750 ng of housekeeping RNA, extracted and purified from baby hamster kidney (BHK)-21 cells, serving as a qualitative control for the extraction efficiency. TRIzol extraction was performed as described below, and RT-qPCR was performed using primers targeting HEV ORF2 and the β2 microglobulin (B2M) gene in the BHK spike-in. The number of GE/mL was calculated based on the dilutions performed during the RNA extraction, reverse transcription (RT), and qPCR.

4.3.5 Electroporation of WT and Mutant HEV RNA

EPO with IVT RNA of HEV WT or the mutants ΔORF2, ΔORF2g, ΔORF2i, ΔORF3, or GNN was performed as described previously. HEV-electroporated cells were mixed 1:1 with mock-electroporated cells or directly seeded at densities of 2 x 10^5 cells/well on 24-well plates for RT-qPCR analysis, 1 x 10^5 cells/well on 48-well plates for IF staining or RNA-FISH, or 3 x 10^4 cells/well on 96-well plates for analysis of cell viability. The respective figure legends indicate whether cells were mixed with mock-electroporated cells or directly seeded. Final cell densities were calculated based on the input cell number used for the EPO, and the electroporated cell suspensions were diluted in cDMEM accordingly. One day post-EPO, all wells were washed twice with PBS, and fresh cDMEM was added. If required, 6 µM BX795 or 0.06% DMSO was added to the respective wells, 48 h prior to harvesting. The culture medium of all wells was exchanged every 2 days, and samples were harvested on day 1, day 3, day 5, and day 7 post-EPO for the respective downstream analyses.

Huh7.5 cells were electroporated with WT and ΔORF2 HEV RNA as described above and transferred to a T75 cell culture flask. On day 3 post-EPO, the cells from ~80% confluent T75 flasks were resuspended in 40 mL cDMEM, and 1 mL/well was seeded on 24-well plates to reach a final confluency of ~80%. One day later, the cells were treated with 10,000 IU/mL IFNα2A or 10 ng/mL IFNλ1 in cDMEM. Medium with IFNs was exchanged daily until samples were harvested on day 7 post-EPO for RT-qPCR analysis.

4.3.6 General HEV Infection

Cells were infected with HEV particles according to the determined FFU or GE, as indicated in the respective figure legend. Hepatoma cells were infected in Minimal Essential Medium (MEM), supplemented with 10% FBS (Capricorn) and 1% pen/strep (cMEM), while HLCs were infected in HCM + OSM. The inoculum was removed after 16-24 h, cells were washed twice with PBS (hepatoma cells) or DPBS (HLCs), and fresh cDMEM or HCM + OSM was added. Infected cells were treated and harvested for downstream analysis as described in the respective Methods sections and in the respective figure legends.

4.3.7 Synchronized, Time-Resolved HEV Infection

HepG2/C3A cells were seeded at a density of 6 x 10^4 cells/well in 24-well plates. The following day, cells were cooled to 4 °C in a refrigerator ~15 min prior to the infection. Virus suspensions were prepared in cold cMEM. Cold plates were placed on ice, infected at 12 or 30 GE/cell in 400 µL cMEM per well, incubated for 2 h at 4 °C in a refrigerator, followed by internalization for 8 h at 37 °C. Wells were then washed twice with PBS, and 1 mL warm cDMEM was added per well. Cells were incubated at 37 °C until harvested with TRIzol for RT-qPCR analysis.

4.4 Quantitative Reverse Transcription Polymerase Chain Reaction

4.4.1 RNA Extraction

Hepatoma cells in 24-well plates were lysed by adding 450 µL RL lysis buffer of the Roboklon Universal RNA Kit, supplemented with 1% 2-mercaptoethanol. Cells were scraped with a P1000 pipette tip and transferred to RNase-free tubes. The manufacturer's instructions were followed, and RNA was eluted in 30–50 µL nuclease-free H_2O. Cell lysates from time-resolved, synchronized infections, stem cell-derived HLCs, and virus stocks were extracted using TRIzol. Briefly, 500 µL TRIzol was directly added to cells seeded on 24-well plates or to 100 µL virus stocks diluted in PBS. The cells were scraped with a P1000 pipette tip, resuspended, transferred to RNase-free tubes, and 100 µL chloroform was added per 500 µL TRIzol. The tubes were vortexed, incubated for 2–3 min at room temperature, and centrifuged at 12,000 x *g* for 15 min at 4 °C. 210 µL of the upper aqueous phase was transferred to a fresh RNase-free tube, and an equal volume of isopropanol was added to precipitate the RNA. The tubes were vortexed thoroughly, incubated for a minimum of 20 min at -20 °C or overnight at -80 °C, and centrifuged at 12,000 x *g* for 15 min at 4 °C. RNA pellets were washed twice with 500 µL 75% ethanol and centrifuged in between at 12,000 x *g* for 5 min at 4 °C. After the last centrifugation step, the ethanol was removed completely, and pellets were dried at room temperature for 20–30 min. RNA pellets were resuspended in 20 µL nuclease-free H_2O and stored at -80 °C. RNA concentrations were measured with a NanoPhotometer. RNA from A549-derived cell lines was extracted by Sebastian Stegmaier in the research group of Dr. Marco Binder (DKFZ, Heidelberg) using the Monarch Total RNA Miniprep Kit.

4.4.2 Reverse Transcription

For gene expression analysis, 300 ng to 1 µg of RNA per sample was reverse transcribed using the iScript cDNA Synthesis Kit according to Table 33 and the thermal cycler program in Table 34. The cDNA was diluted 1:10 with nuclease-free H_2O for reactions with 750 ng–1 µg RNA and 1:5 for 300 ng–750 ng RNA. RT of A549-derived RNA was performed by Sebastian Stegmaier in the research group of Dr. Marco Binder (DKFZ, Heidelberg) with the High Capacity cDNA Reverse Transcription Kit. cDNA was generally stored at -20 °C.

Table 33: Reaction mix for RT using the iScript cDNA Synthesis Kit.

Component	Volume
300 ng–1 µg RNA	Variable
5X iScript Reaction Mix	4 µL
iScript Reverse Transcriptase	1 µL
Nuclease-free H_2O	To 20 µL

Table 34: Thermal cycler program for RT.

Step	Temperature	Time
Priming	25 °C	5 min
Reverse transcription	46 °C	30 min
Reverse transcriptase inactivation	95 °C	1 min
Hold	4 °C	Hold

4.4.3 Quantitative (Real-Time) Polymerase Chain Reaction

HEV genome copy quantification and relative target gene expression analysis was performed with iTaq Universal SYBR Green Supermix, using the primers in Table 13. For quantification of HEV genome copies, eight 10-fold serial dilutions of a 10 ng/µL pBSK-HEV-3 Kernow-C1/p6 plasmid stock were prepared as a standard curve. 5 µL of either diluted cDNA, diluted standard, or H_2O control were mixed in 96-well PCR plates with target-specific primers, iTaq Universal SYBR Green Supermix, and H_2O according to Table 35. Plates were sealed and analyzed on a CFX96 Touch Real-Time PCR Detection System with the qPCR cycler program shown in Table 36. Gene expression relative to the housekeeping gene *RPS11* was calculated using the $2^{-\Delta Ct}$ method. HEV genome copies per microgram total RNA were determined by normalization of Ct values over the housekeeping gene *RPS11* and subsequent extrapolation of genome copy numbers from the standard curve, considering the different dilution steps. Normalized antiviral gene expression over HEV RNA and the housekeeping gene *RPS11* was determined using the $2^{-\Delta\Delta Ct}$ method.

Table 35: Reaction mix for qPCR analysis.

Component	Volume
cDNA / standard / H_2O	5 µL
10 µM primer fw	1 µL
10 µM primer rv	1 µL
iTaq Universal SYBR Green Supermix	10 µL
Nuclease-free H_2O	3 µL

fw, forward; rv, reverse

Table 36: Thermal cycler program for qPCR.

Step	Temperature	Time	
Polymerase activation and DNA denaturation	95 °C	2 min	
Denaturation	95 °C	10 sec	40 cycles
Annealing, extension, and plate read	60 °C	30 sec	
Melt curve analysis 65–95 °C (0.5 °C increments at 5 sec/step)			

4.5 Cell Viability Assay

Cell viability measurements were performed using the CellTiter 96 AQueous One Solution Cell Proliferation Assay, following the manufacturer's instructions. Per well of a 96-well plate, 100 µL cDMEM was mixed with 20 µL CellTiter 96 AQueous One Solution Reagent and added to the cells. Plates were incubated at 37 °C for 1 h and absorbance was measured at 490 nm using a Tecan Infinite M200 plate reader.

4.6 Co-Immunoprecipitation

HEK293T cells were seeded at a density of 1.2 x 10^7 cells per 10-cm dish, which was coated with 3.5 mL of 100 µg/mL poly-L-lysine for 15–30 min at room temperature and washed twice with PBS. After 20–24 h or once ~80% confluency was reached, HEK293T cells were co-transfected with a DNA:polyethylenimine (PEI) ratio of 1 µg:3 µL and a total of 20 µg DNA per dish. At least one hour prior to transfection, the medium was exchanged with pen/strep-free cDMEM. The reaction mixes were assembled according to Table 37 and Table 38, and the PEI-containing tube was vortexed for 3 sec. The plasmid suspension was added to the PEI suspension, vortexed immediately, and incubated for 30 min at room temperature. The transfection mix was added dropwise to different areas of the dish with the seeded HEK293T cells, and the medium was replaced with cDMEM after 6 h. The cells were harvested for co-IP 24 h post-transfection. Each dish was washed twice with 5 mL cold PBS, and the cells were scraped in 2 mL cold PBS containing 0.5X cOmplete Mini Protease Inhibitor Cocktail and transferred to a 15 mL Falcon tube. The dishes were rinsed with 2 mL cold PBS containing 0.5X cOmplete Mini Protease Inhibitor Cocktail. The scraped cells were centrifuged at 1,700 x *g* for 2 min, the supernatant was removed, and the cell pellet was gently resuspended in 1 mL Co-IP Lysis Buffer containing 1X cOmplete Mini Protease Inhibitor Cocktail. The lysate was transferred to a 1.5 mL Protein LoBind tube and incubated on ice for 30 min. During the incubation time, 25 µL Pierce Anti-HA Magnetic Beads per sample were washed twice with Co-IP Lysis Buffer in Protein LoBind tubes on a magnetic rack and resuspended in 25 µL Co-IP Lysis Buffer per sample, containing 1X cOmplete Mini Protease Inhibitor Cocktail. Beads were always pipetted with trimmed P200 pipette tips. The lysates were centrifuged at 13,000 rpm for 15 min at 4 °C, and the DNA pellet was removed. 60 µL input sample was transferred to a fresh Protein LoBind tube, 1X Laemmli sodium dodecyl sulfate (SDS) sample buffer was added, samples were boiled at 95 °C for 10 min, and stored at -20 °C. To the remaining sample, 25 µL equilibrated Pierce Anti-HA Magnetic Beads were added, and samples were incubated for 2 h at 4 °C under rotation at 10 rpm. Afterwards, the samples were transferred to fresh 1.5 mL Protein LoBind tubes, and the beads were washed three times with Co-IP Lysis Buffer, containing 1X cOmplete Mini Protease Inhibitor Cocktail, by placing the

tubes on a magnetic rack and removing them for gentle resuspension. Following the last wash, 100 µL of 1X Laemmli SDS sample buffer was added to the beads, and beads were boiled at 95 °C for 10 min at 550 rpm. The tubes were placed on a magnetic rack, and the supernatant was transferred to a fresh 1.5 mL Protein LoBind tube. Samples were frozen at -20 °C.

Table 37: Reaction mix per dish containing plasmid DNA.

Component	Volume / Amount
Plasmid 1	10 µg
Plasmid 2	10 µg
OptiMEM	To 391 µL

Table 38: Reaction mix per dish containing transfection reagent.

Component	Volume / Amount
PEI	60 µL
OptiMEM	331 µL

4.7 Protein Analysis

4.7.1 Peptide-*N*-Glycosidase F Treatment

To remove *N*-linked oligosaccharides, supernatants and cell lysates were treated using the Peptide-*N*-Glycosidase F (PNGase F) Kit. Based on the manufacturer's instructions, two times 18 µL of cell lysate in Pierce RIPA Lysis Buffer or supernatant, both containing 1X cOmplete Mini Protease Inhibitor Cocktail, were mixed with 2 µL of the provided 10X Glycoprotein Denaturing Buffer and incubated at 100 °C for 10 min. The reactions were cooled on ice and centrifuged briefly. Next, 4 µL of 10X GlycoBuffer, 4 µL Nonidet P-40 (NP-40), and 12 µL H_2O were added per sample. 2 µL of PNGase F was added to one of the two tubes, 2 µL H_2O to the other, serving as a control. The reactions were incubated at 37 °C for 1 h, mixed with 1X Laemmli SDS sample buffer, and stored at -20 °C.

4.7.2 Sodium Dodecyl Sulfate Polyacrylamide Gel Electrophoresis and Western Blot

Cells were washed once with cold PBS and lysed in an appropriate volume of Pierce RIPA Lysis Buffer, supplemented with 1X cOmplete Mini Protease Inhibitor Cocktail. Scraped cells were transferred to 1.5 mL tubes and incubated on ice for 30 min. The samples were centrifuged at 13,000 rpm for 15 min, and the DNA pellet was removed. If cell number or density were not comparable between samples, protein quantification was performed using the Pierce BCA Protein Assay Kit according to the manufacturer's instructions and a Tecan Infinite M200 plate reader for readout at 490 nm. The samples were then mixed with 1X

Laemmli SDS sample buffer, boiled at 95 °C for 10 min, and either loaded immediately in the case of ORF3 detection, or otherwise, frozen at -20 °C until further use. The samples were re-boiled at 95 °C for 10 min after each thawing. SDS-polyacrylamide gel electrophoresis (PAGE) gels were prepared at percentages ranging from 8–15%, depending on the target protein size. Equal sample volumes or equal protein amounts were loaded, together with a protein ladder. Samples were stacked at 50 V for ~30 min, followed by protein separation at 100 V for 1.5–2 h. Proteins were transferred at 100 V for 1.5 h onto methanol-activated polyvinylidene fluoride (PVDF) membranes with pore sizes of 0.2 µm for co-IP samples or 0.45 µm for other sample types. Membranes were blocked with 5% milk in 0.1% Tween 20 in PBS (PBS-T) for 1 h at room temperature. Membranes were incubated with primary antibodies (Table 17) in 5% milk in PBS-T overnight at 4 °C in sealed plastic pockets. After three 10-minute washes with PBS-T, the membranes were incubated with horseradish peroxidase (HRP)-coupled secondary antibodies (Table 18) in 5% milk in PBS-T for 1 h at room temperature. Membranes were washed three times with PBS-T and once with PBS. The chemiluminescent signal was developed using Pierce ECL Western Blotting Substrate and the Intas ECL Chemostar imager.

4.8 Immunofluorescence Analysis

Cell layers were fixed with 4% PFA in PBS for 15–20 min at room temperature and washed twice with PBS. Samples were permeabilized and blocked for 30 min with PBTG, containing 10% goat serum, 1% BSA, and 0.1% Triton X-100 in PBS. Primary antibodies (Table 17) were incubated in PBTG overnight at 4 °C. The next day, the samples were washed three times with PBS and incubated with fluorophore-coupled secondary antibodies (Table 18) and Hoechst in PBTG for 1 h at room temperature, protected from light. After three washes with PBS, images were taken using a Nikon Eclipse Ts2-FL widefield epifluorescence microscope or the ZEISS Celldiscoverer 7 microscope.

4.9 RNA Fluorescence *In Situ* Hybridization

RNA-FISH was performed using the RNAscope Multiplex Fluorescent V2 Assay according to the manufacturer's protocol. Briefly, probes were warmed to 40 °C in a water bath for 10 min and then cooled to room temperature. Hydrogen peroxide, supplied by the manufacturer, was applied to the fixed samples and incubated for 10 min at room temperature. The samples were washed twice with PBS. If IF staining was to be performed after RNA-FISH, samples were permeabilized with 0.1% Triton- X 100 in PBS for 10 min at room temperature. Then, all samples were permeabilized with a 1:15 dilution of Protease III in PBS for 10 min at room temperature and washed twice with PBS. If not indicated otherwise, all following steps were performed at 40 °C in the RNAscope HybEZ Oven and the samples were washed twice with

1X RNAscope Wash Buffer after each steps. The probes of the different channels (C1, C2, and C3) were combined and hybridized for 2 h. AMP 1, AMP 2, and AMP 3 were then hybridized for 30 min, 30 min, and 15 min, respectively. The following steps were performed separately for each of the channels used: the samples were incubated with HRP-C1, -C2, or -C3 for 15 min, TSA Vivid Fluorophores 520/570/650 were diluted 1:3000 in RNAscope TSA Buffer and incubated for 30 min, and HRP Blocker was applied for 15 min. After the last round of HRP, dye, and HRP Blocker incubation, the samples were counterstained with Hoechst in PBS for 5 min at room temperature. Alternatively, IF staining was performed according to the standard procedure as described in chapter 4.8, starting from the blocking step, but omitting the detergent from the blocking solution. Samples were imaged with a Leica TCS SP8 confocal microscope or a Nikon Eclipse Ts2-FL widefield epifluorescence microscope.

4.10 3'-Targeted 10x Genomics and Illumina Sequencing

HepG2/C3A cells were seeded at 8 x 10^4 cells/well in 24-well plates and infected the following day with HEV WT and ΔORF2^{trans} virus particles using a synchronized infection setup with 30 GE/cell as described previously. Cells were harvested at 56 h and on day 6 plus 16 h (referred to as day 7) post-internalization, and GEM generation and barcoding was immediately performed. The cells were washed with 1 mL PBS and trypsinized with 500 µL for 10 min at 37 °C. Per well, 500 µL cDMEM was added, and the cells were gently but thoroughly resuspended with a P1000 pipette tip. The cell suspensions of two wells per infection condition were pooled in a 2 mL DNA LoBind tube, resuspended 10–15 times, and strained once through a 70 µm cell strainer. The cells were then centrifuged at 300 x *g* for 3 min and washed with 1 mL of 0.04% BSA in PBS. Following another centrifugation step, the cells were resuspended in 0.5–1 mL of 0.04% BSA/PBS, depending on the size of the cell pellet, strained twice through a 70 µm cell strainer, and counted. The concentration of the cell suspension was adjusted, counted again, and then loaded onto a Chromium Next Gem Chip G according to the manufacturer's instructions, aiming for a targeted cell recovery of 5,000. Following GEM-RT incubation, the samples from the 56 h time point were stored at -20 °C and processed further together with the samples of the day 7 time point. GEM generation and barcoding, post GEM-RT cleanup and cDNA amplification, and 3' gene expression library construction steps were performed following the protocols of the Chromium Next GEM Single Cell 3' Reagents Kits v3.1. Index PCR for multiplexing was performed using the Dual Index Plate TT Set A. Quantification and quality control of cDNA was performed using a Qubit 4 Fluorometer and the 5200 Fragment Analyzer System. Final sequencing libraries were quality-controlled with the 5200 Fragment Analyzer System and quantified with the NEBNext Library Quant Kit for Illumina. The 5200 Fragment Analyzer was operated by Céline Schneider in the research group of Prof. Dr. Henrik Kaessmann at the Center for Molecular Biology at Heidelberg

University (ZMBH). Two sequencing runs were performed on Illumina NextSeq550 with the help of Daniel Kirrmaier in the research group of Prof. Dr. Michael Knop at the ZMBH. The first sequencing run contained uninfected, WT-, and ΔORF2-infected libraries of the 56 h time point. The second sequencing run contained uninfected and WT-infected libraries of the day 7 time point as well as WT-infected library of the 56 h time point. The libraries were first diluted to 4 nM, according to the manufacturer's instructions of the NextSeq 500/550 High Output Kit v2.5 (150 Cycles). Then, libraries were pooled at equal volumes, except for the respective uninfected samples, of which 10 times less library was added compared to the other samples. The pooled libraries were further denatured and diluted to a final concentration of 1.7 pM with a 1% PhiX control spike-in (provided by Daniel Kirrmaier, Research group of Prof. Dr. Michael Knop at ZMBH, Heidelberg), following the manufacturer's instructions. Sequencing was performed on Illumina NextSeq550 with high-output mode, paired-end sequencing, and 150 cycles.

4.11 Single-Cell RNA-Sequencing Data Analysis

The single-cell RNA-sequencing (scRNA-seq) data analysis was performed by Dr. Carlos Ramírez Álvarez in the research group of Prof. Dr. Carl Herrmann at the Institute for Pharmacy and Molecular Biotechnology (IPMB) at Heidelberg University. The methods used for the analysis were described by Dr. Carlos Ramírez Álvarez in our joint preprint by Mehnert *et al.*[245]. The data is accessible under the GEO accession number GSE288400.

4.12 AlphaFold Modeling

AlphaFold 2.3-based predictions of the ORF2-TBK1 interaction were performed by Dr. Thibault Tubiana at the Institute for Integrative Biology of the Cell (I2BC) in Gif-sur-Yvette, France. The methodology was described by Dr. Thibault Tubiana in our joint preprint by Mehnert *et al.*[245].

4.13 Data Analysis, Statistics, and Use of Software

4.12.1 General Microscopy Image Processing

Images were acquired either with a Nikon Eclipse Ts2-FL widefield epifluorescence microscope, a ZEISS Celldiscoverer 7 Microscope, or a Leica TCS SP8 confocal microscope. Images were inspected, merged, and brightness and contrast were adjusted using Fiji[243]. FFU were counted in the ZEN 3.3 (ZEN lite) software.

4.12.2 Quantification of HEV RNA-Positive Cells

Images of HepG2/C3A cells electroporated with HEV WT or the ΔORF2 mutant, stained by RNA-FISH, were acquired using a Nikon Eclipse Ts2-FL widefield epifluorescence

microscope. For each condition, five positions were acquired arbitrarily. The HEV RNA signal was segmented by pixel classification in ilastik[246], using a modified pipeline originally established by my colleague Jungen Hu. Nuclei were segmented in CellProfiler[247] and overlaid with the segmented binary images of the HEV RNA signal. The percentage of masked nuclei was calculated in CellProfiler to obtain the percentage of HEV RNA-positive cells.

4.12.3 Data Presentation and Statistical Analysis

All graphs shown in this dissertation, except for the scRNA-seq data analysis performed by Dr. Carlos Ramírez Álvarez, were generated using GraphPad Prism 8.0.1. Statistical analysis was also performed in GraphPad Prism, using the statistical tests indicated in the respective figure legends. Schematic figures were created with BioRender.com, indicated accordingly in the respective figure legends, or otherwise, with Inkscape 1.4.

4.12.4 Use of Artificial Intelligence Tools

The language artificial intelligence platform DeepL was used to enhance the clarity of individual sentences within this dissertation and obtain translation suggestions of German words. Neither full paragraphs nor entire sentences were generated using DeepL. All suggestions were carefully reviewed and incorporated, only if appropriate, into the autonomously written dissertation text.

4.14 Declaration of Ethics

The use of hESCs in this project (AZ: 3.04.02/0137) has been approved by the *Zentrale Ethik-Kommission für Stammzellenforschung* of the Robert Koch Institute (RKI) and fulfills all legal requirements according to the German Stem Cell Act.

5 Results

5.1 Evaluation and Optimization of Different Hepatocellular Systems to Study the HEV-Specific Cell-Intrinsic Antiviral Response

In the first step, I sought to exploit, characterize, and optimize different hepatocellular systems to study the HEV-specific cell-intrinsic antiviral response. HepG2/C3A cells and stem cell-derived HLCs have been demonstrated to upregulate IFNs and ISGs in response to HEV infection[195,197,198,200], suggesting at least partially intact antiviral signaling pathways, which, however, have not been characterized in detail[199,201,202,204]. Therefore, I first sought to assess the integrity of their responses to PRR and IFN stimulation. Then, I aimed to expand our methodological portfolio for genetic manipulation of HLCs, enabling the knockout of an integral component of the IFN system. Finally, I attempted to determine the contribution of individual PRRs to the HEV-induced cell-intrinsic antiviral response.

5.1.1 Assessing Antiviral and Inflammatory Pathways in HepG2/C3A Cells and hESC-Derived HLCs

HepG2/C3A cells harbor intact RLR and IFN responses but are defective in TLR3 signaling

Transfected poly(I:C) activates the cytosolic PRRs RIG-I and MDA5 and its helper LGP2, but also partly the endosomal TLR3. Supernatant feeding of poly(I:C) in turn results in stimulation of TLR3 in the endosome. I focused on type III IFNs in my RT-qPCR analysis, as they appear to be more relevant in HEV infection than type I IFNs[201,204]. I further selected *IFIT1* and *ISG15* as representative ISGs due to their strong induction upon HEV infection[201,202]. Transfection of poly(I:C) gave rise to detectable *IFNL1* expression (Figure 10A) and resulted in increased levels of *IFIT1* and *ISG15* mRNA in HepG2/C3A cells (Figure 10B, C). In contrast, they were only weakly responsive to TLR3 stimulation by poly(I:C) supernatant feeding, as indicated by the lack of *IFNL1* and *ISG15* induction and a minor 7.5-fold increase in *IFIT1* expression (Figure 10A–C). Overall, this indicated a negligible activity of TLR3 in these cells but intact signaling capacity of RIG-I, MDA5, or both. In agreement, I observed basal protein expression of RIG-I, MDA5, and LGP2 by Western blot (Figure 10D). As these PRRs are ISGs, their activation leads to a positive feedback loop, resulting in increased protein levels upon poly(I:C) transfection (Figure 10D). Basal TLR3 expression was detectable (Figure 10E), however, neither RIG-I, MDA5, nor LGP2 protein levels were enhanced upon poly(I:C) supernatant feeding (Figure 10E). This supported the presence of a weakly or non-functional TLR3 in these cells. Furthermore, they upregulated *IFIT1* and *ISG15* in response to type I IFN (IFNα2A) and type III IFN (IFNλ1) stimulation (Figure 10A–C). I also observed a minor increase of TNF alpha induced protein 3 (*TNFAIP3*) and *TNF* expression upon stimulation with TNF, suggesting a generally intact NF-κB signaling pathway (Figure 10F).

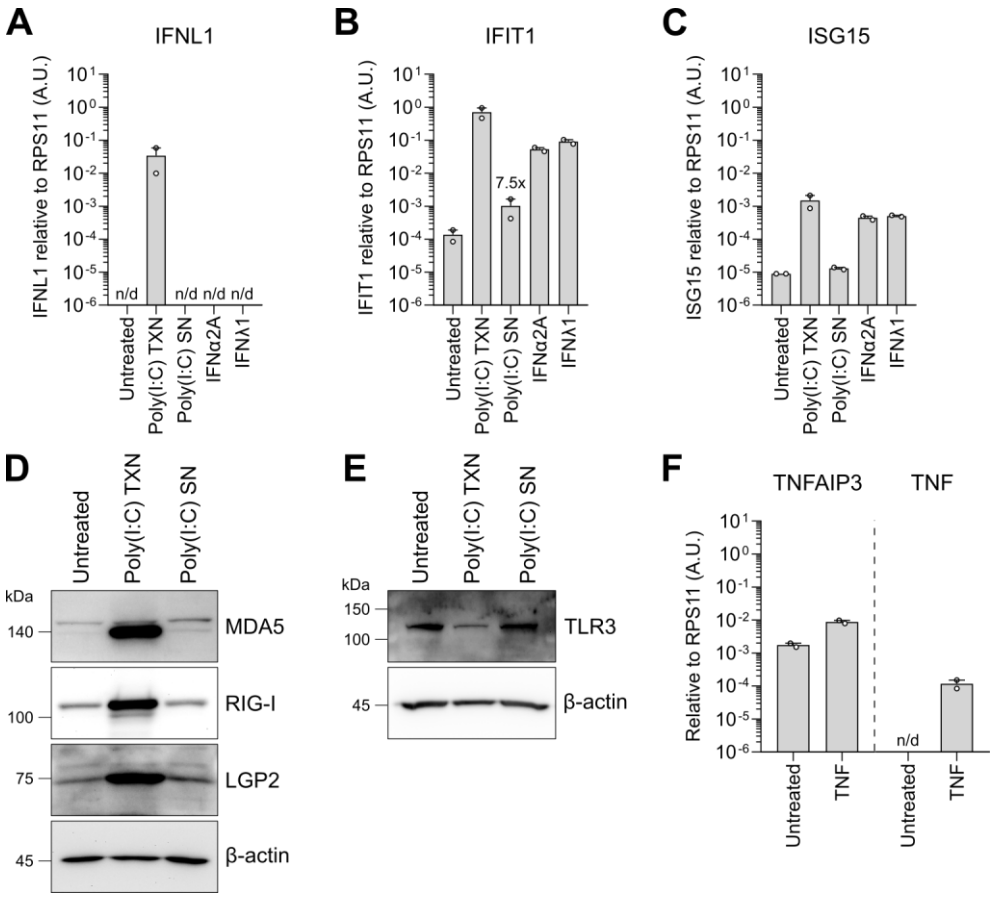

Figure 10: HepG2/C3A cells harbor intact RLR and IFN responses but are defective in TLR3 signaling.
(A) HepG2/C3A cells were stimulated by transfection (TXN) with 500 ng poly(I:C), supernatant (SN) feeding with 50 µg poly(I:C), 500 IU/mL IFNα2A treatment, or 5 ng/mL IFNλ1 treatment. Cell lysates were harvested after 8 h and analyzed for *IFNL1*, (B) *IFIT1*, and (C) *ISG15* expression by RT-qPCR, normalized to the housekeeping gene *RPS11* using the $2^{-\Delta Ct}$ method. Data show mean ± SEM of n = 2 independent experiments with two biological replicates each. For *IFIT1*, the fold change of poly(I:C) SN feeding over untreated is indicated above the respective bar. A.U., arbitrary units; n/d, not detectable. (D) Lysates of HepG2/C3A cells stimulated as described in A–C were harvested after 24 h and subjected to SDS-PAGE and Western blot to detect the proteins MDA5, RIG-I, LGP2, and the loading control β-actin. Representative blot of n = 2 independent experiments. kDa, kilodalton. (E) Lysates of HepG2/C3A cells, stimulated as described in D, were harvested after 24 h and subjected to SDS-PAGE and Western blot to detect TLR3 and the loading control β-actin. The blot of a single experiment is shown. kDa, kilodalton. (F) HepG2/C3A cells were stimulated with 40 ng/mL TNF for 8 h, lysed, and analyzed by RT-qPCR for expression of *TNFAIP3* and *TNF*, normalized to the housekeeping gene *RPS11* using the $2^{-\Delta Ct}$ method. Data show mean ± SEM of n = 2 independent experiments with two biological replicates each. A.U., arbitrary units; n/d, not detectable.

In summary, I demonstrated expression and responsiveness of the RLRs RIG-I, MDA5, and LGP2 in HepG2/C3A cells, as well as integrity of NF-κB and both type I and type III IFN receptor signaling pathways. In contrast, I found negligible responsiveness to TLR3 stimulation. Previously, reconstitution of TLR3 in defective Huh7.5 cells resulted in diminished replication of an HEV replicon, although to a lesser extent than RIG-I, suggesting involvement of both PRRs in the HEV-induced antiviral response[199]. However, since HEV is believed to replicate in the cytosol of its host cell, the RLRs are the most likely candidates to sense HEV. Therefore, I concluded that HepG2/C3A cells are suitable to study the cell-intrinsic antiviral response in the context of HEV infection, while taking their TLR3 defectiveness into consideration.

hESC-derived HLCs have functional RLR, TLR3, and IFN responses

Recently, pluripotent stem cell-derived HLCs were introduced as a promising and more physiologically relevant alternative compared to hepatoma cells to study the HEV life cycle[200,202,203]. Here, I differentiated the hESC line RUES2 (R2) to definitive endoderm (DE) cells, hepatocyte progenitors (HepProgs), immature hepatocytes (imHeps), and finally HLCs over a 20-day period (Figure 11A), as described previously[204]. I characterized the stages of differentiation by immunofluorescence (IF) staining for distinct marker proteins. Pluripotent hESCs expressed the octamer-binding transcription factor 4A (Oct-4A) (Figure 11B), whereas DE cells upregulated forkhead box protein A2 (FOXA2) (Figure 11C), both displaying the expected nuclear localization. The hepatocyte nuclear factor 4 alpha (HNF4α) was continuously expressed at the imHep and HLC stages (Figure 11D, E). During imHep differentiation, expression of alphafetoprotein (AFP) was induced (Figure 11D), which was also expressed in mature HLCs (Figure 11E). HLCs were identified based on expression of the hepatocyte marker albumin (Figure 11E). Mature HLCs grew in patches, as shown in Figure 11E, surrounded by AFP-positive imHeps and likely other endoderm-derived cell types.

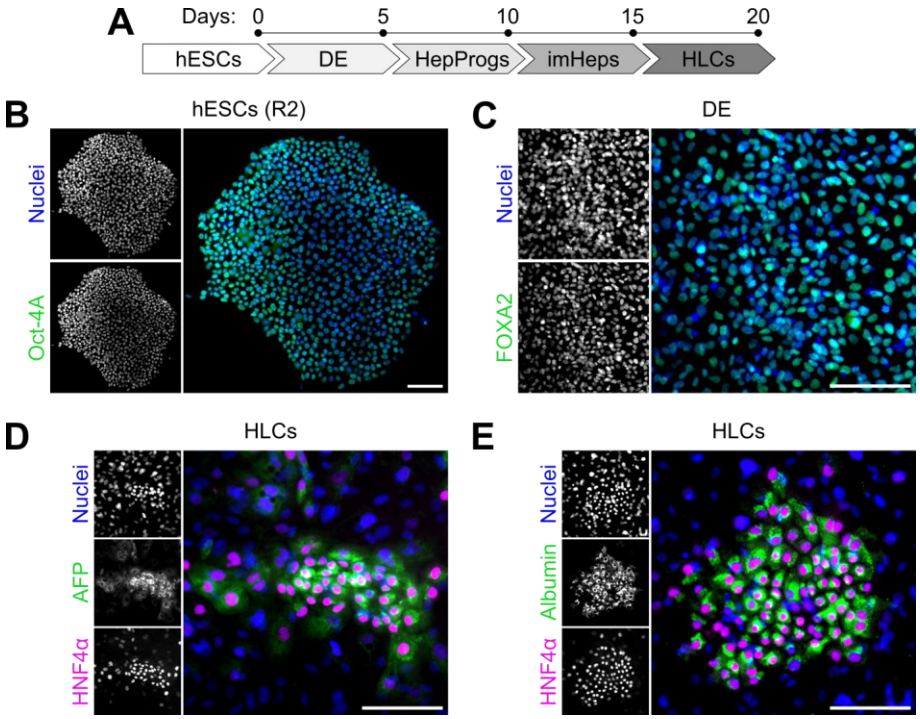

Figure 11: Differentiation of hESCs to HLCs is characterized by expression of specific marker proteins.
(A) Human embryonic stem cells (hESCs) were differentiated to hepatocyte-like cells (HLCs) through definitive endoderm (DE), hepatocyte progenitors (HepProgs), and immature hepatocytes (imHeps) over a period of 20 days. (B) hESCs were fixed before the start of differentiation, stained for the pluripotent stem cell marker Oct-4A (green) by IF, and counterstained for nuclei (blue) with Hoechst. Scale bar, 100 µm. (C) DE cells were fixed on day 5 of the differentiation, stained for FOXA2 (green) by IF, and counterstained for nuclei (blue) with Hoechst. Scale bar, 100 µm. (D) HLCs were fixed on day 20 of the differentiation, stained for AFP (green) and HNF4α (magenta), or (E) albumin (green) and HNF4α (magenta) by IF, and counterstained for nuclei (blue) with Hoechst. Scale bars, 100 µm. All images were taken with a Nikon Eclipse Ts2-FL widefield epifluorescence microscope.

To characterize the integrity of PRR and IFN signaling pathways, I stimulated HLCs as previously described for HepG2/C3A cells. In response to poly(I:C) transfection, *IFNL1* mRNA became detectable, and I observed increased expression of *IFIT1* and *ISG15* (Figure 12A–C). In contrast to HepG2/C3A cells, HLCs were responsive to TLR3 stimulation by poly(I:C) supernatant feeding, resulting in increased expression of *IFNL1*, *IFIT1*, and *ISG15* (Figure 12A–C). The RLRs MDA5, RIG-I, and LGP2 were expressed at basal levels in HLCs, and expression was enhanced upon poly(I:C) transfection and supernatant feeding (Figure 12D). Despite their responsiveness to stimulation, the TLR3 protein was undetectable by Western blot (data not shown). HLCs were also responsive to both type I and type III IFN stimulation, leading to upregulation of *IFIT1* and *ISG15* (Figure 12B, C). *IFNL1* was also weakly induced in response to treatment with IFNα2A and IFNλ1 (Figure 12A). This was surprising as IFNs are not replenished immediately downstream of the IFN receptor[161]. As HLCs were only harvested 24 h post-stimulation, it is possible that upregulation of RLRs triggered an IFN response towards a cytosolic nucleic acid stimulus. Furthermore, I observed intact NF-κB signaling, indicated by upregulation of the inflammatory cytokines *TNFAIP3*, *TNF*, *IL6*, and *CCL5* in response to TNF stimulation (Figure 12E). Altogether, hESC-derived HLCs appeared to be more immunocompetent than HepG2/C3A cells as they efficiently responded to TLR3 stimulation and exhibited intact RLR, IFN, and NF-κB-dependent signaling pathways. Therefore, I concluded that HLCs are a suitable model to study cell-intrinsic antiviral responses upon HEV infection.

5.1.2 Generation of an *IFNLR1* Knockout in hESCs Using CRISPR/Cas9

Early during my PhD, I aimed to perform single-cell RNA-sequencing (scRNA-seq) on hESC-derived HLCs to dissect IFN sensing and signaling in HEV-infected cells and uninfected bystanders. For this, a knockout (KO) of the type III IFN receptor is crucial to differentiate between IFN induction and IFN-dependent signaling. As the IL10RB subunit is not exclusively involved in type III IFN signaling, I decided to delete the IFNLR1 subunit of the type III IFN receptor, which is largely restricted to cell types of epithelial origin (reviewed in [159]). Different approaches have been employed to genetically manipulate human pluripotent stem cells (reviewed in [248]), including lentivirus or adeno-associated virus (AAV) transduction, and CRISPR/Cas9. Previously, my supervisor, Dr. Viet Loan Dao Thi, used the HUES8-iCas9 stem cell line, which expresses Cas9 under control of a doxycycline-inducible promoter[204,249]. Here, I aimed to implement a strategy that does not require the transduction with Cas9 constructs, thereby minimizing the risk for off-target effects caused by constitutive or leaky Cas9 expression.

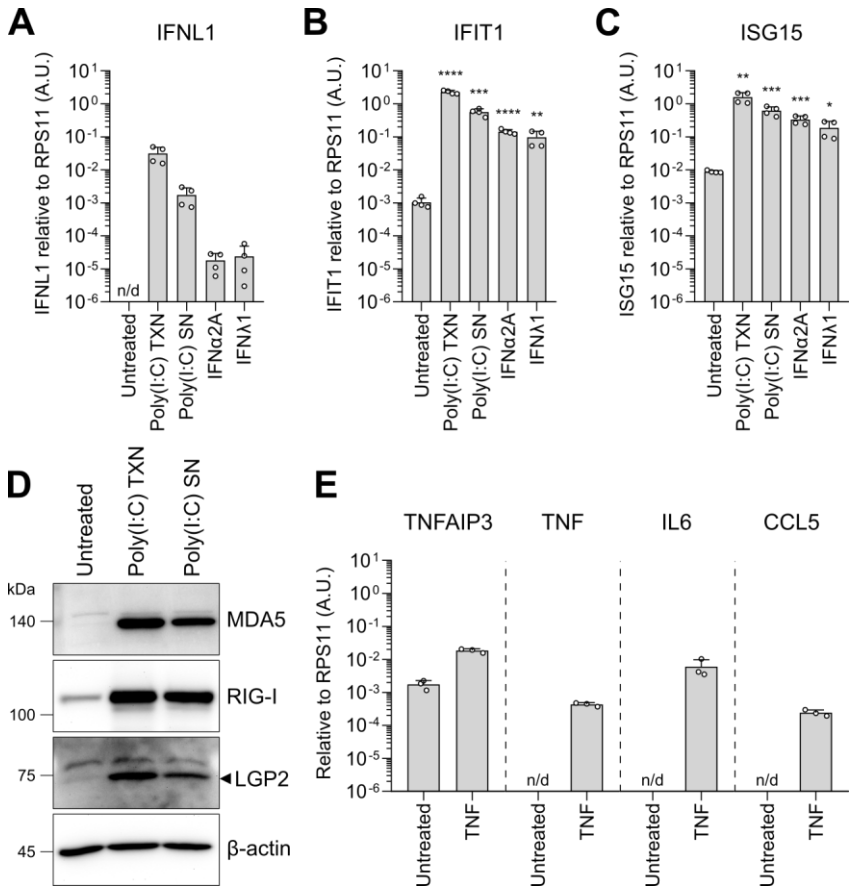

Figure 12: hESC-derived HLCs have functional RLR, TLR3, and IFN responses.
(A) HLCs were stimulated by transfection (TXN) with 500 ng poly(I:C), supernatant (SN) feeding with 50 µg poly(I:C), 500 IU/mL IFNα2A treatment, or 5 ng/mL IFNλ1 treatment on day 20 of the differentiation. Lysates were harvested after 24 h and analyzed for *IFNL1*, (B) *IFIT1*, and (C) *ISG15* expression by RT-qPCR, normalized to the housekeeping gene *RPS11* using the $2^{-\Delta Ct}$ method. Data show mean ± SD of n = 4 biological replicates of two independent HLC differentiations. Statistical analysis compared to the untreated condition in B and C was performed using unpaired two-tailed Student's t-test. *: $p < 0.05$; **: $p < 0.01$; ***: $p < 0.001$; ****: $p < 0.0001$. A.U., arbitrary units; n/d, not detectable. (D) Lysates of HLCs stimulated as described in A–C were harvested 24 h post-stimulation and analyzed by Western blot to detect MDA5, RIG-I, LGP2, and the loading control β-actin. Representative blot of n = 2 independent HLC differentiations. kDa, kilodalton. (E) HLCs were stimulated with 40 ng/mL TNF for 8 h and analyzed by RT-qPCR for *TNFAIP3*, *TNF*, *IL6*, and *CCL5* expression, normalized to the housekeeping gene *RPS11* using the $2^{-\Delta Ct}$ method. Data show mean ± SD of n = 3 biological replicates of one HLC differentiation. A.U., arbitrary units; n/d, not detectable.

Cas9 RNP transfection in hESCs yields homozygous and heterozygous *IFNLR1* KO clones

In somatic cells, a double strand break (DSB) introduced by Cas9 usually results in so-called insertion-deletion (indel) mutations through non-homologous end joining (NHEJ). However, hESCs have been reported to preferentially employ homologous recombination (HR) over NHEJ (reviewed in [250]). To increase the probability of generating a homozygous KO in hESCs, I therefore decided to combine two guide RNAs to obtain a full deletion of the *IFNLR1* exon 3 (Figure 13A). This approach has been successfully used in the HUES8-iCas9 stem cell line for a different gene[204]. Importantly, I verified that deletion of exon 3 would abrogate production of all isoforms of the IFNLR1 protein. I further ensured that all splice signals at the exon-intron junctions were deleted and that excision between the guide RNA target sites would result in a frameshift and thus, in a premature stop codon. To generate transduction-free KOs in hESCs,

I made use of Cas9 ribonucleoprotein (RNP) transfection, relying on *in vitro* assembly of the guide RNAs with a recombinant Cas9 enzyme. Transfected RNPs are degraded after approximately one day, decreasing the likelihood of off-target effects[251].

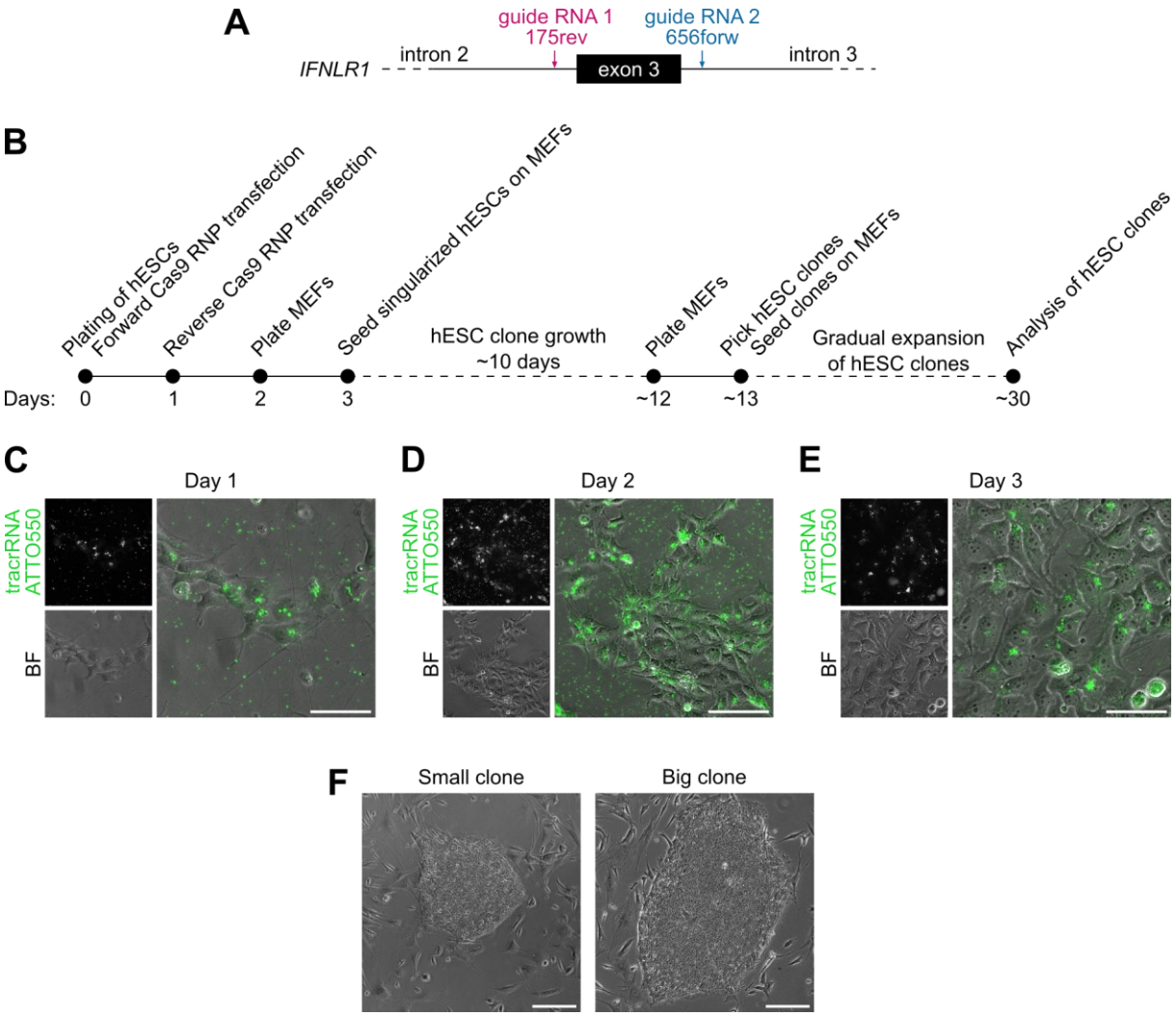

Figure 13: Single hESC clones of varying sizes are obtained after double Cas9 RNP transfection.
(A) Schematic representation of the *IFNLR1* exon 3 and the surrounding introns with indicated positions of the two guide RNAs to delete exon 3. (B) Workflow for obtaining single hESC clones following forward and reverse Cas9 RNP transfections, singularization of hESCs and seeding on MEFs, clone selection and picking, gradual expansion of clones, and analysis. (C) hESCs transfected with a Cas9 RNP complex assembled from a non-targeting crRNA and a fluorescent ATTO550-coupled tracrRNA were imaged on day 1, (D) day 2, and (E) day 3 of the workflow depicted in B. Scale bar, 50 µm. BF, brightfield. (F) Representative small and big hESC clones were imaged on day 13 of the workflow depicted in B. Images were taken with a Nikon Eclipse Ts2-FL widefield epifluorescence microscope. Scale bar, 200 µm.

I established a workflow with two rounds of RNP transfection, followed by expansion of hESC clones on mouse embryonic fibroblasts (MEFs), serving as feeder cells (Figure 13B). Individual hESC colonies were manually picked and expanded. To control for successful Cas9 RNP transfection, I included a non-targeting CRISPR RNA (crRNA), duplexed with a fluorescent ATTO550-coupled *trans*-activating RNA (tracrRNA). One day after the first transfection, fluorescent Cas9 RNP complexes were clearly visible in the majority of hESCs, however, also

in the empty spaces between the cells (Figure 13C). I did not observe a specific localization of the Cas9 RNPs in the nucleus of hESCs. The second transfection visibly increased the strength of the ATTO550 signal, indicating an increased amount of Cas9 RNP complexes (Figure 13D). One day later, the ATTO550 signal was notably decreased (Figure 13E), consistent with rapid degradation of the Cas9 RNP complexes, as suggested by existing literature[251]. I successfully picked and expanded several hESC clones with varying sizes, which I named accordingly (Figure 13F and Figure 14B; S = small, M = medium, B = big).

Once the hESC clones had been expanded, I extracted genomic DNA and analyzed the clones by PCR-based screening for successful KO. I designed one PCR primer pair to assess the presence of wild type (WT) or KO alleles (KO fw:KO rv) and two additional primer pairs to validate the absence of an inversion (INV) of the excised gene fragment between the two guide RNAs (KO fw:INV rv) or the presence of an INV (KO fw:INV fw) (Figure 14A). First, I excluded clones with an unclear band pattern, namely B10, B4, and B8 (Figure 14B). Then, I identified 13 out of the 24 clones as supposedly WT, based on the presence of a single WT allele band with a size of 1.0 kb (Figure 14B, upper panel). However, Sanger sequencing of clone B11, for instance, suggested at least one allele to harbor a small deletion around the DSB site of guide RNA 1, likely resulting from a successful DSB and subsequent repair by NHEJ. Sequencing of the supposedly WT alleles from heterozygous clones, including B2, B12, and M10, revealed short indel mutations around both guide RNA sites. This might indicate successful yet timely distinct introduction of DSBs at both sites, followed by fast repair through NHEJ. These observations highlighted the importance of a detailed sequence analysis in order to allow unequivocal proof of the integrity of the WT alleles. I did not sequence all alleged WT clones, but I identified the clone M6 (Figure 14B, C) to harbor two intact WT alleles, evidenced by unanimous nucleotide peaks in the Sanger sequencing. Nonetheless, potential off-target effects of the Cas9 RNP transfection would only become evident by whole genome sequencing, which should be considered for future analysis. Unfortunately, I only identified M4 as a homozygous *IFNLR1* KO clone, harboring the expected 470-base pair (bp) deletion between the two guide RNA sites (Figure 14B, C). With the aim of finding a second KO clone, I further assessed the clone S8, a potentially heterozygous clone with one KO allele and one inverted allele. This should equally result in a non-functional IFNLR1 protein. As each allele yielded a distinct PCR amplicon (Figure 14B), I could characterize them separately by Sanger sequencing. The KO allele harbored a 470-bp deletion, and the INV allele contained a 9-bp resection at the guide RNA 1 site, followed by the expected INV of the sequence between guide RNA 1 and guide RNA 2 (Figure 14C). Hence, I selected the M6 WT clone and the homo- and heterozygous M4 KO1 and S8 KO2 clones as suitable candidates for further characterization.

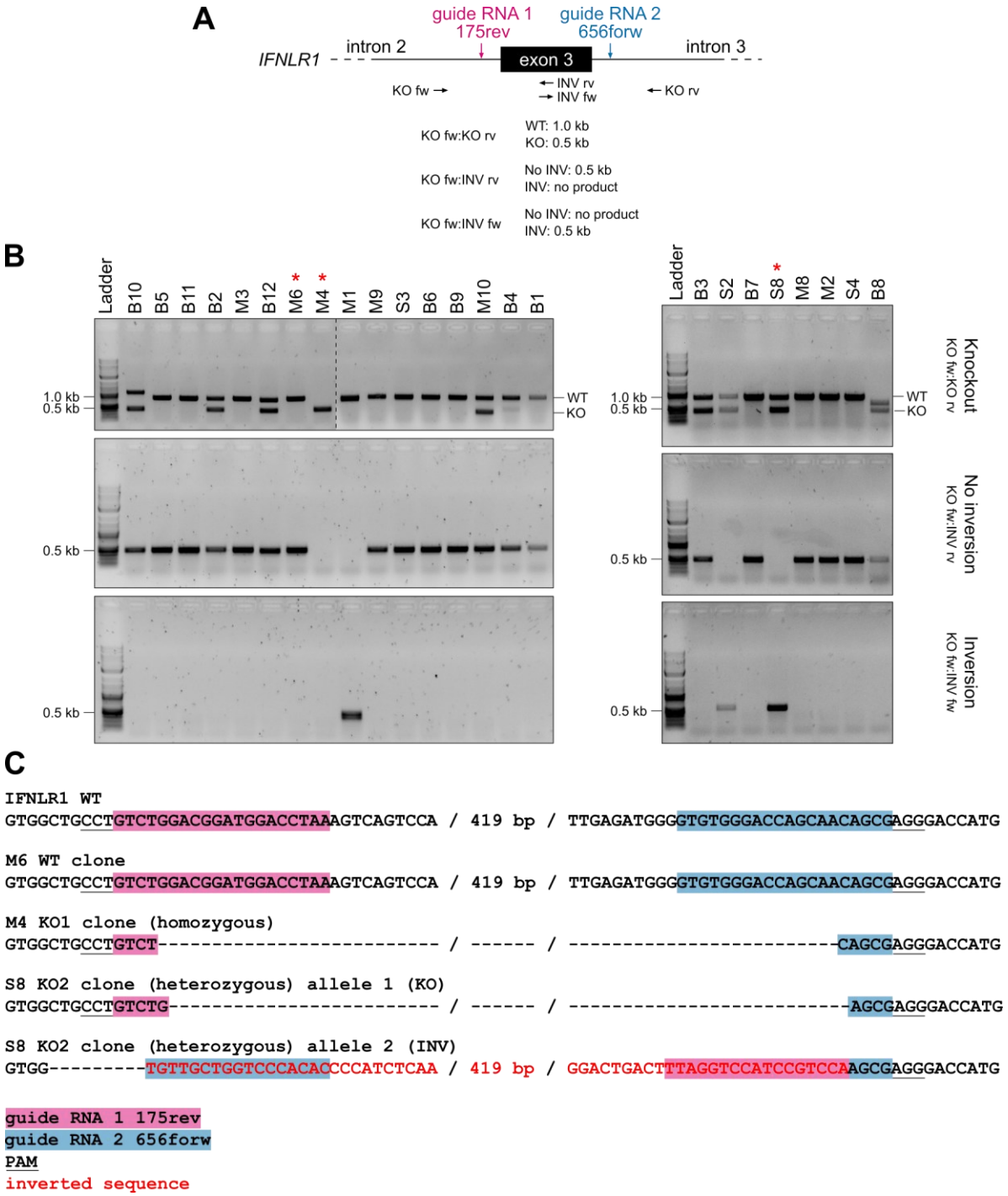

Figure 14: PCR- and Sanger sequencing-based screening identifies *IFNLR1* WT and KO clones.
(A) Schematic representation of exon 3 and the surrounding introns of the *IFNLR1* gene with indicated positions of the two guide RNAs and primers used for PCR-based screening of hESC clones. fw, forward; INV, inversion; kb, kilobases; KO, knockout; rv, reverse; WT, wild type. (B) Genomic DNA of hESC clones was extracted and analyzed by PCR using the primers depicted in A. Positions of WT and KO bands of 1.0 and 0.5 kb, respectively, are indicated on the right-hand side of the “Knockout” gels. Bands of 0.5 kb on the “No inversion” and “Inversion” gels represent absence or presence of an inverted target sequence, respectively. The red asterisks mark the WT and KO clones selected for further characterization. fw, forward; INV, inversion; kb, kilobases; KO, knockout; rv, reverse; WT, wild type. (C) Sequences of the *IFNLR1* WT allele as well as the selected M6 *IFNLR1* WT clone, the homozygous M4 KO1 clone, and the two alleles of the heterozygous S8 KO2 clone. Guide RNA target sequences are highlighted in magenta and blue, the PAM is underlined, and the inverted sequence of the S8 KO2 INV allele is indicated in red. bp, base pairs; fw, forward; INV, inversion; KO, knockout; rv, reverse; WT, wild type.

HLC differentiations of *IFNLR1* WT and KO clones are highly variable but confirm a functional deletion of the IFNLR1 protein

After validating the *IFNLR1* KO on the genomic level, I needed to confirm that the selected hESC clones had retained their pluripotency. Using our standard HLC differentiation protocol, I observed a significant variation in the differentiation efficiencies among the M6 WT, M4 KO1, and S8 KO2 clones. The M6 WT clone formed large clusters of albumin-positive HLCs (Figure 15A), indicating an enhanced differentiation efficiency compared to the parental R2 cells. Differentiation of the M4 KO1 clone resulted in considerably smaller albumin- and HNF4α-positive HLC clusters (Figure 15B), more reminiscent of the typical differentiation efficiency obtained with the parental cells. Interestingly, I did not observe any albumin-positive HLC clusters upon differentiation of the S8 KO2 clone (Figure 15C). The HNF4α signal was considerably weaker compared to the M6 WT and the M4 KO1 clone, suggesting successful differentiation to HepProgs but impaired maturation to HLCs (Figure 15A, B). Unknown Cas9 off-target effects in the S8 KO2 clone or a heterogeneous pluripotency in the parental R2 population could be possible explanations for the diminished HLC differentiation efficiency. Repeated passaging, for example, may have resulted in the accumulation of epigenetic changes, leading to different transcriptional profiles in individual cells and thus, heterogeneity.

Western blot analysis of the differentiated HLCs validated the abrogation of IFNLR1 protein expression in the M4 KO1 and S8 KO2 clones (Figure 15D). To further confirm the functional loss of the type III IFN receptor, I stimulated the differentiated HLCs with type I IFN (IFNβ1a) and type III IFN (IFNλ1). While the M6 WT clone responded to both IFN types by upregulation of *IFIT1*, the M4 KO1 and S8 KO2 clones only responded to stimulation with IFNβ1a (Figure 15E). These results ultimately confirmed a functional KO of the IFNLR1 protein in both KO clones, whereas responsiveness to type I IFNs, which bind to the IFNAR1/2 heterodimer, was retained.

In summary, I successfully established a transduction-free protocol to genetically manipulate hESCs by Cas9. Unfortunately, I was unable to perform scRNA-seq on HLCs due to difficulties with the singularization of these cells. Nonetheless, the established Cas9 RNP transfection procedure and the *IFNLR1* M4 KO1 clone will be a powerful tool for future studies conducted by the research group of Dr. Viet Loan Dao Thi.

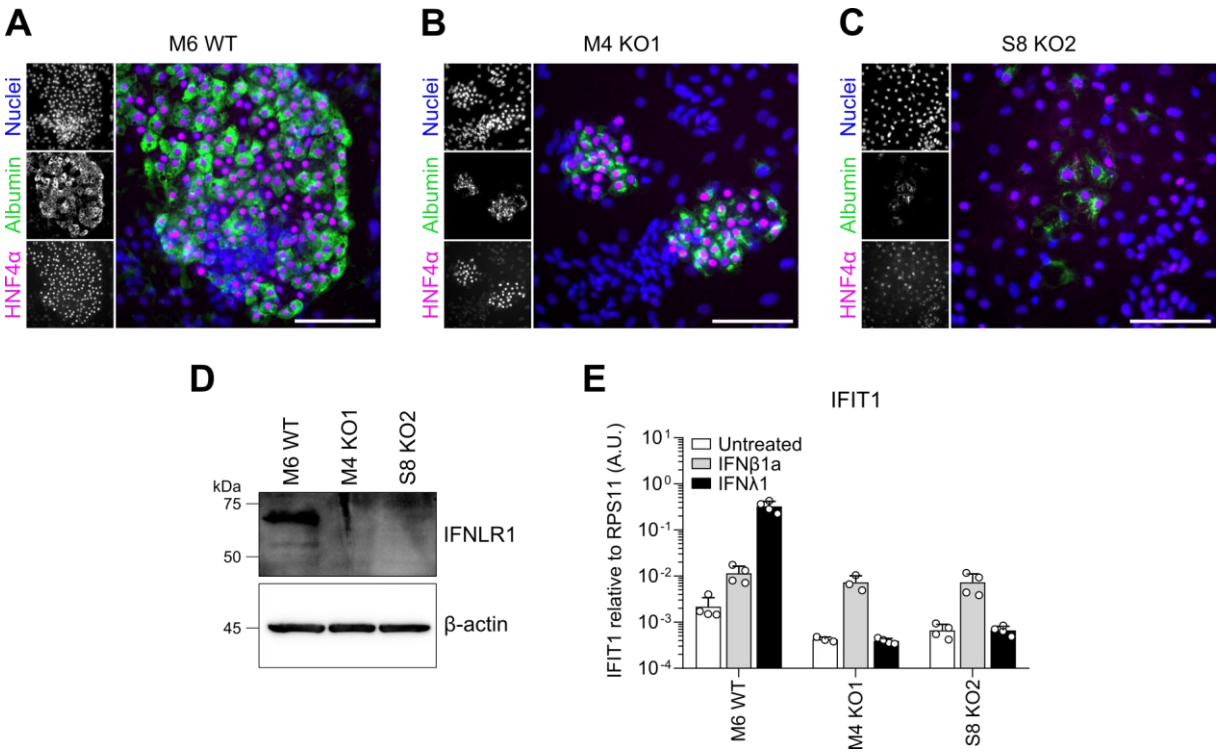

Figure 15: HLC differentiations of *IFNLR1* WT and KO clones are highly variable but confirm a functional deletion of the IFNLR1 protein.
(A) The M6 WT, (B) M4 KO1, and (C) S8 KO2 clones were differentiated to HLCs and fixed on day 20 of the differentiation. The cells were stained for albumin (green) and HNF4α (magenta), and counterstained for nuclei (blue) with Hoechst. Images were taken with a Nikon Eclipse Ts2-FL widefield epifluorescence microscope. Representative images of n = 2 independent differentiations. Scale bar, 100 µm. (D) Differentiated M6 WT, M4 KO1, and S8 KO2 clones were lysed and subjected to SDS-PAGE and Western blot analysis to detect the IFNLR1 protein and the loading control β-actin. kDa, kilodalton. (E) Differentiated M6 WT, M4 KO1, and S8 KO2 clones were stimulated with 500 IU/mL IFNβ1a or 5 ng/mL IFNλ1 for 8 h. RNA was extracted and analyzed by RT-qPCR for *IFIT1* induction relative to the housekeeping gene *RPS11* using the $2^{-\Delta Ct}$ method. Data show mean ± SD of n = 4 biological replicates from two independent differentiations.

5.1.3 Attempts to Identify the PRRs Contributing to the HEV-Specific Antiviral Response

Previous studies have shown that HEV infection in hepatocytes results in a robust type III IFN and ISG response[201,204]. Consequently, viral replication intermediates, most likely the dsRNA produced during viral replication, must be sensed by PRRs. MDA5, RIG-I, and TLR3 have all been implicated in HEV recognition[199,201,214,215], however, exhaustive comparative studies have not been performed. For a comprehensive evaluation of the PRRs relevant for sensing HEV, I took advantage of previously established immune-impaired Huh7.5 cells, reconstituted with ectopic expression of either MDA5, RIG-I, or TLR3[198]. These cells were kindly provided by the research group of Prof. Dr. Volker Lohmann (Heidelberg University Hospital). Theoretically, the individual contributions of the PRRs should be distinguishable in this simplified cellular model system. To validate the expression and responsiveness of the respective PRRs, I stimulated parental and derived Huh7.5 cells, expressing MDA5, RIG-I, or TLR3, with poly(I:C) by transfection or supernatant feeding. Due to their negligible basal expression of MDA5, LGP2, and TLR3, and the presence of a mutant, inactive version of RIG-I[197,198], parental

Huh7.5 cells did not respond to stimulation, as expected (Figure 16). In contrast, I observed increased *IFIT1* expression in the presence of ectopically expressed MDA5 or RIG-I (Figure 16). TLR3-reconstituted Huh7.5 cells responded to both poly(I:C) transfection and supernatant feeding (Figure 16). I concluded that the cell lines responded as expected.

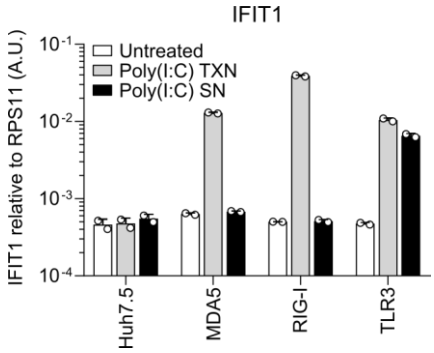

Figure 16: Huh7.5 cells expressing individual PRRs respond to poly(I:C) stimulation.
Parental Huh7.5 cells and MDA5-, RIG-I-, or TLR3-expressing derivatives were stimulated with 250 ng poly(I:C) by transfection (TXN) or with 25 µg poly(I:C) by supernatant (SN) feeding. Lysates were harvested 8 h post-stimulation, and *IFIT1* expression was analyzed relative to the housekeeping gene *RPS11* using the $2^{-\Delta Ct}$ method. Data show mean ± SD of a single experiment with two biological replicates. A.U., arbitrary units.

Next, I electroporated these cell lines with *in vitro* transcribed (IVT) HEV WT RNA or a replication-incompetent mutant carrying a GDD-to-GAD mutation in the RdRp sequence. As HEV is a positive-sense, ssRNA virus, EPO of viral RNA kickstarts viral replication and bypasses the relatively inefficient HEV entry process. Consequently, almost 100% of cells carry replicating viral RNA, indicated by ORF2 protein expression (Figure 17I–L). Changes in the antiviral responses are thus expected to be prominently detectable. Parental Huh7.5 cells and derived cell lines with ectopic expression of MDA5, RIG-I, or TLR3 showed an increase in HEV RNA from day 2 to day 7 post-EPO, indicating viral replication, whereas the GAD mutant steeply decreased over time (Figure 17A–D). Surprisingly, I did not observe *IFIT1* induction on either time point following EPO in any of the RLR- or TLR3-expressing cell lines (Figure 17E–H). IF staining of the ORF2 protein further validated viral replication in all cell lines, whereas cells electroporated with the GAD mutant remained ORF2-negative (Figure 17I–L). I therefore concluded that HEV successfully replicated in Huh7.5 cells. However, the expression of individual PRRs appeared insufficient to elicit an HEV-specific cell-intrinsic antiviral response.

In several downstream experiments, I explored the hypothesis that a combination of several PRRs is necessary to induce an HEV-specific antiviral response. For this, two MSc rotation students, Carl Niklas Schneider and Miriam Martens, ectopically co-expressed MDA5 and LGP2 in Huh7.5 cells by standard lentiviral transduction under my direct supervision. Even though the proteins were expressed according to Western blot analysis and LGP2 enhanced MDA5 stimulation as expected, these cell lines did not induce ISG expression upon HEV

infection (Supplementary Figure 1). Similarly, co-expression of RIG-I and MDA5 did not yield an HEV-induced antiviral response (data not shown).

In summary, I was unable to identify the PRRs essential for inducing an HEV-specific cell-intrinsic antiviral response using Huh7.5-derived cell lines. After several further attempts not discussed here, including PRR-targeted shRNA-expressing HepaRG cells and stable PRR KO cell lines in a HepG2 background, I decided to not further pursue this research question.

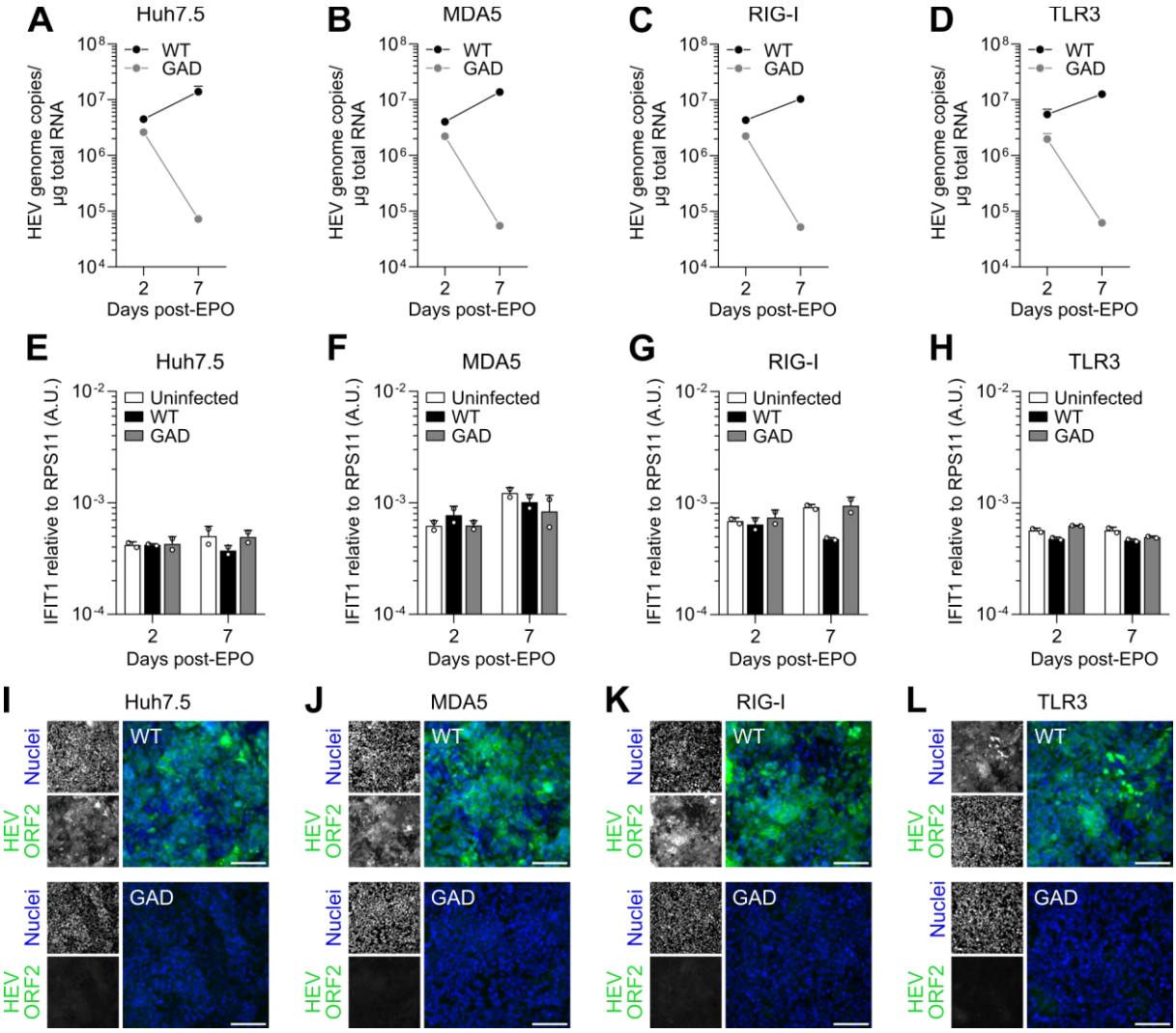

Figure 17: HEV replicates in Huh7.5-derived cell lines but is not sensed by individually expressed PRRs. (A) Parental Huh7.5 cells and derived cell lines ectopically expressing (B) MDA5, (C) RIG-I, or (D) TLR3 were electroporated with IVT RNA of HEV WT or a replication-incompetent GAD mutant. Cell lysates were harvested for RT-qPCR analysis on day 2 and day 7 post-EPO, and HEV RNA was quantified over time. Data show mean ± SD of a single experiment with two replicates. (E) Cell lysates of parental Huh7.5 cells and derived cell lines ectopically expressing (F) MDA5, (G) RIG-I, or (H) TLR3 were additionally analyzed for expression of *IFT1* relative to the housekeeping gene *RPS11* using the $2^{-\Delta Ct}$ method. Data show mean ± SD of a single experiment with two replicates. A.U., arbitrary units. (I) On day 7 post-EPO with HEV WT or GAD RNA, parental Huh7.5 cells and derived cell lines ectopically expressing (J) MDA5, (K) RIG-I, or (L) TLR3 were fixed and stained for ORF2 (green), and nuclei (blue) were counterstained with Hoechst. Images were taken with a Nikon Eclipse Ts2-FL widefield epifluorescence microscope. Representative images of a single experiment. Scale bar, 200 µm.

5.2 The HEV ORF2 Protein Antagonizes Antiviral Signaling Through Interaction With TBK1

It has been demonstrated that HEV replication persists in the presence of a sustained type III IFN and ISG response, suggesting intricate viral evasion strategies to escape elimination by the antiviral response. While all HEV proteins have been independently proposed to antagonize different steps of the cell-intrinsic antiviral and inflammatory signaling pathways (reviewed in [209,252]), side-by-side comparisons within the same cellular system are lacking. Furthermore, it is unclear how the proposed antagonisms relate to full-length HEV infection, and their contributions to enabling HEV persistence remain to be clarified. Therefore, I aimed to comprehensively assess the interference of different HEV-encoded proteins with the antiviral and inflammatory signaling pathways and identify their cellular targets.

5.2.1 ORF2 Antagonizes Both Antiviral and Inflammatory Signaling Pathways

First, I aimed to elucidate whether the HEV proteins ORF2 and ORF3 interfere with antiviral and inflammatory signaling. As the ORF1 protein is only expressed at low levels in infected hepatocytes[99,237,253] and the processing of the individual subdomains is unclear (reviewed in [49]), I decided to omit this protein from my investigations. In contrast to previous studies, I attempted a systematic side-by-side comparison of ORF2 and ORF3 in an immunocompetent, well-characterized cellular system. For these experiments, I collaborated with Sebastian Stegmaier from the research group of Dr. Marco Binder at the German Cancer Research Center (DKFZ) in Heidelberg. I cloned the lentiviral plasmids encoding ORF2 from the cell culture-adapted HEV-3 Kernow-C1/p6 strain, ORF2 from the HEV-1 Sar55 strain, HEV-3 ORF3, and GFP as a control. I included HEV-1 ORF2 to assess potential differences between antagonisms mediated by the ORF2 protein from acute versus chronic HEV genotypes, as proposed previously[224,230]. Sebastian Stegmaier performed the lentiviral transductions to generate cell lines with ectopic expression of the different viral proteins and GFP. In close consultation, he performed the downstream experiments, including stimulation of the respective cell lines, RT-qPCR analysis, and enzyme-linked immunosorbent assay (ELISA).

We made use of A549 cells, which harbor intact antiviral and inflammatory signaling pathways and are competent in producing and responding to IFNs. The research group of Dr. Marco Binder previously established a panel of A549-derived cells, carrying a double knockout (DKO) of RIG-I and MDA5 (A549-RIG-I/MDA5^{DKO}), in addition to their intrinsically low expression of TLR3[254]. For targeted analysis of a specific PRR, they reconstituted expression of either RIG-I or MDA5 under control of a weak ROSA26 promoter to obtain moderate protein expression[240]. For our collaboration, Sebastian Stegmaier further established A549-RIG-I/MDA5^{DKO} cells with reconstituted TLR3 expression. Then, he introduced the HEV-3 ORF2, HEV-1 ORF2, ORF3,

and GFP expression constructs to the three basal A549-derived cell lines, harboring ectopic expression of either RIG-I, MDA5, or TLR3 (Figure 18A). The resulting cell lines were treated with different stimuli specific to the respective reconstituted PRR. Mengo-Zn virus and Sendai virus (SeV) infections were used to activate MDA5- and RIG-I-mediated signaling, respectively, whereas poly(I:C) supernatant feeding was applied to promote TLR3-dependent signaling. With these cell lines, we first aimed to investigate whether any of the HEV proteins interfered specifically with the signaling induced by one or several PRRs.

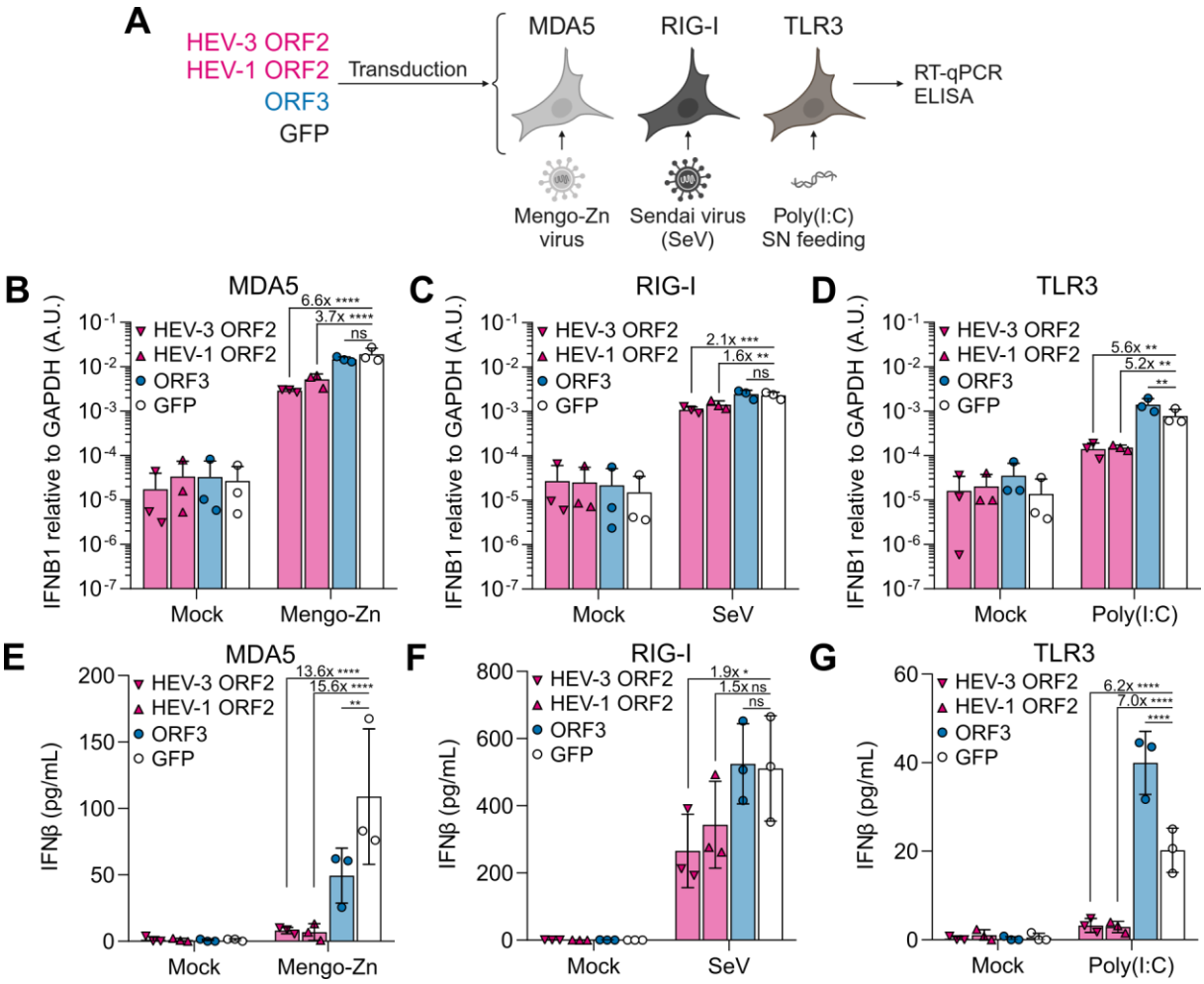

Figure 18: HEV ORF2 interferes with antiviral signaling downstream of MDA5, RIG-I, and TLR3.
(A) A549 cells harboring a DKO of MDA5 and RIG-I and weak reconstitution of MDA5, RIG-I, or TLR3 were transduced with HEV-3 ORF2, HEV-1 ORF2, ORF3, or GFP. MDA5-, RIG-I-, and TLR3-expressing cells were stimulated with Mengo-Zn virus, Sendai virus (SeV), or poly(I:C) supernatant (SN) feeding and analyzed by RT-qPCR and ELISA. (Created with BioRender.com) (B) MDA5-expressing cells were infected with Mengo-Zn virus at MOI 1 for 24 h, (C) RIG-I-expressing cells were infected with Sendai virus (SeV) at MOI 0.75 for 4 h, and (D) TLR3-expressing cells were stimulated by poly(I:C) SN feeding at 50 µg/mL for 24 h. *IFNB1* expression was analyzed by RT-qPCR, relative to the housekeeping gene *GAPDH* using the $2^{-\Delta Ct}$ method. Data show mean ± SD of n = 3 independent experiments with one biological replicate each. Numbers indicate fold-reductions compared to GFP, and statistical analysis was performed using two-way ANOVA. **: $p < 0.01$; ***: $p < 0.001$; ****: $p < 0.0001$; ns, not significant. A.U., arbitrary units. (E) Stimulation of MDA5-, (F) RIG-I-, and (G) TLR3-expressing cells was performed as stated in B–D. All supernatants were collected after 24 h and analyzed by ELISA for IFNβ protein secretion. Data show mean ± SD of n = 3 independent experiments with one biological replicate each. Numbers indicate fold-reductions compared to GFP, and statistical analysis was performed using two-way ANOVA. *, $p < 0.05$; **: $p < 0.01$; ****: $p < 0.0001$; ns, not significant. These experiments were performed by Sebastian Stegmaier at DKFZ Heidelberg. Panels B–G were published in a preprint by Mehnert *et al.*[245].

In the presence of the GFP control, all cell lines responded to the respective stimuli by *IFNB1* upregulation, analyzed by RT-qPCR (Figure 18B–D). Ectopic expression of ORF3 did not result in a significant difference in *IFNB1* expression downstream of MDA5 or RIG-I stimulation compared to the GFP control (Figure 18B, C). However, *IFNB1* induction in response to TLR3 stimulation with poly(I:C) was moderately yet significantly enhanced in the presence of ORF3 (Figure 18D). This phenotype was also observed when measuring IFNβ protein secretion by ELISA (Figure 18G). In contrast, ectopic expression of HEV-3 ORF2, but also HEV-1 ORF2, resulted in a significantly dampened *IFNB1* induction downstream of all three PRRs compared to the GFP control (Figure 18B–D). IFNβ protein secretion was also decreased in the presence of ORF2 (Figure 18E–G). Although this reduction was not statistically significant for RIG-I and HEV-1 ORF2 (Figure 18F), the ELISA results further substantiated the interference of ectopic ORF2 with IFN induction downstream of all PRRs.

Overall, we observed that ORF2 interferes with type I IFN induction downstream of MDA5, RIG-I, and TLR3. Therefore, the putative antagonism mediated by ORF2 appears not to be PRR-specific and thus likely targets a common step in the downstream signaling cascade. This phenotype was not exclusive to HEV-3 ORF2 but could also be observed upon expression of ORF2 from an acute genotype (HEV-1 ORF2), which is in agreement with previous literature[68,231]. The ORF3 protein did not interfere with antiviral signaling from any PRR but rather enhanced the antiviral response downstream of TLR3.

We then analyzed the potential interference of ORF2 and ORF3 with NF-κB-dependent signaling. Upon stimulation with TNF, *TNFAIP3* induction was dampened in the presence of HEV-3 ORF2 and HEV-1 ORF2, but not ORF3 (Figure 19A). This suggested that ORF2 does not only antagonize IRF3- but also NF-κB-mediated signaling, similar to what has been suggested previously[69,238]. Furthermore, neither ORF2 nor ORF3 reduced *IFIT1* induction downstream of JAK/STAT signaling, which was assessed by stimulation with IFNβ (Figure 19B). Hence, we could not reproduce the previously observed impairment of IFN-dependent signaling by ORF3[226].

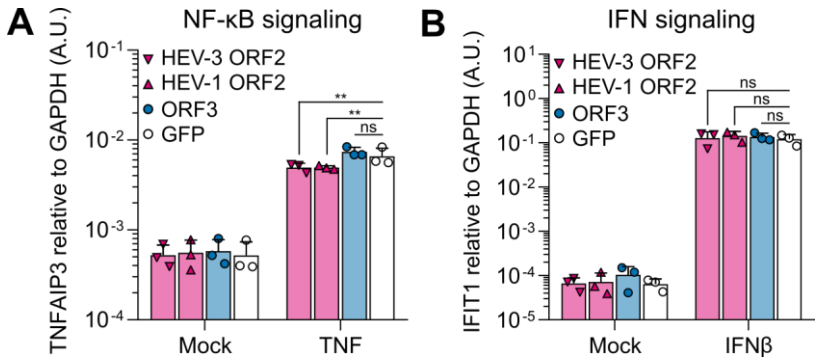

Figure 19: HEV ORF2 interferes with NF-κB-dependent but not IFN-induced signaling.
(A) A549-derived cells ectopically expressing MDA5 and either HEV-3 ORF2, HEV-1 ORF2, ORF3, or GFP were stimulated with 10 ng/mL TNF and analyzed for *TNFAIP3* expression by RT-qPCR, or (B) they were stimulated with 500 IU/mL IFNβ for 8 h and analyzed for *IFIT1* expression. Gene expression was analyzed relative to the housekeeping gene *GAPDH* using the $2^{-\Delta Ct}$ method. Data show mean ± SD of n = 3 independent experiments with one biological replicate each. Statistical analysis was performed using two-way ANOVA. **: $p < 0.01$; ns, not significant. A.U., arbitrary units. These experiments were performed by Sebastian Stegmaier at DKFZ Heidelberg. This figure was published in a preprint by Mehnert *et al.*[245].

Next, I wanted to assess whether the putative ORF2 antagonism influenced the PRR-induced signaling kinetics. For this, Sebastian Stegmaier electroporated MDA5-reconstituted A549-RIG-I-MDA5^{DKO} cells with poly(I:C) or a poly(C) control and analyzed the induction of different antiviral and inflammatory response genes in a time-resolved manner (Figure 20A). We observed continuously lower induction of *IFNB1* in the presence of HEV-3 ORF2 compared to GFP (Figure 20B), substantiating our previous findings at different time points post-stimulation. The induction kinetics, however, were neither delayed nor accelerated in the presence of ORF2. We observed a similar phenotype for *IFIT1* expression at early time points (Figure 20C). At 24 h post-EPO, however, *IFIT1* induction in the presence of ORF2 was comparable to GFP (Figure 20C). This might be explained by autocrine and paracrine IFN signaling resulting in reinforced *IFIT1* expression, eventually masking the antagonistic effect of ORF2. Interestingly, *IRF9* expression was not affected by the presence of ORF2 (Figure 20D). Since this is an ISG that is only induced downstream of IFN signaling[242], also evident by its delayed expression compared to *IFNB1* and *IFIT1* (Figure 20B, C), this confirms that ORF2 does not interfere with JAK/STAT signaling. Lastly, *TNFAIP3* induction was considerably lower in the presence of ORF2 compared to GFP (Figure 20E), but the kinetics were unaffected. This demonstrated that ORF2 does not only disrupt NF-κB-dependent signaling downstream of the TNF receptor, as previously shown (Figure 20A), but also downstream of PRR activation.

Altogether, our results demonstrated that ORF2 but not ORF3 antagonizes antiviral and inflammatory signaling induced by MDA5, RIG-I, and TLR3, indicating that ORF2 interferes with components downstream of these PRRs. As NF-κB signaling downstream of the TNF receptor was also affected by ORF2, it is likely that the viral protein antagonizes different targets that are specifically involved in either IRF3- or NF-κB-dependent signaling.

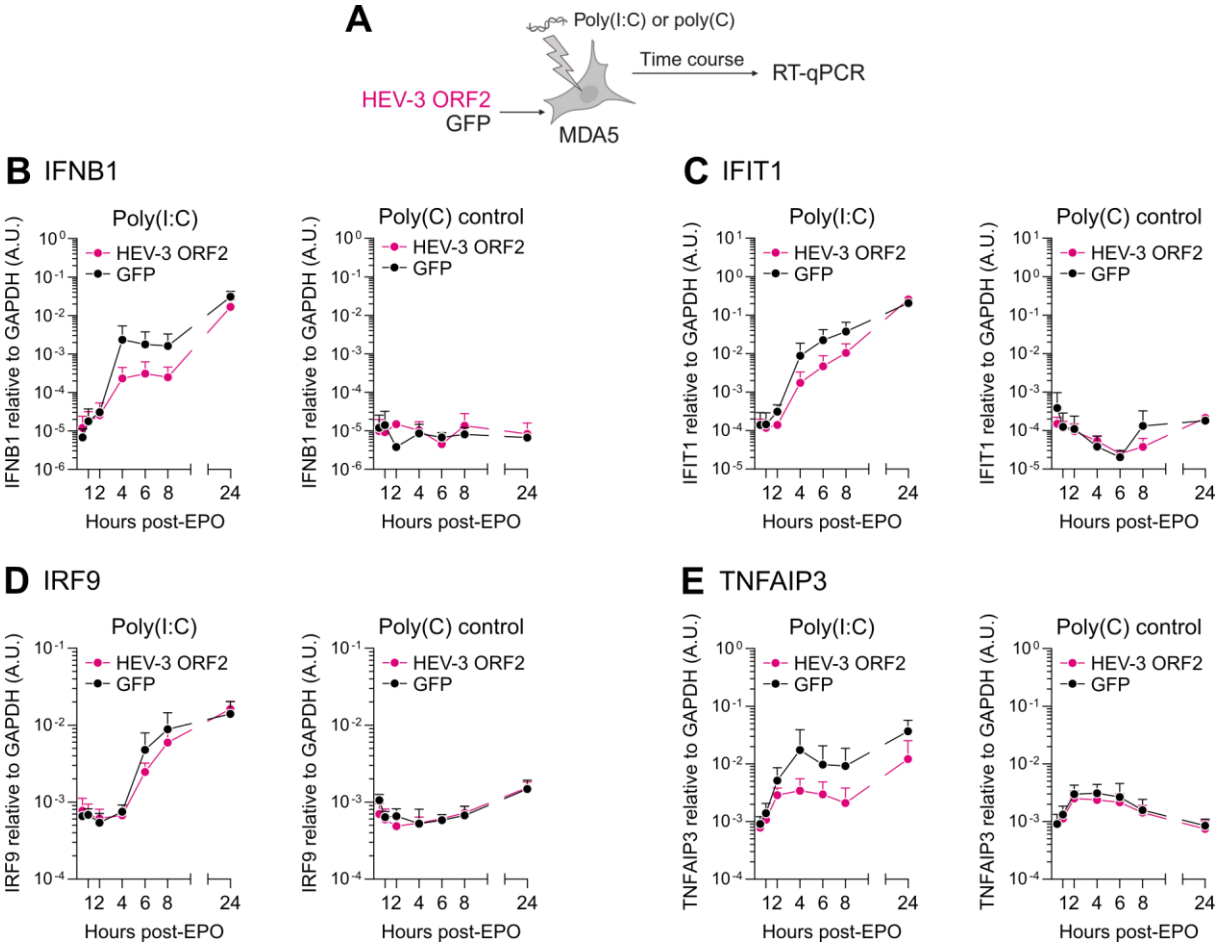

Figure 20: HEV ORF2 changes the strength of PRR-induced signaling rather than its kinetics.
(A) A549-RIG-I-MDA5^{DKO} cells with ectopic expression of MDA5 and either HEV-3 ORF2, HEV-1 ORF2, ORF3, or GFP were electroporated with poly(I:C) or poly(C) control, and gene expression was analyzed over time by RT-qPCR. (Created with BioRender.com) (B) A549-derived cells were electroporated with 500 ng poly(I:C) or poly(C) control and analyzed by RT-qPCR at indicated time points for *IFNB1*, (C) *IFIT1*, (D) *IRF9*, and (E) *TNFAIP3* expression relative to the housekeeping gene *GAPDH* using the $2^{-\Delta Ct}$ method. Data show mean ± SD of n = 3 independent experiments with one biological replicate each. These experiments were performed by Sebastian Stegmaier at DKFZ Heidelberg. Panel B was published in a preprint by Mehnert *et al.*[245].

5.2.2 ORF2 Directly Interacts With TBK1 but Not the Related Kinase IKKβ

Following our mechanistic investigation, which revealed that the HEV capsid protein ORF2 interferes with antiviral and inflammatory signaling downstream of the PRRs, I aimed to identify the cellular targets of the ORF2 antagonism. A previous study has shown that ORF2 directly interacts with TBK1, resulting in reduced phosphorylation of IRF3 upon activation of the pathway[68]. However, interaction with TBK1 does not explain the impact of ORF2 on NF-κB-mediated signaling downstream of TNF stimulation. Therefore, I hypothesized that ORF2 likely interacts with a different component specifically involved in inflammatory cytokine induction. As TBK1 is only one member of a larger family of canonical and non-canonical IKK-related kinases, I hypothesized that ORF2 might also interact with another member of this family, for example, IKKβ.

To validate the interaction of ORF2 with TBK1 and identify a potential interaction with IKKβ, I performed co-IP experiments by co-transfection of HEK293T cells with C-terminally tagged ORF2-HA and C-terminally V5-tagged TBK1 or IKKβ. I also transfected GFP-HA together with TBK1-V5 or IKKβ-V5 to monitor the specificity of the pulldown with ORF2. Previously, it was suggested that the ORF2 ARM is the motif responsible for the interaction between ORF2 and TBK1[68]. However, loss of the interaction between the two proteins upon mutation of the ARM was not demonstrated by co-IP but only indirectly through restored phosphorylation levels of IRF3. Therefore, I also sought to investigate the interaction between TBK1 and a mutant ORF2, harboring two R-to-A substitutions at the last two positions of the ARM (Figure 21A). V5-tagged TBK1 and IKKβ, along with the ORF2-2R/2A-HA mutant, were cloned by Carla Siebenkotten, an MSc lab rotation student, under my direct supervision. She further established and optimized the co-IP protocol, which I eventually used for the experiments presented here (Figure 21B).

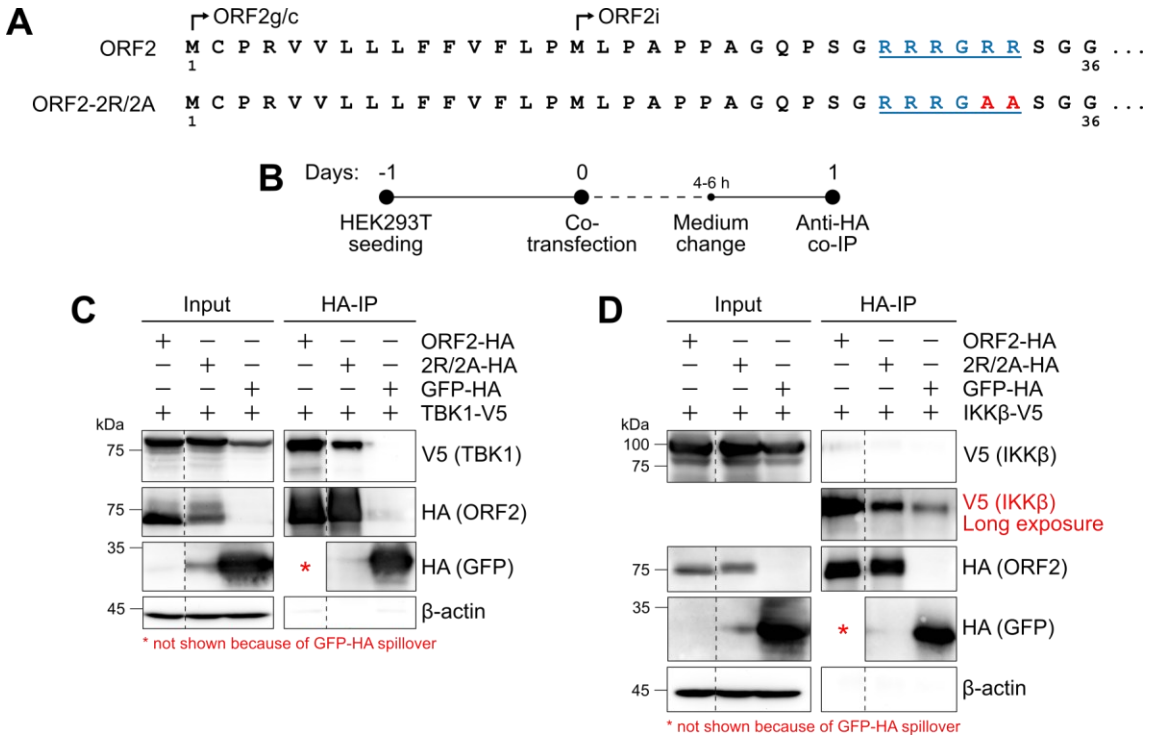

Figure 21: ORF2 interacts with TBK1 but not the related kinase IKKβ.
(A) Schematic representation of the ORF2 amino acid sequence, showing start codons of ORF2g/c and ORF2i and the ARM underlined in blue. Amino acids in red highlight the 2R/2A mutation of the ARM. Numbers indicate amino acid positions starting from the ORF2g/c start codon. (B) HEK293T cells were co-transfected, the medium was exchanged after 4–6 h, and co-IP was performed 24 h post-transfection. (C) HEK293T cells were co-transfected with ORF2-HA, ORF2-2R/2A-HA, or GFP-HA, and TBK1-V5 and lysed for co-IP 24 h later. Samples were subjected to SDS-PAGE and Western blot to detect TBK1 by its V5-tag, ORF2 or GFP by their HA tag, and the loading control β-actin. Dashed lines indicate cutting of the membrane. Representative blot of n = 2 independent biological experiments. kDa, kilodalton. (D) HEK293T cells were co-transfected with ORF2-HA, ORF2-2R/2A-HA, or GFP-HA, and IKKβ-V5 and lysed for co-IP 24 h later. Samples were subjected to SDS-PAGE and Western blot to detect IKKβ by its V5-tag, ORF2 or GFP by their HA tag, and the loading control β-actin. Dashed lines indicate cutting of the membrane. Representative blot of n = 2 independent biological experiments. kDa, kilodalton.

I confirmed a direct interaction between ORF2 and TBK1 by co-IP, which appeared to be specific, based on the lack of TBK1 co-immunoprecipitated with GFP (Figure 21C). Interestingly, the amount of TBK1 co-immunoprecipitated with the ORF2-2R/2A mutant was considerably diminished (Figure 21C). This might validate the ARM as the putative interaction motif between ORF2 and TBK1. However, a more recent publication suggested the ARM to be the master regulator of ORF2 secretion and intracellular retention[69]. Mutation of the ARM resulted in enhanced glycosylation and secretion of ORF2[69]. A mutated ARM might thus simply reduce the cytosolic availability of ORF2 for interaction with TBK1, thereby indirectly affecting the co-IP of TBK1 with ORF2-2R/2A. Furthermore, I could not validate IKKβ as a second putative interaction partner of ORF2 within the IKK protein family. Under the same conditions as TBK1, co-IP of IKKβ with ORF2 was only weakly detectable upon long exposure of the membrane (Figure 21D). Furthermore, IKKβ was also co-immunoprecipitated with GFP, suggesting unspecific pulldown of IKKβ (Figure 21D).

In summary, I validated that ORF2 directly interacts with TBK1, explaining our observed impairment of antiviral signaling downstream of PRR activation in the presence of ORF2. In contrast, I found that ORF2 appears not to interact with IKKβ. Instead, the previously published interaction between ORF2 and βTRCP, resulting in decreased proteasomal degradation of IκBα[238], might contribute to the ORF2-dependent reduction of NF-κB-mediated inflammatory responses that we observed here.

5.2.3 A Putative WRD Motif Identified by AlphaFold Modeling is Not Essential for the ORF2-TBK1 Interaction

To determine the true interaction sites between ORF2 and TBK1, Dr. Thibault Tubiana (Institute for Integrative Biology of the Cell (I2BC), Gif-sur-Yvette, France) performed AlphaFold-based modeling of the protein-protein interaction. He predicted putative interactions between a TBK1 homodimer, the functional arrangement of this kinase, and individual segments of the ORF2 protein, separated into the unstructured N-terminus (until aa128), the S, M, and P domains. Among the 195 generated models, he only identified the last three amino acids (WRD) of a 7-amino acid motif within the N-terminus of ORF2 as a potential interaction site between the two proteins. Neither the ARM, also located within the N-terminal segment, nor other ORF2 domains yielded confident AlphaFold models of the ORF2-TBK1 interaction. The identified putative WRD motif appeared to interact with amino acids of both N- and C-terminus of the TBK1 dimer, suggesting contact at the interface between the two monomers (Figure 22A). Predicted local distance difference test (pLDDT) scores were high to very high for the TBK1 dimer but low for ORF2, likely due to the unstructured nature of the ORF2 N-terminus (Figure 22B). As this was the only suggested interaction site, I mutated the WRD

motif to triple alanine (WRD/AAA) (Figure 22C) and performed co-IP with TBK1. Unfortunately, I observed neither fully abrogated nor reduced interaction between ORF2 and TBK1 upon mutation of this motif, whereas the 2R/2A mutant reproducibly resulted in a decreased co-IP of TBK1 with ORF2 (Figure 22D). This suggested that the identified WRD motif is not essential for the ORF2-TBK1 interaction.

In conclusion, AlphaFold modeling neither yielded a novel, putative interaction site between TBK1 and ORF2, nor did it confirm the previously proposed ARM. One plausible explanation might be that interaction motifs located within an unstructured region, such as the ORF2 N-terminus, can be challenging to determine using AlphaFold. Structural studies thus appear to be necessary to reliably identify the mode of interaction between ORF2 and TBK1.

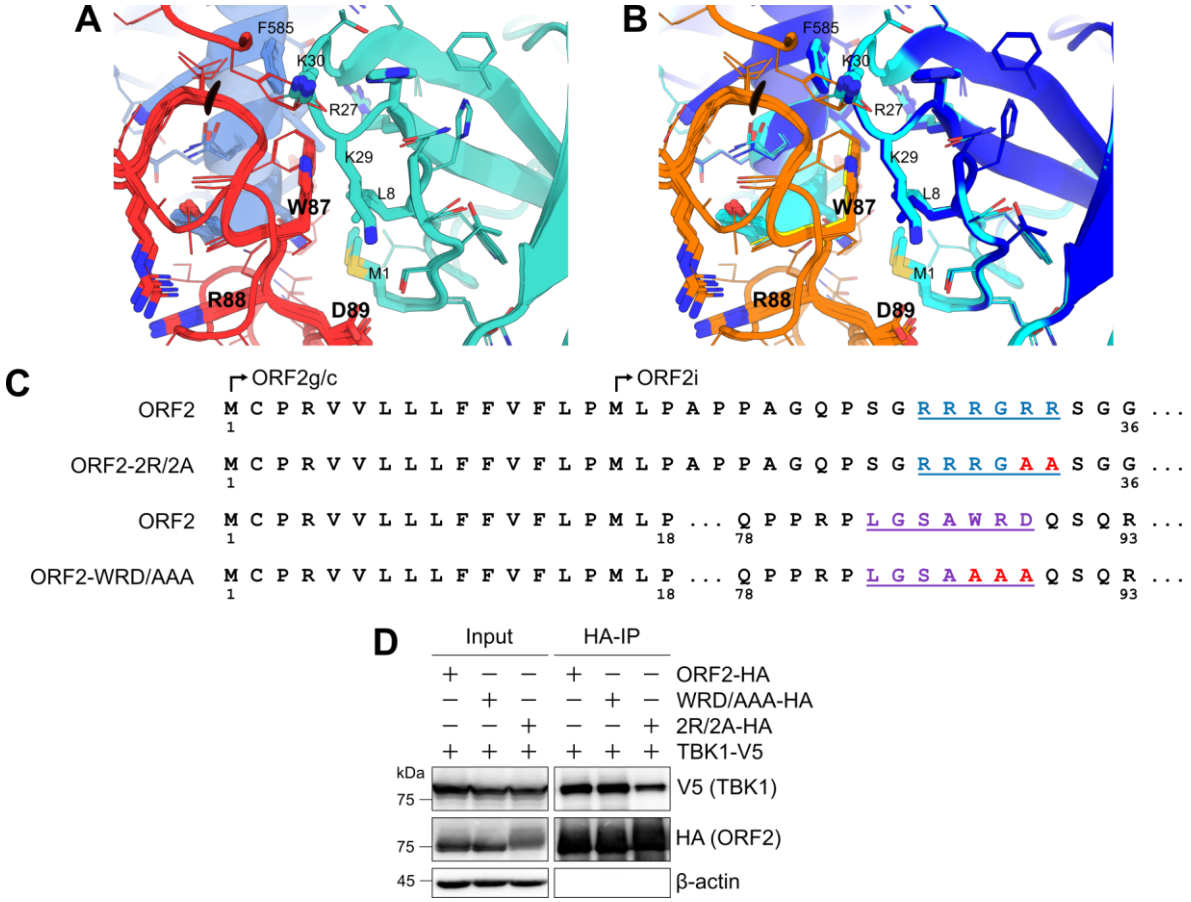

Figure 22: A putative WRD motif identified by AlphaFold modeling is not essential for the ORF2-TBK1 interaction.
(A) AlphaFold 2.3-based prediction of the ORF2-TBK1 interaction was used to identify novel putative interaction motifs. The top five-ranked models for the interaction between the N-terminal amino acids 1–128 of ORF2 and the TBK1 dimer are depicted. ORF2 is highlighted in red, and the identified WRD motif is depicted in bold. The N-terminal kinase domain of the first TBK1 monomer is highlighted in cyan and the C-terminal domain of the second TBK1 monomer is shown in blue in the background. Amino acids of the two TBK1 monomers are indicated in the smaller font size. (B) The same region as in A is depicted but colored according to predicted local distance difference test (pLDDT) scores, indicating the confidence of the model. Orange, very low; yellow, low; cyan, high; blue, very high. AlphaFold modeling and structural analysis was performed by Dr. Thibault Tubiana at the Institute for Integrative Biology of the Cell (I2BC) in Gif-sur-Yvette, France. (C) Schematic representation of the ORF2 amino acid sequence, showing start codons of ORF2g and ORF2i, the ARM underlined in blue, and the identified WRD

motif in purple. Amino acids in red highlight the 2R/2A mutation of the ARM and the WRD/AAA mutation. Numbers indicate amino acid positions starting from the ORF2g/c start codon. (D) HEK293T cells were transfected with ORF2-HA, ORF2-WRD/AAA-HA, or ORF2-2R/2A-HA, and TBK1-V5. Co-IP was performed 24 h post-transfection and analyzed by Western blot for V5, HA, and the loading control β-actin. Representative blot of n = 2 independent biological experiments. kDa, kilodalton. Panels A and B were published in a preprint by Mehnert *et al.*[245].

5.3 Persistent HEV Replication is Facilitated by ORF2 Following a Bottleneck Imposed by the Antiviral Response

The mechanistic investigations I performed in collaboration with Sebastian Stegmaier and Dr. Thibault Tubiana revealed that the HEV ORF2 protein interferes with antiviral and inflammatory signaling pathways downstream of the PRRs MDA5, RIG-I, and TLR3. This antagonism is, at least partly, mediated by the direct interaction of ORF2 with the integral kinase TBK1 through a hitherto unidentified interaction motif. These results have validated and extended previous studies, clarifying the abilities of the viral proteins ORF2 and ORF3 to antagonize different steps of antiviral signaling. However, ectopic expression of viral proteins does not adequately represent the conditions of authentic viral infection and replication. The expression levels of the viral proteins might differ, and protein-protein interactions might be favored or hindered in the context of viral replication and other viral proteins. Furthermore, it is essential to determine the impact of the proposed antagonism on the progression of infection. Therefore, I aimed to analyze the extent to which the ORF2-mediated antiviral immune evasion contributes to persistent HEV replication in the previously characterized immunocompetent cell culture models (chapter 5.1.1).

5.3.1 The Presence of the ORF2 Protein is Key to Efficient Viral Replication

To tackle this question, I made use of full-length viral genomic mutants in the background of the cell culture-adapted HEV-3 Kernow-C1/p6 strain. I fully depleted expression of the ORF2 protein by mutating the two start codons suggested to give rise to the ORF2g/c and ORF2i isoforms[66], and termed this mutant ΔORF2 (Figure 23A). Even though it remains unclear whether these start codons are functionally used during the HEV replication cycle, or whether the ARM controls the fate and the downstream processing of the full-length ORF2 protein, they can be exploited to artificially abrogate ORF2 expression[66]. Importantly, I ensured to maintain the amino acid sequence of the overlapping ORF3 protein. Additionally, I made use of a ΔORF3 mutant, established by my former colleague Charlotte Decker during her PhD. This mutant harbors a mutated ORF3 start codon to abrogate ORF3 protein expression. To validate the lack of the respective viral protein in the ΔORF2 and ΔORF3 mutants, I electroporated HepG2/C3A cells with HEV WT or mutant IVT RNA. As expected, I observed ORF2 expression only in the WT and ΔORF3 but not the ΔORF2 condition (Figure 23B). While I failed to detect

ORF3 by Western blot analysis in this experiment, I managed to detect it upon ΔORF2 EPO in a different cell line, as detailed later (Figure 28B). By IF analysis, I further confirmed that WT-electroporated cells were ORF2- and ORF3-positive, whereas the ΔORF2 mutant resulted in ORF2-negative and ORF3-positive cells, and the ΔORF3 mutant in ORF2-positive and ORF3-negative staining (Figure 23C–F).

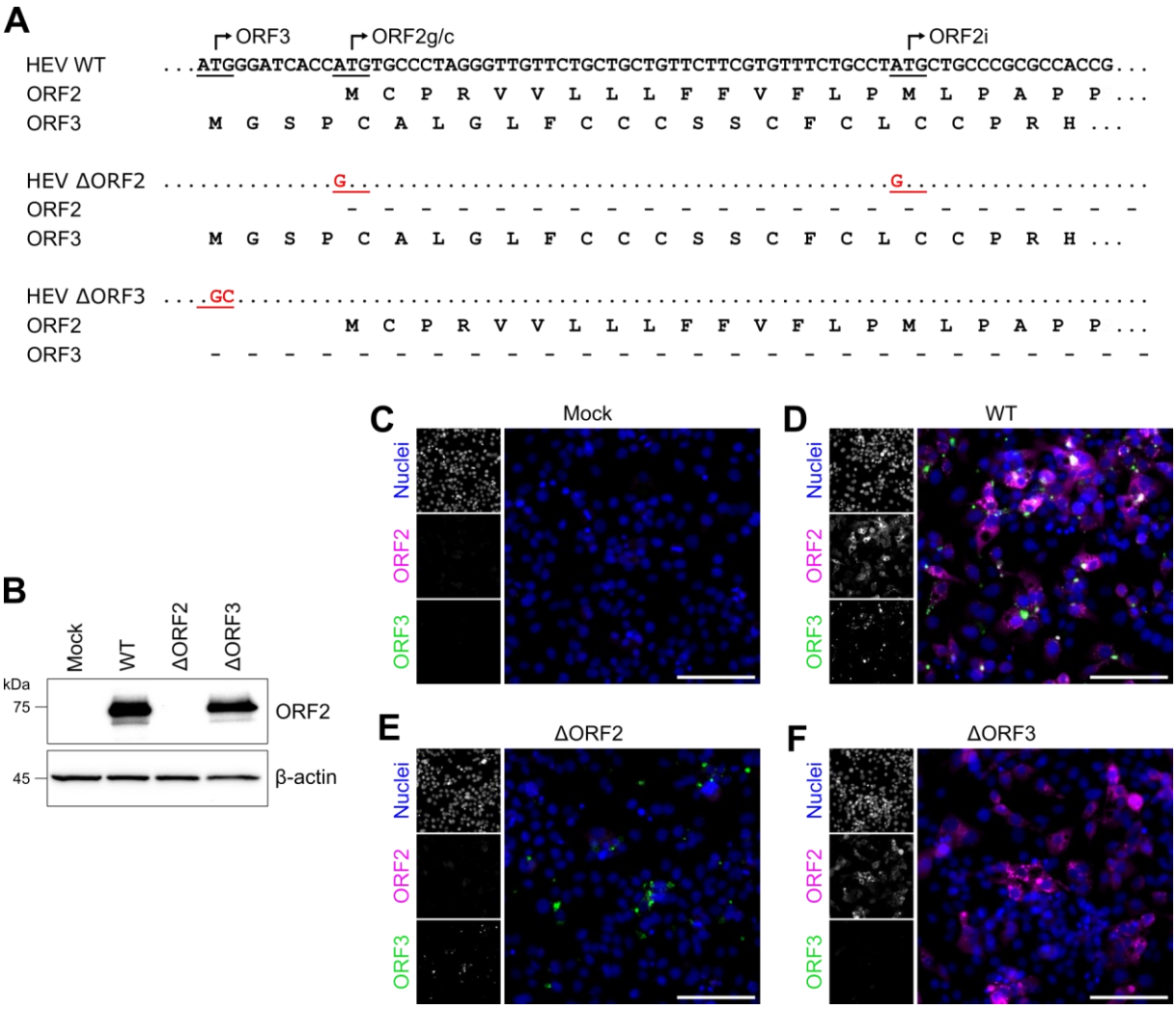

Figure 23: Generation and validation of the HEV mutants ΔORF2 and ΔORF3.
(A) Schematic representation of the HEV-3 Kernow-C1/p6 WT and derived ΔORF2 and ΔORF3 genomes with indicated start codons (underlined) and resulting amino acid sequences of the viral proteins ORF3 and ORF2, and its isoforms ORF2g/c and ORF2i. Mutations of the respective start codons are highlighted in red, and resulting lack of protein expression is shown with dashed lines. (B) HepG2/C3A cells were electroporated with WT, ΔORF2, or ΔORF3 IVT RNA and harvested on day 7 post-EPO. Cell lysates were analyzed for ORF2 protein expression and the loading control β-actin by Western blot. Representative blot of n = 2 independent experiments. kDa, kilodalton. (C) HepG2/C3A cells were mock-electroporated or electroporated with (D) WT, (E) ΔORF2, or (F) ΔORF3 IVT RNA, mixed 1:1 with mock-electroporated cells, and fixed for IF analysis on day 5 post-EPO. Cells were stained for ORF2 (magenta) and ORF3 (green), and counterstained for nuclei (blue) with Hoechst. Images were taken with a Nikon Eclipse Ts2-FL widefield epifluorescence microscope. Representative images of n = 3 independent experiments. Scale bars, 100 µm.

Next, I aimed to analyze the progression of viral replication of these mutants and the HEV-specific cell-intrinsic antiviral response over time. I electroporated HepG2/C3A cells with IVT RNA of HEV WT, ΔORF2, ΔORF3, or a replication-incompetent mutant, harboring a GDD-to-GNN mutation in the RdRp sequence of ORF1. I harvested samples on day 1, day 3, day 5, and day 7 post-EPO and analyzed them by RT-qPCR and RNA fluorescence *in situ* hybridization (RNA-FISH). Quantification of HEV RNA over time revealed that WT and the ΔORF3 mutant replicated to similar levels (Figure 24A). The minor decline in HEV RNA between day 1 and day 5 can likely be attributed to the substantial input of HEV RNA during the EPO process. The replication-incompetent GNN mutant further confirmed this observation, as I could only observe a significant decrease in GNN RNA on day 5 and day 7 post-EPO (Figure 24A), suggesting RNA degradation. Importantly, replication of the ΔORF2 mutant was significantly lower compared to WT and ΔORF3 on day 5 and day 7 post-EPO (Figure 24A), indicating less efficient replication of this mutant. However, the decline in ΔORF2 RNA was considerably less pronounced than the decrease in GNN RNA (Figure 24A). This confirmed that the ΔORF2 mutant was still able to replicate, however, less efficiently than HEV WT, and was not simply degraded.

HEV WT, as well as the ΔORF2 and ΔORF3 mutants, induced expression of the antiviral response genes *IFNL1* and *ISG15* (Figure 24B, C). However, this induction was significantly stronger for the ΔORF2 mutant on day 5 post-EPO compared to WT and ΔORF3. On day 7 post-EPO, *IFNL1* and *ISG15* expression was similar among WT, ΔORF2, and ΔORF3. Considering the significantly lower amounts of ΔORF2 RNA, however, the antiviral response in the ΔORF2 mutant was still relatively stronger at this time point compared to the response for WT and ΔORF3 (Figure 24D, E). Despite the delivery of a high HEV RNA input, the GNN mutant did not trigger an antiviral response, indicated by the lack of *IFNL1* and *ISG15* induction (Figure 24B, C). This suggested that a double-stranded replication intermediate, rather than the ssRNA genome itself, is recognized by the PRRs and induces an antiviral response. Consequently, I excluded the possibility that an intracellular accumulation of unpackaged HEV genome due to the absence of the capsid protein was the trigger for the enhanced antiviral response induction in the ΔORF2 mutant. Instead, I hypothesized that the lack of the ORF2-mediated antagonism targeting TBK1, which I identified previously, contributed to the enhanced expression of antiviral response genes, impairing the replication of the ΔORF2 mutant.

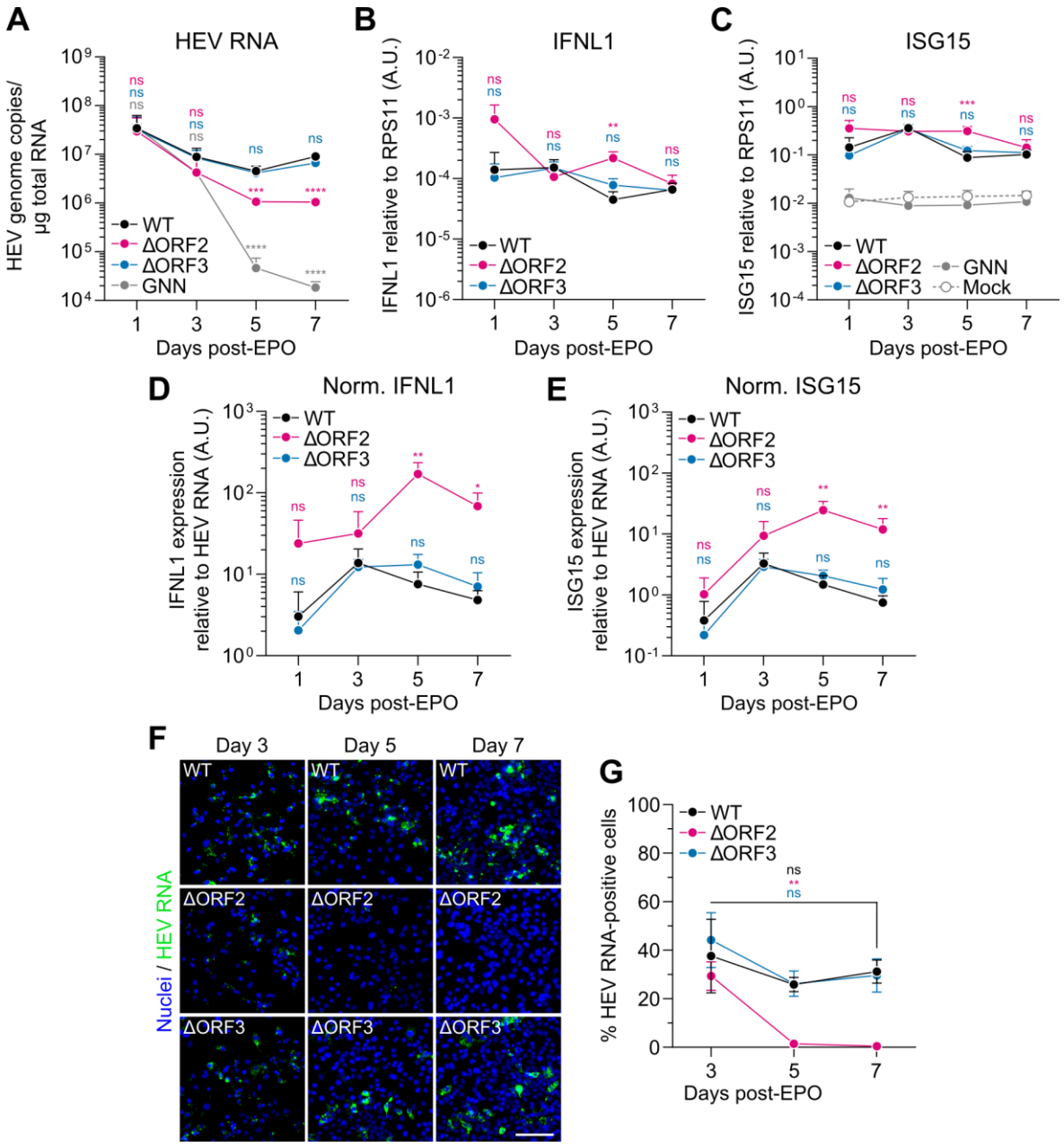

Figure 24: The ΔORF2 mutant replicates less efficiently and induces a stronger antiviral response.
(A) HepG2/C3A cells were mock-electroporated or electroporated with HEV WT, ΔORF2, ΔORF3, or GNN RNA and mixed 1:1 with mock-electroporated cells. Cells were treated with 0.06% DMSO 48 h prior to harvesting on day 3, day 5, and day 7 post-EPO. HEV RNA genome copies were quantified by RT-qPCR, and (B) *IFNL1* and (C) *ISG15* expression were determined relative to the housekeeping gene *RPS11* using the $2^{-\Delta Ct}$ method. *IFNL1* expression was undetectable in mock-electroporated and GNN samples. Data show mean ± SD of n = 3 independent experiments with one biological replicate each. Statistical analysis over WT was performed using one-way ANOVA of each time point independently, indicated above the respective time points in the corresponding color. **: $p < 0.01$; ***: $p < 0.001$; ****: $p < 0.0001$; ns, not significant. A.U., arbitrary units. (D) *IFNL1* and (E) *ISG15* expression was normalized to HEV RNA using the $2^{-\Delta\Delta Ct}$ method. Data show mean ± SD of n = 3 independent experiments with one biological replicate each. Statistical analysis was performed using one-way ANOVA of each time point independently, and comparison to WT is indicated above the respective time points in the corresponding color. *: $p < 0.05$; **: $p < 0.01$; ns, not significant. A.U., arbitrary units; norm., normalized. (F) Electroporated HepG2/C3A cells from A–E were fixed and stained for HEV RNA by RNA-FISH. Images were taken with a Nikon Eclipse Ts2-FL widefield epifluorescence microscope. Exemplary images of n = 3 independent experiments. Scale bar, 100 µm. (G) Images from F were quantified using ilastik and CellProfiler. Data show mean ± SEM of n = 3 independent experiments and 5 images per experiment. Statistical analysis was performed using unpaired two-tailed Student's t-test of each condition independently. Significance is indicated in the corresponding color. **: $p < 0.01$; ns, not significant. This figure was published in a preprint by Mehnert *et al.*[245].

I also analyzed the fate of the HEV RNA-positive cells over time at the single-cell level, staining electroporated HepG2/C3A cells for HEV RNA using a specific RNA-FISH assay, called RNAscope[255]. Images of day 1 post-EPO are not shown because of strong background noise from incoming, electroporated HEV RNA. Qualitatively, the HEV RNA signal was already weaker on day 3 post-EPO in the ΔORF2 mutant compared to WT and ΔOR3, and it further decreased over time (Figure 24F). Upon quantification, I observed a significant reduction in the percentage of ΔORF2-positive cells between day 3 and day 7 post-EPO. In contrast, the percentages of WT and ΔORF3 RNA-positive cells were sustained between day 5 and day 7 post-EPO. A minor reduction between day 3 and day 5 suggested that the induced antiviral response might be partly infection-limiting, even in the presence of ORF2. Interestingly, ΔORF2 HEV RNA was still detectable by RT-qPCR on day 7 post-EPO (Figure 24A), but not by RNA-FISH. While RNA-FISH is based on hybridization of 20 probe pairs across a ~1,000 nucleotide stretch of the *ORF2* RNA sequence, RT-qPCR of HEV RNA relies on the amplification of short, 70 nucleotide-long fragments in bulk. Consequently, it is possible that the ΔORF2 RNA detected by RT-qPCR contained significant amounts of degraded RNA, which might explain the discrepancy with the RNA-FISH results.

In the same experimental setup, I analyzed the effects of exogenous inhibition of the antiviral response with the drug BX795, an inhibitor of TBK1, on viral replication. Apart from its central role in transmitting antiviral signaling downstream of PRR activation, TBK1 is a kinase involved in many cellular processes, including cell proliferation (reviewed in [256]). Therefore, I reduced the incubation time with BX795 to 48 h to minimize cytotoxicity, resulting in a noticeable effect on cell viability only on day 7 post-EPO in ΔORF2 and ΔORF3 samples (Supplementary Figure 2A–C). However, the cell morphology was still considerably altered on all days post-EPO, following application of the inhibitor (Supplementary Figure 2D). Importantly, BX795 treatment effectively inhibited *ISG15* expression in all samples, although not to baseline levels of mock-electroporated cells on day 5 and day 7 post-EPO (Figure 25D–F). Interestingly, the TBK1 inhibitor appeared to be less effective towards later time points, which might be explained by the increased cell confluency, thereby resulting in a reduced effective drug concentration per cell.

Analyzing HEV RNA by RT-qPCR, I found that HEV WT replication was not significantly enhanced upon BX795 treatment (Figure 25A), which is in agreement with a previous report[204]. Similarly, I only observed a minor yet significant increase of ΔORF3 replication (Figure 25B). In contrast, TBK1 inhibition resulted in a clearly significant and stronger enhancement of ΔORF2 replication on day 5 and day 7 post-EPO compared to WT and ΔORF3 (Figure 25C). This suggested that, in addition to the overall stronger induction of antiviral response genes

(Figure 24B, C and Figure 25E), replication of the ΔORF2 mutant is more sensitive to the antiviral response compared to WT and ΔORF3.

In conclusion, I found that the absence of ORF2 resulted in reduced viral replication and increased induction of antiviral response genes. Furthermore, the replication of the ΔORF2 mutant was more sensitive to the antiviral response, which could be rescued by exogenous inhibition of TBK1, the kinase targeted by the ORF2 antagonism. Overall, my findings suggested that the ORF2-mediated evasion of the antiviral response is relevant in the context of authentic HEV replication.

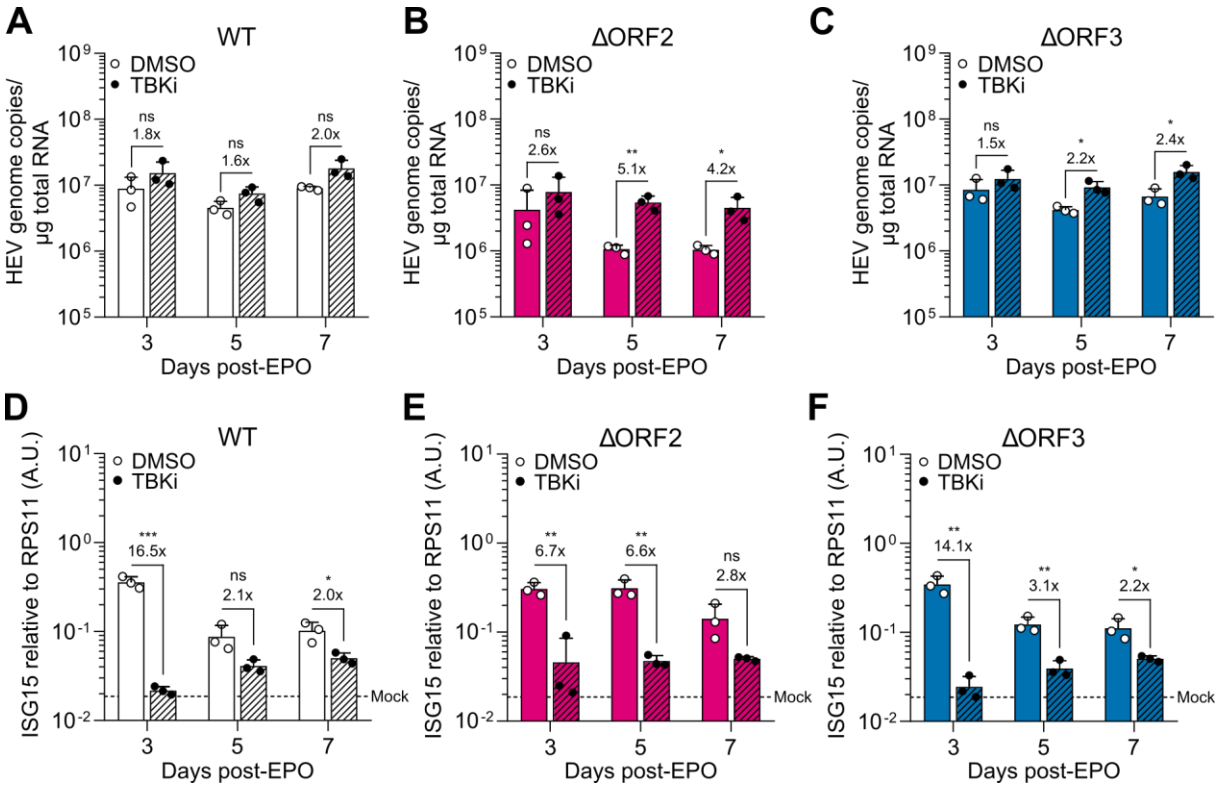

Figure 25: Exogenous inhibition of TBK1 rescues ΔORF2 replication.
(A) HepG2/C3A cells were mock-electroporated or electroporated with HEV WT, (B) ΔORF2, or (C) ΔORF3 RNA and mixed 1:1 with mock-electroporated cells. Treatment with 6 µM of the TBK1 inhibitor BX795 (TBKi) or respective DMSO vehicle control (0.06%) was started 48 h prior to the indicated time points post-EPO. HEV RNA was quantified by RT-qPCR, and fold changes over DMSO vehicle control are shown above the respective bars. Data show mean ± SD of n = 3 independent experiments with one biological replicate each. Statistical analysis was performed using unpaired two-tailed Student's t-test of each time point independently. *: $p < 0.05$; **: $p < 0.01$; ns, not significant. (D) The samples from A–C were analyzed for *ISG15* expression relative to the housekeeping gene *RPS11* using the $2^{-\Delta Ct}$ method. The dashed line indicates the mean of basal *ISG15* expression in mock-electroporated cells under TBKi treatment across day 3, day 5, and day 7. Data show mean ± SD of n = 3 independent experiments with one biological replicate each. Numbers indicate the respective fold-reductions of TBKi compared to DMSO. Statistical analysis was performed using unpaired two-tailed Student's t-test of each time point independently. *: $p < 0.05$; **: $p < 0.01$; ***: $p < 0.001$; ns, not significant. This figure was published in a preprint by Mehnert *et al.*[245].

5.3.2 The Intracellular ORF2 Isoform is Sufficient to Rescue the ΔORF2 Phenotype

Despite the ongoing controversy regarding the maturation of the ORF2 isoforms[66,69], the two start codons of the ORF2 coding sequence can be used to artificially discriminate between ORF2g/c (hereafter referred to as ORF2g) and ORF2i. To study the contributions of the different ORF2 isoforms to the ΔORF2 phenotype, I mutated the first ORF2 start codon to abrogate expression of ORF2g (ΔORF2g mutant) or the second start codon to deplete the ORF2i isoform (ΔORF2i mutant) in the full-length HEV-3 Kernow-C1/p6 genome (Figure 26A). Consequently, both mutants were expected to exclusively express the corresponding isoform of the respective other start codon. The mutation of the ORF2i start codon entailed a single M-to-V amino acid change at the respective position within the ORF2g protein sequence (Figure 26A).

To validate the generated ΔORF2 isoform mutants, I electroporated the respective IVT RNA into HepG2/C3A cells and harvested supernatants and cell lysates to perform Western blot analysis. To identify ORF2g in the supernatant, I treated all samples with PNGase F to remove most *N*-linked oligosaccharides from the glycosylated ORF2. Western blot confirmed that neither intracellular nor secreted ORF2 was present in the ΔORF2 mutant (Figure 26B). Upon deletion of the ORF2g isoform, secretion of ORF2 into the supernatant was fully abrogated (Figure 26B). Intracellular ORF2i was still detectable, however, the protein level was considerably reduced compared to WT-electroporated cells. This finding is in agreement with previous literature, suggesting that translation from the second start codon is less efficient, resulting in lower ORF2 protein production[66]. In contrast, the ΔORF2i mutant still secreted ORF2 into the supernatant, and PNGase F treatment confirmed that this ORF2 portion was glycosylated, as evidenced by its size shift (Figure 26B). Interestingly, I still observed non-glycosylated ORF2 in the lysate of the ΔORF2i mutant. This might either suggest the detection of ER-translocated ORF2 prior to glycosylation and secretion, or retention of an intracellular, cytosolic ORF2 fraction derived from the ORF2g start codon. This phenomenon was also observed in a previous study, but not explained or explored further[66]. Overall, I confirmed that the ORF2 expression and secretion patterns of the different isoform mutants were as expected.

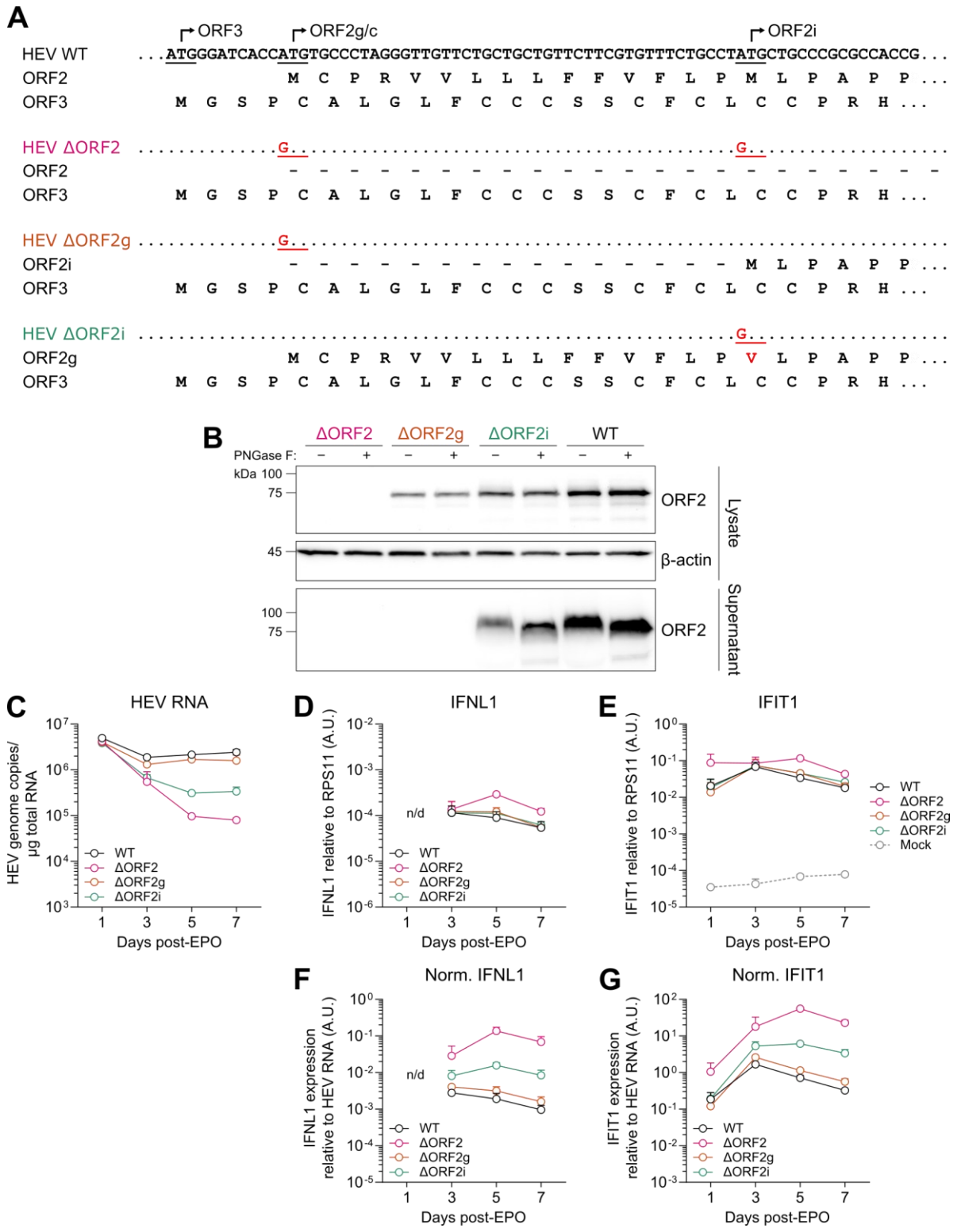

Figure 26: The intracellular ORF2 isoform is sufficient to rescue the ΔORF2 phenotype.
(A) Schematic representation of the HEV-3 Kernow-C1/p6 WT genome and derived ΔORF2, ΔORF2g, and ΔORF2i mutants, resulting in ablated protein expression of both ORF2 isoforms, ORF2g, or ORF2i, respectively. Start codons are underlined, and mutations of the respective start codons as well as the resulting amino acid change in the ORF2g protein sequence of the ΔORF2i mutant are highlighted in red. The resulting lack of protein expression is indicated by dashed lines. (B) HepG2/C3A cells were electroporated with WT, ΔORF2, ΔORF2g, or ΔORF2i mutant RNA and mixed 1:1 with mock-electroporated cells. On day 7 post-EPO, supernatants and cell lysates were harvested and subjected to PNGase F treatment to remove *N*-glycosylations. Protein expression of ORF2 and the loading control β-actin was then assessed by Western blot in PNGase F-treated and untreated lysates and supernatants. Representative blot of n = 2 independent experiments. kDa, kilodalton. (C) HepG2/C3A cells were

electroporated as described in B, and cell lysates were harvested for RT-qPCR analysis on indicated days post-EPO. HEV RNA was quantified with ORF1-specific primers, and (D) *IFNL1* and (E) *IFIT1* expression was analyzed relative to the housekeeping gene *RPS11* using the $2^{-\Delta Ct}$ method. *IFNL1* was not detectable in mock-electroporated samples. Data show mean ± SEM of n = 2 independent experiments with two biological replicates each. A.U., arbitrary units; n/d, not detectable. (F) *IFNL1* expression from D and (G) *IFIT1* expression from E were additionally normalized to HEV RNA using the $2^{-\Delta\Delta Ct}$ method. Data show mean ± SEM of n = 2 independent experiments with two biological replicates each. A.U., arbitrary units; n/d, not detectable; norm., normalized.

Next, I explored HEV replication and induction of a cell-intrinsic antiviral response upon EPO with the different ORF2 isoforms. Expression of the ORF2i isoform in the ΔORF2g mutant resulted in a complete rescue of the ΔORF2 replication phenotype (Figure 26C). The minor decrease in HEV RNA might be a direct consequence of the lower intracellular ORF2 levels compared to WT (Figure 26B). Interestingly, expression of only ORF2g in the ΔORF2i mutant led to a moderate reduction in HEV replication, with HEV RNA levels between WT and ΔORF2. This intermediate rescue phenotype might be explained by intracellular retention of a small ORF2 fraction in the cytosol, as already suggested in the Western blot analysis of the ΔORF2i lysate (Figure 26B). Of note, I used ORF1-specific primers in this experiment, exclusively amplifying the gRNA, whereas ORF2-specific primers, binding to both gRNA and sgRNA, were used in all other experiments of this dissertation. Interestingly, the decrease in ΔORF2 HEV RNA on day 7 post-EPO compared to WT HEV RNA was considerably stronger when using ORF1-specific primers. This resulted in a ~30-fold reduction of ΔORF2 gRNA (Figure 26C) compared to a ~9-fold decrease in gRNA and sgRNA (Figure 24A). This suggested that the genomic RNA might be more sensitive to the effects of absent ORF2. Possibly, the sgRNA is more protected due to its association with ribosomes for ORF2 and ORF3 protein translation.

Analysis of the antiviral response revealed the same ΔORF2 phenotype as already described in Figure 24B and C, characterized by increased *IFNL1* and, in this experiment, *IFIT1* expression, particularly on day 5 post-EPO (Figure 26D, E). As expected from the rescue of HEV replication, the antiviral response induced upon EPO with the ΔORF2g mutant was comparable to WT levels. Since the differences in *IFNL1* and *IFIT1* expression between WT and ΔORF2 are generally not very pronounced, the ΔORF2i-induced antiviral response resembled the WT phenotype, despite the intermediate effect observed for HEV replication (Figure 26C, D). However, normalization over the different HEV RNA levels revealed an intermediate increase of *IFNL1* and *IFIT1* expression for ΔORF2i compared to WT, whereas ΔORF2g completely reverted the enhanced induction observed for ΔORF2 (Figure 26F, G).

Collectively, I found that the intracellular ORF2i isoform is sufficient to fulfill the protein's antagonistic functions targeting the cell-intrinsic antiviral response, whereas the ORF2g isoform appears dispensable. Assuming that ORF2 is needed in the cytosol to interact with TBK1, at least part of the ORF2g fraction detected intracellularly (Figure 26B) must be located in the cytosol, thereby resulting in an intermediate rescue of the ΔORF2 phenotype.

5.3.3 The HEV ΔORF2 Mutant is More Sensitive to the Action of ISGs

I previously observed a striking difference between gRNA and sgRNA levels in the ΔORF2 mutant (Figure 24A and Figure 26C). Furthermore, the effect of TBK1 inhibition was more pronounced on ΔORF2 replication compared to WT and ΔORF3, indicating an increased sensitivity of ΔORF2 towards the antiviral response (Figure 25). Collectively, these findings suggested that the ORF2 protein might have further functions in immune evasion, in addition to the direct TBK1 antagonism. I therefore investigated whether the ΔORF2 RNA is more sensitive to the antiviral actions of ISGs than the WT RNA. For this, I made use of Huh7.5 cells, which express a mutant, non-responsive RIG-I and lack detectable expression of MDA5, LGP2, and TLR3[193,194]. I demonstrated previously that Huh7.5 cells do not respond to HEV replication (Figure 17E). However, Huh7.5 cells remain capable of ISG upregulation in response to IFN stimulation. Therefore, I exploited this cell line to study the direct antiviral effect of exogenously induced ISGs on HEV replication in the absence of a virus-induced antiviral response.

I electroporated Huh7.5 cells with HEV WT and ΔORF2 IVT RNA and treated them with 10 ng/mL IFNλ1 or 10,000 IU/mL IFNα2A between day 4 and day 7 post-EPO. On day 7 post-EPO, I analyzed the effect of the IFN treatment on HEV replication by determining HEV genome copies by RT-qPCR. WT replication showed a minor, but statistically not significant, decrease upon treatment with both IFNλ1 and IFNα2A (Figure 27A). In contrast, IFNλ1 and, even more pronounced, IFNα2A treatment prominently reduced ΔORF2 RNA compared to the untreated condition (Figure 27A), suggesting that ΔORF2 replication is indeed more sensitive to IFN treatment. Interestingly, ΔORF2 RNA was 2.3-fold lower compared to WT RNA in the untreated condition (Figure 27B), which was a minor yet significant difference. Conversely, EPO experiments performed by my colleague Jungen Hu have resulted in equal HEV WT and ΔORF2 RNA copy numbers in Huh7.5 cells over time (data not shown). Hence, the small difference I observed between WT and ΔORF2 replication in the untreated condition could be due to experimental variation and should therefore be replicated for confirmation. Nonetheless, ΔORF2 replication was generally much less affected in Huh7.5 cells compared to immunocompetent HepG2/C3A cells, as demonstrated in chapter 5.3.1. Therefore, I concluded that the antiviral response is the main driver of the dampened ΔORF2 replication. Importantly, ΔORF2 replication was significantly reduced compared to WT replication upon IFNλ1 and IFNα2a treatment (Figure 27B), substantiating the increased sensitivity of ΔORF2 to the antiviral ISGs. Notably, ISG expression was induced to the same extent in WT- and ΔORF2-electroporated cells upon IFNλ1 and IFNα2A stimulation (Figure 27C).

Of note, I detected neither *IFNB1* nor *IFNL1* expression upon IFN stimulation (data not shown). The opposite outcome would have indicated upregulation of PRRs, and thus, sensing of viral RNA and enhanced ISG induction in a positive feedback loop. As this was not the case, I could exclude that the lack of the direct TBK1-targeted antagonism mediated by ORF2 was responsible for the observed reduction in ΔORF2 replication in this experiment. Instead, I concluded that ORF2 likely serves an additional purpose by shielding the viral RNA from the antiviral effects of ISGs, even in the absence of a directly virus-induced antiviral response.

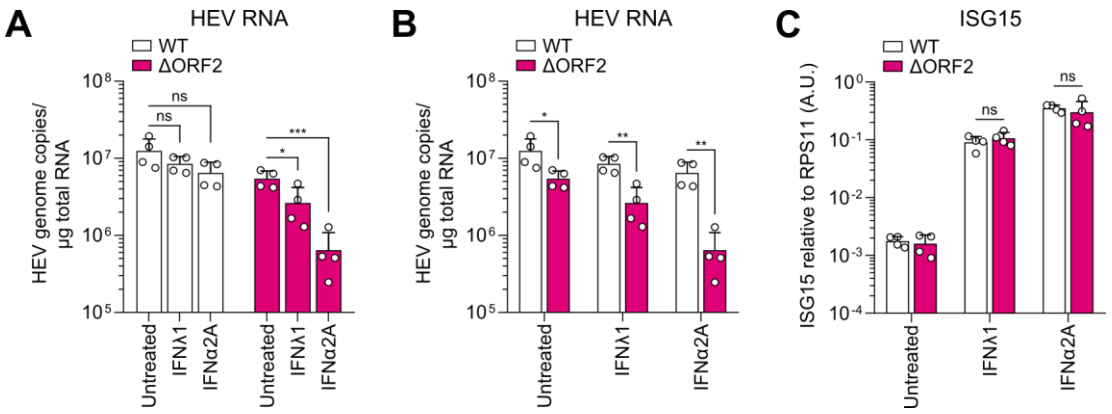

Figure 27: The HEV ΔORF2 mutant is more sensitive to the action of ISGs.
(A) Huh7.5 cells were electroporated with WT and ΔORF2 IVT RNA and treated with 10 ng/mL IFNλ1 or 10,000 IU/mL IFNα2A between day 4 and day 7 post-EPO. IFNs were replenished daily. On day 7 post-EPO, cell lysates were harvested for RT-qPCR analysis and HEV RNA was quantified. Data show mean ± SD of n = 4 biological replicates from two independent experiments. Statistical analysis was performed using one-way ANOVA of WT and ΔORF2 independently. *: $p < 0.05$; ***: $p < 0.001$; ns, not significant. (B) HEV genome copies determined in A were compared between WT and ΔORF2 using multiple unpaired two-tailed Student's t-tests. *: $p < 0.05$; **: $p < 0.01$. (C) Samples from A–B were additionally analyzed for *ISG15* expression relative to the housekeeping gene *RPS11* using the $2^{-\Delta Ct}$ method. Statistical analysis was performed using multiple unpaired two-tailed Student's t-tests. ns, not significant. A.U., arbitrary units.

5.3.4 ORF2 Enables the Equilibration of Viral Replication and Antiviral Response Following a Replication-Limiting Bottleneck

So far, I performed all experiments characterizing the differences between HEV WT and ΔORF2 by EPO of IVT RNA. However, this method does not fully resemble a virus infection, since entry is bypassed. Furthermore, large quantities of RNA are introduced during the EPO process, masking early replication of the virus, as described previously (Figure 24A). Therefore, I aimed to validate my findings using authentic ΔORF2 virus infection.

Infectious ΔORF2^{trans} virus particles can be produced by trans-complementation

As the ΔORF2 mutant lacks expression of the capsid protein, I established a trans-complementation system to package ΔORF2 RNA with ORF2 protein expressed by a producer cell (Figure 28A). I made use of an S10-3/ORF2 cell line, previously established by Lars Maurer, a former MD student in the research group of Dr. Viet Loan Dao Thi. I electroporated S10-3/ORF2 cells with ΔORF2 RNA and performed the virus production according to our standard protocol. The resulting ΔORF2^{trans} virus particles were used for single rounds of

infection in downstream experiments. First, I evaluated the expression of ORF2 and ORF3 proteins in the producer cells. Mock-electroporated S10-3/ORF2 cells expressed ORF2 to a level comparable to HEV WT-electroporated S10-3 cells, while ORF3 was absent in S10-3/ORF2 cells (Figure 28B). Upon EPO of S10-3 cells with the ΔORF2 mutant, the ORF3 protein was clearly detectable, but ORF2 expression was undetectable (Figure 28B). In contrast, S10-3/ORF2 cells electroporated with ΔORF2 RNA were characterized by virus-derived ORF3 protein expression and producer cell-derived ORF2 expression (Figure 28B). Furthermore, both ORF2 and ORF3 proteins were detectable upon IF staining of ΔORF2-electroporated producer cells (Figure 28C). Naked ΔORF2^{trans} virus particles were harvested from cell lysates, and I could detect ORF2-negative but ORF3-positive foci upon re-infection of HepG2/C3A cells (Figure 28D). In conclusion, I successfully established a trans-complementation system for the production of ΔORF2^{trans} virus particles.

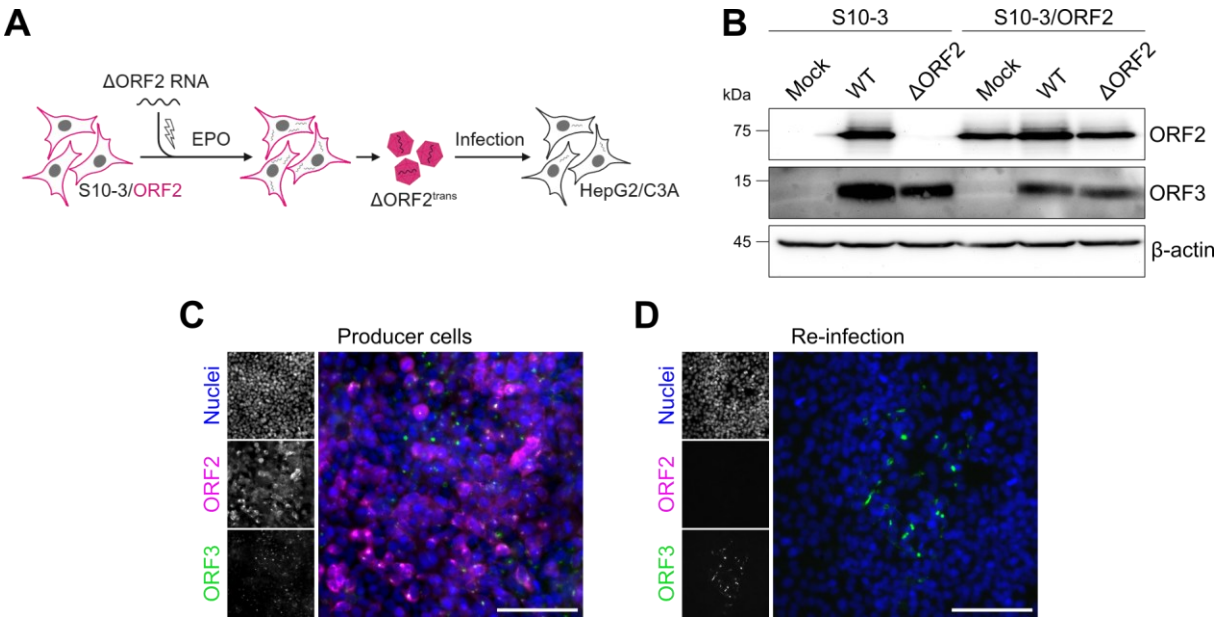

Figure 28: Infectious ΔORF2^{trans} virus particles can be produced by trans-complementation.
(A) Schematic workflow for ΔORF2^{trans} virus particle production. S10-3/ORF2 cells were electroporated with ΔORF2 RNA and cultured for 7 days. Naked ΔORF2^{trans} virus particles were harvested from cell lysates and used for single rounds of downstream infection of HepG2/C3A cells. (B) Parental S10-3 and derived S10-3/ORF2 cells were electroporated with HEV WT and ΔORF2 RNA, and cell lysates were harvested on day 7 post-EPO for SDS-PAGE and Western blot analysis to detect ORF2, ORF3, and the loading control β-actin. The blot from a single experiment is shown. kDa, kilodalton. (C) S10-3/ORF2 cells electroporated with ΔORF2 RNA were fixed on day 7 post-EPO and stained for ORF2 (magenta) and ORF3 (green) by IF, and counterstained with Hoechst for nuclei (blue). Representative image of a single experiment is shown. Scale bar, 100 µm. (D) HepG2/C3A cells were infected with 2 µL crude ΔORF2^{trans}-containing lysate overnight and treated with 1 µM of the JAK1/2 inhibitor Ruxolitinib until the time point of harvest to suppress ISG responses. Cells were fixed on day 6 post-infection and stained for ORF2 (magenta) and ORF3 (green) by IF, and counterstained with Hoechst for nuclei (blue). All images were taken with a Nikon Eclipse Ts2-FL widefield epifluorescence microscope. Representative image of a single experiment is shown. Scale bar, 100 µm. Panels A and B were published in a preprint by Mehnert *et al.*[245].

Authentic ΔORF2 infection leads to stronger antiviral responses and impaired viral replication in HepG2/C3A cells and HLCs

Next, I evaluated whether the ΔORF2 phenotype, characterized by lower viral replication and a stronger antiviral response, was reproducible upon authentic ΔORF2 infection. First, I used crude cell lysates containing WT and ΔORF2^{trans} HEV particles, directly harvested from the corresponding producer cells by repeated freeze-thaw cycles. ΔORF2^{trans} virus particles were titrated on HepG2/C3A cells in the presence of the JAK1/2 inhibitor Ruxolitinib to inhibit ISG responses and allow efficient HEV replication (Figure 28D). I selected this drug as a trade-off between low cytotoxicity upon application over a six-day period and incomplete repression of the antiviral response due to residual ISG induction immediately downstream of IRF3. Because of the absent ORF2 expression in ΔORF2-infected cells, I used ORF3 IF staining to count foci for WT and ΔORF2. Due to variations in the ORF3 expression between infected cells, and the characteristically speckled distribution of the ORF3 signal (Figure 28D), foci counts based on this protein may underestimate the virus titer. This highlights the importance of titrating WT and ΔORF2^{trans} virus particles side-by-side. I estimated the titer of crude WT and ΔORF2^{trans} lysates to be 6.5 x 10^5 and 5.1 x 10^5 FFU/mL, respectively, indicating efficient ΔORF2 trans-complementation. This was further corroborated by comparable HEV genome copy numbers detected on day 1 post-infection of HepG2/C3A cells, following inoculum removal (Figure 29A). Replication of both viruses increased until day 3 post-infection, followed by a stronger decrease in ΔORF2 infection compared to WT infection. Despite the detection of comparable HEV RNA on day 3, *IFNL1* and *IFIT1* induction was significantly stronger in ΔORF2-infected HepG2/C3A cells (Figure 29B, C). On day 5 and day 7 post-infection, expression of the antiviral response genes in WT and ΔORF2 infections aligned, similar to my previous observations (Figure 24A). Despite the lower ΔORF2 RNA levels, *IFNL1* and *IFIT1* induction remained relatively robust. With these findings, I confirmed that the ORF2 phenotype was reproducible and might be even more pronounced in authentic infection. Differences in replication and the antiviral response as well as the earlier onset of a stronger antiviral response in ΔORF2 infection compared to the previous EPO experiments can likely be explained by the overall stronger antiviral response and high HEV RNA input upon EPO. Thus, the precise time points observed in ΔORF2 EPO and infection are not directly comparable.

For later experiments, I concentrated ΔORF2^{trans} virus particles by ultracentrifugation through a 20% sucrose cushion according to our standard protocol for HEV WT production. Since the reproducibility of ORF3 IF stainings is challenging due to variable ORF3 protein expression in infected cells, I decided to determine HEV genome copies in the WT and ΔORF2^{trans} virus stocks by RT-qPCR, enabling infection with equal genome equivalents (GE) per cell. However, I consistently detected approximately 2- to 2.4-fold lower HEV RNA after inoculum removal

when infecting with this method (Figure 29D and Figure 30E). One explanation could be a lower specific infectivity of the ΔORF2^{trans} virus due to assembly errors in the producer cells. However, I also noticed that repeated determination of GE by RT-qPCR resulted in variable outcomes, and two-fold differences between repeats were not uncommon. Lastly, ultracentrifugation might change the nature of the virus stocks, affecting their comparability, for instance, by causing the formation of virus aggregates. Even though I continued to use infection based on equal GE per cell, infections with crude lysates and titration by foci counts based on ORF3 staining should be considered in the future.

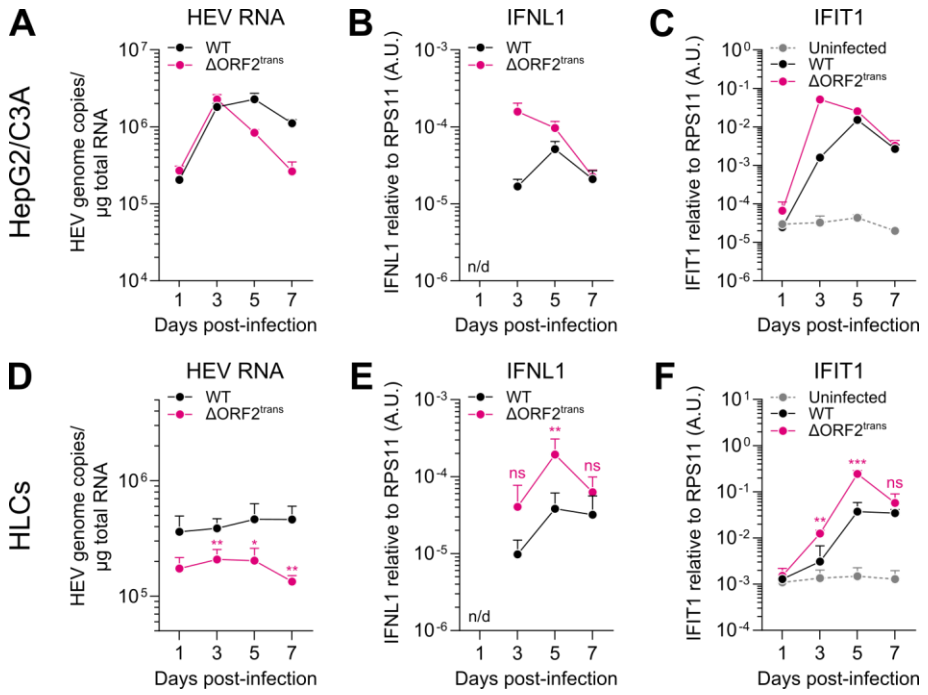

Figure 29: Authentic ΔORF2 infection leads to stronger antiviral responses and impaired viral replication in HepG2/C3A cells and HLCs.
(A) HepG2/C3A cells were infected with crude lysates of HEV WT and ΔORF2^{trans} virus productions at an FFU-based MOI of 0.1. On day 1 post-infection, the inoculum was removed, and cells were washed twice with PBS. Cell lysates were harvested for RT-qPCR analysis at indicated time points. HEV genome copies were quantified, and (B) *IFNL1* and (C) *IFIT1* expression was analyzed relative to the housekeeping gene *RPS11* using the $2^{-\Delta Ct}$ method. *IFNL1* expression was not detectable in uninfected samples. Data show mean ± SD of a single experiment with two biological replicates. A.U., arbitrary units; n/d, not detectable. (D) R2-derived HLCs were infected with 20% sucrose-concentrated HEV WT and ΔORF2^{trans} virus particles at equal MOI (~1.4 x 10^6 GE/HLC well of a 24-well plate). On day 1 post-infection, the inoculum was removed, and cells were washed twice with DPBS. Cell lysates were harvested for RT-qPCR at indicated time points. HEV genome copies were quantified, and (E) *IFNL1* and (F) *IFIT1* expression was analyzed relative to the housekeeping gene *RPS11* using the $2^{-\Delta Ct}$ method. *IFNL1* expression was not detectable in uninfected samples. Data show mean ± SD of n = 4 biological replicates of two independent HLC differentiations. Statistical analysis of ΔORF2 over WT was performed using unpaired two-tailed Student's t-test of each time point independently. *: $p < 0.05$; **: $p < 0.01$; ***: $p < 0.001$; ns, not significant. A.U., arbitrary units; n/d, not detectable. Panels D and E were published in a preprint by Mehnert *et al.*[245].

The establishment of a ΔORF2 trans-complementation system was particularly important for studying the ΔORF2 phenotype in hESC-derived HLCs. I used equal GE per well to infect HLCs with WT and ΔORF2^{trans} virus particles and analyzed HEV replication and antiviral response induction over time. In comparison to the infection of HepG2/C3A cells, HEV WT

RNA did not increase over time but was rather sustained at a constant level (Figure 26D). In contrast, ΔORF2 replication decreased between day 5 and day 7 post-infection compared to WT. *IFNL1* induction was significantly stronger at its peak on day 5 post-ΔORF2 infection in comparison with WT (Figure 29E), while *IFIT1* expression was significantly increased on both day 3 and day 5 (Figure 29F). Overall, this suggested that the antiviral response to ΔORF2 infection peaked at a later time point than that observed in HepG2/C3A cells. This is not surprising as the onset of HEV replication has been demonstrated to be delayed in HLCs compared to infection of hepatoma cells[204].

Collectively, I could validate that authentic infection with ΔORF2^{trans} virus particles resulted in decreased replication and induction of a stronger antiviral response in HepG2/C3A cells and hESC-derived HLCs, which represent a more physiological hepatocellular system compared to hepatoma cells.

Time-resolved infection reveals a critical bottleneck for the establishment of an equilibrium between viral replication and the antiviral response

My previous results suggested that the decisive time point for establishment of persistent HEV replication and control of the antiviral response by ORF2 is around day 3 post-infection in HepG2/C3A cells (Figure 29A–C). To refine this time point, I adapted a standard entry assay procedure to achieve a more synchronized and time-resolved HEV infection. Instead of infecting overnight, I bound HEV WT and ΔORF2^{trans} virus particles on seeded HepG2/C3A cells for 2 h at 4 °C to prevent endocytosis, followed by synchronized internalization at 37 °C (Figure 30A). After 8 h, I removed the inoculum and washed the cells twice with PBS to remove unbound and non-internalized virus particles. In a standard entry assay, unbound virus particles are removed immediately after the binding period. However, HEV binding to cells is quite inefficient[86,95], and therefore, large quantities of virus particles are needed to assess differences in infection using bulk readouts such as RT-qPCR. Consequently, I decided to remove the viral inoculum after internalization, reducing the number of required virus particles while still enabling a more synchronized infection.

Upon synchronized infection of HepG2/C3A cells with HEV WT and ΔORF2^{trans} virus particles at equal MOI (30 GE/cell), I observed a steady increase in HEV RNA until 48 ± 8 h post-internalization, where both WT and ΔORF2 replication peaked (Figure 30B). Because infection with equal GE resulted in a 2.4-fold lower HEV RNA input in ΔORF2 infection (Figure 30E), I normalized viral replication over day 0 post-internalization (Figure 30B). Interestingly, replication of both viruses declined after their peak at 48 ± 8 h post-internalization (Figure 30B, E). However, WT HEV RNA levels decreased by only 2-fold until day 7, which was statistically not significant (Figure 30B). In contrast, ΔORF2 replication was significantly

reduced by 8.5-fold on day 7 compared to 56 h post-internalization (Figure 30B). Furthermore, the onset of WT and ΔORF2 replication was accompanied by the induction of an antiviral response, characterized by *IFNL1* and *ISG15* expression (Figure 30C, D). Shortly after the peak of viral replication, antiviral response gene expression also peaked and declined thereafter (Figure 30C, D). The direct comparison of *IFNL1* and *ISG15* expression levels did not reveal a significant difference between WT and ΔORF2 infection (Figure 30C, D). However, considering the reduced viral replication and the lower input RNA, the antiviral response upon ΔORF2 infection was significantly stronger on day 7 post-internalization, when normalized to HEV RNA (Figure 30F, G). The general increase in HEV RNA genome copies over time was weaker compared to my previous experiments, for example, upon infection with crude WT and ΔORF2^{trans} lysates (Figure 29A). This could be due to the short internalization period during the synchronized infection approach. This is further supported by the relatively weak antiviral response, considering the average *IFNL1* and *ISG15* expression between day 1 and day 7 post-internalization (Figure 30C, D). Interestingly, the distinct peak in the antiviral response around 56 h post-internalization was not apparent in my previous experiments, likely due to the EPO setup or the overnight infection, as well as the less refined time points of analysis. Hence, I was only able to identify a bottleneck in viral replication, coinciding with the induction of an antiviral response, through synchronized and time-resolved infection.

In summary, the presence of ORF2 appeared to be crucial for establishing an equilibrium between viral replication and the antiviral response, following an early bottleneck in infection at around 56 h. The absence of ORF2 disrupted this balance, leading to a relatively stronger antiviral response and a subsequent decline in viral replication due to the antiviral effects inflicted by the induced ISGs. In turn, the presence of ORF2 resulted in a dampened antiviral response, likely due to the direct antagonism of TBK1, which I identified previously. Furthermore, the protective function of ORF2, shielding viral RNA from the antiviral effectors, resulted in a diminished effect of the antiviral response on HEV WT replication, following the bottleneck. Overall, the various protective roles mediated by ORF2 seem essential for ensuring efficient viral replication in the presence of a sustained yet dampened antiviral response, following a decisive bottleneck early in infection.

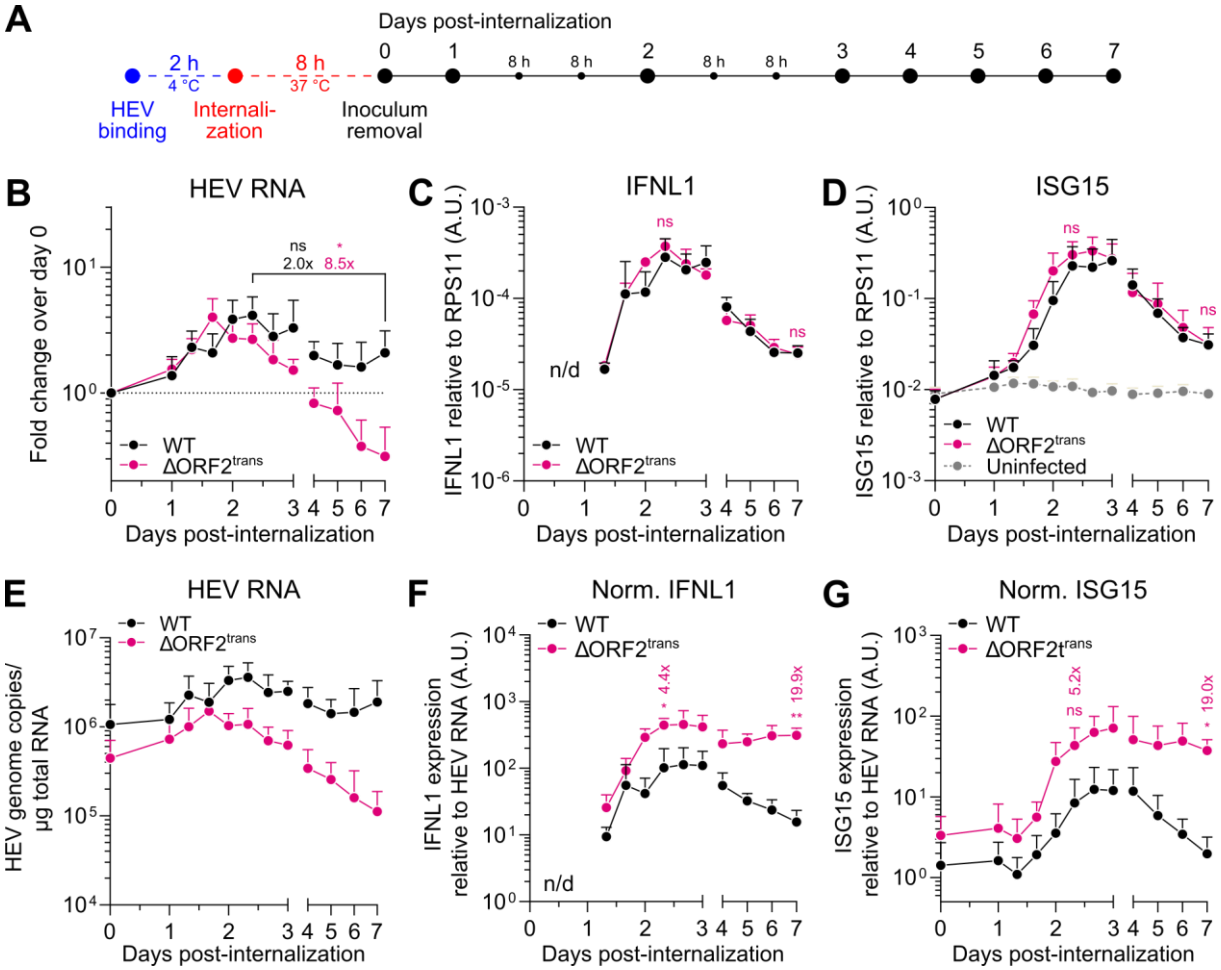

Figure 30: Time-resolved infection reveals a critical bottleneck for the establishment of an equilibrium between viral replication and the antiviral response.
(A) Workflow of the time-resolved, synchronized infection. HEV virus particles were bound on seeded HepG2/C3A cells for 2 h at 4 °C, followed by internalization for 8 h at 37 °C. The inoculum was removed, and the cells were washed twice with PBS. Samples were harvested for RT-qPCR analysis every 8 h between day 1 and day 3 post-internalization and every 24 h thereafter. (B) HepG2/C3A cells were infected with equal MOI (30 GE/cell) of WT and ΔORF2^{trans} virus particles as described in A and harvested accordingly. HEV genome copies were quantified by RT-PCR and normalized to day 0 post-internalization, and (C) *IFNL1* and (D) *ISG15* expression was analyzed relative to the housekeeping gene *RPS11* using the $2^{-\Delta Ct}$ method. *IFNL1* expression was not detectable in uninfected samples. Statistical analysis of fold changes over time in B and ΔORF2^{trans} compared to WT in C and D are indicated above the respective time points in the corresponding color. Data show mean ± SD of n = 3 independent experiments with one biological replicate each. Statistical analysis was performed using unpaired two-tailed Student's t-test of the respective conditions or days independently. *: $p < 0.05$; ns, not significant. A.U., arbitrary units; n/d, not detectable. (E) Non-normalized data of B showing quantified HEV genome copies over time. (F) *IFNL1* and (G) *ISG15* expression was additionally normalized to HEV RNA using the $2^{-\Delta\Delta Ct}$ method. Statistical analysis of ΔORF2^{trans} over WT is indicated above the respective time points in the corresponding color. Data show mean ± SD of n = 3 independent experiments with one biological replicate each. Statistical analysis was performed using unpaired two-tailed Student's t-test of the respective days independently. *: $p < 0.05$; **: $p < 0.01$; ns, not significant. A.U., arbitrary units; n/d, not detectable; norm., normalized. Panels B–G were published in a preprint by Mehnert *et al.*[245].

5.4 ORF2 Globally Dampens the ISG Response in HEV-Infected Cells and Uninfected Bystanders

So far, all my experiments were focused on bulk analysis of the cell-intrinsic antiviral response upon HEV infection. However, analysis at the single-cell level has the potential to reveal heterogeneities in the antiviral response across a cell population. Actively infected cells, defined by the presence of viral RNA, may display a distinct ISG program compared to the so-called bystanders, which are uninfected cells that display an enhanced expression of antiviral response genes. Moreover, entirely non-responsive cell populations might be uncovered by analysis at the single-cell level, and it can help identify the source of the antiviral response within an infected cell population. In bulk analysis, it remains unclear whether IFN expression is induced exclusively in the infected cells downstream of the PRRs or whether uninfected bystanders also upregulate IFNs in response to HEV infection. IFN signaling primarily results in a reinforced IFN production by upregulation of PRRs and thereby, through enhanced sensing in actively infected cells. However, studies have shown that transfer of viral RNA to neighboring cells via extracellular vesicles can lead to IFN expression in uninfected cells (reviewed in [257]). And finally, it remains to be clarified whether the ISG response detected in bulk might originate mainly from the bystander cells due to the previously described protective functions that ORF2 exerts within infected cells.

In order to answer these questions, one aim of this project was to characterize the antiviral response upon HEV infection at the single-cell level using spatial RNA-FISH and scRNA-seq. Originally, we aimed to perform these experiments in HEV-infected HLCs due to their physiological relevance and the presence of different endoderm-derived hepatic cell types. Previously, I had established a functional *IFNLR1* KO in hESCs, as described in chapter 5.1.2, to distinguish between IFN-dependent and -independent responses in the single-cell analysis. However, I consistently encountered difficulties in singularizing differentiated HLCs without inducing significant cell death. As the success of scRNA-seq relies significantly on a homogeneously singularized cell population and low cytotoxicity, HLCs proved to be unsuitable for this type of analysis. Furthermore, as most of my previous observations were made in HepG2/C3A cells, I decided to continue with this cell line for the single-cell analysis.

5.4.1 Strong ISG Responses are Detectable Around the Replication-Limiting Bottleneck by RNA-FISH Analysis

To study the antiviral response at the single-cell level by RNA-FISH, I first established several type III IFN- and ISG-specific RNAscope probes. The IFNL probe was originally designed by the company providing the RNAscope assay to detect *IFNL3* mRNA. Cross-detection of *IFNL1* and *IFNL2*, however, is possible due to a high sequence similarity. Since I did not aim to

distinguish between the different type III IFNs, this did not pose a problem for my analysis and might even facilitate amplification of the signal. To validate the probes, I stimulated HepG2/C3A cells with poly(I:C) and performed RNAscope, followed by anti-IRF3 IF staining to identify the stimulated cells. The probes for *IFNL*, *IFIT1*, and *ISG15* all resulted in specific signals in cells showing nuclear translocation of IRF3 (Figure 31A–C). However, I observed clear differences in the intensities of the RNA-FISH signals. While the IFNL and IFIT1 probes showed a distinct, dotted signal (Figure 31A, B), the ISG15 probe produced a strong and dispersed staining across all cells with considerably stronger intensity in cells with IRF3 nuclear translocation (Figure 31C). This might be explained, at least in part, by the higher concentration of poly(I:C) used in the case of ISG15, as the basal signal detected in a later experiment was considerably weaker (Figure 33B).

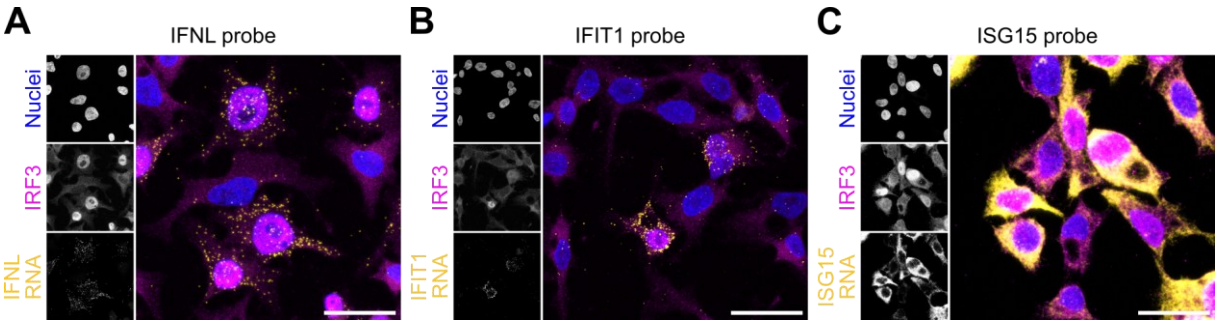

Figure 31: *IFNL*, *IFIT1*, and *ISG15* are detectable by RNA-FISH with varying efficiencies.
(A) HepG2/C3A cells were stimulated with 250 ng poly(I:C) by transfection, fixed after 8 h, and stained for *IFNL* RNA (yellow) or (B) *IFIT1* RNA (yellow) by RNA-FISH, followed by anti-IRF3 IF staining (magenta). Nuclei (blue) were counterstained with Hoechst. Images were taken with a Leica TCS SP8 confocal microscope. Representative images of a single experiment. Scale bar, 25 µm. (C) HepG2/C3A cells were stimulated with 1 µg poly(I:C) for 8 h, fixed and stained for *ISG15* RNA (yellow) by RNA-FISH, followed by anti-IRF3 IF staining (magenta). Nuclei (blue) were counterstained with Hoechst. Images were taken with a Leica TCS SP8 confocal microscope. Representative images of a single experiment. Scale bar, 25 µm.

Basal expression of type III IFNs is low in non-stimulated cells (Figure 10A), making the absence of *IFNL* RNAscope signal in cells not transfected with poly(I:C) plausible (Figure 31A). In contrast, *ISG15* and *IFIT1* are expressed at basal levels in non-stimulated cells (Figure 10B, C), and therefore, RNAscope signal is expected in cells not transfected with poly(I:C), which I observed for the ISG15 probe (Figure 31C). However, the *IFIT1* signal was very weak and barely detectable in cells without nuclear translocation of IRF3 (Figure 31B). In contrast, RT-qPCR analysis usually showed a much stronger induction of *IFIT1* compared to *ISG15* (Figure 10B, C). To understand this discrepancy, I analyzed the hybridization region of the IFIT1 probe and confirmed that all transcript variants were covered. Generally, the RNAscope assay relies on the hybridization of up to 20 probe pairs to a sequence stretch of 500–1000 nucleotides, depending on the gene of interest. The combination of several probe pairs is supposed to enhance the specificity and sensitivity of the signal by increasing the likelihood that at least a fraction of the probe pairs binds reliably to the target, and by decreasing the

likelihood of detecting off-target signals[255]. The true number of probe pairs binding to a target sequence, however, can differ between probes and thereby result in differences in signal intensities, as observed here. These results highlighted a discrepancy between my RT-qPCR and RNA-FISH results regarding the basal and induced expression levels of individual ISGs.

HEV-infected cells show a strong *IFNL* and *IFIT1* RNA signal on day 3 post-infection

To visualize the HEV-specific cell-intrinsic antiviral response at the single-cell level, I infected HepG2/C3A cells with HEV WT and stained for *IFNL* and *IFIT1* together with HEV RNA by RNA-FISH. The ISG15 probe was established subsequently and was therefore not used in this experiment. On day 1 post-infection, only individual spots of HEV RNA-positive signal were detected, indicating incoming HEV RNA and limited viral replication (Figure 32A). On day 2 post-infection, clusters of strongly HEV RNA-positive cells emerged (Figure 32A), suggesting the onset of replication between day 1 and day 2, consistent with the RT-qPCR data obtained by the synchronized, time-resolved infection (Figure 30B), and as published previously[201]. Thereafter, the HEV RNA signal did not change considerably until day 7 post-infection (Figure 32A).

Interestingly, I observed neither *IFNL* nor *IFIT1* RNA on day 1 and day 2 post-infection (Figure 32A), supporting the notion that HEV replication is required to induce a detectable antiviral response. Generally, the detection of *IFNL*- or *IFIT1* RNA-positive cells by RNA-FISH was challenging and remained a rare event. Considering our scRNA-seq data obtained later (chapter 5.4.2), which revealed an antiviral response in the majority of cells, this might indicate technical problems with the RNAscope procedure, such as incomplete permeabilization or inefficient probe hybridization. On day 3 and day 4 post-infection, I succeeded in detecting some *IFNL* and *IFIT1* RNA-positive cells in the HEV-infected samples (Figure 32A). Importantly, *IFNL* and *IFIT1* RNA signals were partly found in HEV RNA-positive cells (Figure 32B), suggesting that, at least at this time point, the ISG response does not exclusively originate from the surrounding bystander cells. However, the threshold for the detection of strongly positive cells remained high, and I could not further identify any visibly *IFNL*- or *IFIT1*-positive cells between day 5 and day 7 post-infection (Figure 32A, day 6 not shown).

In summary, the highest probability of detecting a visible antiviral response was on day 3 post-infection, consistent with the previously observed peak of the antiviral response (Figure 29A). Hence, this time point likely corresponds to the replication-limiting antiviral response bottleneck at 48 ± 8 h identified by synchronized infection (Figure 30), considering the shorter infection time. Despite its technical limitations, the RNA-FISH data support the concept of a stronger antiviral response induction at a bottleneck early in infection, after which the antiviral response is dampened and is thus likely not detectable by RNA-FISH thereafter.

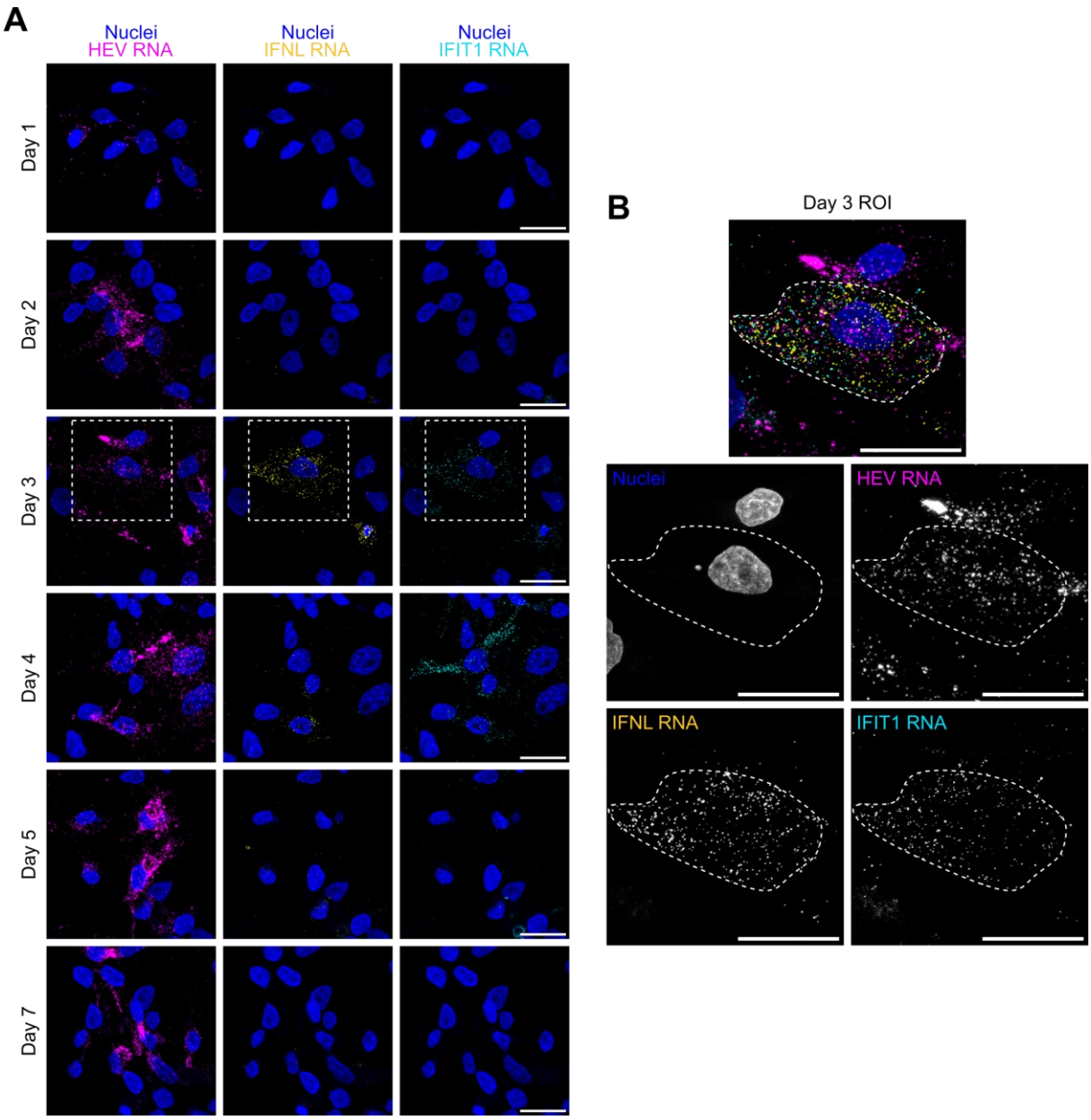

Figure 32: HEV-infected cells show a strong *IFNL* and *IFIT1* RNA signal on day 3 post-infection.
(A) HepG2/C3A cells were infected with HEV WT at an FFU-based MOI of 0.1. The inoculum was removed on day 1, and the cells were fixed at the indicated time points. The samples were stained for HEV RNA (magenta) with an ORF1-specific probe, *IFNL* RNA (yellow), and *IFIT1* RNA (cyan) using RNAscope. Nuclei were counterstained with Hoechst. Images were taken with a Leica TCS SP8 confocal microscope. The dashed square indicates the region of interest (ROI) shown in B. Data show representative images of a single experiment. Scale bar, 25 µm. (B) Zoomed-in ROI indicated with a white dashed square in A. Nuclei are shown in blue, HEV RNA in magenta, *IFNL* RNA in yellow, and *IFIT1* RNA in cyan. Scale bar, 25 µm.

RNA-FISH analysis reveals a visibly stronger ISG response upon ΔORF2 infection

Next, I sought to compare the ISG induction at the single-cell level upon infection with HEV WT and ΔORF2^{trans} virus particles. For this experiment, I used the newly established ISG15 probe because of its increased efficiency compared to the IFIT1 probe. I infected cells following the previously described synchronized infection approach. Samples were fixed on day 1, day 2, and day 3 post-internalization, with the aim of capturing time points around the replication-limiting bottleneck, and stained for HEV and *ISG15* RNA by RNAscope (Figure 33A).

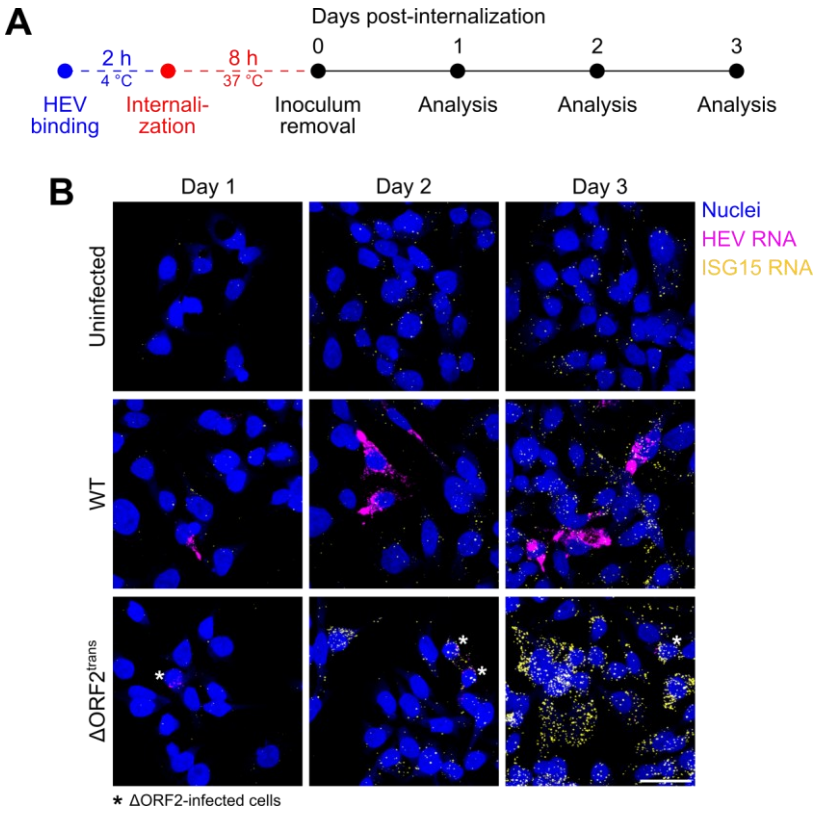

Figure 33: RNA-FISH reveals a visibly stronger ISG response upon ΔORF2 infection.
(A) Schematic workflow of synchronized, time-resolved HEV infection until day 3 post-internalization. HepG2/C3A cells were infected with HEV at equal MOI (~12 GE/cell) with WT and ΔORF2^{trans} virus particles for 2 h at 4 °C, followed by internalization for 8 h at 37 °C. The inoculum was removed by washing, and samples were fixed on day 1, day 2, and day 3 post-internalization. (B) HepG2/C3A cells were infected as described in A, and RNAscope was performed to detect HEV RNA (magenta) with an ORF1-specific probe and *ISG15* RNA (yellow). Nuclei (blue) were counterstained with Hoechst. The white asterisks indicate ΔORF2-infected cells. Images were taken with a Leica TCS SP8 confocal microscope. Representative images of a single experiment. Scale bar, 25 µm.

I observed basal *ISG15* expression in the uninfected samples (Figure 33B), consistent with prior RT-qPCR results (Figure 30D). Upon infection with HEV WT, the *ISG15* RNA signal appeared to be stronger on day 3 post-internalization compared to the uninfected sample (Figure 33B). The *ISG15* staining could not be unambiguously assigned to HEV-infected cells or uninfected bystanders. Interestingly, the HEV RNA signal observed upon ΔORF2 infection was considerably weaker than the HEV WT signal on all days (Figure 33B), complicating the identification of actively ΔORF2-infected cells. Particularly on day 3 post-internalization, I

observed a considerably stronger *ISG15* signal in ΔORF2-infected and surrounding cells (Figure 33B), supporting the previously observed enhanced antiviral response induction in the absence of ORF2. Considering the weaker HEV RNA signal detected in the ΔORF2-infected samples by RNA-FISH, this finding substantiates that a stronger antiviral response is induced despite the lower availability of HEV RNA for sensing. On the other hand, it might also indicate that the overall replication capacity of the ΔORF2^{trans} virus is impaired, independently of the induced antiviral response. This, however, does not invalidate the conclusion that ΔORF2 induces a stronger antiviral response, originating from both HEV-infected cells and uninfected bystanders at the single-cell level.

5.4.2 scRNA-Seq Uncovers a Globally Enhanced ISG Response in Infected Cells and Bystanders in the Absence of ORF2

Next, I aimed to analyze the cell-intrinsic antiviral response to HEV infection at the single-cell level in a more unbiased fashion using scRNA-seq, employing 3'-targeted 10x Genomics, followed by Illumina sequencing. 10x Genomics is based on a microfluidics approach that encapsulates single cells with geld beads in emulsion (GEMs), when combined at limiting dilution[258]. The functionalized gel beads are covered with oligo(dT) primers to amplify poly(A)-containing RNAs and with barcoded oligonucleotides, marking the transcripts of individual cells[258]. The RT takes place in the GEMs, followed by disruption of the emulsion and further processing of the cDNA to generate the sequencing libraries[258]. For this experiment, I infected HepG2/C3A cells with HEV WT and ΔORF2^{trans} virus particles at equal MOI by synchronized, time-resolved infection, as shown in Figure 34A and as described previously. I harvested samples for scRNA-seq analysis at 56 h post-internalization, corresponding to the time point of the replication-limiting bottleneck. Additionally, I collected a later time point on day 6 plus 16 h, from here on referred to as day 7. At this time point, only uninfected and WT-infected samples were analyzed due to the strongly impaired replication of ΔORF2, as described previously, and the therefore limited chances of detecting HEV RNA-positive cells by scRNA-seq. I performed the infection, harvested the samples, and prepared the sequencing libraries. Illumina sequencing on NextSeq550 was supported by Daniel Kirrmaier in the research group of Prof. Dr. Michael Knop at the ZMBH at Heidelberg University. The scRNA-seq data analysis was conducted by Dr. Carlos Ramírez Álvarez in the research group of Prof. Dr. Carl Herrmann at the IPMB at Heidelberg University. In regular meetings with Dr. Carlos Ramírez Álvarez, Prof. Dr. Carl Herrmann, and Dr. Viet Loan Dao Thi, I significantly contributed to gearing the scRNA-seq data analysis towards our biological questions.

ISGs dominate the transcriptional response in HEV-infected HepG2/C3A cells

First, Dr. Carlos Ramírez Álvarez performed a gene set enrichment analysis using the hallmark gene sets of the Human MSigDB Collections[259]. At 56 h post-internalization, we detected significant upregulation of interferon gamma and alpha responses in both WT- and ΔORF2-infected samples (Figure 34B, C). The predominance of ISGs in these gene sets highlights that the global response to HEV infection in HepG2/C3A cells is primarily characterized by an antiviral response. Upregulation of genes related to oxidative phosphorylation and glycolysis indicated enhanced metabolic activity of the infected samples. On day 7, ISG responses were even more prominently represented in the enriched gene sets of the WT-infected sample (Figure 34D). This reinforced the notion that the antiviral response is not fully suppressed in HEV-infected samples at later time points of infection, following the replication-limiting bottleneck.

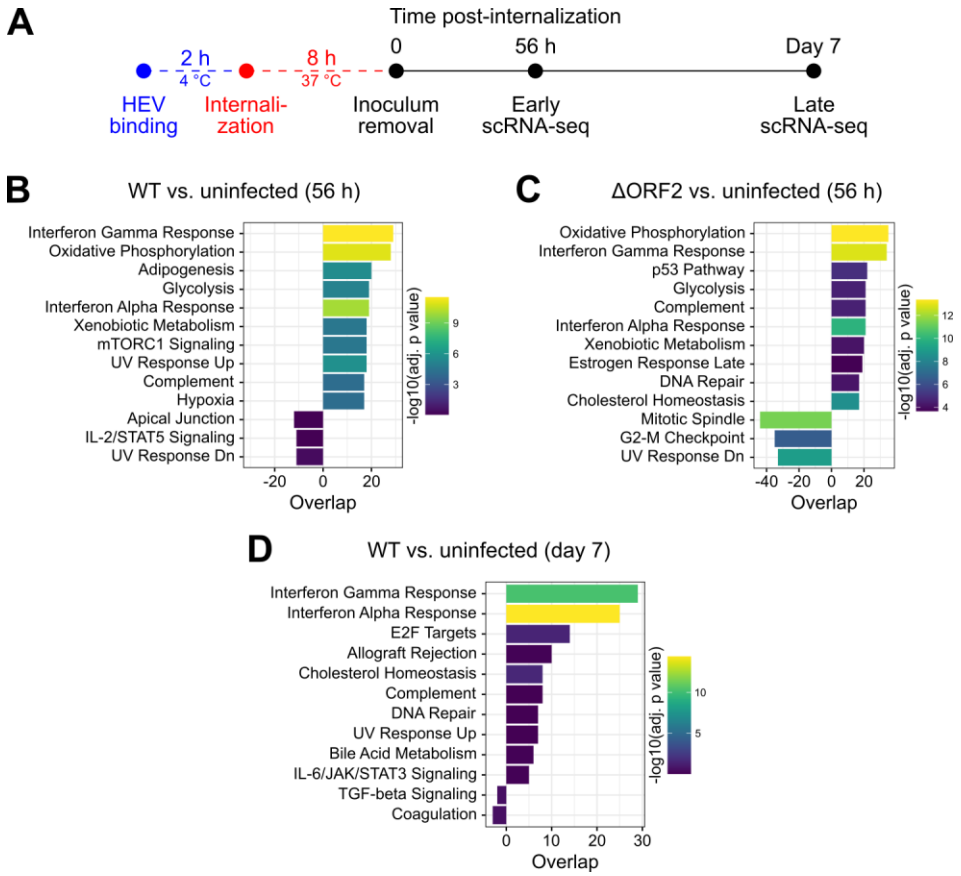

Figure 34: ISGs dominate the transcriptional response in HEV-infected HepG2/C3A cells.
(A) HepG2/C3A cells were infected with HEV WT and ΔORF2^{trans} virus particles at equal MOI (~30 GE/cell) by synchronized infection. Virus particles were bound at 4 °C for 2 h, followed by internalization at 37 °C for 8 h. The inoculum was removed by washing, and samples were harvested at 56 h and day 7 post-internalization for 3'-targeted 10x Genomics-based library preparation, followed by Illumina sequencing. (B) scRNA-seq data was assessed by gene set enrichment analysis using the hallmark gene sets of the Human MSigDB Collections[259], comparing WT vs. uninfected samples at 56 h, (C) ΔORF2 vs. uninfected samples at 56 h, and (D) WT vs. uninfected samples on day 7 post-internalization. Panels B–D were published in a preprint by Mehnert *et al.*[245].

HEV-infected cells and uninfected bystanders are distributed across responding and non-responding populations

Next, we focused on the analysis of the early 56 h time point of uninfected, HEV WT-, and ΔORF2-infected samples. Since we aimed to gear our analysis towards differences in the antiviral response, Dr. Carlos Ramírez Álvarez clustered the cells of each sample based on a list of approximately 400 ISGs (Figure 35A–C), which I selected from a publication by Schoggins *et al.*[260] (Supplementary Table 1). The resulting uniform manifold approximation and projection (UMAP) graphs revealed two major subpopulations in both WT- and ΔORF2-infected samples (Figure 35B, C). One population overlapped with the uninfected sample, suggesting that these cells did not induce an antiviral response (Figure 35D). We concluded that the second population, which was, however, not clearly separated from the first cluster, was transcriptionally distinct from the uninfected sample. We highlighted all cells with significantly upregulated ISGs and thereby separated the samples into an active and an inactive cluster (Figure 35E). In agreement with this distinction, the active cluster appeared to be more transcriptionally active, as indicated by an increased number of genes and transcripts detected per cell (Figure 35F, G). This was further supported by the globally enhanced metabolic activity observed for the infected samples in the gene set enrichment analysis (Figure 34B, C).

We counted the HEV RNA-positive cells and observed 28.1% WT- and 17.2% ΔORF2-infected cells. Previous infections with ΔORF2^{trans} virus particles at equal MOI have always resulted in lower HEV RNA input levels than HEV WT (Figure 29D and Figure 30E), indicating a potential impairment of the specific infectivity of the ΔORF2^{trans} virus. The reduced proportion of HEV RNA-positive cells detected by scRNA-seq might support this hypothesis. On the other hand, I observed a weaker HEV RNA signal per cell already 24 h post-internalization by RNA-FISH (Figure 33B). Therefore, it is also plausible that the scRNA-seq analysis underestimates the true percentage of ΔORF2-positive cells, as lower HEV RNA copy numbers may not be detected due to limited sequencing depth.

Importantly, the majority of actively infected cells, characterized by the detection of at least one HEV RNA copy per cell, in WT- and ΔORF2-infected samples were found in the active cluster, together with many uninfected bystanders (Figure 35I, J). This indicated that the ISG response at the replication-limiting bottleneck originates from uninfected bystanders as well as HEV-infected cells themselves, irrespective of the virus type. We analyzed the infected cells within the inactive cluster further and observed lower HEV RNA counts compared to the active cluster (Figure 35K). It is possible that these cells are at an earlier stage of infection despite the relatively synchronized infection setup, and thus, viral replication has not yet triggered an antiviral response. Alternatively, they could be the result of secondary infections due to

extracellular virus spread. However, this is quite unlikely given the early time point of infection and the quasi-enveloped nature of the virus particles released into the cell culture supernatant. Furthermore, the presence of an entirely non-responsive cell population within the HepG2/C3A cell line might be another possibility. Overall, these results demonstrated that the antiviral ISG response is induced in both actively HEV-infected cells and uninfected bystanders at the previously identified replication-limiting bottleneck. These findings further confirm the observations already made using spatial RNA-FISH (Figure 32 and Figure 33).

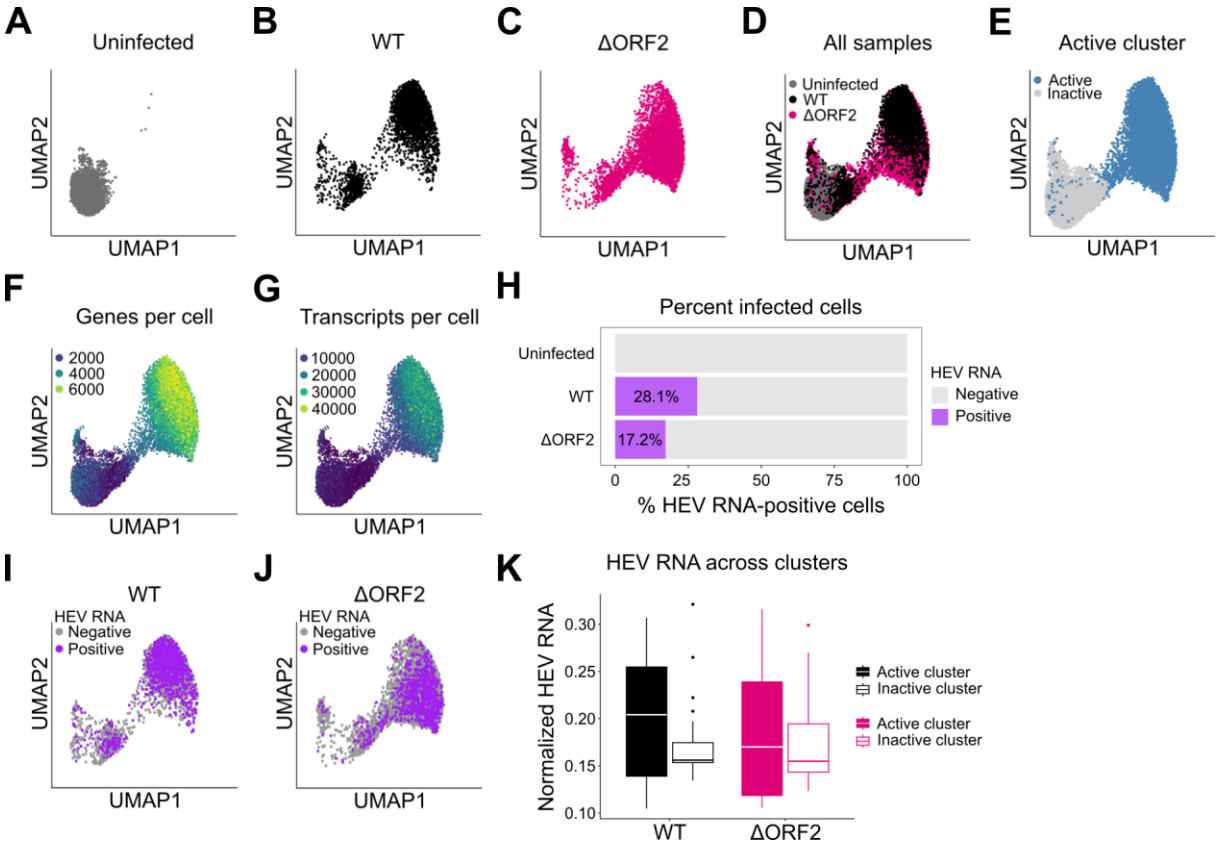

Figure 35: HEV WT- and ΔORF2-infected samples are divided into responding and non-responding clusters early in infection.
(A) UMAP projections of uninfected, (B) WT-infected, or (C) ΔORF2-infected samples at 56 h post-internalization were generated by clustering based on a list of ~400 ISGs. (D) Combined UMAP projections from A–C of uninfected (grey), WT- (black), and ΔORF2-infected samples (magenta). (E) Combined UMAP projections of uninfected, WT-, and ΔORF2-infected samples. Cells with upregulated ISG expression are highlighted in blue, termed the active cluster, while cells lacking significant upregulation of ISGs are colored in grey. (F) Combined UMAP projections of uninfected, WT-, and ΔORF2-infected samples, indicating the number of genes and (G) the number of transcripts detected per cell. (H) The percentages of infected cells, defined by detection of at least one HEV RNA copy, were determined for uninfected, WT-, and ΔORF2-infected samples. (I) UMAP projections of WT- and (J) ΔORF2-infected samples with binarized HEV RNA counts, showing actively infected cells in purple, defined by the detection of at least one HEV RNA copy per cell, and uninfected cells in grey. (K) Normalized HEV RNA counts were determined across infected cells in the active and inactive clusters of WT- and ΔORF2-infected samples. The individual panels of this figure were published in a preprint by Mehnert *et al.*[245].

Dr. Carlos Ramírez Álvarez applied the same clustering method based on the list of ~400 ISGs (Supplementary Table 1) to the uninfected and WT-infected samples harvested on day 7 post-internalization. This revealed a clear separation into two distinct subclusters (Figure 36A, B), in contrast to 56 h post-internalization, where the two subclusters were interconnected. At the earlier time point, viral replication and the antiviral response are still in the process of establishment, and the stages of infection might differ among cells, resulting in an incomplete separation of the active and inactive clusters. On day 7 post-infection, however, viral replication and the antiviral response have equilibrated, resulting in two clearly distinct populations (Figure 36A–C). One subcluster overlapped with the uninfected sample (Figure 36C), suggesting the absence of an ISG response. Importantly, most actively HEV-infected cells, characterized by at least one HEV RNA copy per cell, were clearly located within the second subcluster, defined by the upregulation of ISGs. In contrast, a minority of HEV RNA-positive cells was found within the inactive cluster (Figure 36D). This demonstrated that actively infected cells still upregulate ISG expression at later time points of infection, despite the antagonistic functions of ORF2. Furthermore, it reinforced my previous observation that a balance between viral replication and the antiviral response is established following the early replication-limiting bottleneck. Consequently, these findings clearly demonstrated that HEV replication persists in the presence of a dampened antiviral response within the same cell.

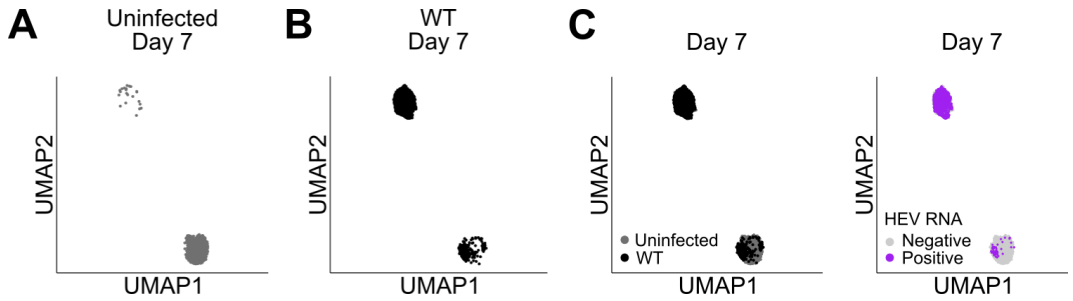

Figure 36: Actively HEV WT-infected cells still respond by ISG upregulation on day 7 post-infection.
(A) UMAP projections of uninfected and (B) WT-infected HepG2/C3A cells, harvested on day 6 + 16 h (= day 7) post-internalization for scRNA-seq analysis and clustered based on a list of ~400 ISGs. (C) Combined UMAP projections from A and B of uninfected (grey) and WT-infected samples (black). (D) UMAP projections of uninfected and WT-infected samples with binarized HEV RNA counts, showing actively infected cells in purple, defined by the detection of at least one HEV RNA copy per cell, and uninfected cells in grey. This figure was published in a preprint by Mehnert *et al.*[245].

<u>The ISG response induced by ΔORF2 infection is similar but globally enhanced compared to WT infection</u>

Following the general inspection of the scRNA-seq data, I aimed to characterize the ISGs induced upon WT and ΔORF2 infection in more detail. Furthermore, I aimed to assess the contribution of actively infected cells and uninfected bystanders to the ISG response and identify potential differences in their respectively induced ISG subsets. First, Dr. Carlos Ramírez Álvarez assessed the enrichment of an ISG signature, containing the approximately 400 ISGs (Supplementary Table 1), in the HEV RNA-positive and HEV RNA-negative cells of

WT- and ΔORF2-infected samples, as well as in the uninfected sample. As already suggested by the previous analysis (Figure 35I, J), both HEV RNA-positive and HEV RNA-negative cells showed an enhanced ISG signature upon WT and ΔORF2 infection compared to the uninfected sample (Figure 37A). Interestingly, this ISG response was globally and significantly increased in both ΔORF2-infected and uninfected cells, in comparison with the respective populations of the WT infection (Figure 37A).

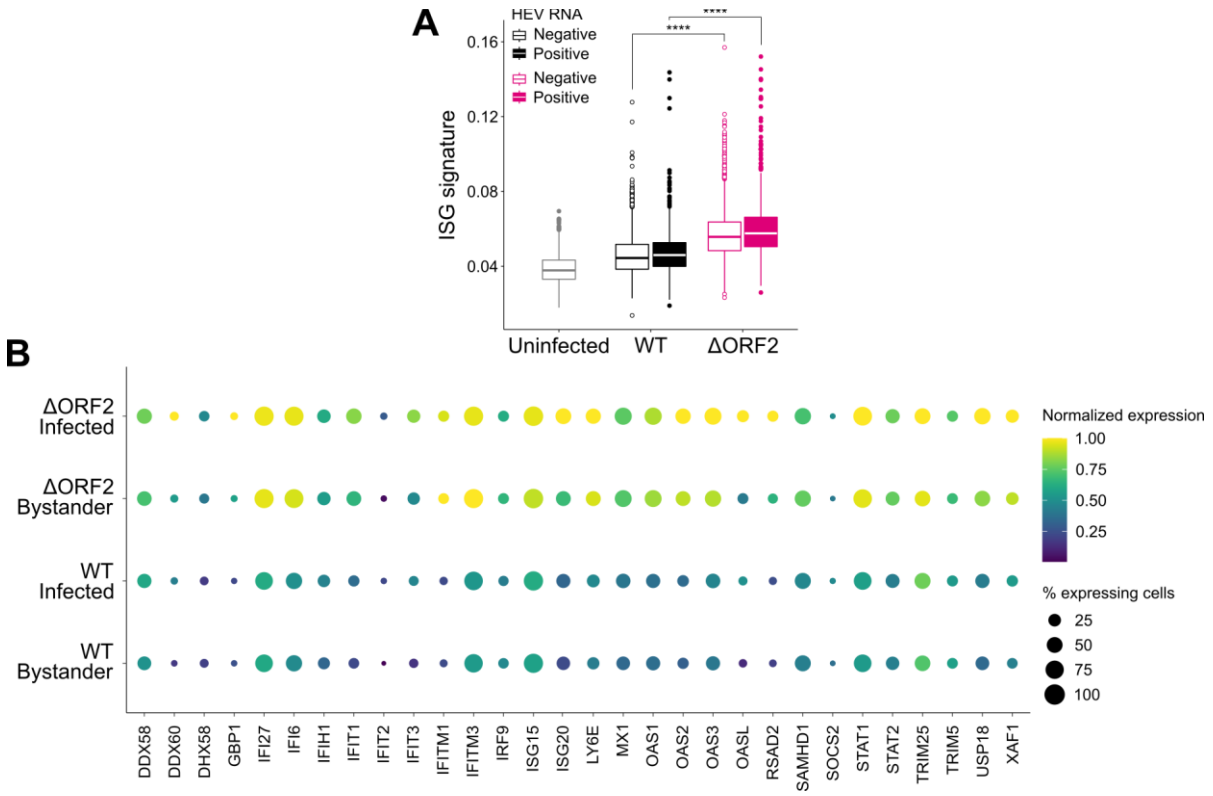

Figure 37: The ISG response induced by ΔORF2 infection is similar but globally enhanced compared to WT infection.
(A) HEV RNA-positive and HEV RNA-negative cells of WT and ΔORF2 infection as well as the uninfected sample at 56 h post-internalization were analyzed for relative expression of an ISG signature, containing approximately 400 ISGs. The area under the curve (AUC) was used to assign scores based on whether a critical subset of the ISG signature was enriched within each cell of every sample. Statistical analysis was performed using a two-sided Wilcoxon rank sum test. ****: $p < 0.0001$. (B) Normalized expression and the percentages of cells expressing 30 selected ISGs were plotted for the active clusters of WT- and ΔORF2-infected samples, split into actively infected cells and uninfected bystanders. This figure was published in a preprint by Mehnert *et al.*[245].

Next, I sought to analyze the ISG subsets induced in HEV-infected cells and bystanders of WT and ΔORF2 infection. I selected 30 common ISGs, based on their relevance in the HEV-specific antiviral response observed in different hepatocellular systems[201,202,204,210]. Dr. Carlos Ramírez Álvarez then compared the normalized expression of these ISGs across infected cells and bystanders in the active clusters of WT- and ΔORF2-infected samples. Interestingly, the percentages of cells expressing the individual ISGs were comparable between infected cells and bystanders of both WT and ΔORF2 infection (Figure 37B). This indicated the induction of a similar ISG subset across all samples. In contrast, the percentages of expressing cells varied

considerably between the different ISGs, regardless of the cell population or virus type (Figure 37B). This suggested a certain degree of underlying heterogeneity in the ISG subsets expressed and induced in individual cells of the HepG2/C3A population. The most striking differences, however, were observed in the extent of the normalized ISG expression between WT and ΔORF2. Besides the qualitatively similar response, I found that ΔORF2 infection induced a globally stronger expression of the individual ISGs in both infected cells and bystanders compared to WT infection (Figure 37B). Of note, we did not detect any type I or type III IFN in our scRNA-seq data, likely due to low transcript counts and insufficient sequencing depth. Therefore, I was unable to identify whether the actively HEV-infected cells were the sole source of IFN production.

In conclusion, the scRNA-seq analysis further substantiated that the absence of ORF2 results in a globally stronger ISG response at the replication-limiting bottleneck at around 56 h post-infection. A similar ISG subset is induced in both actively infected cells and uninfected bystanders upon infection with HEV WT and ΔORF2. Nonetheless, an underlying heterogeneity in the HepG2/C3A cells seemed to cause differences in the expression of individual ISGs across the entire cell population. IFN secretion from the infected cells, followed by paracrine and autocrine IFN signaling, is the likely cause of the ISG upregulation in uninfected bystanders and a reinforced ISG expression within the infected cells. The presence of ORF2 leads to a dampening of the ISG response across all cell populations, likely due to its interaction with TBK1, resulting in diminished IFN and ISG expression. The finding that actively HEV WT-infected cells still induce ISGs on day 7 post-infection reinforces the establishment of an equilibrium between viral replication and the antiviral response early in infection. This bottleneck is controlled by the ORF2 protein and enables persistent HEV replication in the presence of a sustained yet dampened antiviral response within the same cell.

6 Discussion

The cell-intrinsic antiviral response induced upon HEV infection of hepatocytes remains insufficiently characterized. It has been demonstrated that HEV replication persists despite sustained antiviral signaling, and various HEV proteins harbor the potential to interfere with the antiviral response. However, the contributions of these antagonisms to persistent viral replication in authentic and full-length HEV infection remain elusive. In the present study, I employed various hepatocellular culture systems and generated tools to gain a better understanding of the HEV-specific cell-intrinsic antiviral response. I performed a detailed characterization of the immune repertoire of HepG2/C3A cells and HLCs, and I attempted to identify the PRRs that sense HEV. In a comprehensive side-by-side comparison, I clarified that ORF2, rather than ORF3, interferes with antiviral and inflammatory signaling pathways. Apart from its direct interaction with TBK1, ORF2 additionally protects viral replication from the effects of the induced antiviral response. I described that the ORF2-mediated antiviral immune evasion is essential to enable a balance between viral replication and the antiviral response at a bottleneck early in infection. Collectively, the data I obtained during this PhD significantly advances our understanding of the determinants contributing to persistent HEV replication in hepatocytes.

6.1 Lessons Learned From Different Hepatocellular Systems About the HEV-Induced Cell-Intrinsic Antiviral Response

6.1.1 MDA5 and RIG-I Contribute to HEV Sensing Through Unidentified PAMPs

A comprehensive characterization of the PRRs contributing to the induction of an HEV-specific cell-intrinsic antiviral response is still lacking. Different studies have reported that knockdown of either MDA5 or RIG-I results in enhanced HEV replication in different hepatoma cell lines and in A549 cells[201,214,215]. TLR3 might also contribute to HEV recognition in hepatocytes[199], but it has primarily been studied in PBMCs, highlighting its relevance in the activation of innate immune cells, such as DCs and macrophages[220-222].

During my PhD, I attempted a comparative analysis of the separate contributions of MDA5, RIG-I, and TLR3 to the sensing of HEV RNA, using the immunodeficient Huh7.5 cell line, reconstituted with ectopic expression of individual PRRs. Theoretically, this approach should have allowed a clear identification of the PRRs that induce an HEV-specific antiviral response. Although all cell lines were responsive to stimulation with poly(I:C) (Figure 16), and I confirmed successful HEV replication through RT-qPCR and detection of ORF2 protein expression, I did not observe any ISG response upon EPO with HEV WT RNA (Figure 17). Similar to my findings, a recently published study found that Huh7.5 cells reconstituted with MDA5, RIG-I, or

TLR3 expression did not respond to HAV infection[198]. Co-expression of LGP2 and MDA5 marginally enhanced *IFIT1* expression in response to HAV, suggesting that sensing is dependent on the cooperation of these two RLRs. In contrast, I did not detect an ISG response upon HEV infection when MDA5 and LGP2 were co-expressed (Supplementary Figure 1). Overall, Huh7.5 cells appear to be unsuitable for studying the antiviral response towards HEV. One possible explanation might be the moderate replication efficiency of HEV in these cells (Figure 16), potentially resulting in a limited and non-detectable IFN and ISG induction when measured in bulk by RT-qPCR. Furthermore, Huh7.5 cells might harbor additional defects in the signaling cascades of the cell-intrinsic antiviral response pathways that are essential for an HEV-induced response.

A previous study proposed that both MDA5 and RIG-I contribute to the IFN response upon HEV infection in HepG2/C3A cells[201]. In agreement with this, I also observed a robust IFN and ISG response in this cell line (Figure 24). Furthermore, I characterized the integrity of RLR and TLR3 signaling in HepG2/C3A cells (Figure 10), which had been lacking previously. My results showed that TLR3 is expressed but non-responsive in HepG2/C3A cells. Thus, this PRR might be dispensable or only partially contributing to the HEV-induced cell-intrinsic antiviral response. Ectopic expression of TLR3 in HepG2/C3A cells might facilitate the characterization of whether this PRR can enhance the antiviral response to HEV. However, I previously experienced difficulties upon overexpression of antiviral signaling components in this cell line, resulting in the selection of subclones with a generally dampened antiviral response.

Stem cell-derived HLCs might be a promising alternative to study the PRRs contributing to HEV sensing. The integrity of the antiviral signaling pathways had not been characterized previously in R2-derived HLCs. Here, I confirmed intact TLR3 and RLR signaling in HLCs, although TLR3 protein levels were not detectable by Western blot (Figure 12). This is in agreement with a study that found low TLR3 expression but responsiveness to TLR3 stimulation in HLCs differentiated from various iPSC and hESC lines[261]. Therefore, shRNA-based knockdown of RLRs and TLR3, delivered with AAVs to HLCs[262], might shed further light on the relevance of TLR3 to the HEV-induced cell-intrinsic antiviral response in hepatocytes.

It is generally difficult to deduce the PRR that senses a virus solely by its genome structure, which likely serves as the basis for the PAMPs that are recognized by the host cell. Sensing by RIG-I or MDA5 can be mutually exclusive in many cases. For instance, IAV only activates RIG-I, whereas sensing of many members of the *Picornaviridae* family fully relies on MDA5 (reviewed in [263]). In contrast, some positive-sense RNA viruses are recognized by both RIG-I and MDA5. While MDA5 appears to be the major PRR sensing SARS-CoV-2[264,265], RIG-I still substantially contributes to the IFN response[240,266]. Moreover, several *Flaviviridae*, including

HCV, dengue virus, and West Nile virus, are sensed by both RIG-I and MDA5 (reviewed in [263]). The HEV genome is a positive-sense RNA, carrying a 5'-methylguanosine cap and a poly(A) tail, and thus resembles a cellular mRNA. Nonetheless, it triggers an IFN and ISG response. It was previously suggested that a uracil-rich region in the 3'-UTR of the HEV genome is the PAMP sensed by RIG-I[216], similar to what has been proposed for HCV[137]. However, this study was performed by transfection of RNA fragments shorter than 300 nucleotides, which are ideal RIG-I agonists. Therefore, it remains unclear whether this motif is also sensed in the full-length genomic context during HEV infection. Apart from the uracil-rich region, the negative strand of the HEV genome might be another potential PAMP. As it bears a 5'-triphosphate, it might serve as a potent RIG-I substrate. Even though the stability and half-life of the negative strand remain uncharacterized, it appears to be less abundant than the positive strand[267], thereby questioning its availability for sensing. Furthermore, the HEV PAMP sensed by MDA5 requires further investigation. Double-stranded RNA replication intermediates consisting of complementary positive- and negative-sense HEV RNA as well as RNA secondary structures might be potent PAMPs for MDA5. Collectively, future studies should focus on the identification of the HEV RNA structures and sequences recognized by the different RLRs, for example, by sequencing of the RLR-RNA interaction motif using crosslinking immunoprecipitation (CLIP)-seq. Together with the knockdown approaches in HLCs, as suggested above, this might shed further light on how HEV is recognized by the components of the cell-intrinsic antiviral response in hepatocytes.

6.1.2 Immunocompetence Appears to be Advantageous for HEV Replication in Hepatocytes

In the present study, I made use of different hepatocellular systems to study the cell-intrinsic antiviral response in the face of an HEV infection. HepG2/C3A cells and stem cell-derived HLCs are permissive for HEV despite the induction of a robust type III IFN and ISG response (Figure 24, Figure 29, and Figure 30). As demonstrated previously[201,204], HEV persistently continues to replicate in such immunocompetent systems, despite sustained antiviral signaling. In contrast, HEV only replicates moderately in Huh7.5 cells and the derived PRR-expressing cell lines. The strong impairment in the expression and functionality of their PRRs leads to a diminished upregulation of antiviral response genes upon HEV infection (Figure 16 and Supplementary Figure 1). At first sight, this seems counterintuitive, as the absence of a cell-intrinsic antiviral response should offer favorable conditions for HEV replication. However, some of the ISGs induced in infected cells are hijacked by viruses to support their replication cycle, and thus, these ISGs become proviral (reviewed in [268]). For instance, adenosine deaminases acting on RNA 1 (ADAR1) is essential for progression of the HDV replication cycle[269], and IFITM proteins enhance the entry process of SARS-CoV-2[270]. It might be possible

that HEV replication relies on such proviral ISGs and is therefore inefficient in cell culture systems where an ISG response is lacking or only moderately induced. Unbiased gain-of-function and loss-of-function screens with lentiviral libraries and by CRISPR/Cas9, respectively, might help identify antiviral and proviral ISGs, together with other host factors essential for HEV. This might shed light on the reasons for the poor permissiveness of some cell lines for HEV infection and replication.

6.2 The Multiple Roles of ORF2 in Evading the Cell-Intrinsic Antiviral Response

6.2.1 Interaction of ORF2 With TBK1 Dampens PRR-Induced Antiviral Signaling

Many different studies have suggested that individual HEV proteins or ORF1 subdomains interfere with PRR- and IFN-induced signaling pathways (reviewed in [209,252]). However, side-by-side comparisons of different HEV proteins in the same cellular system have been lacking, and the physiological relevance of the antagonisms for authentic HEV infection remains unclear. Therefore, I made use of a well-characterized A549-derived cell culture system harboring ectopic expression of individual PRRs to compare the impact of HEV ORF2 and ORF3 on the cell-intrinsic antiviral response in collaboration with the research group of Dr. Marco Binder. As the domain assignment and proteolytic processing of ORF1 remain a matter of debate (reviewed in [49]), I omitted this viral protein from my studies. Furthermore, both ORF1 and ORF3 are found at low levels in cell culture and in patients[66,233,234], suggesting that the effect of respective antagonisms on the HEV-induced antiviral response might be limited. Nonetheless, the potency of ORF1 to interfere with antiviral signaling should be studied in the future, once the processing of ORF1 has been clarified.

In the presence of ORF2 from both HEV-1 and HEV-3, we observed a reduction in *IFNB1* expression downstream of the PRRs MDA5, RIG-I, and TLR3 upon stimulation (Figure 18). This is in agreement with previous studies[68,231], but we demonstrated for the first time that signaling downstream of all relevant PRRs is affected by ORF2. The reductions in *IFNB1* mRNA were reflected by a comparable decrease in IFNβ protein secretion from the stimulated cells. Only the MDA5-expressing cells presented a roughly 3-fold stronger decrease in IFNβ protein secretion compared to the mRNA level. The kinetics of the antiviral and inflammatory signaling pathways were not affected by the presence of HEV-3 ORF2 (Figure 20).

The results obtained from ectopic expression of ORF3 were more ambiguous. Downstream of TLR3, we observed a roughly 2-fold increase in *IFNB1* expression and IFNβ protein secretion compared to the GFP control (Figure 18). A previous study found that ORF3 can enhance IFNβ promoter activity by stabilizing RIG-I through direct interaction[235]. However, we could not find a specific enhancement of *IFNB1* expression or IFNβ secretion downstream of RIG-I. On

the other hand, we observed a decrease in IFNβ protein secretion upon stimulation of MDA5 in the presence of ORF3, but the effect was not observed at the mRNA level. Furthermore, strong fluctuations in the ELISA measurements make this result questionable, which would thus require further validation. Previously, ORF3 was reported to impair JAK/STAT signaling[226] and NF-κB activation[233] in A549 cells, which we did not observe here (Figure 19). Overall, ORF3 might have a theoretical potential for antagonizing or even enhancing the cell-intrinsic antiviral response. However, EPO of HepG2/C3A cells with the ΔORF3 mutant did not reveal a direct impact on the progression of viral replication and the induction of a cell-intrinsic antiviral response (Figure 24). Thus, the minor ORF3-specific phenotypes observed in A549 cells appear to be negligible in an authentic HEV replication context.

ORF2 was previously reported to interact with TBK1 and prevent phosphorylation and nuclear translocation of IRF3[68], explaining the antagonism of PRR-induced antiviral signaling that we observed. Here, I confirmed this interaction in a similar experimental setup, using transient transfection of HEK293T cells (Figure 21). Lin *et al.* previously suggested that the ARM is the interaction motif between ORF2 and TBK1, as IRF3 phosphorylation was rescued by mutating the ARM[68]. In the present study, I demonstrated a reduced interaction between TBK1 and the ORF2-2R/2A mutant (Figure 21). However, it was published more recently that the ARM is the master regulator of the maturation and fate of the ORF2 isoforms[69]. Upon mutation of the ARM, ORF2 is preferentially secreted as ORF2g, while intracellular ORF2i levels are reduced and nuclear translocation is prevented[69]. Therefore, it is possible that the interaction between TBK1 and ORF2 is decreased simply due to the lower cytoplasmic availability of ORF2-2R/2A. In agreement with this hypothesis, I observed less ORF2-2R/2A protein in the IP input, and the protein band appeared to be more smeared compared to ORF2 WT (Figure 21C). The latter might suggest enhanced glycosylation of ORF2, which should be clarified in the future by employing PNGase F treatment to remove *N*-glycosylations. Subcellular fractionation using differential centrifugation to separate the cytosol from organelles might help identify whether the ORF2-2R/2A mutant is preferentially located in the ER/Golgi compartment, from where it would be secreted. Alternatively, IF-based co-localization studies of ORF2 with respective marker proteins for these organelles could be performed.

We attempted validation of the ARM or identification of a novel putative interaction motif between ORF2 and TBK1 using AlphaFold 2-assisted modeling in collaboration with Dr. Thibault Tubiana. However, no putative interactions between the ORF2 S, M, or P domain with the TBK1 homodimer were found. The structures of these domains were solved previously[60], and interaction of the S domain with a cellular protein has been successfully predicted by AlphaFold[70], increasing the reliability of our results. Consequently, the 129 amino acid-long

ORF2 N-terminal domain appears to be the portion of ORF2 that interacts with TBK1. AlphaFold modeling did not suggest the ARM, which is located within the ORF2 N-terminus, as the ORF2-TBK1 interaction site. Instead, we identified a putative WRD-containing interaction motif. However, the mutation to triple alanine did not result in a reduced co-IP of TBK1 with ORF2-WRD/AAA (Figure 22). Our inability to identify a putative interaction motif might have several reasons. First, the N-terminus of ORF2 is intrinsically disordered[271] and might only adopt a specific structure upon interaction with its target, which has similarly been reported for many intrinsically disordered proteins (reviewed in [272]). Consequently, the accurate prediction of interactions with such regions is challenging using AlphaFold[273,274]. Furthermore, AlphaFold models of protein-protein interactions make use of co-evolutionary signals, which are based on the assumption that interacting motifs within a protein or between two proteins mutate and evolve together over time to compensate for the loss of folding and function (reviewed in [275]). Instead of such co-evolutionary signals, the ORF2-TBK1 interaction might rather depend on physico-chemical properties (reviewed in [276]). Therefore, structural studies such as X-ray crystallography or cryo-EM appear unavoidable for identifying the interaction motif between ORF2 and TBK1. Afterwards, respective mutants of both proteins should be generated to validate the disruption of the interaction and to analyze their impact on the progression of HEV replication and the induction of a cell-intrinsic antiviral response.

It will be important to study the functional consequences and the mode of the ORF2-mediated inhibition of TBK1 in more detail. Several studies have shown that IRF3 phosphorylation and IFNβ promoter activity are impaired in the presence of HEV[68,226,228]. However, it remains unclear how exactly the interaction between ORF2 and TBK1 causes the reduced phosphorylation of IRF3. Lin *et al.* demonstrated that neither the interaction between MAVS and TBK1 nor the level of TBK1 phosphorylation were affected in the presence of ORF2[68]. This might suggest that ORF2 does not sequester or misplace TBK1, a strategy used, for example, by SFTSV. Through a direct interaction with the SFTSV non-structural protein NSs, TBK1 is relocated to viral inclusion bodies, making it inaccessible to MAVS and IRF3[175,176]. Nonetheless, co-localization studies should be performed in the future, preferably in a full-length HEV infection context, to study whether the interaction between ORF2 and TBK1 takes place at the mitochondria, the cellular sublocalization of MAVS, or whether TBK1 is relocated by ORF2. The successful recruitment of IRF3 to the MAVS-TBK1 complex but the lack of its phosphorylation observed previously[68], however, might rather speak for a failed activation of TBK1. As phosphorylation of TBK1 appeared not to be affected[68], future studies should focus on the impact of ORF2 on K63-linked ubiquitination of TBK1. The inhibition of ubiquitin ligases such as TRAF3 or, alternatively, the recruitment of deubiquitinases might indirectly explain the reduced IRF3 phosphorylation phenotype.

6.2.2 ORF2 Interferes With the NF-κB-Mediated Inflammatory Response

Upon ectopic expression in A549 cells, we observed that ORF2 also antagonizes NF-κB-mediated signaling downstream of the TNF receptor and the RLRs (Figure 19). This highlights that a shared component of the PRR- and TNF receptor-mediated inflammatory signaling cascades is likely affected by ORF2, potentially at or downstream of the IKK complex. The future identification of the interacting residues between ORF2 and TBK1, as proposed previously, might also help identify the interaction potential of ORF2 with IKKα, IKKβ, and IKKε. The canonical and non-canonical IKK kinases share 50% sequence identity each and 30% overall[149]. Furthermore, they all harbor a similar subdomain structure, increasing the likelihood that ORF2 does not exclusively interact with TBK1. Direct interaction with IKKα or IKKβ could be an additional strategy of interfering with NF-κB signaling, besides the inhibition of βTRCP, which was proposed in a past study for HEV-1 ORF2[238]. I attempted co-IP of ORF2 and IKKβ, which was, however, unsuccessful. Furthermore, Carla Siebenkotten, an MSc rotation student, established TBK1 and IKKβ truncation mutants under my direct supervision to identify the respective domain interacting with ORF2 (data not shown), which also yielded inconclusive results. Consequently, the identification of the interaction motifs of each ORF2 and TBK1 by structural studies, as suggested above, may lay the foundation for further investigations into potential interactions between ORF2 and other IKK kinases. In the present study, I did not investigate the impact of ORF2 on NF-κB-mediated signaling in the context of authentic and full-length HEV infection, as its importance in a hepatocyte monoculture is limited. However, inflammatory cytokines are essential for the communication with and recruitment of innate immune cells *in vivo* (reviewed in [111]). Therefore, future investigations should focus on the crosstalk between HEV-infected hepatocytes and, for example, pDCs and macrophages, as discussed in chapter 6.4. Such studies will need to consider the potential effects of an ORF2-mediated NF-κB antagonism on the activation of these cell types.

6.2.3 Nuclear ORF2 Might Expand the Repertoire of Immune Evasion Strategies

In a previous study, Hervouet *et al.* observed that basal expression of several inflammatory cytokines was inhibited upon HEV-3 Kernow-C1/p6 EPO in a PLC/PRF/5-derived subclone[69]. This phenotype was not observed upon mutation of the ARM when compared to mock-electroporated cells[69]. As this motif partly serves as a nuclear localization signal, the authors concluded that the nuclear ORF2 is responsible for the direct suppression of NF-κB-dependent genes[69]. However, as a mutated ARM also results in a decreased cytosolic localization of ORF2i and enhanced secretion of ORF2g[69], this phenotype cannot unambiguously be attributed to nuclear ORF2. Furthermore, a recent study demonstrated that the PLC/PRF/5-derived subclone shows a limited antiviral and inflammatory responsiveness[277], further

complicating the interpretation of the findings made by Hervouet *et al.*[69]. Overall, the functions of nuclear ORF2 in the HEV life cycle and its potential to directly modulate host gene expression remain enigmatic.

In the scRNA-seq analysis, I could not identify any striking differences between actively infected cells in WT and ΔORF2 infection regarding the up- or downregulation of individual ISGs. Such findings might have suggested a more direct impact of the ORF2 protein on gene expression. However, the fold changes observed in the scRNA-seq data were minor, even for the most significantly upregulated ISGs, which is in stark contrast to the fold changes I obtained by RT-qPCR. This may indicate technical limitations, such as insufficient sequencing depth. Consequently, subtle differences in gene expression between WT and ΔORF2 may be masked. As 10x Genomics and scRNA-seq are challenging procedures, future efforts should focus on repeating the comparison between WT and ΔORF2 infection at the replication-limiting bottleneck. Increasing the read number per cell and lowering the cellular input might help unveil a potential direct effect of ORF2 on host gene expression.

Furthermore, the potential of ORF2, in particular nuclear ORF2, to modulate the host chromatin or interfere with transcription, as demonstrated for other viruses, should be assessed in detail. The hepatitis B virus (HBV) protein HBx, for instance, was shown to upregulate DNA methyltransferases, thereby introducing epigenetic changes and affecting host gene expression[278]. Using IF, I frequently observed nuclear ORF2 staining in the nucleoli of cells electroporated with HEV WT (data not shown). The nucleolus has been reported as a target site for several RNA viruses, despite the location of their replication sites in the cytoplasm (reviewed in [279,280]). It remains to be clarified whether the nucleolar localization of ORF2 is connected with an indirect modulation of the expression of cellular genes, such as the inflammatory cytokines suggested previously[69]. Other proposed functions of viral proteins in the nucleolus include, for example, hijacking and misplacement of cellular proteins required for viral replication (reviewed in [279,280]). The application of different next generation sequencing approaches such as chromatin immunoprecipitation (ChIP)-seq and assay for transposase-accessible chromatin (ATAC)-seq might elucidate whether ORF2 directly binds to specific DNA regions or induces changes in chromatin accessibility. Furthermore, IP-mass spectrometry on the nuclear fraction of cells electroporated with HEV could facilitate the identification of nuclear or nucleolar interaction partners of ORF2.

6.2.4 ORF2 Protects Viral Replication Against the Actions of Antiviral Effectors

In order to analyze the impact of the ORF2-mediated antagonism in the full-length viral replication context, I electroporated HepG2/C3A cells with a ΔORF2 mutant. I observed a

stronger induction of type III IFN and ISG expression on day 5 post-EPO compared to HEV WT (Figure 24 and Figure 25). Concurrently, the detected levels of ΔORF2 RNA were significantly reduced. Therefore, I concluded that the increased presence of the ISGs, which are antiviral effectors that target different steps of a viral life cycle, dampened and partly eliminated ΔORF2 replication. I proposed that the increased antiviral response in the ΔORF2 mutant is an immediate consequence of the absent TBK1 inhibition and the subsequently enhanced IFN signaling. By unbiased scRNA-seq, I further substantiated that the lack of the HEV ORF2 protein causes a globally enhanced ISG response in both infected cells and uninfected bystanders (Figure 37). I could partially rescue the ΔORF2 replication by exogenous inhibition of TBK1 with the drug BX795 (Figure 25B), mimicking the ORF2-mediated antagonism. While replication of the ΔORF2 mutant was strongly enhanced (Figure 25B), depletion of the cell-intrinsic antiviral response by TBK1 inhibition did not significantly favor replication of HEV WT (Figure 25A), as suggested previously[204]. This indicated that either the ΔORF2 replication or the viral RNA itself is more vulnerable to the virus-induced cell-intrinsic antiviral response, compared to WT replication. I confirmed the increased sensitivity of ΔORF2 replication to the effects of ISGs, induced by exogenous IFN stimulation, in Huh7.5 cells (Figure 27). Without IFN treatment, these cells support a comparable level of basal WT and ΔORF2 replication due to the lack of a virus-induced antiviral response. Hence, I concluded that the HEV ORF2 protein confers resistance to IFN treatment by protecting viral replication from the actions of ISGs. Previously, Yin and colleagues demonstrated that HEV-induced IFN signaling in immunocompetent cells renders them refractory to exogenous IFN stimulation, characterized by the retention of phosphorylated STAT1 in the cytosol[201]. Here, I propose that both mechanisms, the protection of viral replication from antiviral effectors by ORF2 and the refractoriness of the JAK/STAT signaling, function in a synergistic manner.

However, it remains to be clarified how ORF2 mediates this protective function. As ORF2 is the capsid protein, shielding of RNA might occur simply by packaging newly produced HEV genomes. Even though previous studies have suggested sensing of the single-stranded HEV genome[200,211], I did not observe an antiviral response upon EPO with non-replicative GNN RNA (Figure 24C). Therefore, I excluded that sensing of unpackaged genomes contributes to the enhanced antiviral response towards ΔORF2. Instead, it seems plausible that the presence of ORF2 is required to constitute the viral replication site. Many positive-strand RNA viruses replicate in host membrane-derived organelles, which are formed with the help of viral transmembrane proteins (reviewed in [98]). However, such structures have not been reported for HEV until today, and the lack of transmembrane domains within the viral proteins argues against such replication organelles. Instead, HEV RNA and viral proteins have been found to be jointly located at structures of the endosomal network, the ERGIC, or MVBs[99-103]. Only

recently, one study proposed that ORF2i is recruited to the putative viral factories at the endocytic recycling compartment by the cellular AP-1 adaptor complex[70]. Thus, HEV ORF2 might be a central factor for gathering all viral components at the replication site. Consequently, the absence of ORF2 would render the viral RNA and the remaining proteins more accessible to an interference by ISGs. At the same time, this theory might infer an intrinsic replication defect of the ΔORF2 mutant. However, this possibility appears unlikely, as inhibition of the HEV-induced antiviral response with a TBK1 inhibitor was sufficient to rescue the ΔORF2 replication (Figure 25). Co-stainings of HEV RNA and the remaining viral proteins with the previously suggested markers of the viral replication compartment, such as Rab5, CD63, and Rab11[99-102], in ΔORF2-infected cells might provide insights into possible changes to the viral replication site in the absence of ORF2.

Alternatively, ORF2 might interfere with the ISGs that specifically target HEV replication, thereby fulfilling a more indirect shielding function. However, very little is known about the direct antiviral effects of individual ISGs on the HEV life cycle. Interestingly, a recent study has shown that, in the case of an alphavirus, only a small subset of the large number of induced ISGs potently restricts virus replication[281]. Potentially, ORF2 might specifically antagonize the expression of such a limited number of anti-HEV ISGs, for instance, by modulating host gene expression or inducing chromatin changes, as described in chapter 6.2.3. Moreover, it is equally possible that ORF2 interferes with these ISGs at the protein level, which would thus not be detectable in our scRNA-seq data. Therefore, I propose that a combination of bulk and scRNA-seq, mass spectrometry, and gain-of-function screens will be necessary to identify the ISGs that potently restrict HEV replication and might be targeted by ORF2 to shield viral replication from their antiviral effects.

Due to the fact that the HEV genome only harbors three ORFs, and because ORF1 and ORF3 are expressed at comparatively low levels[66,233,234], the ORF2 protein remains the most likely candidate to fulfill several important functions in evading the cell-intrinsic antiviral response. I validated the direct interaction of ORF2 with TBK1, I demonstrated the potency of this antagonism to dampen the antiviral response in authentic virus infection, and I identified an additional role of ORF2 in protecting viral replication from the effects of ISGs. However, many questions remain, including the mechanisms of the ORF2-mediated TBK1 inhibition, the role of nuclear ORF2, and the functional consequences of the NF-κB-targeted antagonism. Hence, future studies need to continue elucidating the manifold interference mechanisms of ORF2 with the cell-intrinsic antiviral response.

6.3 An Equilibrium Between Viral Replication and the Antiviral Response Imposed by the ORF2-Mediated Immune Evasion

6.3.1 Intracellular ORF2 Dampens the Replication-Limiting Effect of the Antiviral Response

In contrast to HEV WT, I found that the lack of the HEV ORF2 protein resulted in impaired viral replication and an enhanced antiviral response (Figure 24 and Figure 29). This is a result of the multiple roles of ORF2 in evading the cell-intrinsic antiviral response, as discussed in detail in chapter 6.2. In the present study, I used different approaches to study the impact of the ORF2-mediated immune evasion on the progression of HEV infection and replication. Besides two hepatocellular culture systems, namely HepG2/C3A cells and hESC-derived HLCs, I employed different methods of delivering HEV WT and the derived mutants. While HepG2/C3A cells were electroporated or infected, either overnight or in a synchronized manner, HLCs were infected exclusively overnight. Due to these different approaches, a direct comparison of the replication and antiviral response kinetics observed in the present study is challenging.

For example, I found lower replication of the ΔORF2 mutant from day 5 onwards upon EPO of HepG2/C3A cells, resulting from the significantly stronger induction of *IFNL1* and *ISG15* around this time point (Figure 24A–C). Consequently, a reduced amount of viral RNA was available for sensing by the PRRs, leading to a reduction in the antiviral response, induced by the ΔORF2 mutant, to the same level as WT on day 7 post-EPO. However, considering the significantly lower replication of ΔORF2 at this time point, the induced response was relatively stronger compared to WT, which was highlighted when *IFNL1* and *ISG15* expression was normalized over HEV RNA (Figure 24D, E). On the one hand, the viral RNA is the basis for sensing and inducing an antiviral response. On the other hand, viral replication is affected by the induced antiviral response, complicating the interpretation of such data and highlighting the intricate interplay between the virus and the host cell.

Infection of HepG2/C3A cells with crude, trans-complemented ΔORF2^{trans} virus particles, in turn, resulted in a decreased replication and a clearly stronger expression of *IFNL1* and *IFIT1* already from day 3 onwards (Figure 29A–C). The observed increase in HEV RNA between day 1 and day 3 post-infection by RT-qPCR (Figure 29A) and RNA-FISH (Figure 32) is in agreement with previously published data, suggesting an onset of viral replication around day 2 in this cell line[201]. The level of IFN and ISG expression in WT and ΔORF2 infection assimilated on day 7 post-infection, which was again a consequence of the reduced availability of the ΔORF2 RNA for sensing by PRRs. As EPO circumvents virus entry and delivers large amounts of viral RNA per cell, its kinetics are not comparable with authentic infection. Likely, the high RNA input delays the effects that the cell-intrinsic antiviral response exerts on viral

replication. In HLCs, the peak of the ΔORF2 antiviral response was observed on day 5 post-infection (Figure 29E, F), which is in line with the previously observed onset of viral replication around day 3 in this hepatocellular culture system[204]. Despite the discrepancies in the kinetics of viral replication and in the peak of the antiviral response in different hepatocellular systems, the general phenotype observed for the ΔORF2 mutant was comparable.

I further clarified the contribution of the different ORF2 isoforms to the observed ΔORF2 phenotype upon EPO of HepG2/C3A cells (Figure 26). I found that ORF2i was sufficient to rescue the reduced viral replication and stronger antiviral response induction of ΔORF2. This appears plausible, considering that the various functions of the ORF2-mediated immune evasion are likely performed in the cytosol of the host cell. Interestingly, expression of ORF2g in the ΔORF2i mutant was able to partially alleviate the ΔORF2 phenotype. Western blot analysis revealed a partly cytoplasmic localization of this mutant, although it remains unclear whether this portion of the protein is rather located in the ER/Golgi than in the cytosol. The intermediate rescue indeed favors a partly cytosolic retainment of ORF2g, thereby explaining the compensation of the functions of ORF2i to some extent. Until today, it remains a matter of debate whether the different ORF2 isoforms are derived from the two identified start codons[66], or whether the ARM is the driver of ORF2 processing, expressed from the first start codon[69]. Therefore, a clarification of the ORF2 isoform maturation might also shed light on processing and secretion of ORF2g and clarify its potential cytosolic retention.

As infection overnight can result in virus attachment and entry at different time points, I employed a synchronized and time-resolved infection approach to determine the time point at which the presence of the ORF2 protein becomes relevant for HEV replication. I identified that replication of both WT and ΔORF2 peaked at around 56 h post-internalization, after which the levels of WT RNA declined and then stabilized, whereas ΔORF2 continued to decrease (Figure 30B). The antiviral response peaked shortly after the 56-hour time point and decreased for both WT and ΔORF2 (Figure 30C, D). Normalization of IFN and ISG expression over the HEV RNA emphasized the stronger antiviral response induction by the ΔORF2 mutant. Collectively, these findings revealed the establishment of a balance between viral replication and the antiviral response, which was only feasible in the presence of ORF2. Thus, the various ORF2-mediated evasion strategies from the antiviral response, as detailed previously, appear to be essential for enabling continued viral replication, following the identified replication-limiting bottleneck. However, the need for normalization of the antiviral response over the respective HEV RNA levels revealed an inherent problem with the viral inoculum. While infection with crude ΔORF2^{trans} virus harvested directly from cell lysates by freeze-thawing yielded a similar WT and ΔORF2 input (Figure 29A), concentration of virus stocks by ultracentrifugation and

calculation of equal GEs for infection introduced many errors. As a consequence, the HEV RNA input differed between WT and ΔORF2 in HepG2/C3A cells and HLCs (Figure 29D and Figure 30), replication curves appeared flatter due to the higher inoculum, differences in the antiviral response were masked, and normalization over HEV RNA became necessary (Figure 30). Hence, I would recommend the use of crude cell lysates for future experiments aimed at comparing the antiviral response between viral mutants.

Nonetheless, I identified a bottleneck at which the presence of the ORF2 protein appears to be decisive for the progression of HEV infection. While viral replication and the antiviral response equilibrate in the presence of ORF2, the replication-limiting effect of the antiviral response is more significant if ORF2 is not present. In agreement with this, I only observed a minor decrease in the percentage of HEV RNA-positive cells in WT-electroporated HepG2/C3A cells between day 3 and day 5 post-EPO, whereas ΔORF2-positive cells became barely detectable (Figure 24G). Together, these findings highlight the infection-limiting potential of the HEV-induced antiviral response, which is kept at bay by ORF2 at a critical bottleneck early in infection. Collectively, I concluded that the various functions of ORF2 that mediate immune evasion are the driving forces behind the establishment of a fine balance between HEV replication and the antiviral response, enabling their coexistence.

6.3.2 Single-Cell Level Analysis Reveals an Underlying Heterogeneity in the ISG Response of Both HEV-Infected Cells and Uninfected Bystanders

At the single-cell level, I further confirmed the presence of a peak in the antiviral response around day 3 post-HEV infection using spatial RNA-FISH. At this time point, I observed *IFNL*- and *IFIT1*-RNA positive cells at the highest frequency (Figure 32). Thereafter, I was unable to detect any positive cells using this method, reinforcing a dampening of the antiviral response following the bottleneck, mediated by ORF2. This lack of RNA-FISH signal despite the clear upregulation of IFNs and ISGs, as observed in bulk by RT-qPCR and at the single-cell level by scRNA-seq, emphasizes the challenges of the RNAscope assay. Even though all established IFN and ISG probes resulted in a detectable signal in artificially poly(I:C)-stimulated cells, the intensities differed significantly and did not align with results obtained by RT-qPCR (Figure 31). As the number of binding probes can vary between the targets, the signal intensities may not be representative of the true number of mRNA transcripts found in the cell. Therefore, I assumed that I was only able to reliably detect cells with an exceptionally strong IFN/ISG response, even though the majority of cells should upregulate ISG expression, as evidenced by scRNA-seq. On the other hand, scRNA-seq analysis revealed that the percentages of HepG2/C3A cells expressing a specific ISG were frequently below 100% across infected cells and bystanders in both WT and ΔORF2 infection (Figure 37C). This suggested an underlying

heterogeneity in the basal ISG expression. *IFIT1*, for instance, which I attempted to visualize by RNA-FISH, was only detectable in less than 25% of cells in WT infection, according to the scRNA-seq data (Figure 37C). This underlying heterogeneity, which is further discussed below, thus offers another possible explanation for the low probability of detecting *IFIT1* RNA-positive cells by RNA-FISH, adding to the challenges of this assay.

Nonetheless, it would be interesting to study the fate of this potentially highly responsive cell population detected by RNA-FISH, as the antiviral response might be infection-limiting in these cells. Elimination of viral replication in these cases might thus correspond to the minor decrease in the percentages of HEV RNA-positive cells that I observed between day 3 and day 5 post-EPO for HEV WT and ΔORF3 (Figure 24G). A correlation with ORF2 protein and HEV RNA levels in this cell population might help identify a threshold necessary to efficiently dampen the antiviral response and enable the establishment of an equilibrium. This could be facilitated by an elegant live-cell imaging approach, as, for instance, employed by Bruurs *et al.*[282]. They inserted a small peptide tag into the genome of encephalomyocarditis virus (EMCV), which is recognized by a single-chain variable fragment antibody, ectopically expressed by the host cell. Together with a second strategy to visualize *IFIT1* transcripts, this enabled simultaneous live-cell imaging of the onset and strength of both viral replication and the antiviral response. If adapted to HEV, live-cell imaging between 24 h and 72 h post-synchronized infection might be able to visualize the equilibration of viral replication and the antiviral response, determine the prerequisites for weak and strong antiviral responses, and reveal the fate of the highly responsive cell fraction. Bruurs *et al.*, for example, found that a slowly progressing EMCV replication results in a stronger activation of an antiviral response, likely due to a delayed production of antagonizing viral proteins[282]. Similarly, a slow HEV replication, and thus a slow accumulation of ORF2 protein, might favor a strong antiviral response, resulting in elimination of the infection. My findings have thus laid the foundation for more in-depth investigations into the kinetics of the antiviral response in HEV infection.

By RNA-FISH analysis at 72 h post-synchronized infection, I observed a visibly stronger *ISG15* signal in both HEV RNA-positive cells and uninfected bystanders of ΔORF2 infection, compared to WT (Figure 33). I could further substantiate this globally enhanced ISG response in a more unbiased manner using scRNA-seq (Figure 37). Gene set enrichment analysis identified the antiviral response to be among the most significantly upregulated pathways, consistent with published bulk RNA-seq data of HEV-infected PHH[202]. Importantly, I identified that both HEV-infected cells and uninfected bystanders are the sources of the ISG response, not only at the replication-limiting bottleneck but also on day 7 post-infection (Figure 35 and Figure 36). Together with the synchronized, time-resolved infection (Figure 30), this

conclusively demonstrated the establishment of an equilibrium between viral replication and the antiviral response, resulting in actively HEV-replicating cells with a continued yet dampened ISG upregulation. Even though IFN transcripts were not detectable in the scRNA-seq data due to insufficient sequencing depth, the observed ISG expression in bystanders is likely induced by paracrine IFN, secreted from HEV-infected cells. Consequently, a dampening of the antiviral response within infected cells by ORF2 also results in a diminished ISG response within the bystanders. Future studies should focus on distinguishing the IFN-dependent and -independent ISG repertoires induced in HEV-infected cell populations. ISG induction in uninfected bystanders harboring an *IFNLR1* KO, which I established during the course of this PhD, might, for instance, indicate sensing of capsid-independent viral RNA, as suggested for HCV[283], or a potential impact of ORF2g/c on neighboring cells.

Most studies employing scRNA-seq have been conducted on heterogeneous patient material or organoids, for instance, for SARS-CoV-2 infections[240,284,285]. Samples that contain many different cell types are particularly informative. However, some studies have also used 10x Genomics-based scRNA-seq to analyze viral infections of monocultures. Despite the lack of multiple cell types, A549 cells, for example, displayed significant transcriptional heterogeneity in the expression of host genes in response to IAV infection[286,287]. Similarly, I also observed a certain degree of heterogeneity in the ISG response towards HEV infection in my scRNA-seq analysis, as none of the selected ISGs were upregulated in 100% of cells within the responding cluster (Figure 37C). Accordingly, different cells appeared to upregulate different subsets of ISGs. However, we could not identify separate clusters in our UMAP analysis that were characterized by expression of distinct ISG signatures (Figure 35). Hence, these differences appeared to be independent of the virus infection but were rather the result of an underlying heterogeneity within the HepG2/C3A cells. It has been widely appreciated that this heterogeneity in immune signaling and in the expression of ISGs are at least partly driven by stochasticity. Even in a seemingly homogeneous cell population, there is cell-to-cell variability in the timing, the quality, and the strength of the antiviral response, particularly the early IFN response[288-290]. Variability in the virus populations, the infection process, the genetic heterogeneity of the cell population, and differences in the cell cycle state further add to the intrinsic stochasticity of these signaling pathways (reviewed in [291]). Autocrine and paracrine signaling mediated by IRF7 and STAT proteins appear to be essential for the propagation and the reinforcement of the antiviral signaling in a larger proportion of cells[288,290]. Hence, the analysis of various time points leading up to the replication-limiting bottleneck by scRNA-seq may shed further light on the variability during the onset of the HEV-induced cell-intrinsic antiviral response. Furthermore, this might allow the identification of defined responding and non-responding cell populations, or early and late responders.

6.4 Possible Links Between ORF2-Mediated Immune Evasion, Chronicity, and Species Tropism

6.4.1 Species-Dependent Antagonisms of the Antiviral Response Might Dictate HEV Tropism

In the present study, I observed that HEV-1 ORF2 interferes with IRF3- as well and NF-κB-dependent signaling to a similar extent as HEV-3 ORF2 (Figure 18 and Figure 19), which is in agreement with past reports[224,230]. However, I did not further characterize the role of HEV-1 ORF2 for immune evasion in a full-length infection context. As a cDNA clone of the Sar55 strain has been available for many years[40] and the first cell culture-adapted HEV-1 strain was only recently established[208], it is feasible to generate an HEV-1 ΔORF2 mutant. Hence, HLCs could be transfected with Sar55 WT and ΔORF2 IVT RNA or infected with HEV-1 ΔORF2^{trans} virus particles produced with the cell-cultured adapted HEV-1 strain in S10-3/ORF2 cells. With these approaches, the importance of HEV-1 ORF2 for the progression of viral replication could be studied in more detail, similar to the experiments I performed in this study for HEV-3[68,231].

While HEV-1 and HEV-2 are restricted to humans, HEV-3 and HEV-4 have been found in different mammalian species and are transmitted to humans zoonotically (reviewed in [17,19]). The determinants of this diverse species tropism remain largely unknown. Mutations acquired within the viral genome due to the error-prone replication process likely play an important role, resulting in amino acid substitutions but also changes in the RNA secondary structure (reviewed in [292]). Furthermore, HEV-3 has been shown to tolerate insertions into its genomic sequence. This is exemplified by the Kernow-C1/p6 strain, which harbors a human-derived 174-nucleotide-long sequence in its HVR[56,57]. Experimental transfer of this insertion to a human-restricted HEV-1 strain enabled more efficient replication in non-human cell types[56,57]. It has thus been suggested that mostly ORF1, but also ORF3, might dictate the host species tropism of the different HEV genotypes (reviewed in [292]). ORF2 has so far not been considered, as one study demonstrated that chimeric HEV-1 viruses encoding the HEV-3 ORF2 protein failed to infect pigs[293]. However, the sole focus on the role of ORF2 as the viral capsid neglects the additional functions of this protein, discovered by me and others[68,69,238], in modulating host cell responses. Therefore, it will be interesting to study the potential of ORF2 from acute and chronic HEV genotypes to counteract antiviral and inflammatory signaling components from different host species. For instance, simple overexpression studies of human compared to pig- or rabbit-derived TBK1 together with HEV-3 or HEV-1 ORF2 might shed light on their respective interactions. More sophisticated porcine pluripotent stem cell-derived HLCs[294,295] could be used for transfection with full-length HEV-1 or HEV-3. Such studies might facilitate the assessment of the impact of the induced antiviral response on the corresponding viral replication and the potency of the respective ORF2-mediated antiviral immune evasion.

6.4.2 The Antiviral Response Might Influence the Crosstalk of Acute and Chronic HEV Genotypes With Innate Immune Cells

In the present study, I investigated some of the determinants that enable persistent HEV replication in cell culture. Naturally, sustained viral replication and the establishment of an equilibrium with the cell-intrinsic antiviral response in a monoculture is not representative of chronic HEV infection *in vivo*, where innate and adaptive immune responses are critical. Nonetheless, studying the mechanisms of antiviral immune evasion can lay a foundation for more complex studies and aid the interpretation of findings made in co-culture settings or animal models. Antagonizing PRR-induced antiviral and inflammatory signaling can impact the crosstalk of HEV-infected hepatocytes with professional innate immune cells. As these eventually facilitate the recruitment of adaptive immune cells, the cell-intrinsic antiviral response is one of the cornerstones leading to successful elimination of a viral pathogen such as HEV. Thus, the mechanisms involved in the development of chronicity may also be affected by the interplay of HEV ORF2 with the cell-intrinsic antiviral response in the first place. A prominent example highlighting the importance of the PRR-induced inflammatory signaling is the cytokine storm observed, for example, in severe outcomes of SARS-CoV-2 infections. Here, the dysbalanced cytokine release from airway epithelial cells is amplified by activated innate immune cells[296,297].

It was previously observed that infection of stem cell-derived HLCs with an HEV-1 clinical isolate resulted in a stronger ISG induction than infection with an HEV-3 clinical isolate[204]. Possibly, this phenotype might be related to the potential of HEV-3 to give rise to chronic infections, whereas all HEV-1 infections remain acute (reviewed in [17,19]). Moderate but prolonged IFN, ISG, and inflammatory cytokine responses induced by HEV-3 in hepatocytes might lead to a delayed or less efficient recruitment of innate immune cells. Consequently, clearance of HEV by cell-intrinsic antiviral responses and recruited macrophages, NK cells, and other innate immune cell types may be insufficient. Instead, elimination of HEV-3 infections may rely more on adaptive immune responses including CD4+ and CD8+ T cells as well as B cells and antibodies. Immunosuppressants such as tacrolimus, which has been strongly associated with chronic hepatitis E, act by a mechanism that eventually reduces T cell activation[298,299]. Consequently, clearance of HEV-3 appears to be heavily dependent on T cell responses, mostly CD8+ T cells[300]. If clearance through innate immune cells is insufficient and the adaptive responses are impaired, progression to chronicity might become more likely. Repeated antigenic exposure and persistent inflammatory signaling as a consequence of failed viral clearance can give rise to so-called exhausted CD8+ T cells, as demonstrated for HBV and HCV, but also HEV (reviewed in [209,301]). This cell population is characterized by diminished proliferative and effective capacities, reinforcing chronic HBV and HCV infections. In contrast,

the stronger initial IFN induction in HEV-1-infected hepatocytes might favor faster and more efficient recruitment of innate immune cells and clearance of the infection. This decreased dependency on adaptive responses might be one of the factors contributing to the exclusively acute outcomes of HEV-1 infections.

Until now, genotype-specific differences in the potential to recruit innate immune cells have not been studied in detail (reviewed in [209]). Furthermore, the mechanisms underlying the stronger induction of ISG responses by HEV-1 isolates compared to HEV-3 observed previously remain unclear[204]. In agreement with other investigations[68,231], I did not observe a difference in the abilities of HEV-1 and HEV-3 ORF2 to interfere with TBK1-mediated antiviral signaling as well as inflammatory signaling (Figure 18 and Figure 19). Thus, the ORF2-mediated antiviral immune evasion through a direct antagonism is by itself not sufficient to explain the discrepancies in the induced antiviral response between genotypes. However, differences in the abilities of HEV-1 and HEV-3 ORF2 to shield viral replication from antiviral effectors and directly modulate gene expression should be studied in the future. Moreover, the progression of the antiviral response and its direct effects on HEV-1 replication need to be investigated over a longer time period, as this was only done until day 7 post-infection in a previous study[204].

Future investigations should further focus on the crosstalk of HEV-1- and HEV-3-infected hepatocytes with innate immune cells, such as macrophages, NK cells, and others. Only recently, contact-dependent activation of pDCs by HEV-infected hepatoma cells was reported[277]. The potential of the different HEV genotypes to activate these innate immune cells, the breadth of the induced type I IFN secretion from the innate immune cells, and the sensitivity of the infected hepatocytes to the secreted type I IFN should be studied in detail. This could be achieved by co-culture systems of, for instance, HLCs with patient- or stem cell-derived innate immune cell types. Co-cultures of stem cell-derived liver parenchymal and non-parenchymal cells have already been successfully established[302,303], and differentiation into several innate immune cell types is feasible[304,305]. The simultaneous use of pluripotent stem cells as the source for HLCs and innate immune cells offers the clear advantages of isogenicity and genetic amenability. For example, my previously established *IFNLR1* KO hESC line, together with an *IFNAR1/2* KO, will prove useful in deciphering the respective impacts of type I and type III IFN signaling on HEV replication and immune cell activation in different co-culture settings. Furthermore, the role of the ORF2-mediated immune evasion for different HEV genotypes and its impact on the crosstalk with innate immune cells should be investigated further. Altogether, these findings will help elucidate the determinants of acute and chronic HEV infections, for which the results of my dissertation lay an important foundation.

7 Working Model and Conclusion

In this study, I demonstrated that the HEV capsid protein ORF2 fulfills different functions in limiting the virus-induced cell-intrinsic antiviral response in hepatocytes (Figure 38). On the one hand, ORF2 directly interacts with TBK1, thereby antagonizing IRF3-dependent IFN and ISG induction. On the other hand, ORF2 protects the viral replication from the actions of the induced antiviral effectors. These functions become decisive at a replication-limiting bottleneck imposed by the rising antiviral response early in infection. As a collective consequence of the ORF2-mediated immune evasion strategies, the antiviral response is directly dampened at this bottleneck, and viral replication is protected from the effects of the antiviral response. The reduced IFN secretion further diminishes the autocrine and paracrine reinforcement of the ISG response in infected cells and uninfected bystanders. Following this bottleneck, an equilibrium between viral replication and the antiviral response is established, enabling persistent HEV replication in the presence of sustained but dampened cell-intrinsic antiviral signaling. Lack or insufficient expression of ORF2 can in turn result in the restriction, and potentially elimination, of viral replication through the antiviral response. Altogether, the results obtained during my PhD contribute to clarifying the multifaceted role of ORF2 in the HEV life cycle and to uncovering some of the driving forces in persistent HEV infection.

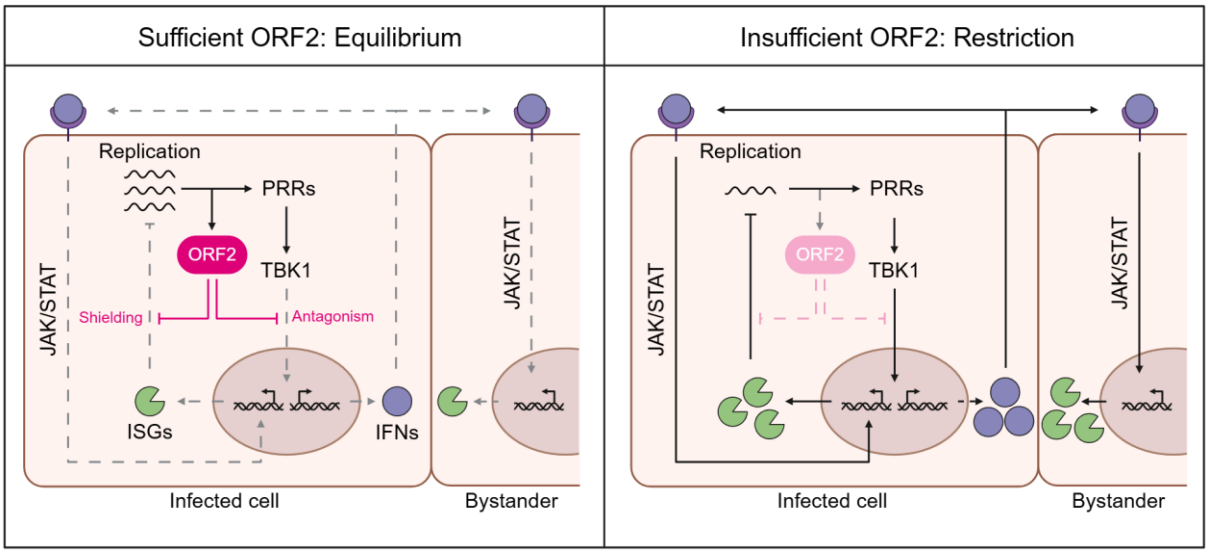

Figure 38: Working model on the role of ORF2-mediated antiviral immune evasion in persistent hepatocyte infection.
If early replication results in sufficient production of ORF2, the ORF2-mediated immune evasion strategies, which include direct counteraction of TBK1 and shielding of viral replication from ISGs, dampen the IFN and ISG responses in infected cells and bystanders. Consequently, an equilibrium between viral replication and the antiviral response is established, and HEV replication can persist. If ORF2 is absent, or insufficient ORF2 is produced early in infection, the lack of the ORF2-mediated immune evasion leads to a strong IFN and ISG response in infected cells and uninfected bystanders. Hence, viral replication is dampened, and infection is restricted. A modification of this figure was published in a preprint by Mehnert *et al.*[245]. (Created with BioRender.com)

Nonetheless, many open questions remain, and future studies need to elucidate the precise molecular mechanisms underlying the TBK1 counteraction and the protection of viral replication. Furthermore, the functions of the ORF2 isoform found in the nucleus and its suggested impact on host gene modulation should be clarified, which might further expand the repertoire of ORF2-mediated antiviral immune evasion strategies. Moreover, the impact of intergenotypic differences in the antiviral response and of the ORF2-mediated immune evasion on the crosstalk with innate immune cells requires further investigation.

The discoveries I made during my PhD significantly contribute to the understanding of HEV persistence. Thus, they lay an important foundation for future studies, aimed at advancing our insights into the determinants of acute and chronic manifestations of HEV infection. Eventually, such studies will aid the identification of novel therapeutic options for the treatment of hepatitis E.

Bibliography

1 Khuroo, M. S. Study of an epidemic of non-A, non-B hepatitis. Possibility of another human hepatitis virus distinct from post-transfusion non-A, non-B type. *The American journal of medicine* **68**, 818-824, doi:10.1016/0002-9343(80)90200-4 (1980).

2 Balayan, M. S., Andjaparidze, A. G., Savinskaya, S. S., Ketiladze, E. S., Braginsky, D. M., Savinov, A. P. & Poleschuk, V. F. Evidence for a virus in non-A, non-B hepatitis transmitted via the fecal-oral route. *Intervirology* **20**, 23-31, doi:10.1159/000149370 (1983).

3 Meng, X. J., Purcell, R. H., Halbur, P. G., Lehman, J. R., Webb, D. M., Tsareva, T. S., Haynes, J. S., Thacker, B. J. & Emerson, S. U. A novel virus in swine is closely related to the human hepatitis E virus. *Proc Natl Acad Sci U S A* **94**, 9860-9865, doi:10.1073/pnas.94.18.9860 (1997).

4 Thomas, D. L., Yarbough, P. O., Vlahov, D., Tsarev, S. A., Nelson, K. E., Saah, A. J. & Purcell, R. H. Seroreactivity to hepatitis E virus in areas where the disease is not endemic. **35**, 1244-1247, doi:doi:10.1128/jcm.35.5.1244-1247.1997 (1997).

5 Schlauder, G. G., Desai, S. M., Zanetti, A. R., Tassopoulos, N. C. & Mushahwar, I. K. Novel hepatitis E virus (HEV) isolates from Europe: evidence for additional genotypes of HEV. *J Med Virol* **57**, 243-251, doi:10.1002/(sici)1096-9071(199903)57:3<243::aid-jmv6>3.0.co;2-r (1999).

6 Kupferschmidt, K. Europe's new hepatitis problem. *Science* **353**, 862-863, doi:10.1126/science.353.6302.862 (2016).

7 Rein, D. B., Stevens, G. A., Theaker, J., Wittenborn, J. S. & Wiersma, S. T. The global burden of hepatitis E virus genotypes 1 and 2 in 2005. *Hepatology* **55**, 988-997, doi:10.1002/hep.25505 (2012).

8 World Health Organization. *Hepatitis E fact sheet*. https://www.who.int/news-room/fact-sheets/detail/hepatitis-e (2023) Accessed 13 March 2025.

9 Li, P., Liu, J., Li, Y., Su, J., Ma, Z., Bramer, W. M., Cao, W., de Man, R. A., Peppelenbosch, M. P. & Pan, Q. The global epidemiology of hepatitis E virus infection: A systematic review and meta-analysis. *Liver Int* **40**, 1516-1528, doi:10.1111/liv.14468 (2020).

10 Yazbek, S., Kreidieh, K. & Ramia, S. Hepatitis E virus in the countries of the Middle East and North Africa region: an awareness of an infectious threat to blood safety. *Infection* **44**, 11-22, doi:10.1007/s15010-015-0807-5 (2016).

11 Kmush, B., Wierzba, T., Krain, L., Nelson, K. & Labrique, A. B. Epidemiology of hepatitis E in low- and middle-income countries of Asia and Africa. *Seminars in liver disease* **33**, 15-29, doi:10.1055/s-0033-1338111 (2013).

12 Purdy, M. A., Drexler, J. F., Meng, X. J., Norder, H., Okamoto, H., Van der Poel, W. H. M., Reuter, G., de Souza, W. M., Ulrich, R. G. & Smith, D. B. ICTV Virus Taxonomy Profile: Hepeviridae 2022. *J Gen Virol* **103**, doi:10.1099/jgv.0.001778 (2022).

13 Lee, G. H., Tan, B. H., Teo, E. C., Lim, S. G., Dan, Y. Y., Wee, A., Aw, P. P., Zhu, Y., Hibberd, M. L., Tan, C. K., Purdy, M. A. & Teo, C. G. Chronic Infection With Camelid Hepatitis E Virus in a Liver Transplant Recipient Who Regularly Consumes Camel Meat and Milk. *Gastroenterology* **150**, 355-357.e353, doi:10.1053/j.gastro.2015.10.048 (2016).

14 Sridhar, S., Yip, C. C. Y., Wu, S., Cai, J., Zhang, A. J., Leung, K. H., Chung, T. W. H., Chan, J. F. W., Chan, W. M., Teng, J. L. L., Au-Yeung, R. K. H., Cheng, V. C. C., Chen, H., Lau, S. K. P., Woo, P. C. Y., Xia, N. S., Lo, C. M. & Yuen, K. Y. Rat Hepatitis E Virus as Cause of Persistent Hepatitis after Liver Transplant. *Emerging infectious diseases* **24**, 2241-2250, doi:10.3201/eid2412.180937 (2018).

15 Andonov, A., Robbins, M., Borlang, J., Cao, J., Hatchette, T., Stueck, A., Deschambault, Y., Murnaghan, K., Varga, J. & Johnston, L. Rat Hepatitis E Virus Linked to Severe Acute Hepatitis in an Immunocompetent Patient. *J Infect Dis* **220**, 951-955, doi:10.1093/infdis/jiz025 (2019).

16 Rivero-Juarez, A., Frias, M., Perez, A. B., Pineda, J. A., Reina, G., Fuentes-Lopez, A., Freyre-Carrillo, C., Ramirez-Arellano, E., Alados, J. C. & Rivero, A. Orthohepevirus C infection as an emerging cause of acute hepatitis in Spain: First report in Europe. *J Hepatol* **77**, 326-331, doi:10.1016/j.jhep.2022.01.028 (2022).

17 Nelson, K. E., Labrique, A. B. & Kmush, B. L. Epidemiology of Genotype 1 and 2 Hepatitis E Virus Infections. *Cold Spring Harb Perspect Med* **9**, doi:10.1101/cshperspect.a031732 (2019).

18 Hakim, M. S., Wang, W., Bramer, W. M., Geng, J., Huang, F., de Man, R. A., Peppelenbosch, M. P. & Pan, Q. The global burden of hepatitis E outbreaks: a systematic review. *Liver Int* **37**, 19-31, doi:10.1111/liv.13237 (2017).

19 Dalton, H. R. & Izopet, J. Transmission and Epidemiology of Hepatitis E Virus Genotype 3 and 4 Infections. *Cold Spring Harb Perspect Med* **8**, doi:10.1101/cshperspect.a032144 (2018).

20 Li, P., Ji, Y., Li, Y., Ma, Z. & Pan, Q. Estimating the global prevalence of hepatitis E virus in swine and pork products. *One health (Amsterdam, Netherlands)* **14**, 100362, doi:10.1016/j.onehlt.2021.100362 (2022).

21 Pallerla, S. R., Schembecker, S., Meyer, C. G., Linh, L. T. K., Johne, R., Wedemeyer, H., Bock, C. T., Kremsner, P. G. & Velavan, T. P. Hepatitis E virus genome detection in commercial pork livers and pork meat products in Germany. *J Viral Hepat* **28**, 196-204, doi:10.1111/jvh.13396 (2021).

22 Mrzljak, A., Balen, I., Barbic, L., Ilic, M. & Vilibic-Cavlek, T. Hepatitis E virus in professionally exposed: A reason for concern? *World journal of hepatology* **13**, 723-730, doi:10.4254/wjh.v13.i7.723 (2021).

23 Doceul, V., Bagdassarian, E., Demange, A. & Pavio, N. Zoonotic Hepatitis E Virus: Classification, Animal Reservoirs and Transmission Routes. *Viruses* **8**, doi:10.3390/v8100270 (2016).

24 Cheung, C. K. M., Wong, S. H., Law, A. W. H. & Law, M. F. Transfusion-transmitted hepatitis E: What we know so far? *World J Gastroenterol* **28**, 47-75, doi:10.3748/wjg.v28.i1.47 (2022).

25 Cordes, A. K., Goudeva, L., Lütgehetmann, M., Wenzel, J. J., Behrendt, P., Wedemeyer, H. & Heim, A. Risk of transfusion-transmitted hepatitis E virus infection from pool-tested platelets and plasma. *J Hepatol* **76**, 46-52, doi:10.1016/j.jhep.2021.08.018 (2022).

26 Nimgaonkar, I., Ding, Q., Schwartz, R. E. & Ploss, A. Hepatitis E virus: advances and challenges. *Nat Rev Gastroenterol Hepatol* **15**, 96-110, doi:10.1038/nrgastro.2017.150 (2018).

27 Perez-Gracia, M. T., Suay-Garcia, B. & Mateos-Lindemann, M. L. Hepatitis E and pregnancy: current state. *Rev Med Virol* **27**, e1929, doi:10.1002/rmv.1929 (2017).

28 EASL Clinical Practice Guidelines on hepatitis E virus infection. *J Hepatol* **68**, 1256-1271, doi:10.1016/j.jhep.2018.03.005 (2018).

29 Debing, Y., Gisa, A., Dallmeier, K., Pischke, S., Bremer, B., Manns, M., Wedemeyer, H., Suneetha, P. V. & Neyts, J. A mutation in the hepatitis E virus RNA polymerase promotes its replication and associates with ribavirin treatment failure in organ transplant recipients. *Gastroenterology* **147**, 1008-1011.e1007; quiz e1015-1006, doi:10.1053/j.gastro.2014.08.040 (2014).

30 Debing, Y., Ramière, C., Dallmeier, K., Piorkowski, G., Trabaud, M. A., Lebossé, F., Scholtès, C., Roche, M., Legras-Lachuer, C., de Lamballerie, X., André, P. & Neyts, J. Hepatitis E virus mutations associated with ribavirin treatment failure result in altered viral fitness and ribavirin sensitivity. *J Hepatol* **65**, 499-508, doi:10.1016/j.jhep.2016.05.002 (2016).

31 Todt, D., Gisa, A., Radonic, A., Nitsche, A., Behrendt, P., Suneetha, P. V., Pischke, S., Bremer, B., Brown, R. J., Manns, M. P., Cornberg, M., Bock, C. T., Steinmann, E. & Wedemeyer, H. In vivo evidence for ribavirin-induced mutagenesis of the hepatitis E virus genome. *Gut* **65**, 1733-1743, doi:10.1136/gutjnl-2015-311000 (2016).

32 Peron, J. M., Larrue, H., Izopet, J. & Buti, M. The pressing need for a global HEV vaccine. *J Hepatol* **79**, 876-880, doi:10.1016/j.jhep.2023.03.024 (2023).

33 Pischke, S., Hartl, J., Pas, S. D., Lohse, A. W., Jacobs, B. C. & Van der Eijk, A. A. Hepatitis E virus: Infection beyond the liver? *J Hepatol* **66**, 1082-1095, doi:10.1016/j.jhep.2016.11.016 (2017).

34 Zhou, X., Huang, F., Xu, L., Lin, Z., de Vrij, F. M. S., Ayo-Martin, A. C., van der Kroeg, M., Zhao, M., Yin, Y., Wang, W., Cao, W., Wang, Y., Kushner, S. A., Marie Peron, J., Alric, L., de Man, R. A., Jacobs, B. C., van Eijk, J. J., Aronica, E. M. A., Sprengers, D., Metselaar, H. J., de Zeeuw, C. I., Dalton, H. R., Kamar, N., Peppelenbosch, M. P. & Pan, Q. Hepatitis E Virus Infects Neurons and Brains. *J Infect Dis* **215**, 1197-1206, doi:10.1093/infdis/jix079 (2017).

35 Knegendorf, L., Drave, S. A., Dao Thi, V. L., Debing, Y., Brown, R. J. P., Vondran, F. W. R., Resner, K., Friesland, M., Khera, T., Engelmann, M., Bremer, B., Wedemeyer, H., Behrendt, P., Neyts, J., Pietschmann, T., Todt, D. & Steinmann, E. Hepatitis E virus replication and interferon responses in human placental cells. *Hepatol Commun* **2**, 173-187, doi:10.1002/hep4.1138 (2018).

36 Jagst, M., Gömer, A., Augustyniak, S., Klöhn, M., Rehm, A., Ulrich, R. G., Bader, V., Winklhofer, K. F., Brüggemann, Y., Gold, R., Gisevius, B., Todt, D. & Steinmann, E. Modeling extrahepatic hepatitis E virus infection in induced human primary neurons. *Proc Natl Acad Sci U S A* **121**, e2411434121, doi:10.1073/pnas.2411434121 (2024).

37 Leblond, A. L., Helmchen, B., Ankavay, M., Lenggenhager, D., Jetzer, J., Helmchen, F., Yurtsever, H., Parrotta, R., Healy, M. E., Pöschel, A., Markkanen, E., Semmo, N., Ferrié, M., Cocquerel, L., Seeger, H., Hopfer, H., Müllhaupt, B., Gouttenoire, J., Moradpour, D., Gaspert, A. & Weber, A. HEV ORF2 protein-antibody complex deposits are associated with glomerulonephritis in hepatitis E with reduced immune status. *Nat Commun* **15**, 8849, doi:10.1038/s41467-024-53072-0 (2024).

38 Wang, B. & Meng, X. J. Structural and molecular biology of hepatitis E virus. *Computational and structural biotechnology journal* **19**, 1907-1916, doi:10.1016/j.csbj.2021.03.038 (2021).

39 Nair, V. P., Anang, S., Subramani, C., Madhvi, A., Bakshi, K., Srivastava, A., Shalimar, Nayak, B., Ranjith Kumar, C. T. & Surjit, M. Endoplasmic Reticulum Stress Induced Synthesis of a Novel Viral Factor Mediates Efficient Replication of Genotype-1 Hepatitis E Virus. *PLoS Pathog* **12**, e1005521, doi:10.1371/journal.ppat.1005521 (2016).

40 Emerson, S. U., Zhang, M., Meng, X. J., Nguyen, H., St Claire, M., Govindarajan, S., Huang, Y. K. & Purcell, R. H. Recombinant hepatitis E virus genomes infectious for primates: importance of capping and discovery of a cis-reactive element. *Proc Natl Acad Sci U S A* **98**, 15270-15275, doi:10.1073/pnas.251555098 (2001).

41 Graff, J., Nguyen, H., Yu, C., Elkins, W. R., St Claire, M., Purcell, R. H. & Emerson, S. U. The open reading frame 3 gene of hepatitis E virus contains a cis-reactive element and encodes a protein required for infection of macaques. *J Virol* **79**, 6680-6689, doi:10.1128/jvi.79.11.6680-6689.2005 (2005).

42 Ju, X., Xiang, G., Gong, M., Yang, R., Qin, J., Li, Y., Nan, Y., Yang, Y., Zhang, Q. C. & Ding, Q. Identification of functional cis-acting RNA elements in the hepatitis E virus genome required for viral replication. *PLoS Pathog* **16**, e1008488, doi:10.1371/journal.ppat.1008488 (2020).

43 Cao, D., Huang, Y. W. & Meng, X. J. The nucleotides on the stem-loop RNA structure in the junction region of the hepatitis E virus genome are critical for virus replication. *J Virol* **84**, 13040-13044, doi:10.1128/jvi.01475-10 (2010).

44 Ding, Q., Nimgaonkar, I., Archer, N. F., Bram, Y., Heller, B., Schwartz, R. E. & Ploss, A. Identification of the Intragenomic Promoter Controlling Hepatitis E Virus Subgenomic RNA Transcription. *mBio* **9**, doi:10.1128/mBio.00769-18 (2018).

45 Graff, J., Torian, U., Nguyen, H. & Emerson, S. U. A bicistronic subgenomic mRNA encodes both the ORF2 and ORF3 proteins of hepatitis E virus. *J Virol* **80**, 5919-5926, doi:10.1128/jvi.00046-06 (2006).

46 Koonin, E. V., Gorbalenya, A. E., Purdy, M. A., Rozanov, M. N., Reyes, G. R. & Bradley, D. W. Computer-assisted assignment of functional domains in the nonstructural polyprotein of hepatitis E virus: delineation of an additional group of positive-strand RNA plant and animal viruses. *Proc Natl Acad Sci U S A* **89**, 8259-8263, doi:10.1073/pnas.89.17.8259 (1992).

47 Magden, J., Takeda, N., Li, T., Auvinen, P., Ahola, T., Miyamura, T., Merits, A. & Kääriäinen, L. Virus-specific mRNA capping enzyme encoded by hepatitis E virus. *J Virol* **75**, 6249-6255, doi:10.1128/jvi.75.14.6249-6255.2001 (2001).

48 Ahola, T. & Karlin, D. G. Sequence analysis reveals a conserved extension in the capping enzyme of the alphavirus supergroup, and a homologous domain in nodaviruses. *Biology direct* **10**, 16, doi:10.1186/s13062-015-0050-0 (2015).

49 Karpe, Y. A. Processing of the Hepatitis E virus ORF1 nonstructural polyprotein. *Frontiers in Virology* **3**, doi:10.3389/fviro.2023.1327745 (2024).

50 Zhang, F., Xu, L. D., Wu, S., Wang, B., Xu, P. & Huang, Y. W. Deciphering the hepatitis E virus ORF1: Functional domains, protein processing, and patient-derived mutations. *Virology* **603**, 110350, doi:10.1016/j.virol.2024.110350 (2025).

51 Wang, B., Subramaniam, S., Tian, D., Mahsoub, H. M., Heffron, C. L. & Meng, X. J. Phosphorylation of Ser711 residue in the hypervariable region of zoonotic genotype 3 hepatitis E virus is important for virus replication. *mBio* **15**, e0263524, doi:10.1128/mbio.02635-24 (2024).

52 Agrawal, S., Gupta, D. & Panda, S. K. The 3' end of hepatitis E virus (HEV) genome binds specifically to the viral RNA-dependent RNA polymerase (RdRp). *Virology* **282**, 87-101, doi:10.1006/viro.2000.0819 (2001).

53 Wang, X. & Gillam, S. Mutations in the GDD motif of rubella virus putative RNA-dependent RNA polymerase affect virus replication. *Virology* **285**, 322-331, doi:10.1006/viro.2001.0939 (2001).

54 Fieulaine, S., Tubiana, T. & Bressanelli, S. De novo modelling of HEV replication polyprotein: Five-domain breakdown and involvement of flexibility in functional regulation. *Virology* **578**, 128-140, doi:10.1016/j.virol.2022.12.002 (2023).

55 Goulet, A., Cambillau, C., Roussel, A. & Imbert, I. Structure Prediction and Analysis of Hepatitis E Virus Non-Structural Proteins from the Replication and Transcription Machinery by AlphaFold2. *Viruses* **14**, doi:10.3390/v14071537 (2022).

56 Shukla, P., Nguyen, H. T., Torian, U., Engle, R. E., Faulk, K., Dalton, H. R., Bendall, R. P., Keane, F. E., Purcell, R. H. & Emerson, S. U. Cross-species infections of cultured cells by hepatitis E virus and discovery of an infectious virus-host recombinant. *Proc Natl Acad Sci U S A* **108**, 2438-2443, doi:10.1073/pnas.1018878108 (2011).

57 Shukla, P., Nguyen, H. T., Faulk, K., Mather, K., Torian, U., Engle, R. E. & Emerson, S. U. Adaptation of a genotype 3 hepatitis E virus to efficient growth in cell culture depends on an inserted human gene segment acquired by recombination. *J Virol* **86**, 5697-5707, doi:10.1128/JVI.00146-12 (2012).

58 Cancela, F., Noceti, O., Arbiza, J. & Mirazo, S. Structural aspects of hepatitis E virus. *Archives of Virology* **167**, 2457-2481, doi:10.1007/s00705-022-05575-8 (2022).

59 Xing, L., Kato, K., Li, T., Takeda, N., Miyamura, T., Hammar, L. & Cheng, R. H. Recombinant hepatitis E capsid protein self-assembles into a dual-domain T = 1 particle presenting native virus epitopes. *Virology* **265**, 35-45, doi:10.1006/viro.1999.0005 (1999).

60 Guu, T. S., Liu, Z., Ye, Q., Mata, D. A., Li, K., Yin, C., Zhang, J. & Tao, Y. J. Structure of the hepatitis E virus-like particle suggests mechanisms for virus assembly and receptor binding. *Proc Natl Acad Sci U S A* **106**, 12992-12997, doi:10.1073/pnas.0904848106 (2009).

61 Surjit, M., Jameel, S. & Lal, S. K. The ORF2 protein of hepatitis E virus binds the 5' region of viral RNA. *J Virol* **78**, 320-328, doi:10.1128/jvi.78.1.320-328.2004 (2004).

62 Xing, L., Li, T. C., Mayazaki, N., Simon, M. N., Wall, J. S., Moore, M., Wang, C. Y., Takeda, N., Wakita, T., Miyamura, T. & Cheng, R. H. Structure of hepatitis E virion-sized particle reveals an RNA-dependent viral assembly pathway. *J Biol Chem* **285**, 33175-33183, doi:10.1074/jbc.M110.106336 (2010).

63 Nishiyama, T., Umezawa, K., Yamada, K., Takahashi, M., Kunita, S., Mulyanto, Kii, I. & Okamoto, H. The Capsid (ORF2) Protein of Hepatitis E Virus in Feces Is C-Terminally Truncated. *Pathogens* **11**, doi:10.3390/pathogens11010024 (2021).

64 Ankavay, M., Montpellier, C., Sayed, I. M., Saliou, J. M., Wychowski, C., Saas, L., Duvet, S., Aliouat-Denis, C. M., Farhat, R., de Masson d'Autume, V., Meuleman, P., Dubuisson, J. & Cocquerel, L. New insights into the ORF2 capsid protein, a key player of the hepatitis E virus lifecycle. *Sci Rep* **9**, 6243, doi:10.1038/s41598-019-42737-2 (2019).

65 Jameel, S., Zafrullah, M., Ozdener, M. H. & Panda, S. K. Expression in animal cells and characterization of the hepatitis E virus structural proteins. *J Virol* **70**, 207-216, doi:10.1128/jvi.70.1.207-216.1996 (1996).

66 Yin, X., Ying, D., Lhomme, S., Tang, Z., Walker, C. M., Xia, N., Zheng, Z. & Feng, Z. Origin, antigenicity, and function of a secreted form of ORF2 in hepatitis E virus infection. *Proc Natl Acad Sci U S A* **115**, 4773-4778, doi:10.1073/pnas.1721345115 (2018).

67 Montpellier, C., Wychowski, C., Sayed, I. M., Meunier, J. C., Saliou, J. M., Ankavay, M., Bull, A., Pillez, A., Abravanel, F., Helle, F., Brochot, E., Drobecq, H., Farhat, R., Aliouat-Denis, C. M., Haddad, J. G., Izopet, J., Meuleman, P., Goffard, A., Dubuisson, J. & Cocquerel, L. Hepatitis E Virus Lifecycle and Identification of 3 Forms of the ORF2 Capsid Protein. *Gastroenterology* **154**, 211-223 e218, doi:10.1053/j.gastro.2017.09.020 (2018).

68 Lin, S., Yang, Y., Nan, Y., Ma, Z., Yang, L. & Zhang, Y. J. The Capsid Protein of Hepatitis E Virus Inhibits Interferon Induction via Its N-terminal Arginine-Rich Motif. *Viruses* **11**, doi:10.3390/v11111050 (2019).

69 Hervouet, K., Ferrie, M., Ankavay, M., Montpellier, C., Camuzet, C., Alexandre, V., Dembele, A., Lecoeur, C., Foe, A. T., Bouquet, P., Hot, D., Vausselin, T., Saliou, J. M., Salome-Desnoulez, S., Vandeputte, A., Marsollier, L., Brodin, P., Dreux, M., Rouille, Y., Dubuisson, J., Aliouat-Denis, C. M. & Cocquerel, L. An Arginine-Rich Motif in the ORF2 capsid protein regulates the hepatitis E virus lifecycle and interactions with the host cell. *PLoS Pathog* **18**, e1010798, doi:10.1371/journal.ppat.1010798 (2022).

70 Ferrié, M., Alexandre, V., Montpellier, C., Bouquet, P., Tubiana, T., Mézière, L., Ankavay, M., Bentaleb, C., Dubuisson, J., Bressanelli, S., Aliouat-Denis, C. M., Rouillé, Y. & Cocquerel, L. The AP-1 adaptor complex is essential for intracellular trafficking of the ORF2 capsid protein and assembly of Hepatitis E virus. *Cell Mol Life Sci* **81**, 335, doi:10.1007/s00018-024-05367-0 (2024).

71 Zafrullah, M., Ozdener, M. H., Panda, S. K. & Jameel, S. The ORF3 protein of hepatitis E virus is a phosphoprotein that associates with the cytoskeleton. *J Virol* **71**, 9045-9053, doi:10.1128/jvi.71.12.9045-9053.1997 (1997).

72 Gouttenoire, J., Pollán, A., Abrami, L., Oechslin, N., Mauron, J., Matter, M., Oppliger, J., Szkolnicka, D., Dao Thi, V. L., van der Goot, F. G. & Moradpour, D. Palmitoylation mediates membrane association of hepatitis E virus ORF3 protein and is required for infectious particle secretion. *PLoS Pathog* **14**, e1007471, doi:10.1371/journal.ppat.1007471 (2018).

73 Yamada, K., Takahashi, M., Hoshino, Y., Takahashi, H., Ichiyama, K., Nagashima, S., Tanaka, T. & Okamoto, H. ORF3 protein of hepatitis E virus is essential for virion release from infected cells. *J Gen Virol* **90**, 1880-1891, doi:10.1099/vir.0.010561-0 (2009).

74 Nagashima, S., Takahashi, M., Kobayashi, T., Nishizawa, T., Nishiyama, T., Primadharsini, P. P. & Okamoto, H. Characterization of the Quasi-Enveloped Hepatitis E Virus Particles Released by the Cellular Exosomal Pathway. *J Virol* **91**, doi:10.1128/jvi.00822-17 (2017).

75 Emerson, S. U., Nguyen, H., Torian, U. & Purcell, R. H. ORF3 protein of hepatitis E virus is not required for replication, virion assembly, or infection of hepatoma cells in vitro. *J Virol* **80**, 10457-10464, doi:10.1128/jvi.00892-06 (2006).

76 Emerson, S. U., Nguyen, H. T., Torian, U., Burke, D., Engle, R. & Purcell, R. H. Release of genotype 1 hepatitis E virus from cultured hepatoma and polarized intestinal cells depends on open reading frame 3 protein and requires an intact PXXP motif. *J Virol* **84**, 9059-9069, doi:10.1128/JVI.00593-10 (2010).

77 Nagashima, S., Takahashi, M., Jirintai, S., Tanaka, T., Nishizawa, T., Yasuda, J. & Okamoto, H. Tumour susceptibility gene 101 and the vacuolar protein sorting pathway are required for the release of hepatitis E virions. *J Gen Virol* **92**, 2838-2848, doi:10.1099/vir.0.035378-0 (2011).

78 Ding, Q., Heller, B., Capuccino, J. M., Song, B., Nimgaonkar, I., Hrebikova, G., Contreras, J. E. & Ploss, A. Hepatitis E virus ORF3 is a functional ion channel required for release of infectious particles. *Proc Natl Acad Sci U S A* **114**, 1147-1152, doi:10.1073/pnas.1614955114 (2017).

79 Treyer, A. & Musch, A. Hepatocyte polarity. *Compr Physiol* **3**, 243-287, doi:10.1002/cphy.c120009 (2013).

80 Kubes, P. & Jenne, C. Immune Responses in the Liver. *Annu Rev Immunol* **36**, 247-277, doi:10.1146/annurev-immunol-051116-052415 (2018).

81 Ronca, V., Gerussi, A., Collins, P., Parente, A., Oo, Y. H. & Invernizzi, P. The liver as a central "hub" of the immune system: pathophysiological implications. *Physiological reviews* **105**, 493-539, doi:10.1152/physrev.00004.2023 (2025).

82 Tsuchida, T. & Friedman, S. L. Mechanisms of hepatic stellate cell activation. *Nat Rev Gastroenterol Hepatol* **14**, 397-411, doi:10.1038/nrgastro.2017.38 (2017).

83 Bram, Y., Nguyen, D. T., Gupta, V., Park, J., Richardson, C., Chandar, V. & Schwartz, R. E. Cell and Tissue Therapy for the Treatment of Chronic Liver Disease. *Annual review of biomedical engineering* **23**, 517-546, doi:10.1146/annurev-bioeng-112619-044026 (2021).

84 Das, A., Rivera-Serrano, E. E., Yin, X., Walker, C. M., Feng, Z. & Lemon, S. M. Cell entry and release of quasi-enveloped human hepatitis viruses. *Nature reviews. Microbiology* **21**, 573-589, doi:10.1038/s41579-023-00889-z (2023).

85 Takahashi, M., Yamada, K., Hoshino, Y., Takahashi, H., Ichiyama, K., Tanaka, T. & Okamoto, H. Monoclonal antibodies raised against the ORF3 protein of hepatitis E virus (HEV) can capture HEV particles in culture supernatant and serum but not those in feces. *Arch Virol* **153**, 1703-1713, doi:10.1007/s00705-008-0179-6 (2008).

86 Yin, X., Ambardekar, C., Lu, Y. & Feng, Z. Distinct Entry Mechanisms for Nonenveloped and Quasi-Enveloped Hepatitis E Viruses. *J Virol* **90**, 4232-4242, doi:10.1128/JVI.02804-15 (2016).

87 Marion, O., Lhomme, S., Nayrac, M., Dubois, M., Pucelle, M., Requena, M., Migueres, M., Abravanel, F., Peron, J. M., Carrere, N., Suc, B., Delobel, P., Kamar, N. & Izopet, J. Hepatitis E virus replication in human intestinal cells. *Gut* **69**, 901-910, doi:10.1136/gutjnl-2019-319004 (2020).

88 Capelli, N., Marion, O., Dubois, M., Allart, S., Bertrand-Michel, J., Lhomme, S., Abravanel, F., Izopet, J. & Chapuy-Regaud, S. Vectorial Release of Hepatitis E Virus in Polarized Human Hepatocytes. *J Virol* **93**, doi:10.1128/jvi.01207-18 (2019).

89 Dao Thi, V. L., Wu, X., Belote, R. L., Andreo, U., Takacs, C. N., Fernandez, J. P., Vale-Silva, L. A., Prallet, S., Decker, C. C., Fu, R. M., Qu, B., Uryu, K., Molina, H., Saeed, M., Steinmann, E., Urban, S., Singaraja, R. R., Schneider, W. M., Simon, S. M. & Rice, C. M. Stem cell-derived polarized hepatocytes. *Nat Commun* **11**, 1677, doi:10.1038/s41467-020-15337-2 (2020).

90 Brüggemann, Y., Frericks, N., Richter, E., Kinast, V. & Steinmann, E. How hepatitis E virus invades hepatocytes: the mystery of viral entry. *Trends Microbiol*, doi:10.1016/j.tim.2025.03.015 (2025).

91 Kalia, M., Chandra, V., Rahman, S. A., Sehgal, D. & Jameel, S. Heparan sulfate proteoglycans are required for cellular binding of the hepatitis E virus ORF2 capsid protein and for viral infection. *J Virol* **83**, 12714-12724, doi:10.1128/jvi.00717-09 (2009).

92 Gonzalez-Gronow, M., Gopal, U., Austin, R. C. & Pizzo, S. V. Glucose-regulated protein (GRP78) is an important cell surface receptor for viral invasion, cancers, and neurological disorders. *IUBMB life* **73**, 843-854, doi:10.1002/iub.2502 (2021).

93 Schrader, J. A., Burkard, T. L., Brüggemann, Y., Gömer, A., Meister, T. L., Fu, R. M., Mehnert, A. K., Dao Thi, V. L., Behrendt, P., Durantel, D., Broering, R., Vondran, F. W. R., Todt, D., Kinast, V. & Steinmann, E. EGF receptor modulates HEV entry in human hepatocytes. *Hepatology* **77**, 2104-2117, doi:10.1097/hep.0000000000000308 (2023).

94 Shiota, T., Li, T. C., Nishimura, Y., Yoshizaki, S., Sugiyama, R., Shimojima, M., Saijo, M., Shimizu, H., Suzuki, R., Wakita, T., Muramatsu, M. & Ishii, K. Integrin α3 is involved in non-enveloped hepatitis E virus infection. *Virology* **536**, 119-124, doi:10.1016/j.virol.2019.07.025 (2019).

95 Fu, R., Engels, Z., Weihs, J. A., Mürle, J., Klöhn, M., Todt, D., Hu, J., Steinmann, E., Böttler, T., Lozach, P.-Y., Lemon, S. M. & Thi, V. L. D. A high-content RNA-based imaging assay reveals integrin beta 1 as a cofactor for cell entry of non-enveloped hepatitis E virus. 2023.2010.2027.564362, doi:10.1101/2023.10.27.564362 %J bioRxiv (2023).

96 Corneillie, L., Lemmens, I., Montpellier, C., Ferrié, M., Weening, K., Van Houtte, F., Hanoulle, X., Cocquerel, L., Amara, A., Tavernier, J. & Meuleman, P. The phosphatidylserine receptor TIM1 promotes infection of enveloped hepatitis E virus. *Cell Mol Life Sci* **80**, 326, doi:10.1007/s00018-023-04977-4 (2023).

97 Klöhn, M., Burkard, T., Janzen, J., Haase, J. A., Gömer, A., Fu, R., Ssebyatika, G., Nocke, M. K., Brown, R. J. P., Krey, T., Dao Thi, V. L., Kinast, V., Brüggemann, Y., Todt, D. & Steinmann, E. Targeting cellular cathepsins inhibits hepatitis E virus entry. *Hepatology* **80**, 1239-1251, doi:10.1097/hep.0000000000000912 (2024).

98 de Beijer, N. L., Snijder, E. J. & Bárcena, M. A Cool Look at Positive-Strand RNA Virus Replication Organelles: New Insights from Cryo-Electron Microscopy. *Annual review of biochemistry* **93**, 163-187, doi:10.1146/annurev-biochem-052521-115736 (2024).

99 Szkolnicka, D., Pollan, A., Da Silva, N., Oechslin, N., Gouttenoire, J. & Moradpour, D. Recombinant Hepatitis E Viruses Harboring Tags in the ORF1 Protein. *J Virol* **93**, doi:10.1128/JVI.00459-19 (2019).

100 Bentaleb, C., Hervouet, K., Montpellier, C., Camuzet, C., Ferrie, M., Burlaud-Gaillard, J., Bressanelli, S., Metzger, K., Werkmeister, E., Ankavay, M., Janampa, N. L., Marlet, J., Roux, J., Deffaud, C., Goffard, A., Rouille, Y., Dubuisson, J., Roingeard, P., Aliouat-Denis, C. M. & Cocquerel, L. The endocytic recycling compartment serves as a viral factory for hepatitis E virus. *Cell Mol Life Sci* **79**, 615, doi:10.1007/s00018-022-04646-y (2022).

101 Metzger, K., Bentaleb, C., Hervouet, K., Alexandre, V., Montpellier, C., Saliou, J. M., Ferrie, M., Camuzet, C., Rouille, Y., Lecoeur, C., Dubuisson, J., Cocquerel, L. & Aliouat-Denis, C. M. Processing and Subcellular Localization of the Hepatitis E Virus Replicase: Identification of Candidate Viral Factories. *Front Microbiol* **13**, 828636, doi:10.3389/fmicb.2022.828636 (2022).

102 Oechslin, N., Da Silva, N., Ankavay, M., Moradpour, D. & Gouttenoire, J. A genome-wide CRISPR/Cas9 screen identifies a role for Rab5A and early endosomes in hepatitis E virus replication. *Proc Natl Acad Sci U S A* **120**, e2307423120, doi:10.1073/pnas.2307423120 (2023).

103 Glitscher, M., Spannaus, I. M., Behr, F., Murra, R. O., Woytinek, K., Bender, D. & Hildt, E. The Protease Domain in HEV pORF1 Mediates the Replicase's Localization to Multivesicular Bodies and Its Exosomal Release. *Cell Mol Gastroenterol Hepatol* **17**, 589-605, doi:10.1016/j.jcmgh.2024.01.001 (2024).

104 Li, X., Sun, X., Pinpin, J., Zhao, Q. & Sun, Y. Multifunctional ORF3 protein of hepatitis E virus. *J Med Virol* **96**, e29691, doi:10.1002/jmv.29691 (2024).

105 Nagashima, S., Jirintai, S., Takahashi, M., Kobayashi, T., Tanggis, Nishizawa, T., Kouki, T., Yashiro, T. & Okamoto, H. Hepatitis E virus egress depends on the exosomal pathway, with secretory exosomes derived from multivesicular bodies. *J Gen Virol* **95**, 2166-2175, doi:10.1099/vir.0.066910-0 (2014).

106 Delves, P. J. & Roitt, I. M. The immune system. First of two parts. *The New England journal of medicine* **343**, 37-49, doi:10.1056/nejm200007063430107 (2000).

107 Delves, P. J. & Roitt, I. M. The immune system. Second of two parts. *The New England journal of medicine* **343**, 108-117, doi:10.1056/nejm200007133430207 (2000).

108 Wang, R., Lan, C., Benlagha, K., Camara, N. O. S., Miller, H., Kubo, M., Heegaard, S., Lee, P., Yang, L., Forsman, H., Li, X., Zhai, Z. & Liu, C. The interaction of innate immune and adaptive immune system. *MedComm* **5**, e714, doi:10.1002/mco2.714 (2024).

109 Merad, M., Sathe, P., Helft, J., Miller, J. & Mortha, A. The dendritic cell lineage: ontogeny and function of dendritic cells and their subsets in the steady state and the inflamed setting. *Annu Rev Immunol* **31**, 563-604, doi:10.1146/annurev-immunol-020711-074950 (2013).

110 Mace, E. M. Human natural killer cells: Form, function, and development. *The Journal of allergy and clinical immunology* **151**, 371-385, doi:10.1016/j.jaci.2022.09.022 (2023).

111 Commins, S. P., Borish, L. & Steinke, J. W. Immunologic messenger molecules: cytokines, interferons, and chemokines. *The Journal of allergy and clinical immunology* **125**, S53-72, doi:10.1016/j.jaci.2009.07.008 (2010).

112 Schatz, D. G. & Ji, Y. Recombination centres and the orchestration of V(D)J recombination. *Nat Rev Immunol* **11**, 251-263, doi:10.1038/nri2941 (2011).

113 Janeway, C. A., Jr. Approaching the asymptote? Evolution and revolution in immunology. *Cold Spring Harbor symposia on quantitative biology* **54 Pt 1**, 1-13, doi:10.1101/sqb.1989.054.01.003 (1989).

114 Takeuchi, O. & Akira, S. Pattern recognition receptors and inflammation. *Cell* **140**, 805-820, doi:10.1016/j.cell.2010.01.022 (2010).

115 Roh, J. S. & Sohn, D. H. Damage-Associated Molecular Patterns in Inflammatory Diseases. *Immune network* **18**, e27, doi:10.4110/in.2018.18.e27 (2018).

116 Li, D. & Wu, M. Pattern recognition receptors in health and diseases. *Signal transduction and targeted therapy* **6**, 291, doi:10.1038/s41392-021-00687-0 (2021).

117 Trindade, B. C. & Chen, G. Y. NOD1 and NOD2 in inflammatory and infectious diseases. *Immunological reviews* **297**, 139-161, doi:10.1111/imr.12902 (2020).

118 Swanson, K. V., Deng, M. & Ting, J. P. The NLRP3 inflammasome: molecular activation and regulation to therapeutics. *Nat Rev Immunol* **19**, 477-489, doi:10.1038/s41577-019-0165-0 (2019).

119 Geijtenbeek, T. B. & Gringhuis, S. I. Signalling through C-type lectin receptors: shaping immune responses. *Nat Rev Immunol* **9**, 465-479, doi:10.1038/nri2569 (2009).

120 Kumari, P., Russo, A. J., Shivcharan, S. & Rathinam, V. A. AIM2 in health and disease: Inflammasome and beyond. *Immunological reviews* **297**, 83-95, doi:10.1111/imr.12903 (2020).

121 Hopfner, K. P. & Hornung, V. Molecular mechanisms and cellular functions of cGAS-STING signalling. *Nature reviews. Molecular cell biology* **21**, 501-521, doi:10.1038/s41580-020-0244-x (2020).

122 Dvorkin, S., Cambier, S., Volkman, H. E. & Stetson, D. B. New frontiers in the cGAS-STING intracellular DNA-sensing pathway. *Immunity* **57**, 718-730, doi:10.1016/j.immuni.2024.02.019 (2024).

123 O'Neill, L. A., Golenbock, D. & Bowie, A. G. The history of Toll-like receptors - redefining innate immunity. *Nat Rev Immunol* **13**, 453-460, doi:10.1038/nri3446 (2013).

124 Botos, I., Segal, D. M. & Davies, D. R. The structural biology of Toll-like receptors. *Structure (London, England : 1993)* **19**, 447-459, doi:10.1016/j.str.2011.02.004 (2011).

125 Poltorak, A., He, X., Smirnova, I., Liu, M. Y., Van Huffel, C., Du, X., Birdwell, D., Alejos, E., Silva, M., Galanos, C., Freudenberg, M., Ricciardi-Castagnoli, P., Layton, B. & Beutler, B. Defective LPS signaling in C3H/HeJ and C57BL/10ScCr mice: mutations in Tlr4 gene. *Science* **282**, 2085-2088, doi:10.1126/science.282.5396.2085 (1998).

126 Lester, S. N. & Li, K. Toll-like receptors in antiviral innate immunity. *J Mol Biol* **426**, 1246-1264, doi:10.1016/j.jmb.2013.11.024 (2014).

127 Alexopoulou, L., Holt, A. C., Medzhitov, R. & Flavell, R. A. Recognition of double-stranded RNA and activation of NF-kappaB by Toll-like receptor 3. *Nature* **413**, 732-738, doi:10.1038/35099560 (2001).

128 Kawasaki, T. & Kawai, T. Toll-like receptor signaling pathways. *Front Immunol* **5**, 461, doi:10.3389/fimmu.2014.00461 (2014).

129 Bao, M. & Liu, Y. J. Regulation of TLR7/9 signaling in plasmacytoid dendritic cells. *Protein & cell* **4**, 40-52, doi:10.1007/s13238-012-2104-8 (2013).

130 Wu, J. & Chen, Z. J. Innate immune sensing and signaling of cytosolic nucleic acids. *Annu Rev Immunol* **32**, 461-488, doi:10.1146/annurev-immunol-032713-120156 (2014).

131 Rehwinkel, J. & Gack, M. U. RIG-I-like receptors: their regulation and roles in RNA sensing. *Nat Rev Immunol* **20**, 537-551, doi:10.1038/s41577-020-0288-3 (2020).

132 Liu, G., Lu, Y., Thulasi Raman, S. N., Xu, F., Wu, Q., Li, Z., Brownlie, R., Liu, Q. & Zhou, Y. Nuclear-resident RIG-I senses viral replication inducing antiviral immunity. *Nat Commun* **9**, 3199, doi:10.1038/s41467-018-05745-w (2018).

133 Kato, H., Takeuchi, O., Mikamo-Satoh, E., Hirai, R., Kawai, T., Matsushita, K., Hiiragi, A., Dermody, T. S., Fujita, T. & Akira, S. Length-dependent recognition of double-stranded ribonucleic acids by retinoic acid-inducible gene-I and melanoma differentiation-associated gene 5. *J Exp Med* **205**, 1601-1610, doi:10.1084/jem.20080091 (2008).

134 Liu, G. & Zhou, Y. Cytoplasm and Beyond: Dynamic Innate Immune Sensing of Influenza A Virus by RIG-I. *J Virol* **93**, doi:10.1128/jvi.02299-18 (2019).

135 Chazal, M., Beauclair, G., Gracias, S., Najburg, V., Simon-Lorière, E., Tangy, F., Komarova, A. V. & Jouvenet, N. RIG-I Recognizes the 5' Region of Dengue and Zika Virus Genomes. *Cell Rep* **24**, 320-328, doi:10.1016/j.celrep.2018.06.047 (2018).

136 Hertzog, J., Dias Junior, A. G., Rigby, R. E., Donald, C. L., Mayer, A., Sezgin, E., Song, C., Jin, B., Hublitz, P., Eggeling, C., Kohl, A. & Rehwinkel, J. Infection with a Brazilian isolate of Zika virus generates RIG-I stimulatory RNA and the viral NS5 protein blocks type I IFN induction and signaling. *European journal of immunology* **48**, 1120-1136, doi:10.1002/eji.201847483 (2018).

137 Saito, T., Owen, D. M., Jiang, F., Marcotrigiano, J. & Gale, M., Jr. Innate immunity induced by composition-dependent RIG-I recognition of hepatitis C virus RNA. *Nature* **454**, 523-527, doi:10.1038/nature07106 (2008).

138 Chiang, J. J., Sparrer, K. M. J., van Gent, M., Lässig, C., Huang, T., Osterrieder, N., Hopfner, K. P. & Gack, M. U. Viral unmasking of cellular 5S rRNA pseudogene transcripts induces RIG-I-mediated immunity. *Nat Immunol* **19**, 53-62, doi:10.1038/s41590-017-0005-y (2018).

139 Dias Junior, A. G., Sampaio, N. G. & Rehwinkel, J. A Balancing Act: MDA5 in Antiviral Immunity and Autoinflammation. *Trends Microbiol* **27**, 75-85, doi:10.1016/j.tim.2018.08.007 (2019).

140 Wu, B., Peisley, A., Richards, C., Yao, H., Zeng, X., Lin, C., Chu, F., Walz, T. & Hur, S. Structural basis for dsRNA recognition, filament formation, and antiviral signal activation by MDA5. *Cell* **152**, 276-289, doi:10.1016/j.cell.2012.11.048 (2013).

141 Pichlmair, A., Schulz, O., Tan, C. P., Rehwinkel, J., Kato, H., Takeuchi, O., Akira, S., Way, M., Schiavo, G. & Reis e Sousa, C. Activation of MDA5 requires higher-order RNA structures generated during virus infection. *J Virol* **83**, 10761-10769, doi:10.1128/jvi.00770-09 (2009).

142 Zhang, Z., Filzmayer, C., Ni, Y., Sultmann, H., Mutz, P., Hiet, M. S., Vondran, F. W. R., Bartenschlager, R. & Urban, S. Hepatitis D virus replication is sensed by MDA5 and induces IFN-beta/lambda responses in hepatocytes. *J Hepatol* **69**, 25-35, doi:10.1016/j.jhep.2018.02.021 (2018).

143 Rodriguez, K. R., Bruns, A. M. & Horvath, C. M. MDA5 and LGP2: accomplices and antagonists of antiviral signal transduction. *J Virol* **88**, 8194-8200, doi:10.1128/jvi.00640-14 (2014).

144 Rothenfusser, S., Goutagny, N., DiPerna, G., Gong, M., Monks, B. G., Schoenemeyer, A., Yamamoto, M., Akira, S. & Fitzgerald, K. A. The RNA helicase Lgp2 inhibits TLR-independent sensing of viral replication by retinoic acid-inducible gene-I. *J Immunol* **175**, 5260-5268, doi:10.4049/jimmunol.175.8.5260 (2005).

145 Saito, T., Hirai, R., Loo, Y. M., Owen, D., Johnson, C. L., Sinha, S. C., Akira, S., Fujita, T. & Gale, M., Jr. Regulation of innate antiviral defenses through a shared repressor domain in RIG-I and LGP2. *Proc Natl Acad Sci U S A* **104**, 582-587, doi:10.1073/pnas.0606699104 (2007).

146 Komuro, A. & Horvath, C. M. RNA- and virus-independent inhibition of antiviral signaling by RNA helicase LGP2. *J Virol* **80**, 12332-12342, doi:10.1128/jvi.01325-06 (2006).

147 Eisenächer, K. & Krug, A. Regulation of RLR-mediated innate immune signaling--it is all about keeping the balance. *European journal of cell biology* **91**, 36-47, doi:10.1016/j.ejcb.2011.01.011 (2012).

148 Hou, F., Sun, L., Zheng, H., Skaug, B., Jiang, Q. X. & Chen, Z. J. MAVS forms functional prion-like aggregates to activate and propagate antiviral innate immune response. *Cell* **146**, 448-461, doi:10.1016/j.cell.2011.06.041 (2011).

149 Pham, A. M. & TenOever, B. R. The IKK Kinases: Operators of Antiviral Signaling. *Viruses* **2**, 55-72, doi:10.3390/v2010055 (2010).

150 Zhao, T., Yang, L., Sun, Q., Arguello, M., Ballard, D. W., Hiscott, J. & Lin, R. The NEMO adaptor bridges the nuclear factor-kappaB and interferon regulatory factor signaling pathways. *Nat Immunol* **8**, 592-600, doi:10.1038/ni1465 (2007).

151 Izaguirre, A., Barnes, B. J., Amrute, S., Yeow, W. S., Megjugorac, N., Dai, J., Feng, D., Chung, E., Pitha, P. M. & Fitzgerald-Bocarsly, P. Comparative analysis of IRF and IFN-alpha expression in human plasmacytoid and monocyte-derived dendritic cells. *J Leukoc Biol* **74**, 1125-1138, doi:10.1189/jlb.0603255 (2003).

152 Israël, A. The IKK complex, a central regulator of NF-kappaB activation. *Cold Spring Harbor perspectives in biology* **2**, a000158, doi:10.1101/cshperspect.a000158 (2010).

153 Isaacs, A. & Lindenmann, J. Virus interference. I. The interferon. *Proceedings of the Royal Society of London. Series B, Biological sciences* **147**, 258-267, doi:10.1098/rspb.1957.0048 (1957).

154 Schneider, W. M., Chevillotte, M. D. & Rice, C. M. Interferon-stimulated genes: a complex web of host defenses. *Annu Rev Immunol* **32**, 513-545, doi:10.1146/annurev-immunol-032713-120231 (2014).

155 Negishi, H., Taniguchi, T. & Yanai, H. The Interferon (IFN) Class of Cytokines and the IFN Regulatory Factor (IRF) Transcription Factor Family. *Cold Spring Harbor perspectives in biology* **10**, doi:10.1101/cshperspect.a028423 (2018).

156 Schreiber, G. The molecular basis for differential type I interferon signaling. *J Biol Chem* **292**, 7285-7294, doi:10.1074/jbc.R116.774562 (2017).

157 Casanova, J. L., MacMicking, J. D. & Nathan, C. F. Interferon-γ and infectious diseases: Lessons and prospects. *Science* **384**, eadl2016, doi:10.1126/science.adl2016 (2024).

158 Fang, M. Z., Jackson, S. S. & O'Brien, T. R. IFNL4: Notable variants and associated phenotypes(). *Gene* **730**, 144289, doi:10.1016/j.gene.2019.144289 (2020).

159 Broggi, A., Granucci, F. & Zanoni, I. Type III interferons: Balancing tissue tolerance and resistance to pathogen invasion. *J Exp Med* **217**, doi:10.1084/jem.20190295 (2020).

160 Schoggins, J. W. Interferon-Stimulated Genes: What Do They All Do? *Annu Rev Virol* **6**, 567-584, doi:10.1146/annurev-virology-092818-015756 (2019).

161 Burkart, S. S., Schweinoch, D., Frankish, J., Sparn, C., Wüst, S., Urban, C., Merlo, M., Magalhães, V. G., Piras, A., Pichlmair, A., Willemsen, J., Kaderali, L. & Binder, M. High-resolution kinetic characterization of the RIG-I-signaling pathway and the antiviral response. *Life science alliance* **6**, doi:10.26508/lsa.202302059 (2023).

162 Rönnblom, L. The type I interferon system in the etiopathogenesis of autoimmune diseases. *Upsala journal of medical sciences* **116**, 227-237, doi:10.3109/03009734.2011.624649 (2011).

163 Haller, O. & Kochs, G. Mx genes: host determinants controlling influenza virus infection and trans-species transmission. *Human genetics* **139**, 695-705, doi:10.1007/s00439-019-02092-8 (2020).

164 Gómez-Herranz, M., Taylor, J. & Sloan, R. D. IFITM proteins: Understanding their diverse roles in viral infection, cancer, and immunity. *J Biol Chem* **299**, 102741, doi:10.1016/j.jbc.2022.102741 (2023).

165 Ganser-Pornillos, B. K. & Pornillos, O. Restriction of HIV-1 and other retroviruses by TRIM5. *Nature reviews. Microbiology* **17**, 546-556, doi:10.1038/s41579-019-0225-2 (2019).

166 Hyde, J. L. & Diamond, M. S. Innate immune restriction and antagonism of viral RNA lacking 2′-O methylation. *Virology* **479-480**, 66-74, doi:10.1016/j.virol.2015.01.019 (2015).

167 Sarkar, L., Liu, G. & Gack, M. U. ISG15: its roles in SARS-CoV-2 and other viral infections. *Trends Microbiol* **31**, 1262-1275, doi:10.1016/j.tim.2023.07.006 (2023).

168 Shi, H. X., Yang, K., Liu, X., Liu, X. Y., Wei, B., Shan, Y. F., Zhu, L. H. & Wang, C. Positive regulation of interferon regulatory factor 3 activation by Herc5 via ISG15 modification. *Mol Cell Biol* **30**, 2424-2436, doi:10.1128/mcb.01466-09 (2010).

169 Helbig, K. J. & Beard, M. R. The role of viperin in the innate antiviral response. *J Mol Biol* **426**, 1210-1219, doi:10.1016/j.jmb.2013.10.019 (2014).

170 Chathuranga, K., Weerawardhana, A., Dodantenna, N. & Lee, J. S. Regulation of antiviral innate immune signaling and viral evasion following viral genome sensing. *Experimental & molecular medicine* **53**, 1647-1668, doi:10.1038/s12276-021-00691-y (2021).

171 Zhu, J., Chiang, C. & Gack, M. U. Viral evasion of the interferon response at a glance. *Journal of cell science* **136**, doi:10.1242/jcs.260682 (2023).

172 Wang, B., Xi, X., Lei, X., Zhang, X., Cui, S., Wang, J., Jin, Q. & Zhao, Z. Enterovirus 71 protease 2Apro targets MAVS to inhibit anti-viral type I interferon responses. *PLoS Pathog* **9**, e1003231, doi:10.1371/journal.ppat.1003231 (2013).

173 Meylan, E., Curran, J., Hofmann, K., Moradpour, D., Binder, M., Bartenschlager, R. & Tschopp, J. Cardif is an adaptor protein in the RIG-I antiviral pathway and is targeted by hepatitis C virus. *Nature* **437**, 1167-1172, doi:10.1038/nature04193 (2005).

174 Li, X. D., Sun, L., Seth, R. B., Pineda, G. & Chen, Z. J. Hepatitis C virus protease NS3/4A cleaves mitochondrial antiviral signaling protein off the mitochondria to evade innate immunity. *Proc Natl Acad Sci U S A* **102**, 17717-17722, doi:10.1073/pnas.0508531102 (2005).

175 Ning, Y. J., Wang, M., Deng, M., Shen, S., Liu, W., Cao, W. C., Deng, F., Wang, Y. Y., Hu, Z. & Wang, H. Viral suppression of innate immunity via spatial isolation of TBK1/IKKε from mitochondrial antiviral platform. *Journal of molecular cell biology* **6**, 324-337, doi:10.1093/jmcb/mju015 (2014).

176 Wu, X., Qi, X., Qu, B., Zhang, Z., Liang, M., Li, C., Cardona, C. J., Li, D. & Xing, Z. Evasion of antiviral immunity through sequestering of TBK1/IKKε/IRF3 into viral inclusion bodies. *J Virol* **88**, 3067-3076, doi:10.1128/jvi.03510-13 (2014).

177 Xia, C., Vijayan, M., Pritzl, C. J., Fuchs, S. Y., McDermott, A. B. & Hahm, B. Hemagglutinin of Influenza A Virus Antagonizes Type I Interferon (IFN) Responses by Inducing Degradation of Type I IFN Receptor 1. *J Virol* **90**, 2403-2417, doi:10.1128/jvi.02749-15 (2015).

178 Mansfield, K. L., Johnson, N., Cosby, S. L., Solomon, T. & Fooks, A. R. Transcriptional upregulation of SOCS 1 and suppressors of cytokine signaling 3 mRNA in the absence of suppressors of cytokine signaling 2 mRNA after infection with West Nile virus or tick-borne encephalitis virus. *Vector borne and zoonotic diseases (Larchmont, N.Y.)* **10**, 649-653, doi:10.1089/vbz.2009.0259 (2010).

179 Mateo, M., Reid, S. P., Leung, L. W., Basler, C. F. & Volchkov, V. E. Ebolavirus VP24 binding to karyopherins is required for inhibition of interferon signaling. *J Virol* **84**, 1169-1175, doi:10.1128/jvi.01372-09 (2010).

180 Reid, S. P., Leung, L. W., Hartman, A. L., Martinez, O., Shaw, M. L., Carbonnelle, C., Volchkov, V. E., Nichol, S. T. & Basler, C. F. Ebola virus VP24 binds karyopherin alpha1 and blocks STAT1 nuclear accumulation. *J Virol* **80**, 5156-5167, doi:10.1128/jvi.02349-05 (2006).

181 Ashour, J., Laurent-Rolle, M., Shi, P. Y. & García-Sastre, A. NS5 of dengue virus mediates STAT2 binding and degradation. *J Virol* **83**, 5408-5418, doi:10.1128/jvi.02188-08 (2009).

182 Grant, A., Ponia, S. S., Tripathi, S., Balasubramaniam, V., Miorin, L., Sourisseau, M., Schwarz, M. C., Sánchez-Seco, M. P., Evans, M. J., Best, S. M. & García-Sastre, A. Zika Virus Targets Human STAT2 to Inhibit Type I Interferon Signaling. *Cell Host Microbe* **19**, 882-890, doi:10.1016/j.chom.2016.05.009 (2016).

183 Bove, G., Mehnert, A.-K. & Dao Thi, V. L. in *iPSCs for Studying Infectious Diseases* Vol. 8 (ed Alexander Birbrair) 149-213 (Academic Press, 2021).

184 Fu, R. M., Decker, C. C. & Dao Thi, V. L. Cell Culture Models for Hepatitis E Virus. *Viruses* **11**, doi:10.3390/v11070608 (2019).

185 Meister, T. L., Bruening, J., Todt, D. & Steinmann, E. Cell culture systems for the study of hepatitis E virus. *Antiviral Res* **163**, 34-49, doi:10.1016/j.antiviral.2019.01.007 (2019).

186 Fenton, S. E., Saleiro, D. & Platanias, L. C. Type I and II Interferons in the Anti-Tumor Immune Response. *Cancers* **13**, doi:10.3390/cancers13051037 (2021).

187 von Locquenghien, M., Rozalén, C. & Celià-Terrassa, T. Interferons in cancer immunoediting: sculpting metastasis and immunotherapy response. *J Clin Invest* **131**, doi:10.1172/jci143296 (2021).

188 Cheon, H., Wang, Y., Wightman, S. M., Jackson, M. W. & Stark, G. R. How cancer cells make and respond to interferon-I. *Trends in cancer* **9**, 83-92, doi:10.1016/j.trecan.2022.09.003 (2023).

189 Rodríguez-Antona, C., Donato, M. T., Boobis, A., Edwards, R. J., Watts, P. S., Castell, J. V. & Gómez-Lechón, M. J. Cytochrome P450 expression in human hepatocytes and hepatoma cell lines: molecular mechanisms that determine lower expression in cultured cells. *Xenobiotica; the fate of foreign compounds in biological systems* **32**, 505-520, doi:10.1080/00498250210128675 (2002).

190 Tanaka, T., Takahashi, M., Kusano, E. & Okamoto, H. Development and evaluation of an efficient cell-culture system for Hepatitis E virus. *J Gen Virol* **88**, 903-911, doi:10.1099/vir.0.82535-0 (2007).

191 Lorenzo, F. R., Tanaka, T., Takahashi, H., Ichiyama, K., Hoshino, Y., Yamada, K., Inoue, J., Takahashi, M. & Okamoto, H. Mutational events during the primary propagation and consecutive passages of hepatitis E virus strain JE03-1760F in cell culture. *Virus Res* **137**, 86-96, doi:10.1016/j.virusres.2008.06.005 (2008).

192 Tanaka, T., Takahashi, M., Takahashi, H., Ichiyama, K., Hoshino, Y., Nagashima, S., Mizuo, H. & Okamoto, H. Development and characterization of a genotype 4 hepatitis E virus cell culture system using a HE-JF5/15F strain recovered from a fulminant hepatitis patient. *J Clin Microbiol* **47**, 1906-1910, doi:10.1128/jcm.00629-09 (2009).

193 Takahashi, M., Tanaka, T., Takahashi, H., Hoshino, Y., Nagashima, S., Jirintai, Mizuo, H., Yazaki, Y., Takagi, T., Azuma, M., Kusano, E., Isoda, N., Sugano, K. & Okamoto, H. Hepatitis E Virus (HEV) strains in serum samples can replicate efficiently in cultured cells despite the coexistence of HEV antibodies: characterization of HEV virions in blood circulation. *J Clin Microbiol* **48**, 1112-1125, doi:10.1128/jcm.02002-09 (2010).

194 MacNab, G. M., Alexander, J. J., Lecatsas, G., Bey, E. M. & Urbanowicz, J. M. Hepatitis B surface antigen produced by a human hepatoma cell line. *British journal of cancer* **34**, 509-515, doi:10.1038/bjc.1976.205 (1976).

195 Emerson, S. U., Nguyen, H., Graff, J., Stephany, D. A., Brockington, A. & Purcell, R. H. In vitro replication of hepatitis E virus (HEV) genomes and of an HEV replicon expressing green fluorescent protein. *J Virol* **78**, 4838-4846, doi:10.1128/jvi.78.9.4838-4846.2004 (2004).

196 Emerson, S. U., Arankalle, V. A. & Purcell, R. H. Thermal stability of hepatitis E virus. *J Infect Dis* **192**, 930-933, doi:10.1086/432488 (2005).

197 Sumpter, R., Jr., Loo, Y. M., Foy, E., Li, K., Yoneyama, M., Fujita, T., Lemon, S. M. & Gale, M., Jr. Regulating intracellular antiviral defense and permissiveness to hepatitis C virus RNA replication through a cellular RNA helicase, RIG-I. *J Virol* **79**, 2689-2699, doi:10.1128/JVI.79.5.2689-2699.2005 (2005).

198 Colasanti, O., Burm, R., Huang, H. E., Riedl, T., Traut, J., Gillich, N., Li, T. F., Corneillie, L., Faure-Dupuy, S., Grünvogel, O., Heide, D., Lee, J. Y., Tran, C. S., Merle, U., Chironna, M., Vondran, F. F. W., Esser-Nobis, K., Binder, M., Bartenschlager, R., Heikenwälder, M., Meuleman, P. & Lohmann, V. Comparison of HAV and HCV infections in vivo and in vitro reveals distinct patterns of innate immune evasion and activation. *J Hepatol* **79**, 645-656, doi:10.1016/j.jhep.2023.04.023 (2023).

199 Devhare, P. B., Desai, S. & Lole, K. S. Innate immune responses in human hepatocyte-derived cell lines alter genotype 1 hepatitis E virus replication efficiencies. *Sci Rep* **6**, 26827, doi:10.1038/srep26827 (2016).

200 Sooryanarain, H., Heffron, C. L. & Meng, X. J. The U-Rich Untranslated Region of the Hepatitis E Virus Induces Differential Type I and Type III Interferon Responses in a Host Cell-Dependent Manner. *mBio* **11**, doi:10.1128/mBio.03103-19 (2020).

201 Yin, X., Li, X., Ambardekar, C., Hu, Z., Lhomme, S. & Feng, Z. Hepatitis E virus persists in the presence of a type III interferon response. *PLoS Pathog* **13**, e1006417, doi:10.1371/journal.ppat.1006417 (2017).

202 Todt, D., Friesland, M., Moeller, N., Praditya, D., Kinast, V., Brüggemann, Y., Knegendorf, L., Burkard, T., Steinmann, J., Burm, R., Verhoye, L., Wahid, A., Meister, T. L., Engelmann, M., Pfankuche, V. M., Puff, C., Vondran, F. W. R., Baumgärtner, W., Meuleman, P., Behrendt, P. & Steinmann, E. Robust hepatitis E virus infection and transcriptional response in human hepatocytes. *Proc Natl Acad Sci U S A* **117**, 1731-1741, doi:10.1073/pnas.1912307117 (2020).

203 Schwartz, R. E., Fleming, H. E., Khetani, S. R. & Bhatia, S. N. Pluripotent stem cell-derived hepatocyte-like cells. *Biotechnol Adv* **32**, 504-513, doi:10.1016/j.biotechadv.2014.01.003 (2014).

204 Wu, X., Dao Thi, V. L., Liu, P., Takacs, C. N., Xiang, K., Andrus, L., Gouttenoire, J., Moradpour, D. & Rice, C. M. Pan-Genotype Hepatitis E Virus Replication in Stem Cell-Derived Hepatocellular Systems. *Gastroenterology* **154**, 663-674 e667, doi:10.1053/j.gastro.2017.10.041 (2018).

205 Chi, H., Qu, B., Prawira, A., Richardt, T., Maurer, L., Hu, J., Fu, R. M., Lempp, F. A., Zhang, Z., Grimm, D., Wu, X., Urban, S. & Dao Thi, V. L. An hepatitis B and D virus infection model using human pluripotent stem cell-derived hepatocytes. *EMBO reports* **25**, 4311-4336, doi:10.1038/s44319-024-00236-0 (2024).

206 Helsen, N., Debing, Y., Paeshuyse, J., Dallmeier, K., Boon, R., Coll, M., Sancho-Bru, P., Claes, C., Neyts, J. & Verfaillie, C. M. Stem cell-derived hepatocytes: A novel model for hepatitis E virus replication. *J Hepatol* **64**, 565-573, doi:10.1016/j.jhep.2015.11.013 (2016).

207 Dao Thi, V. L., Debing, Y., Wu, X., Rice, C. M., Neyts, J., Moradpour, D. & Gouttenoire, J. Sofosbuvir Inhibits Hepatitis E Virus Replication In Vitro and Results in an Additive Effect When Combined With Ribavirin. *Gastroenterology* **150**, 82-85 e84, doi:10.1053/j.gastro.2015.09.011 (2016).

208 Primadharsini, P. P., Nagashima, S., Tanaka, T., Jirintai, S., Takahashi, M., Murata, K. & Okamoto, H. Development and Characterization of Efficient Cell Culture Systems for Genotype 1 Hepatitis E Virus and Its Infectious cDNA Clone. *Viruses* **15**, doi:10.3390/v15040845 (2023).

209 Bruggemann, Y., Klohn, M., Wedemeyer, H. & Steinmann, E. Hepatitis E virus: from innate sensing to adaptive immune responses. *Nat Rev Gastroenterol Hepatol*, doi:10.1038/s41575-024-00950-z (2024).

210 Yu, C., Boon, D., McDonald, S. L., Myers, T. G., Tomioka, K., Nguyen, H., Engle, R. E., Govindarajan, S., Emerson, S. U. & Purcell, R. H. Pathogenesis of hepatitis E virus and hepatitis C virus in chimpanzees: similarities and differences. *J Virol* **84**, 11264-11278, doi:10.1128/JVI.01205-10 (2010).

211 Wang, W., Wang, Y., Qu, C., Wang, S., Zhou, J., Cao, W., Xu, L., Ma, B., Hakim, M. S., Yin, Y., Li, T., Peppelenbosch, M. P., Zhao, J. & Pan, Q. The RNA genome of hepatitis E virus robustly triggers an antiviral interferon response. *Hepatology* **67**, 2096-2112, doi:10.1002/hep.29702 (2018).

212 Murata, K., Kang, J. H., Nagashima, S., Matsui, T., Karino, Y., Yamamoto, Y., Atarashi, T., Oohara, M., Uebayashi, M., Sakata, H., Matsubayashi, K., Takahashi, K., Arai, M., Mishiro, S., Sugiyama, M., Mizokami, M. & Okamoto, H. IFN-lambda3 as a host immune response in acute hepatitis E virus infection. *Cytokine* **125**, 154816, doi:10.1016/j.cyto.2019.154816 (2020).

213 Xu, L., Zhou, X., Wang, W., Wang, Y., Yin, Y., Laan, L. J., Sprengers, D., Metselaar, H. J., Peppelenbosch, M. P. & Pan, Q. IFN regulatory factor 1 restricts hepatitis E virus replication by activating STAT1 to induce antiviral IFN-stimulated genes. *Faseb j* **30**, 3352-3367, doi:10.1096/fj.201600356R (2016).

214 Xu, L., Wang, W., Li, Y., Zhou, X., Yin, Y., Wang, Y., de Man, R. A., van der Laan, L. J. W., Huang, F., Kamar, N., Peppelenbosch, M. P. & Pan, Q. RIG-I is a key antiviral interferon-stimulated gene against hepatitis E virus regardless of interferon production. *Hepatology* **65**, 1823-1839, doi:10.1002/hep.29105 (2017).

215 Li, Y., Yu, P., Qu, C., Li, P., Li, Y., Ma, Z., Wang, W., de Man, R. A., Peppelenbosch, M. P. & Pan, Q. MDA5 against enteric viruses through induction of interferon-like response partially via the JAK-STAT cascade. *Antiviral Res* **176**, 104743, doi:10.1016/j.antiviral.2020.104743 (2020).

216 Sooryanarain, H., Rogers, A. J., Cao, D., Haac, M. E. R., Karpe, Y. A. & Meng, X. J. ISG15 Modulates Type I Interferon Signaling and the Antiviral Response during Hepatitis E Virus Replication. *J Virol* **91**, doi:10.1128/JVI.00621-17 (2017).

217 Wang, M., Huang, Y., He, M., Peng, W. J. & Tian, D. Y. Effects of hepatitis E virus infection on interferon production via ISG15. *World J Gastroenterol* **24**, 2173-2180, doi:10.3748/wjg.v24.i20.2173 (2018).

218 Glitscher, M., Himmelsbach, K., Woytinek, K., Schollmeier, A., Johne, R., Praefcke, G. J. K. & Hildt, E. Identification of the interferon-inducible GTPase GBP1 as major restriction factor for the Hepatitis E virus. *J Virol* **95**, doi:10.1128/JVI.01564-20 (2021).

219 Devhare, P. B., Chatterjee, S. N., Arankalle, V. A. & Lole, K. S. Analysis of antiviral response in human epithelial cells infected with hepatitis E virus. *PLoS One* **8**, e63793, doi:10.1371/journal.pone.0063793 (2013).

220 Majumdar, M., Ratho, R. K., Chawla, Y. & Singh, M. P. Role of TLR gene expression and cytokine profiling in the immunopathogenesis of viral hepatitis E. *J Clin Virol* **73**, 8-13, doi:10.1016/j.jcv.2015.09.011 (2015).

221 Sehgal, R., Patra, S., David, P., Vyas, A., Khanam, A., Hissar, S., Gupta, E., Kumar, G., Kottilil, S., Maiwall, R., Sarin, S. K. & Trehanpati, N. Impaired monocyte-macrophage functions and defective Toll-like receptor signaling in hepatitis E virus-infected pregnant women with acute liver failure. *Hepatology* **62**, 1683-1696, doi:10.1002/hep.28143 (2015).

222 Arya, R. P., Mishra, N., Biswas, K. & Arankalle, V. A. Association of Toll-like receptor 4 polymorphism with hepatitis E virus-infected Indian patients. *J Viral Hepat* **25**, 1617-1623, doi:10.1111/jvh.12980 (2018).

223 Zhou, X., Xu, L., Wang, W., Watashi, K., Wang, Y., Sprengers, D., de Ruiter, P. E., van der Laan, L. J., Metselaar, H. J., Kamar, N., Peppelenbosch, M. P. & Pan, Q. Disparity of basal and therapeutically activated interferon signalling in constraining hepatitis E virus infection. *J Viral Hepat* **23**, 294-304, doi:10.1111/jvh.12491 (2016).

224 Todt, D., Francois, C., Anggakusuma, Behrendt, P., Engelmann, M., Knegendorf, L., Vieyres, G., Wedemeyer, H., Hartmann, R., Pietschmann, T., Duverlie, G. & Steinmann, E. Antiviral Activities of Different Interferon Types and Subtypes against Hepatitis E Virus Replication. *Antimicrob Agents Chemother* **60**, 2132-2139, doi:10.1128/AAC.02427-15 (2016).

225 Kang, S., Choi, C., Choi, I., Han, K. N., Rho, S. W., Choi, J., Kwon, J., Park, M. K., Kim, S. J. & Myoung, J. Hepatitis E Virus Methyltransferase Inhibits Type I Interferon Induction by Targeting RIG-I. *J Microbiol Biotechnol* **28**, 1554-1562, doi:10.4014/jmb.1808.08058 (2018).

226 Dong, C., Zafrullah, M., Mixson-Hayden, T., Dai, X., Liang, J., Meng, J. & Kamili, S. Suppression of interferon-alpha signaling by hepatitis E virus. *Hepatology* **55**, 1324-1332, doi:10.1002/hep.25530 (2012).

227 Yang, Y., Liang, Y., Qu, L., Chen, Z., Yi, M., Li, K. & Lemon, S. M. Disruption of innate immunity due to mitochondrial targeting of a picornaviral protease precursor. *Proc Natl Acad Sci U S A* **104**, 7253-7258, doi:10.1073/pnas.0611506104 (2007).

228 Nan, Y., Yu, Y., Ma, Z., Khattar, S. K., Fredericksen, B. & Zhang, Y. J. Hepatitis E virus inhibits type I interferon induction by ORF1 products. *J Virol* **88**, 11924-11932, doi:10.1128/jvi.01935-14 (2014).

229 Kim, E. & Myoung, J. Hepatitis E Virus Papain-Like Cysteine Protease Inhibits Type I Interferon Induction by Down-Regulating Melanoma Differentiation-Associated Gene 5. *J Microbiol Biotechnol* **28**, 1908-1915, doi:10.4014/jmb.1809.09028 (2018).

230 Myoung, J. & Min, K. Dose-Dependent Inhibition of Melanoma Differentiation-Associated Gene 5-Mediated Activation of Type I Interferon Responses by Methyltransferase of Hepatitis E Virus. *J Microbiol Biotechnol* **29**, 1137-1143, doi:10.4014/jmb.1905.05040 (2019).

231 Hingane, S., Joshi, N., Surjit, M. & Ranjith-Kumar, C. T. Hepatitis E Virus ORF2 Inhibits RIG-I Mediated Interferon Response. *Front Microbiol* **11**, 656, doi:10.3389/fmicb.2020.00656 (2020).

232 Bagdassarian, E., Doceul, V., Pellerin, M., Demange, A., Meyer, L., Jouvenet, N. & Pavio, N. The Amino-Terminal Region of Hepatitis E Virus ORF1 Containing a Methyltransferase (Met) and a Papain-Like Cysteine Protease (PCP) Domain Counteracts Type I Interferon Response. *Viruses* **10**, doi:10.3390/v10120726 (2018).

233 He, M., Wang, M., Huang, Y., Peng, W., Zheng, Z., Xia, N., Xu, J. & Tian, D. The ORF3 Protein of Genotype 1 Hepatitis E Virus Suppresses TLR3-induced NF-kappaB Signaling via TRADD and RIP1. *Sci Rep* **6**, 27597, doi:10.1038/srep27597 (2016).

234 Lei, Q., Li, L., Zhang, S., Li, T., Zhang, X., Ding, X. & Qin, B. HEV ORF3 downregulates TLR7 to inhibit the generation of type I interferon via impairment of multiple signaling pathways. *Sci Rep* **8**, 8585, doi:10.1038/s41598-018-26975-4 (2018).

235 Nan, Y., Ma, Z., Wang, R., Yu, Y., Kannan, H., Fredericksen, B. & Zhang, Y. J. Enhancement of interferon induction by ORF3 product of hepatitis E virus. *J Virol* **88**, 8696-8705, doi:10.1128/jvi.01228-14 (2014).

236 Allweiss, L., Gass, S., Giersch, K., Groth, A., Kah, J., Volz, T., Rapp, G., Schöbel, A., Lohse, A. W., Polywka, S., Pischke, S., Herker, E., Dandri, M. & Lütgehetmann, M. Human liver chimeric mice as a new model of chronic hepatitis E virus infection and preclinical drug evaluation. *J Hepatol* **64**, 1033-1040, doi:10.1016/j.jhep.2016.01.011 (2016).

237 Lenggenhager, D., Gouttenoire, J., Malehmir, M., Bawohl, M., Honcharova-Biletska, H., Kreutzer, S., Semela, D., Neuweiler, J., Hurlimann, S., Aepli, P., Fraga, M., Sahli, R., Terracciano, L., Rubbia-

Brandt, L., Mullhaupt, B., Sempoux, C., Moradpour, D. & Weber, A. Visualization of hepatitis E virus RNA and proteins in the human liver. *J Hepatol* **67**, 471-479, doi:10.1016/j.jhep.2017.04.002 (2017).

238 Surjit, M., Varshney, B. & Lal, S. K. The ORF2 glycoprotein of hepatitis E virus inhibits cellular NF-κB activity by blocking ubiquitination mediated proteasomal degradation of IκBα in human hepatoma cells. *BMC biochemistry* **13**, 7, doi:10.1186/1471-2091-13-7 (2012).

239 Hato, S. V., Ricour, C., Schulte, B. M., Lanke, K. H., de Bruijni, M., Zoll, J., Melchers, W. J., Michiels, T. & van Kuppeveld, F. J. The mengovirus leader protein blocks interferon-alpha/beta gene transcription and inhibits activation of interferon regulatory factor 3. *Cell Microbiol* **9**, 2921-2930, doi:10.1111/j.1462-5822.2007.01006.x (2007).

240 Magalhães, V. G., Lukassen, S., Drechsler, M., Loske, J., Burkart, S. S., Wüst, S., Jacobsen, E. M., Röhmel, J., Mall, M. A., Debatin, K. M., Eils, R., Autenrieth, S., Janda, A., Lehmann, I. & Binder, M. Immune-epithelial cell cross-talk enhances antiviral responsiveness to SARS-CoV-2 in children. *EMBO reports* **24**, e57912, doi:10.15252/embr.202357912 (2023).

241 Lacoste, A., Berenshteyn, F. & Brivanlou, A. H. An efficient and reversible transposable system for gene delivery and lineage-specific differentiation in human embryonic stem cells. *Cell Stem Cell* **5**, 332-342, doi:10.1016/j.stem.2009.07.011 (2009).

242 Wüst, S., Schad, P., Burkart, S. & Binder, M. Comparative Analysis of Six IRF Family Members in Alveolar Epithelial Cell-Intrinsic Antiviral Responses. *Cells* **10**, doi:10.3390/cells10102600 (2021).

243 Schindelin, J., Arganda-Carreras, I., Frise, E., Kaynig, V., Longair, M., Pietzsch, T., Preibisch, S., Rueden, C., Saalfeld, S., Schmid, B., Tinevez, J. Y., White, D. J., Hartenstein, V., Eliceiri, K., Tomancak, P. & Cardona, A. Fiji: an open-source platform for biological-image analysis. *Nat Methods* **9**, 676-682, doi:10.1038/nmeth.2019 (2012).

244 Wu, X. & Dao Thi, V. L. Embryonic or Induced Pluripotent Stem Cell-Derived Hepatocellular Systems for HCV Culture. *Methods Mol Biol* **1911**, 121-135, doi:10.1007/978-1-4939-8976-8_8 (2019).

245 Mehnert, A.-K., Stegmaier, S., Ramirez, C., Magalhães, V. G., Siebenkotten, C., Hu, J., Costa, A. L., Kirrmaier, D., Knop, M., Wu, X., Tubiana, T., Herrmann, C., Binder, M. & Thi, V. L. D. The hepatitis E virus capsid protein ORF2 counteracts cell-intrinsic antiviral responses to enable persistence in hepatocytes. 2025.2002.2003.636239, doi:10.1101/2025.02.03.636239 %J bioRxiv (2025).

246 Berg, S., Kutra, D., Kroeger, T., Straehle, C. N., Kausler, B. X., Haubold, C., Schiegg, M., Ales, J., Beier, T., Rudy, M., Eren, K., Cervantes, J. I., Xu, B., Beuttenmueller, F., Wolny, A., Zhang, C., Koethe, U., Hamprecht, F. A. & Kreshuk, A. ilastik: interactive machine learning for (bio)image analysis. *Nat Methods* **16**, 1226-1232, doi:10.1038/s41592-019-0582-9 (2019).

247 Stirling, D. R., Swain-Bowden, M. J., Lucas, A. M., Carpenter, A. E., Cimini, B. A. & Goodman, A. CellProfiler 4: improvements in speed, utility and usability. *BMC bioinformatics* **22**, 433, doi:10.1186/s12859-021-04344-9 (2021).

248 Balmas, E., Sozza, F., Bottini, S., Ratto, M. L., Savorè, G., Becca, S., Snijders, K. E. & Bertero, A. Manipulating and studying gene function in human pluripotent stem cell models. *FEBS Lett* **597**, 2250-2287, doi:10.1002/1873-3468.14709 (2023).

249 Gonzalez, F., Zhu, Z., Shi, Z. D., Lelli, K., Verma, N., Li, Q. V. & Huangfu, D. An iCRISPR platform for rapid, multiplexable, and inducible genome editing in human pluripotent stem cells. *Cell Stem Cell* **15**, 215-226, doi:10.1016/j.stem.2014.05.018 (2014).

250 Vitale, I., Manic, G., De Maria, R., Kroemer, G. & Galluzzi, L. DNA Damage in Stem Cells. *Mol Cell* **66**, 306-319, doi:10.1016/j.molcel.2017.04.006 (2017).

251 Kim, S., Kim, D., Cho, S. W., Kim, J. & Kim, J. S. Highly efficient RNA-guided genome editing in human cells via delivery of purified Cas9 ribonucleoproteins. *Genome research* **24**, 1012-1019, doi:10.1101/gr.171322.113 (2014).

252 Lhomme, S., Migueres, M., Abravanel, F., Marion, O., Kamar, N. & Izopet, J. Hepatitis E Virus: How It Escapes Host Innate Immunity. *Vaccines (Basel)* **8**, doi:10.3390/vaccines8030422 (2020).

253 Farhat, R., Ankavay, M., Lebsir, N., Gouttenoire, J., Jackson, C. L., Wychowski, C., Moradpour, D., Dubuisson, J., Rouillé, Y. & Cocquerel, L. Identification of GBF1 as a cellular factor required for hepatitis E virus RNA replication. *Cell Microbiol* **20**, doi:10.1111/cmi.12804 (2018).

254 Plociennikowska, A., Frankish, J., Moraes, T., Del Prete, D., Kahnt, F., Acuna, C., Slezak, M., Binder, M. & Bartenschlager, R. TLR3 activation by Zika virus stimulates inflammatory cytokine

production which dampens the antiviral response induced by RIG-I-like receptors. *J Virol* **95**, doi:10.1128/JVI.01050-20 (2021).

255 Wang, F., Flanagan, J., Su, N., Wang, L. C., Bui, S., Nielson, A., Wu, X., Vo, H. T., Ma, X. J. & Luo, Y. RNAscope: a novel in situ RNA analysis platform for formalin-fixed, paraffin-embedded tissues. *J Mol Diagn* **14**, 22-29, doi:10.1016/j.jmoldx.2011.08.002 (2012).

256 Herhaus, L. TBK1 (TANK-binding kinase 1)-mediated regulation of autophagy in health and disease. *Matrix biology : journal of the International Society for Matrix Biology* **100-101**, 84-98, doi:10.1016/j.matbio.2021.01.004 (2021).

257 Moulin, C., Crupi, M. J. F., Ilkow, C. S., Bell, J. C. & Boulton, S. Extracellular Vesicles and Viruses: Two Intertwined Entities. *Int J Mol Sci* **24**, doi:10.3390/ijms24021036 (2023).

258 Zheng, G. X., Terry, J. M., Belgrader, P., Ryvkin, P., Bent, Z. W., Wilson, R., Ziraldo, S. B., Wheeler, T. D., McDermott, G. P., Zhu, J., Gregory, M. T., Shuga, J., Montesclaros, L., Underwood, J. G., Masquelier, D. A., Nishimura, S. Y., Schnall-Levin, M., Wyatt, P. W., Hindson, C. M., Bharadwaj, R., Wong, A., Ness, K. D., Beppu, L. W., Deeg, H. J., McFarland, C., Loeb, K. R., Valente, W. J., Ericson, N. G., Stevens, E. A., Radich, J. P., Mikkelsen, T. S., Hindson, B. J. & Bielas, J. H. Massively parallel digital transcriptional profiling of single cells. *Nat Commun* **8**, 14049, doi:10.1038/ncomms14049 (2017).

259 Liberzon, A., Birger, C., Thorvaldsdottir, H., Ghandi, M., Mesirov, J. P. & Tamayo, P. The Molecular Signatures Database (MSigDB) hallmark gene set collection. *Cell Syst* **1**, 417-425, doi:10.1016/j.cels.2015.12.004 (2015).

260 Schoggins, J. W., Wilson, S. J., Panis, M., Murphy, M. Y., Jones, C. T., Bieniasz, P. & Rice, C. M. A diverse range of gene products are effectors of the type I interferon antiviral response. *Nature* **472**, 481-485, doi:10.1038/nature09907 (2011).

261 Fischer, L., Lucendo-Villarin, B., Hay, D. C. & O'Farrelly, C. Human PSC-Derived Hepatocytes Express Low Levels of Viral Pathogen Recognition Receptors, but Are Capable of Mounting an Effective Innate Immune Response. *Int J Mol Sci* **21**, doi:10.3390/ijms21113831 (2020).

262 Zhang, C., Freistaedter, A., Schmelas, C., Gunkel, M., Dao Thi, V. L. & Grimm, D. An RNA Interference/Adeno-Associated Virus Vector–Based Combinatorial Gene Therapy Approach Against Hepatitis E Virus. **6**, 878-888, doi:10.1002/hep4.1842 (2022).

263 Goubau, D., Deddouche, S. & Reis e Sousa, C. Cytosolic Sensing of Viruses. *Immunity* **38**, 855-869, doi:10.1016/j.immuni.2013.05.007 (2013).

264 Yin, X., Riva, L., Pu, Y., Martin-Sancho, L., Kanamune, J., Yamamoto, Y., Sakai, K., Gotoh, S., Miorin, L., De Jesus, P. D., Yang, C. C., Herbert, K. M., Yoh, S., Hultquist, J. F., García-Sastre, A. & Chanda, S. K. MDA5 Governs the Innate Immune Response to SARS-CoV-2 in Lung Epithelial Cells. *Cell Rep* **34**, 108628, doi:10.1016/j.celrep.2020.108628 (2021).

265 Rebendenne, A., Valadão, A. L. C., Tauziet, M., Maarifi, G., Bonaventure, B., McKellar, J., Planès, R., Nisole, S., Arnaud-Arnould, M., Moncorgé, O. & Goujon, C. SARS-CoV-2 triggers an MDA-5-dependent interferon response which is unable to control replication in lung epithelial cells. *J Virol* **95**, doi:10.1128/jvi.02415-20 (2021).

266 Thorne, L. G., Bouhaddou, M., Reuschl, A. K., Zuliani-Alvarez, L., Polacco, B., Pelin, A., Batra, J., Whelan, M. V. X., Hosmillo, M., Fossati, A., Ragazzini, R., Jungreis, I., Ummadi, M., Rojc, A., Turner, J., Bischof, M. L., Obernier, K., Braberg, H., Soucheray, M., Richards, A., Chen, K. H., Harjai, B., Memon, D., Hiatt, J., Rosales, R., McGovern, B. L., Jahun, A., Fabius, J. M., White, K., Goodfellow, I. G., Takeuchi, Y., Bonfanti, P., Shokat, K., Jura, N., Verba, K., Noursadeghi, M., Beltrao, P., Kellis, M., Swaney, D. L., García-Sastre, A., Jolly, C., Towers, G. J. & Krogan, N. J. Evolution of enhanced innate immune evasion by SARS-CoV-2. *Nature* **602**, 487-495, doi:10.1038/s41586-021-04352-y (2022).

267 Panda, S. K., Ansari, I. H., Durgapal, H., Agrawal, S. & Jameel, S. The in vitro-synthesized RNA from a cDNA clone of hepatitis E virus is infectious. *J Virol* **74**, 2430-2437, doi:10.1128/jvi.74.5.2430-2437.2000 (2000).

268 King, C. R. & Mehle, A. Retasking of canonical antiviral factors into proviral effectors. *Curr Opin Virol* **56**, 101271, doi:10.1016/j.coviro.2022.101271 (2022).

269 Wong, S. K. & Lazinski, D. W. Replicating hepatitis delta virus RNA is edited in the nucleus by the small form of ADAR1. *Proc Natl Acad Sci U S A* **99**, 15118-15123, doi:10.1073/pnas.232416799 (2002).

270 Prelli Bozzo, C., Nchioua, R., Volcic, M., Koepke, L., Krüger, J., Schütz, D., Heller, S., Stürzel, C. M., Kmiec, D., Conzelmann, C., Müller, J., Zech, F., Braun, E., Groß, R., Wettstein, L., Weil, T., Weiß, J., Diofano, F., Rodríguez Alfonso, A. A., Wiese, S., Sauter, D., Münch, J., Goffinet, C., Catanese, A., Schön, M., Boeckers, T. M., Stenger, S., Sato, K., Just, S., Kleger, A., Sparrer, K. M. J. & Kirchhoff, F. IFITM proteins promote SARS-CoV-2 infection and are targets for virus inhibition in vitro. *Nat Commun* **12**, 4584, doi:10.1038/s41467-021-24817-y (2021).

271 Shafat, Z., Ahmed, A., Parvez, M. K. & Parveen, S. Intrinsic disorder in the open reading frame 2 of hepatitis E virus: a protein with multiple functions beyond viral capsid. *Journal, genetic engineering & biotechnology* **21**, 33, doi:10.1186/s43141-023-00477-x (2023).

272 Arai, M., Suetaka, S. & Ooka, K. Dynamics and interactions of intrinsically disordered proteins. *Current opinion in structural biology* **84**, 102734, doi:10.1016/j.sbi.2023.102734 (2024).

273 Bret, H., Gao, J., Zea, D. J., Andreani, J. & Guerois, R. From interaction networks to interfaces, scanning intrinsically disordered regions using AlphaFold2. *Nat Commun* **15**, 597, doi:10.1038/s41467-023-44288-7 (2024).

274 Versini, R., Sritharan, S., Aykac Fas, B., Tubiana, T., Aimeur, S. Z., Henri, J., Erard, M., Nüsse, O., Andreani, J., Baaden, M., Fuchs, P., Galochkina, T., Chatzigoulas, A., Cournia, Z., Santuz, H., Sacquin-Mora, S. & Taly, A. A Perspective on the Prospective Use of AI in Protein Structure Prediction. *Journal of chemical information and modeling* **64**, 26-41, doi:10.1021/acs.jcim.3c01361 (2024).

275 Durham, J., Zhang, J., Humphreys, I. R., Pei, J. & Cong, Q. Recent advances in predicting and modeling protein-protein interactions. *Trends in biochemical sciences* **48**, 527-538, doi:10.1016/j.tibs.2023.03.003 (2023).

276 Bressanelli, S., Fieulaine, S. & Tubiana, T. Structural biology of single-stranded, positive-sense RNA viruses in the age of accurate atomic-scale predictions of protein structures. *Virology* **608**, 110546, doi:10.1016/j.virol.2025.110546 (2025).

277 Joshi, G., Décembre, E., Brocard, J., Montpellier, C., Ferrié, M., Allatif, O., Mehnert, A. K., Pons, J., Galiana, D., Dao Thi, V. L., Jouvenet, N., Cocquerel, L. & Dreux, M. Plasmacytoid dendritic cell sensing of hepatitis E virus is shaped by both viral and host factors. *Life science alliance* **8**, doi:10.26508/lsa.202503256 (2025).

278 Zheng, D. L., Zhang, L., Cheng, N., Xu, X., Deng, Q., Teng, X. M., Wang, K. S., Zhang, X., Huang, J. & Han, Z. G. Epigenetic modification induced by hepatitis B virus X protein via interaction with de novo DNA methyltransferase DNMT3A. *J Hepatol* **50**, 377-387, doi:10.1016/j.jhep.2008.10.019 (2009).

279 Salvetti, A. & Greco, A. Viruses and the nucleolus: the fatal attraction. *Biochimica et biophysica acta* **1842**, 840-847, doi:10.1016/j.bbadis.2013.12.010 (2014).

280 Iarovaia, O. V., Ioudinkova, E. S., Velichko, A. K. & Razin, S. V. Manipulation of Cellular Processes via Nucleolus Hijaking in the Course of Viral Infection in Mammals. *Cells* **10**, doi:10.3390/cells10071597 (2021).

281 McDougal, M. B., De Maria, A. M., Ohlson, M. B., Kumar, A., Xing, C. & Schoggins, J. W. Interferon inhibits a model RNA virus via a limited set of inducible effector genes. *EMBO reports* **24**, e56901, doi:10.15252/embr.202356901 (2023).

282 Bruurs, L. J. M., Müller, M., Schipper, J. G., Rabouw, H. H., Boersma, S., van Kuppeveld, F. J. M. & Tanenbaum, M. E. Antiviral responses are shaped by heterogeneity in viral replication dynamics. *Nat Microbiol* **8**, 2115-2129, doi:10.1038/s41564-023-01501-z (2023).

283 Grunvogel, O., Colasanti, O., Lee, J. Y., Kloss, V., Belouzard, S., Reustle, A., Esser-Nobis, K., Hesebeck-Brinckmann, J., Mutz, P., Hoffmann, K., Mehrabi, A., Koschny, R., Vondran, F. W. R., Gotthardt, D., Schnitzler, P., Neumann-Haefelin, C., Thimme, R., Binder, M., Bartenschlager, R., Dubuisson, J., Dalpke, A. H. & Lohmann, V. Secretion of Hepatitis C Virus Replication Intermediates Reduces Activation of Toll-Like Receptor 3 in Hepatocytes. *Gastroenterology* **154**, 2237-2251 e2216, doi:10.1053/j.gastro.2018.03.020 (2018).

284 Loske, J., Röhmel, J., Lukassen, S., Stricker, S., Magalhães, V. G., Liebig, J., Chua, R. L., Thürmann, L., Messingschlager, M., Seegebarth, A., Timmermann, B., Klages, S., Ralser, M., Sawitzki, B., Sander, L. E., Corman, V. M., Conrad, C., Laudi, S., Binder, M., Trump, S., Eils, R., Mall, M. A. & Lehmann, I. Pre-activated antiviral innate immunity in the upper airways controls early SARS-CoV-2 infection in children. *Nat Biotechnol* **40**, 319-324, doi:10.1038/s41587-021-01037-9 (2022).

285 Triana, S., Metz-Zumaran, C., Ramirez, C., Kee, C., Doldan, P., Shahraz, M., Schraivogel, D., Gschwind, A. R., Sharma, A. K., Steinmetz, L. M., Herrmann, C., Alexandrov, T., Boulant, S. & Stanifer, M. L. Single-cell analyses reveal SARS-CoV-2 interference with intrinsic immune response in the human gut. *Molecular systems biology* **17**, e10232, doi:10.15252/msb.202110232 (2021).

286 Ramos, I., Smith, G., Ruf-Zamojski, F., Martínez-Romero, C., Fribourg, M., Carbajal, E. A., Hartmann, B. M., Nair, V. D., Marjanovic, N., Monteagudo, P. L., DeJesus, V. A., Mutetwa, T., Zamojski, M., Tan, G. S., Jayaprakash, C., Zaslavsky, E., Albrecht, R. A., Sealfon, S. C., García-Sastre, A. & Fernandez-Sesma, A. Innate Immune Response to Influenza Virus at Single-Cell Resolution in Human Epithelial Cells Revealed Paracrine Induction of Interferon Lambda 1. *J Virol* **93**, doi:10.1128/jvi.00559-19 (2019).

287 Sun, J., Vera, J. C., Drnevich, J., Lin, Y. T., Ke, R. & Brooke, C. B. Single cell heterogeneity in influenza A virus gene expression shapes the innate antiviral response to infection. *PLoS Pathog* **16**, e1008671, doi:10.1371/journal.ppat.1008671 (2020).

288 Shalek, A. K., Satija, R., Adiconis, X., Gertner, R. S., Gaublomme, J. T., Raychowdhury, R., Schwartz, S., Yosef, N., Malboeuf, C., Lu, D., Trombetta, J. J., Gennert, D., Gnirke, A., Goren, A., Hacohen, N., Levin, J. Z., Park, H. & Regev, A. Single-cell transcriptomics reveals bimodality in expression and splicing in immune cells. *Nature* **498**, 236-240, doi:10.1038/nature12172 (2013).

289 Patil, S., Fribourg, M., Ge, Y., Batish, M., Tyagi, S., Hayot, F. & Sealfon, S. C. Single-cell analysis shows that paracrine signaling by first responder cells shapes the interferon-β response to viral infection. *Science signaling* **8**, ra16, doi:10.1126/scisignal.2005728 (2015).

290 Rand, U., Rinas, M., Schwerk, J., Nöhren, G., Linnes, M., Kröger, A., Flossdorf, M., Kály-Kullai, K., Hauser, H., Höfer, T. & Köster, M. Multi-layered stochasticity and paracrine signal propagation shape the type-I interferon response. *Molecular systems biology* **8**, 584, doi:10.1038/msb.2012.17 (2012).

291 Van Eyndhoven, L. C., Singh, A. & Tel, J. Decoding the dynamics of multilayered stochastic antiviral IFN-I responses. *Trends Immunol* **42**, 824-839, doi:10.1016/j.it.2021.07.004 (2021).

292 Kinast, V., Klohn, M., Nocke, M. K., Todt, D. & Steinmann, E. Hepatitis E virus species barriers: seeking viral and host determinants. *Curr Opin Virol* **56**, 101274, doi:10.1016/j.coviro.2022.101274 (2022).

293 Feagins, A. R., Córdoba, L., Sanford, B. J., Dryman, B. A., Huang, Y. W., LeRoith, T., Emerson, S. U. & Meng, X. J. Intergenotypic chimeric hepatitis E viruses (HEVs) with the genotype 4 human HEV capsid gene in the backbone of genotype 3 swine HEV are infectious in pigs. *Virus Res* **156**, 141-146, doi:10.1016/j.virusres.2010.12.011 (2011).

294 Aravalli, R. N., Cressman, E. N. & Steer, C. J. Hepatic differentiation of porcine induced pluripotent stem cells in vitro. *Veterinary journal (London, England : 1997)* **194**, 369-374, doi:10.1016/j.tvjl.2012.05.013 (2012).

295 Park, K. M., Hussein, K. H., Ghim, J. H., Ahn, C., Cha, S. H., Lee, G. S., Hong, S. H., Yang, S. & Woo, H. M. Hepatic differentiation of porcine embryonic stem cells for translational research of hepatocyte transplantation. *Transplantation proceedings* **47**, 775-779, doi:10.1016/j.transproceed.2015.01.020 (2015).

296 Blanco-Melo, D., Nilsson-Payant, B. E., Liu, W. C., Uhl, S., Hoagland, D., Møller, R., Jordan, T. X., Oishi, K., Panis, M., Sachs, D., Wang, T. T., Schwartz, R. E., Lim, J. K., Albrecht, R. A. & tenOever, B. R. Imbalanced Host Response to SARS-CoV-2 Drives Development of COVID-19. *Cell* **181**, 1036-1045.e1039, doi:10.1016/j.cell.2020.04.026 (2020).

297 Neufeldt, C. J., Cerikan, B., Cortese, M., Frankish, J., Lee, J. Y., Plociennikowska, A., Heigwer, F., Prasad, V., Joecks, S., Burkart, S. S., Zander, D. Y., Subramanian, B., Gimi, R., Padmanabhan, S., Iyer, R., Gendarme, M., El Debs, B., Halama, N., Merle, U., Boutros, M., Binder, M. & Bartenschlager, R. SARS-CoV-2 infection induces a pro-inflammatory cytokine response through cGAS-STING and NF-κB. *Communications biology* **5**, 45, doi:10.1038/s42003-021-02983-5 (2022).

298 Kamar, N., Garrouste, C., Haagsma, E. B., Garrigue, V., Pischke, S., Chauvet, C., Dumortier, J., Cannesson, A., Cassuto-Viguier, E., Thervet, E., Conti, F., Lebray, P., Dalton, H. R., Santella, R., Kanaan, N., Essig, M., Mousson, C., Radenne, S., Roque-Afonso, A. M., Izopet, J. & Rostaing, L. Factors associated with chronic hepatitis in patients with hepatitis E virus infection who have received solid organ transplants. *Gastroenterology* **140**, 1481-1489, doi:10.1053/j.gastro.2011.02.050 (2011).

299 Plosker, G. L. & Foster, R. H. Tacrolimus: a further update of its pharmacology and therapeutic use in the management of organ transplantation. *Drugs* **59**, 323-389, doi:10.2165/00003495-200059020-00021 (2000).

300 Kemming, J., Gundlach, S., Panning, M., Huzly, D., Huang, J., Lütgehetmann, M., Pischke, S., Schulze Zur Wiesch, J., Emmerich, F., Llewellyn-Lacey, S., Price, D. A., Tanriver, Y., Warnatz, K., Boettler, T., Thimme, R., Hofmann, M., Fischer, N. & Neumann-Haefelin, C. Mechanisms of CD8+ T-cell failure in chronic hepatitis E virus infection. *J Hepatol* **77**, 978-990, doi:10.1016/j.jhep.2022.05.019 (2022).

301 Knolle, P. A. & Thimme, R. Hepatic immune regulation and its involvement in viral hepatitis infection. *Gastroenterology* **146**, 1193-1207, doi:10.1053/j.gastro.2013.12.036 (2014).

302 Koui, Y., Kido, T., Ito, T., Oyama, H., Chen, S. W., Katou, Y., Shirahige, K. & Miyajima, A. An In Vitro Human Liver Model by iPSC-Derived Parenchymal and Non-parenchymal Cells. *Stem cell reports* **9**, 490-498, doi:10.1016/j.stemcr.2017.06.010 (2017).

303 Park, J., Zhao, Y., Zhang, F., Zhang, S., Kwong, A. C., Zhang, Y., Hoffmann, H. H., Bushweller, L., Wu, X., Ashbrook, A. W., Stefanovic, B., Chen, S., Branch, A. D., Mason, C. E., Jung, J. U., Rice, C. M. & Wu, X. IL-6/STAT3 axis dictates the PNPLA3-mediated susceptibility to non-alcoholic fatty liver disease. *J Hepatol* **78**, 45-56, doi:10.1016/j.jhep.2022.08.022 (2023).

304 Bernareggi, D., Pouyanfard, S. & Kaufman, D. S. Development of innate immune cells from human pluripotent stem cells. *Experimental hematology* **71**, 13-23, doi:10.1016/j.exphem.2018.12.005 (2019).

305 Oliveira, N. A. J. & Sevim, H. Dendritic Cell Differentiation from Human Induced Pluripotent Stem Cells: Challenges and Progress. *Stem cells and development* **31**, 207-220, doi:10.1089/scd.2021.0305 (2022).

Appendix

Supplementary Figures

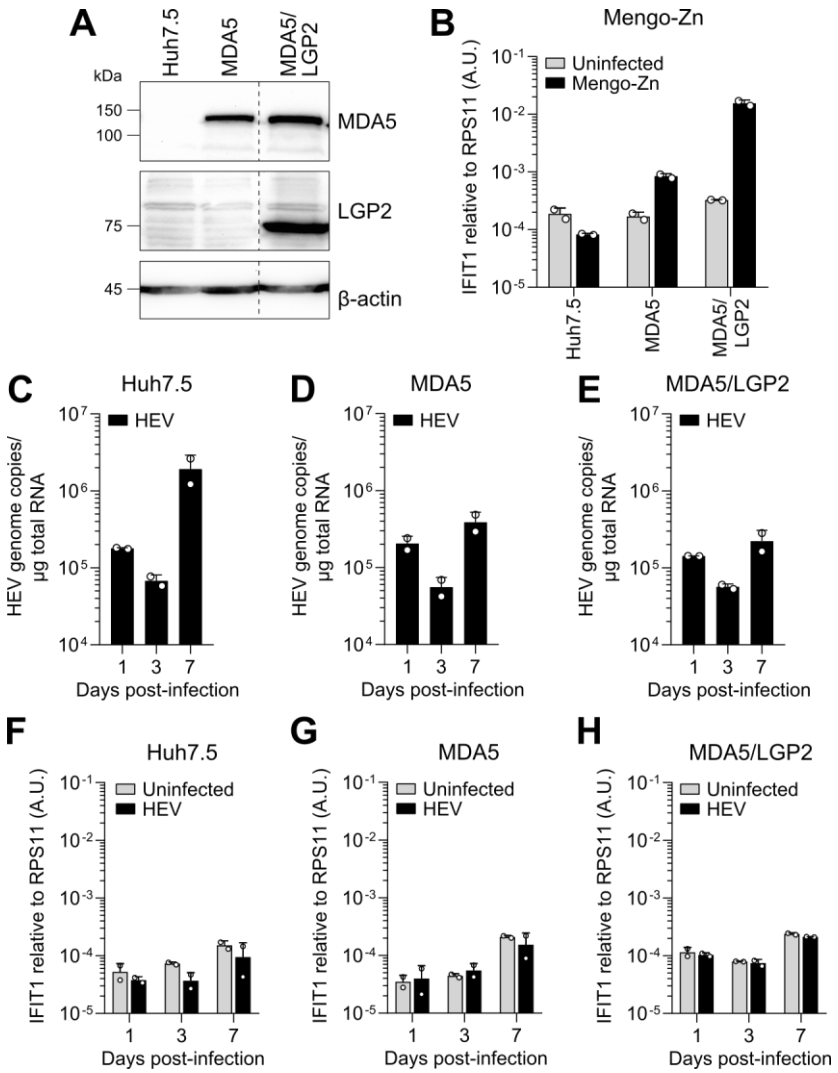

Supplementary Figure 1: Combined expression of MDA5 and LGP2 does not result in an HEV-induced antiviral response in Huh7.5 cells.
(A) Parental Huh7.5 and derived MDA5- and MDA5/LGP2-expressing cells were analyzed for protein expression of MDA5, LGP2, and the loading control β-actin by Western blot. Blot of a single experiment is shown. This experiment was performed by Carl Niklas Schneider under my direct supervision. kDa, kilodalton. (B) Huh7.5-derived cell lines were infected with Mengo-Zn virus at an MOI of 1, and *IFIT1* expression was analyzed by RT-qPCR relative to the housekeeping gene *RPS11* using the $2^{-\Delta Ct}$ method. Data show mean ± SD of a single experiment with two biological replicates. A.U., arbitrary units. This experiment was performed by Miriam Martens under my direct supervision. (C) Parental Huh7.5 cells and derived cell lines ectopically expressing (D) MDA5 and (E) MDA5/LGP2 were infected with HEV overnight at MOI 0.5. Cell lysates were analyzed by RT-qPCR for HEV RNA. Data show mean ± SD of a single experiment with two biological replicates. This experiment was performed by Miriam Martens under my direct supervision. (F) Samples of C–E of parental Huh7.5, (G) MDA5-, and (H) MDA5/LGP2-expressing Huh7.5 cells were analyzed for *IFIT1* expression relative to the housekeeping gene *RPS11* using the $2^{-\Delta Ct}$ method. Data show mean ± SD of a single experiment with two biological replicates. A.U., arbitrary units. This experiment was performed by Miriam Martens under my direct supervision.

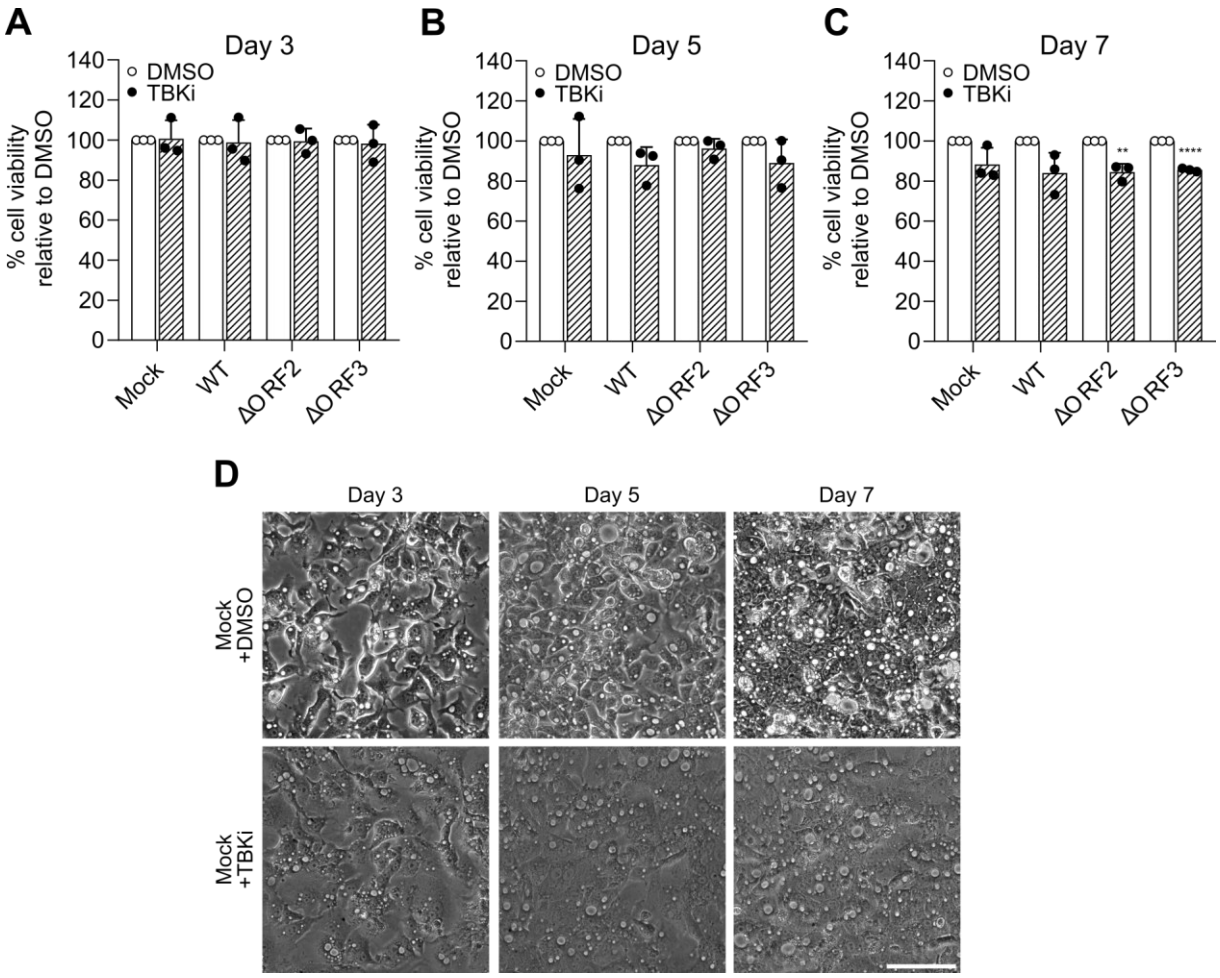

Supplementary Figure 2: BX795 treatment of electroporated HepG2/C3A cells has minor effects on cell viability.
(A) HepG2/C3A cells were mock-electroporated or electroporated with HEV WT, ΔORF2, or ΔORF3 RNA and mixed 1:1 with mock-electroporated cells. Cells were treated with 6 µM BX795 (TBKi) or respective DMSO vehicle control (0.06%) 48 h before the respective harvesting time point. On day 3, day 5, and day 7 post-EPO, MTS assay was performed, and cell viability was calculated relative to the DMSO control. Data show mean ± SD of n = 3 independent experiments with one biological replicate each. Statistical analysis over DMSO control was performed using multiple unpaired two-tailed Student's t-tests. If not indicated, the results were not significant. **: $p < 0.01$; ****: $p < 0.0001$. (D) Mock-electroporated HepG2/C3A cells from A–C were imaged with a Nikon Eclipse Ts2-FL widefield epifluorescence microscope to assess the effects of BX795 on cell morphology. Exemplary images of n = 3 independent experiments. Scale bar, 100 µm.

Supplementary Tables

Supplementary Table 1: List of ISGs used for UMAP projections in the scRNA-seq analysis.

ABCA9	CCDC92	EPSTI	IFI30	MKX	PRKD2	TBX3
ABLIM3	CCL19	ERLIN1	IFI35	MOV10	PSCD1	TCF7L2
ABTB2	CCL2	ETV6	IFI44	MS4A4A	PSMB8	TDRD7
ACSL1	CCL4	ETV7	IFI44	MSR1	PSMB9	TFEC
ADAMDEC1	CCL5	EXT1	IFI44L	MT1F	PTMA	THBD
ADAR	CCL8	FAM125B	IFI6	MT1G	PUS1	THOCA
ADFP	CCNA1	FAM134B	IFIH1	MT1H	PXK	TIMP1
ADM	CCND3	FAM46A	IFIT1	MT1M	RAB27A	TLK2
AGPAT9	CCR1	FAM46C	IFIT2	MT1X	RARRES3	TLR3
AHNAK2	CD163	FAM70A	IFIT3	MTHFD2L	RASGEF1	TLR7
AIM2	CD274	FBX06	IFIT5	MX1	RASSF4	TMEM140
AKT3	CD38	FCGR1A	IFITM1	MX2	RBCK1	TMEM49
ALDH1A1	CD69	FER1L3	IFITM2	MYD88	RBM25	TMEM51
AMPH	CD74	FFAR2	IFITM3	N4BP1	RGS1	TNFAIP3
ANGPTL1	CD80	FKBP5	IFNGR1	NAPA	RIPK2	TNFAIP6
ANKFY1	CD9	FLJ11286	IGFBP2	NCF1	RNASE4	TNFRSF10A
ANKRD22	CDKN1A	FLJ23556	IL15	NCOA3	RNF19B	TNFSF10
APOBEC3A	CEACAM1	FLJ39739	IL15RA	NDC80	RNF24	TNFSF13B
APOBEC3G	CEBPD	FLT1	IL17RB	NFIL3	RPL22	TRAFD1
APOL1	CES1	Fluc	IL1R	NMI	RSAD2	TREX1
APOL2	CFB	FNDC3B	IL1RN	NOD2	RTP4	TRIM14
APOL3	CHMP5	FNDC4	IL28RA	NOS2A	S100A8	TRIM21
APOL6	CLEC2B	FUT4	ILGST	NPAS2	SAA1	TRIM25
AQP9	CLEC4D	G6PC	IMPA2	NRN1	SAMD4A	TRIM34
ARG2	CLEC4E	GAK	IRF1	NT5C3	SAMHD1	TRIM38
ARHGEF3	CMAH	GALNT2	IRF2	NUP50	SAT1	TRIM5
ARNTL	CNP	GBP1	IRF7	OAS1	SAT3	TRIM56
ATF3	COMMD3	GBP2	IRF9	OAS2	SCARB2	TXNIP
ATP10D	CPT1A	GBP3	ISG15	OAS3	SCO2	TYMP
AXUD1	CREB3L3	GBP4	ISG20	OASL	SECTM1	UBA7
B2M	CRP	GBP5	JAK2	ODC1	SERPINB9	UBE2L6
B4GALT5	CRY1	GCA	JUNB	OGFR	SERPINE1	ULK4
BAG1	CSDA	GCH1	KIAA0040	OPTN	SERPING1	UNC84B
BATF2	CTCFL	GEM	KIAA0082	P14K2B	SIRPA	UNC93B1
BCL2L14	CX3CL1	GJA4	KIAA1618	P2RY6	SLC15A3	UPP2
BCL3	CXCL10	GK	LAMP3	PABPC4	SLC16A1	USP18
BLVRA	CXCL11	GLRX	LAP3	PADI2	SLC1A1	VAMP5
BLZF1	CXCL9	Gluc	LEPR	PARP12	SLC25A28	VEGFC
BST2	CYP1B1	GMPR	LGALS3	PBEF1	SLC25A30	WARS
BTN3A3	DCP1A	GPX2	LGALS9	PCTK2	SLFN12	WHDC1

BUB1	DDIT4	GTPBP1	LGMN	PCTK3	SLFN5	XAF1
C10orf10	DDX3X	GTPBP2	LINCR	PDGFRL	SMAD3	ZAP
C15orf48	DDX58	GZMB	LIPA	PDK1	SNN	ZBP1
C1S	DDX60	HEG1	LMO2	PFKFB3	SOCS1	ZNF107
C22orf28	DEFB1	HERC6	LRG1	PHF11	SOCS2	ZNF295
C2orf31	DHX58	HES4	LY6E	PHF15	SP110	ZNF313
C4orf32	DNAPTP6	HESX1	MAB21L2	PIM3	SPSB1	ZNF385B
C4orf33	DTX3L	HK2	MAFB	PLEKHA4	SPTLC2	
C5orf27	DUSP5	HLA-C	MAFF	PLSCR1	SSBP3	
C5orf39	DYNLT1	HLA-E	MAP3K14	PMAIP1	STAP1	
C6orf150	EHD4	HLA-F	MAP3K5	PML	STARD5	
C9orf19	EIF2AK2	HLA-G	MARCKS	PMM2	STAT1	
C9orf91	EIF3L	HPSE	MASTL	PNPT1	STAT2	
CASP1	ELF1	HSH2D	MAX	PNRC1	STEAP4	
CASP7	ENPP1	IDO1	MCL1	PPM1K	TAGAP	
CCDC109B	EPAS1	IFI16	MCOLN2	PRAME	TAP1	
CCDC75	EPST11	IFI27	MICB	PRIC285	TAP2	

Publications

Submitted

Mehnert, A.-K., Stegmaier, S., Ramirez, C., Magalhães, V. G., Siebenkotten, C., Hu, J., Costa, A. L., Kirrmaier, D., Knop, M., Wu, X., Tubiana, T., Herrmann, C., Binder, M. & Thi, V. L. D. The hepatitis E virus capsid protein ORF2 counteracts cell-intrinsic antiviral responses to enable persistence in hepatocytes. 2025.2002.2003.636239, doi:10.1101/2025.02.03.636239 %J bioRxiv (2025).

This publication resulted from part of the data presented in this dissertation. I performed the majority of the experiments, contributed to the conceptualization of the study, designed the figures, wrote the initial draft of the manuscript, and significantly contributed to the final preparation.

Published

Joshi, G., Décembre, E., Brocard, J., Montpellier, C., Ferrié, M., Allatif, O., **Mehnert, A.-K.**, Pons, J., Galiana, D., Dao Thi, V. L., Jouvenet, N., Cocquerel, L. & Dreux, M. Plasmacytoid dendritic cell sensing of hepatitis E virus is shaped by both viral and host factors. Life science alliance 8, doi:10.26508/lsa.202503256 (2025).

I contributed to this study by providing HepG2/C3A cells and the HEV GAD mutant.

Ssebyatika, G., Dinkelborg, K., Ströh, L. J., Hinte, F., Corneillie, L., Hueffner, L., Guzman, E. M., Nankya, P. L., Plückebaum, N., Fehlau, L., Garn, J., Meyer, N., Prallet, S., **Mehnert, A.-K.**, Kraft, A. R. M., Verhoye, L., Jacobsen, C., Steinmann, E., Wedemeyer, H., Viejo-Borbolla, A., Dao Thi, V. L., Pietschmann, T., Lütgehetmann, M., Meuleman, P., Dandri, M., Krey, T. & Behrendt, P. Broadly neutralizing antibodies isolated from HEV convalescents confer protective effects in human liver-chimeric mice. Nat Commun 16, 1995, doi:10.1038/s41467-025-57182-1 (2025).

I contributed to this study by providing differentiated HLCs for a neutralization assay with primary HEV isolates, which was performed by my colleague Sarah Prallet.

Schrader, J. A., Burkard, T. L., Brüggemann, Y., Gömer, A., Meister, T. L., Fu, R. M., **Mehnert, A.-K.**, Dao Thi, V. L., Behrendt, P., Durantel, D., Broering, R., Vondran, F. W. R., Todt, D., Kinast, V. & Steinmann, E. EGF receptor modulates HEV entry in human hepatocytes. Hepatology 77, 2104-2117, doi:10.1097/hep.0000000000000308 (2023).

I provided differentiated HLCs for shRNA knockdowns, which were performed by my colleague Rebecca Fu.

Bove, G., **Mehnert, A.-K**. & Dao Thi, V. L. in iPSCs for Studying Infectious Diseases Vol. 8 (ed Alexander Birbrair) 149-213 (Academic Press, 2021).

I significantly contributed to the conceptualization and the writing, as well as the final preparation and editing of this book chapter.